The thermal behaviour of polyamide-12 in the powder bed fusion process

By

Amrita Kaur Bhogal

UNIVERSITY OF BIRMINGHAM

A thesis submitted to the University of Birmingham for the degree of

DOCTOR OF PHILOSOPHY

School of Metallurgy and Materials

College of Engineering and Physical Sciences

University of Birmingham

March 2023

ABSTRACT

Polyamide-12 (PA-12) powder is used in additive manufacturing (AM) techniques such as selective laser sintering (SLS) and Multi-Jet Fusion (MJF). MJF is a proprietary Hewlett-Packard technique that uses a fusing agent (FA) and detailing agent (DA). These agents are a fundamental and unique part of MJF in comparison to other AM techniques.

PA-12 powder was characterised using a variety of techniques including Differential Scanning Calorimetry (DSC), Fourier Transform Infrared Spectroscopy (FTIR), Scanning Electron Microscopy (SEM), Particle Size Analysis (PSA), Thermogravimetric Analysis (TGA) and optical microscopy. DSC showed that the peak melting and peak crystallisation temperature of PA-12 were 186 and 148 ℃, respectively. TGA was used to measure the mass loss degradation of PA-12, where a 1% mass loss was displayed at 322 ℃. FTIR spectra showed characteristic peaks in line with literature for a part manufactured by MJF. PSA showed that the particle size varied between 11.96 – 164.32 μm. SEM was used to characterise the shape of the powder particles. The powder particles appeared to be elongated and non-uniform, where some particles were more spherical. Optical microscopy was used to observe the interaction of powder particles on melting, it was shown that the powder particles fused together to form a droplet shape.

The isothermal crystallisation kinetics were studied between 162 to 168 ℃. It was demonstrated that as the isothermal crystallisation temperature increased, the time taken for crystallisation increased. This data was used to determine the equilibrium melting temperature (T_M^0) by the Hoffman-Weeks method using the peak melting temperature and last trace of crystallinity; where T_M^0 was equal to 188 and 205 ℃, respectively. The Avrami and Tobin model was used to explore the isothermal crystallisation kinetics. Of which, the Avrami and Tobin model were successful in describing the isothermal crystallisation kinetics of PA-12. In the Avrami model *n* ranged from 2.73 to 3.63 and in the Tobin model *n* ranged from 3.15 to 4.23 for the primary crystallisation process.

The non-isothermal crystallisation kinetics were studied between 5 to 40 ℃/min. It was demonstrated that as the cooling rate increased, the time taken for crystallisation decreased. The Jeziorny-modified Avrami model was successful in describing the non-isothermal crystallisation kinetics of PA-12. In the Jeziorny-modified Avrami model *n* ranged from 4.42 to 7.68.

The influence of the FA, DA and their chemical constituents on the thermal behaviour of PA-12 was studied by creating PA-12 blends at varying wt. % compositions. The blends included PA-12/FA, PA-12/DA, PA-12/water PA-12/carbon black, PA-12/2-PYR and PA-12/2-PYR/water. Since the powder used in MJF often is refreshed, PA-12 was aged artificially in an oven at 170℃ for 7 days to represent aged powder. The thermal behaviour of aged PA-12 powder and aged PA-12 blends was studied. It was demonstrated that the 2-PYR had a significant impact on the thermal properties of PA-12 via its action as plasticiser: DSC revealed a depression in polymer glass transition temperature (T_g), of up to 17 ℃, and a depression in melting temperature, of up to 10 ℃, with increasing composition of 2-PYR. Moreover, the crystallisation behaviour was also affected by the 2-PYR component in that its presence decreased the supercooling required for the onset of crystallisation. FTIR analysis revealed a small peak at 1690 cm^{-1} which was assigned to 2-PYR. This indicated that 2-PYR was retained in the PA-12 and interacted with the polymer via hydrogen bonding. Optical microscopy showed that the 2-PYR constituent did not affect the spherulite sizes, but in the case of the carbon black constituent, it was found to be rejected to the inter-spherulitic regions and this was coupled with a noTable reduction in spherulite size. This showed that carbon black and 2-PYR were fundamental components within the FA and DA with respect to their impact on the thermal properties and microstructure of PA-12.

ACKNOWLEDGMENTS

I would like to thank my supervisor, Mike Jenkins, my family and friends for their continued support and guidance throughout the PhD. I would also like to thank the Manufacturing Technology Centre (MTC) for supplying the HP 3D High Reusability Polyamide-12 powder, Fusing Agent and Detailing Agent to enable this research.

LIST OF ABBREVIATIONS

2-PYR – 2-pyrrolidone.

CB – Carbon black.

DA – Detailing agent

DSC – Differential Scanning Calorimetry.

FA – Fusing Agent.

FTIR – Fourier Transform Infrared Spectroscopy.

HP - Hewlett-Packard.

HSS – High Speed Sintering.

MEX – Material Extrusion.

MJF – Multi-Jet Fusion

PA-11 – Polyamide-11.

PA-12 – Polyamide-12.

PP – Polypropylene.

PBF – Powder Bed Fusion.

SLS – Selective Laser Sintering.

RAM – Radiation Absorbing Material.

TGA – Thermal Gravitational Analysis.

Contents

CHAPTER 1 - INTRODUCTION

1.1 Background to polymers

Polymers are long chain molecules that are made up of many repeat units called monomers. The skeletal structure of a polymer can be linear or non-linear. Examples of linear and non-linear polymer structures include cyclic, branched and network polymers. A linear polymer will have 2 chain ends whereas a non-linear polymer, such as a cyclic polymer, does not have a chain end. All polymers are formed by a process called polymerisation. In this process many polymer chains link together by cross-linking (1). An example of the structure of polymers is shown in Figure 1.1.1.

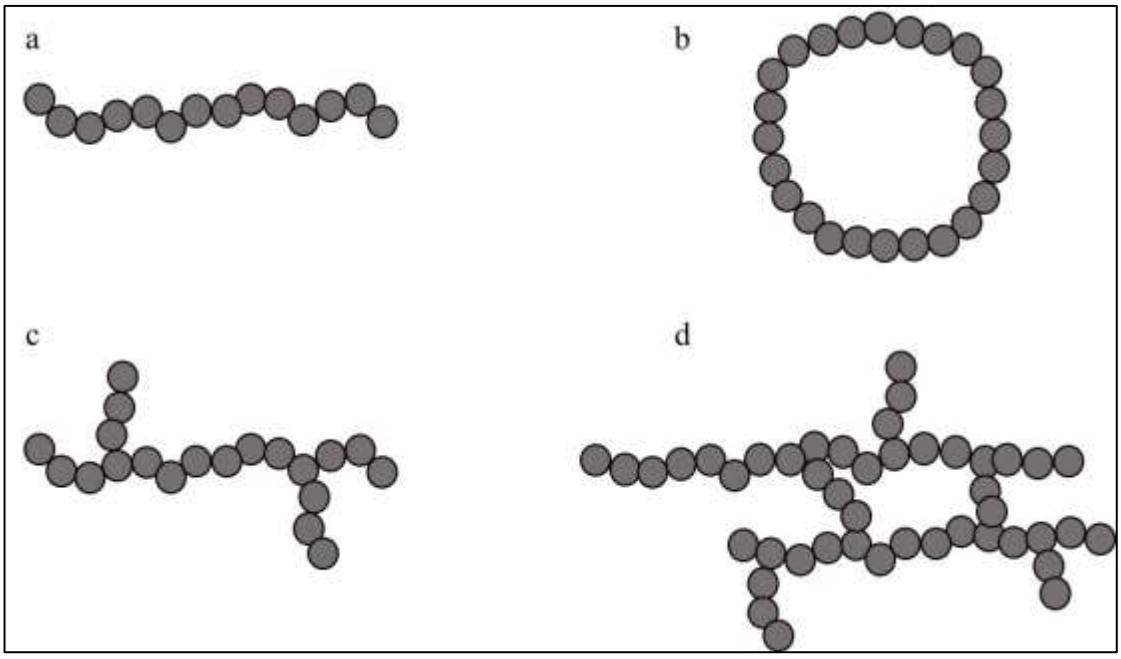

Figure 1.1.1 – An example of different skeletal polymer structures a) linear, b) cyclic, c) branched d) cross-linked.

The term ‘polymer’ covers a large range of materials. Polymers can be categorised as natural, synthetic and elastomers (1). Natural polymers can be further sub-categorised into groups such as proteins and polynucleotides. Synthetic polymers can be further sub-categorised into thermoplastic and thermoset polymers. Elastomers can be further sub-categorised into natural or synthetic elastomers. The structure of a synthetic elastomer can vary from the naturally occurring elastomer equivalent, yet the elastic properties can be comparable to the natural elastomer counterpart. Furthermore, the structure of a polymer will vary, for example, natural polymers have a more complex structure than synthetic polymers (1).

1.2 Amorphous polymers

Amorphous polymers contain highly disordered and entangled polymer chains, whereas crystalline materials are composed of highly ordered and tightly packed polymer chains (2). The structure of a semi-crystalline material contains both amorphous and crystalline regions, in which the amorphous regions are trapped in-between the crystalline regions.

It was mentioned that synthetic polymers can be categorised into thermoplastic and thermoset polymers. The term thermoplastic and thermoset relate to the behaviour of the polymer when heated. A thermoset polymer will irreversibly harden above a certain temperature. Whereas a thermoplastic polymer will soften when heated above the glass transition temperature (T_g) and will transform into a melt when heated above its melting point. A thermoplastic polymer can be moulded into a shape when heated above its melting point and on cooling the shape is retained. Subsequent heating and cooling of a thermoplastic polymer enable further remoulding and reshaping of the material.

In an amorphous polymer, at low temperatures the polymer will exist in a glassy state where the polymer chains are locked in a highly disordered orientation. However, as the temperature rises and thermal energy is introduced into the system, the polymer chains experience an increase in mobility and molecular motion (1). This is known as the T_g and often occurs over a temperature range. The T_g is characteristic to different polymers. The temperature range in which the T_g occurs is influenced by the length of the polymer chain and level of entanglement (1). A polymer that has many highly entangled chains requires more thermal energy to reach the T_g in order to become mobile. The T_g will also be influenced by chain flexibility, molecular structure, molar mass, and branching or crosslinking (3). After passing the T_g, the amorphous regions no longer behave like a brittle glass but behave as rubber-like material. As an amorphous polymer cools from the molten state, the molecular motion reduces until the T_g is reached, at this point the polymer chains are locked in a random disordered orientation. The orientation in which the polymer chains are locked is determined by their orientation at a temperature just above the T_g (1).

1.3 Semi-crystalline polymers

In semi-crystalline polymers, both amorphous and crystalline regions are present. The structure of a semi-crystalline polymer will result in a distinct morphological structure, often formed by melt-recrystallisation (1).

In linear polymers, spherulites can form on crystallisation from the melt. Spherulites are characterised by their distinct circular structures, and their growth is largely determined by the crystallisation temperature and cooling rate. Firstly, polymer chains aggregate in a fibrous subunit to form a rod like structure. After, the edges of the fibrils spread out to form an intermediate structure known as a sheaf, this provides the spherulitic outline. The structure continues to fill out with more fibrous units. Eventually, a spherulite is developed from the chain folded lamellae which make up the crystalline regions with amorphous regions trapped in-between (2,4).

The crystallisation temperature determines the number, size and fine structure of a spherulite. At temperatures closer to the melting temperature of the polymer, few large fibrous structures are formed. Whereas, at lower temperatures the nucleation density is high and a large number of small spherulites are formed (1).

The structure of the lamellae which make up the crystalline region has been a topic of discussion for many years, where many authors have used various characterisation techniques to gain a deeper understanding of the crystalline structure. For example, in the 1950's it was demonstrated by analysis of x-ray diffraction patterns that polymer single crystals could grow from a polymer solution (5). Polymer single crystals were composed of polymer chains that fold back on themselves during crystallisation to form structures known as lamellae, measuring at 10 – 20 nm thick (1,5). Polymers can also be crystallised from the melt, however they do not reach the same level of crystal perfection when compared to when a polymer is crystallised from a dilute polymer solution (6). As a result of neutron scattering techniques, two models were proposed to describe the structure of lamellae formed by melt-recrystallisation. These are called the regular folded array model (or the adjacent re-entry model) and the switchboard model (or the non-adjacent re-entry model) (1). In the regular folded array model, the chain folds are regular and uniform with adjacent re-entry of the chains; some chain ends contribute to a disordered surface. In the switchboard model, chain folding occurs but re-entry is random. The polymer chain may enter the lamella at different points to which it exited the lamella. Additionally, tie molecules may exist where chains may exit one lamella and enter an adjacent lamella (1). These models are illustrated in Figure 1.2.1. In the regular folded array model, the amorphous phase is not represented, however in the switchboard model the amorphous phase makes up most of a semi-crystalline polymer. In general, it is thought that polymers crystallised from the melt are more accurately represented by the switchboard model.

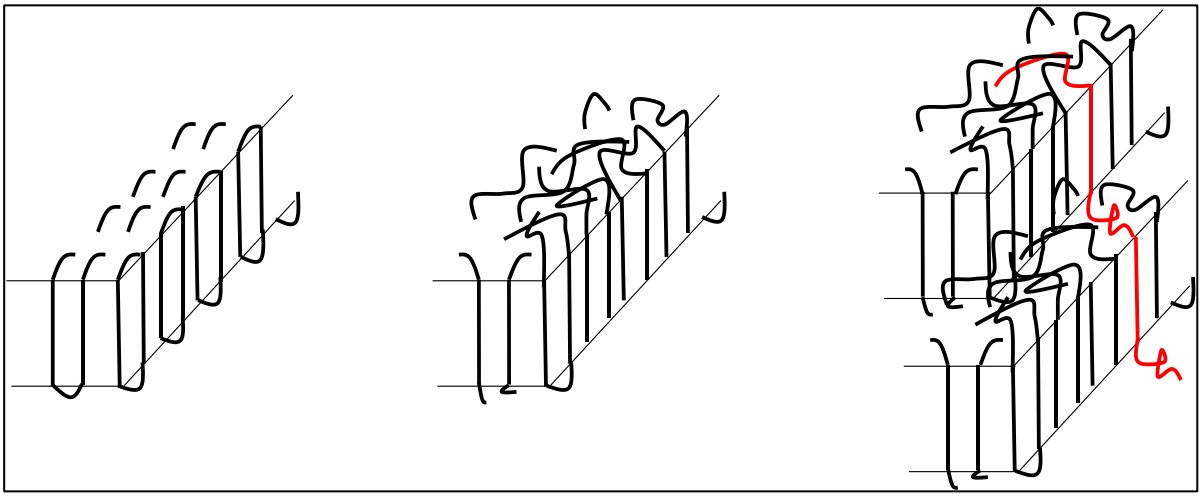

Figure 1.2.1 – Schematic of the regular folded array model (left) switchboard model (middle) and tie molecules, represented in red (right).

The solidification model was presented by Fisher. This model demonstrates that polymer chains straighten and align in regular arrays to form the lamellar structure (1). It is thought that on melt-recrystallisation the polymer chains do not reorder significantly, which would be required in order to create a uniform and nearly packed lamellar structure as demonstrated in the regular folded array model. This means that polymer chains do not need to undergo long range diffusion in a viscous medium. In-between the lamellar regions, the polymer chain enters the amorphous regions. Therefore, the solidification model is thought of as an extension of the switchboard model.

The position at which the polymer chain is reeled in from the melt on recrystallisation is a topic discussed by Hoffman, Flory and Yoon. It was considered for polymers of moderate molecular weights, the majority of polymer chains would be reeled in from the melt by a process called “reptation” (1). Reptation occurs at an adjacent position since this is energetically favourable. However, Florey and Yoon stated that polymer chains would not be reeled in at a site of adjacent re-entry due to the molecular

motion of the melt being too slow. Instead, they proposed that lamellae are formed by the straightening of polymer chains in localised areas. This makes up the crystalline regions. Meanwhile the rest of the polymer chain is entangled and makes up the amorphous regions.

1.3.1 Melting of semi-crystalline polymers

On heating of a semi-crystalline polymer, the amorphous regions undergo glassy to rubber transitions, therefore semi-crystalline polymers will also exhibit a T_g. At this point, the crystalline regions of the polymer remain highly ordered. However, as the temperature continues to rise, the thermal energy input is sufficient to break the intermolecular bonds within the crystalline regions. This is known as the melting point and occurs over a temperature range (1,7). The melting temperature range is influenced by the crystallite size and perfection. Often, small and imperfect crystals melt at lower temperatures since less thermal energy is required to break the existing intermolecular bonds that hold the structure together. Other factors that affect the crystalline arrangement of polymers, and therefore melting temperature, include symmetry, intermolecular bonding, tacticity and branching or molar mass (3).

The effect of crystallite size and perfection has an impact on the melting temperature of a polymer. At low crystallisation temperatures the segmental diffusion rate is low and the nucleation density is high. This produces small and imperfect crystals. At high crystallisation temperatures, the segmental diffusion rate is high and the nucleation density is low. This produces larger crystals with increased crystal perfection (1). The crystallite size and perfection are also affected by the symmetry of the polymer chain, intermolecular bonding, branching and molar mass. This is summarised by author J.M.G. Cowie (1).

At temperatures above the melting temperature of a polymer, the chains are highly entangled and disordered due to the polymer behaving as a viscous liquid (1). In this state, each chain occupies a given

volume and many conformational states are achieved. As the temperature decreases and crystallisation takes place, the free-volume available for each chain decreases. This limits the number of conformational states due to the influence of intermolecular forces which cause the polymer chains to form a rigid structure and align. There are factors that will hinder chain crystallisation. For example, chain entanglements will hinder the diffusion of chains into certain orientations. On cooling, the entropy reduces in favour of the free energy allowing crystallisation to take place (1). The crystalline regions are created from polymer chains that fold adjacent to one another in a tightly packed arrangement, these structures are known as lamellae (1).

In the crystalline state, polymer chains align at specific distances from each other to create crystalline nuclei. The formation of nuclei is influenced by the polymer chain structure, where symmetrical chains will allow regular close packing and chains that have polar groups will encourage strong intermolecular attraction between the chains to stabilise alignment.

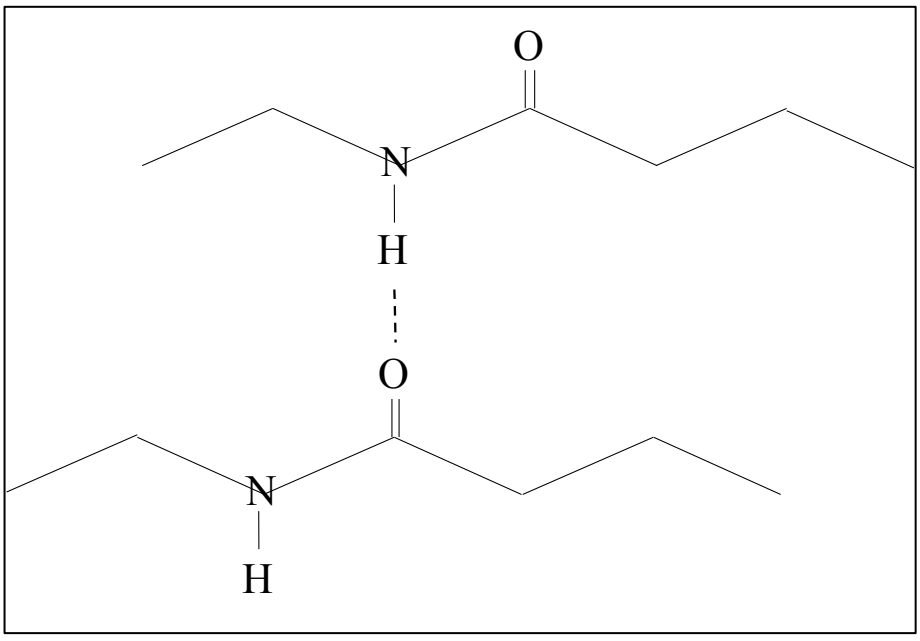

Figure 1.3.1 – Hydrogen bonding in polyamide.

1.4 The thermal stability of polymers at temperature close to the melting temperature

The thermal stability of a polymer when heated close to, or above its melting temperature will have an influence on the polymer chains. Generally, over an extended time period and at elevated temperatures, the thermal stability of a polymer will decrease. Degradation mechanisms such as crosslinking, chain extension and chain scission can occur, as such the T_g of the polymer and the ability of the polymer to crystallise will be affected (8–10). Physical degradation is a reversible process where the post-crystallisation occurs. This is due to the polymer chains re-ordering due to experiencing thermal motion at high temperatures. Chemical degradation is an irreversible process where the polymer chains undergo mechanisms such as chain scission and cross-linking. This is due to processes such as oxidation and hydrolysis by Drummer and Chen (11,12). Polyamides consist of an exposed carbonyl and amide group; this makes polyamides susceptible to molecular changes at elevated temperatures. In polyamide powders, in particular PA-12, mechanisms such as cross-linking, post-condensation and chain-scission occur (13). It was reported that at high temperatures and in the presence of oxygen, thermo-oxidative degradation occurs in polyamide. As a result, cross-linking or chain scission can occur due the formation of free radicals (11). Whereas, in high temperature and oxygen depleted environments cross-linking is predominant (14). Polymer degradation mechanisms have been proposed by Drummer et al and Chen et al (11,12). These processes of degradation influence the melting point, viscosity and mechanical behaviour of the polymer (11).

1.5 Development of crystallinity in polymers

Crystallisation is thought of as a two-stage process, known as nucleation and growth. Nucleation involves the creation of sTable nuclei. A sTable nucleus is a 3D structure that consists of ordered polymer

chains in a parallel sequence. This is stimulated by intramolecular forces and the stabilisation of long-order. This is known as homogenous or thermal nucleation. However, if impurities are present they will act as a site for nucleation, this is known as heterogeneous or athermal range nucleation (15). The second stage involves growth of the crystalline region. The final size of the nucleus will be determined by the rate of addition of polymer chains to the nucleus. This is influenced by the temperature, where the temperature must be low enough to minimise the disordering of polymer chains caused by thermal redispersion at the crystal-melt interface (15).

The development of crystallinity is also described by the Avrami model from a bulk perspective, in which the relationship between the density of the crystalline phase over time is determined (1). The Avrami model makes assumptions such as: nucleation is a random and homogeneous process of the untransformed matter, i.e. the melt; the extent of transformation is not affected by the growth rate; and growth occurs in all directions at the same rate (16). In the Avrami model, the spherulites grow radially from a nucleation point until impingement is reached. This is usually observed as a polyhedral shape. The position of the nucleation point is fixed and does not change in the melt (1). Both nucleation and growth of a spherulite occur over time t until impingement is achieved.

Application of the Avrami equation will produce an Avrami rate content, k, and an Avrami exponent, n. The Avrami exponent is a constant that is representative of the morphology of the crystal. Rapid nucleation is a zeroth order process where growth centres are formed instantaneously, the corresponding value is equal to $n - 1$. Sporadic nucleation is a first-order process, where the corresponding value is equal to $n + 1$ (1). For example, sporadic nucleation of a spherulite; $n = 3 + 1 = 4$. This is demonstrated by the Table below. As a result, the Avrami exponent, n, is a combination of the growth dimension and the nucleation mechanism to produce an integer value.

Table 1.5.1 – The relationship between the nucleation mechanism, growth dimension, Avrami exponent and morphology of the crystalline state.

Nucleation mechanism	**Growth dimension**	**Avrami exponent, *n***	**Morphology**
Sporadic	**1**	**2**	**Rod**
	2	**3**	**Disc**
	3	**4**	**Sphere**
Instantaneous	**1**	**1**	**Rod**
	2	**2**	**Disc**
	3	**3**	**Sphere**

The Hoffman-Lauritzen (H-L) theory is widely accepted theory to describe the development of crystallinity in polymers from a molecular perspective. In the H-L theory, crystallisation begins when a polymer chain deposits itself on to growth plane. This is considered a critical nucleus (6). From this point, chains grow in the lateral direction by folding back on themselves to form lamellae. It should be considered that a free energy barrier must be overcome in order for crystallisation to proceed (5).

The crystallisation process is defined by the following parameters; g, the lateral covering rate i.e. the growth rate parallel to the growth plane which covers the growth front after nucleation; l, the width of the growth front which nucleation and growth covers; G, growth rate perpendicular to the growth plane; and i, the rate of nucleation (5).

The H-L model uses the parameters in 3 regimes to describe crystallisation. Regime I takes place at low degrees of undercooling. Once the critical nucleus is formed, lateral growth occurs quickly and a smooth growth front is produced. Soon after, a new nucleus forms and the next growth front is produced (5). The equation to describe regime I is shown in Table 1.5.2. In the equation b_0 represents the thickness of the crystallised layer and L is the substrate length covered by one surface nucleus, where the condition $L \ll iL$ is met (17).

Regime II takes place as the degree of undercooling increases and growth occurs, such that there is more than one nucleus on the growth plane. Consequently, the growth rate is associated with the terms i and g (5). An important consideration within regime II is the separation between the neighbouring nuclei. At higher crystallisation temperatures, the separation between neighbouring nuclei is large (5). As the degree of undercooling increases and the crystallisation temperature reduces, the separation between neighbouring nuclei reduces. As regime II continues there are changes to crystal growth as the crystallisation temperature decreases. The equation to describe regime II is shown in Table 1.5.2.

Regime III is entered when the crystal growth rate reduces (5). Eventually, the gap between the neighbouring polymer chains closes and the lateral covering rate, g, is no longer considered (5). The equation to describe regime III is shown in Table 1.5.2.

It is assumed that a segment of polymer chain attaches onto the growth front one at a time, ensuring the maximum amount of order is reached. Yet, other models were proposed. Of these models Point et al describes the crystallisation process to be >1 segment attaching to a growth front at any time following nucleation (18). Alternatively, Phillips et al suggested >1 stem attaching instantaneously (19).

Table 1.5.2 – Hoffman-Lauritzen regimes.

Regime 1	$G_I = ib_0L$
Regime 2	$G_{II} = (ib_0g)^{0.5}$
Regime 3	$G_{III} = ib_0L'$

The proposed equation by J.D. Hoffman et al allows for the determination of a temperature independent constant and a nucleation rate constant, K_o and K_g, respectively. This is represented by the equation below.

$$\left(\frac{1}{t_{0.5}}\right) = K_o \exp\left(-\frac{U}{(R(T-T_\infty)}\right) \exp\left(\frac{K_g\left(T+{T_m}^0\right)}{2T^2\Delta T}\right)$$

The parameters in the above equation can be used to determine K_o and K_g. Whereby $t_{0.5}$ denotes half-time to crystallisation, T is the isothermal crystallisation temperature, ${T_m}^0$ is the equilibrium melt temperature, ΔT is the degree of undercooling, $T_\infty = T_g - 30\ K$ and U is a universal constant at 6270 Jmol^{-1} which represents the activation energy for crystallisation.

The construction for a Hoffman-Lauritzen plot involves generating a graph of $\ln\left(\frac{1}{t_{0.5}}\right) + \left(\frac{U}{(R(T-T_\infty)}\right)$ vs $\left(\frac{\left(T+{T_m}^0\right)}{2T^2\Delta T}\right)$, the result is typically a straight line graph with a slope and intercept of K_o and K_g, respectively (20,21).

The temperature and growth rate will influence the crystallisation of a polymer. Typically, crystallisation occurs between T_M – 10K and T_g + 30K. In this temperature range, the polymer chains experience thermal motion. This enables the formation of ordered crystalline regions.

Figure 1.5.1 shows a bell-shaped curve on an axis of growth rate vs temperature. At temperatures close to the melting temperature of the polymer, the polymer chains experience a high level of molecular motion and the formation of sTable nuclei is limited. At temperatures close to the T_g of the polymer, the melt is viscous and the molecular motion is limited.

As the temperature decreases from the melting temperature, the melt viscosity increases and consequently causes the rate of diffusion of polymer chains to decrease. The limited motion of polymer chains encourages the formation of a nucleus. This demonstrates that there is an optimum temperature in which crystallisation takes place. Additionally, this shows that the growth rate of crystalline regions passes through a maximum.

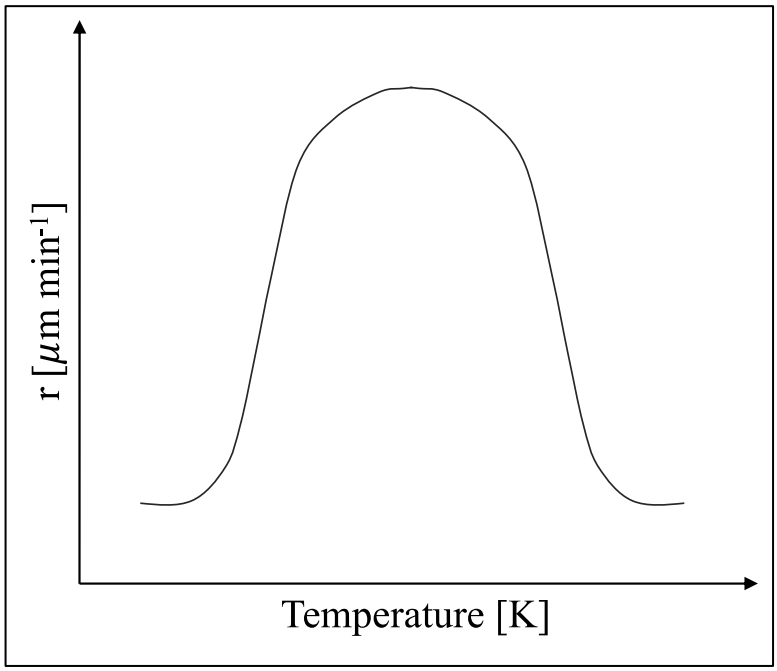

Figure 1.5.1 – Graph of radial growth rate r of a spherulite as a function of crystallisation temperature, represented by a bell-shaped curve.

1.6 Background to additive manufacturing

Conventional manufacturing methods such as Injection Moulding (IM) emerged in the late 1800's and remains a popular manufacturing technique that is used in industries such as the automotive industry. The IM process begins by heating a polymer above its melting temperature and injecting the melt through a nozzle into a mould. The mould is preheated to a set temperature. The polymer is maintained in the mould for a pre-determined length of time where it cools down rapidly and then is removed.

Recent developments in the manufacturing of polymeric components shows that geometrically complex parts can be built without the use of a mould. This branch of manufacturing is called additive manufacturing and is sometimes referred to as "3D printing". In general, the manufacturing process entails progressively depositing layers of polymer onto a build platform to fabricate a net-shape component from CAD or digital model.

One of the earliest forms of AM methods is called Material Extrusion (MEX) In this technique, the polymer is heated above its melting temperature, where it is maintained. The melt is deposited directly onto a build platform through a nozzle to create a 3D object. While MEX is advantageous in respect that moulds are not required, issues involve geometric distortion due to rapid crystallisation of the polymer melt (22).

Alternative AM methods use polymers in the form of powder as the build material, this category of AM is called as Powder Bed Fusion (PBF). According to Chatham et al (23) the first PBF technique was patented in 1989 by Deckard (24), however technologies using a powder bed date to 1971 by Ciraud and 1979 by Householder (23).

In PBF techniques polymer powder is spread onto build platform and selected regions of the polymer powder are sintered or fused to create the final product. Meanwhile, the build chamber is maintained at a set temperature to minimise geometric distortion. The main advantages of PBF technologies are that complex components can be created without the need for support structures. Additionally, the entire build unit is used to create multiple components in one cycle, this demonstrates that PBF techniques are efficient in terms of energy and time but inefficient in terms of material waste too.

Since PBF technology is a developing manufacturing method, a limited number of polymers are commercially available, these include but are not limited to PA-11 and PA-12 (23). Whereas a larger selection of polymers are used in IM, as they have been developed to work specifically with the IM process. This involves taking into account the crystallisation kinetics and thermal properties (23). Examples of PBF technique include Selective Laser Sintering (SLS), High speed sintering (HSS) and Multi-Jet Fusion (MJF). The latter is patented by Hewlett Packard.

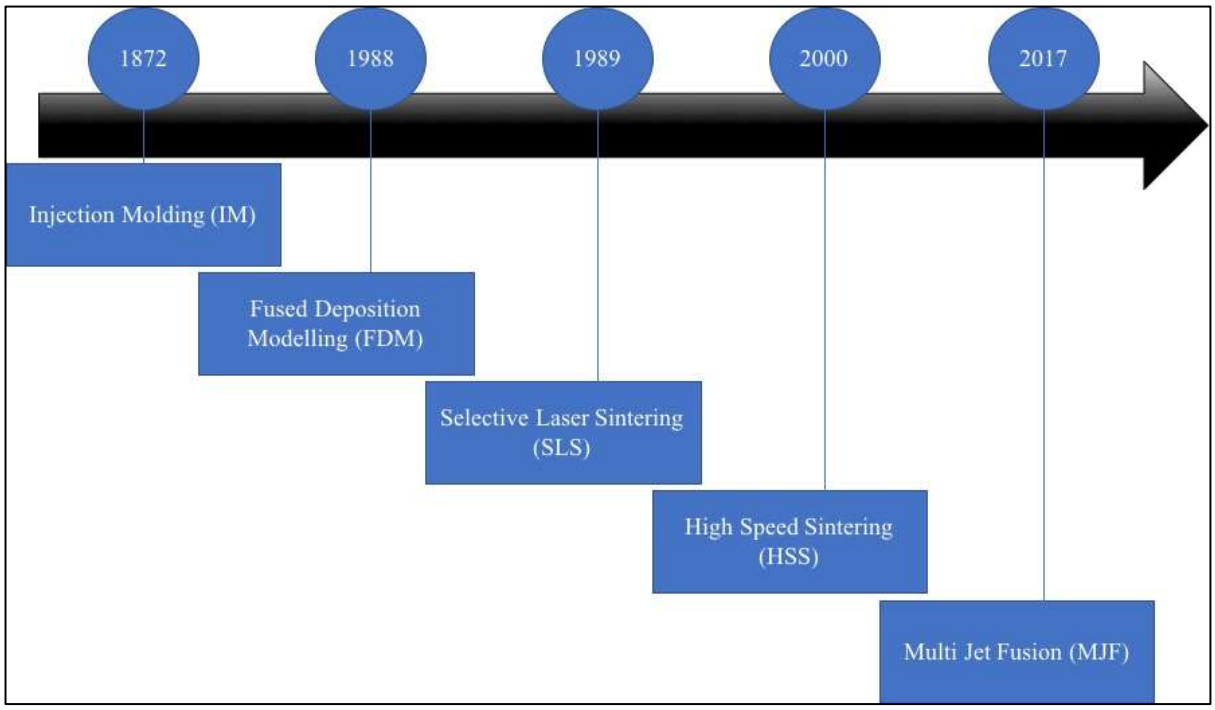

Figure 1.6.1 – Timeline of production techniques including the traditional moulding technique, Injection Moulding (IM) and subsequent additive manufacturing methods (22,25–27).

1.6.1 Selective laser sintering

SLS is one of the most popular AM-PBF techniques to create bespoke objects in low-volume production (28). To fabricate polymeric components, polymer powder is loaded into a feed chamber that is adjacent to the build area. The feed chamber and the build area are pre-heated to a temperature below the melting temperature of the polymer. Additionally, the entire unit is maintained under an inert gas such as nitrogen. The build platform is lowered a set distance, usually 100 μm, and polymer powder is spread onto the build platform from the feed chamber using a roller. The use of a roller allows the spread of powder to be uniform across the build platform. Generally, more powder than required is delivered to the build platform and the excess powder is pushed to an overflow bin. This powder can be re-used in future builds. After, a laser scans selected areas of the powder bed surface to facilitate the adhesion of polymer particles in localised regions (29). This process is repeated until the build is complete. Once

the build is complete, the build chamber will cool down to room temperature. The components are then removed from the powder chamber and excess powder is removed in a step known as “depowdering”. In some instances, a post-depowdering surface treatment such as bead blasting is used which removes excess powder or achieved a desired surface finish (23).

The operating parameters of SLS are determined by the user, these include the laser power, laser scan speed, laser scan spacing, part bed temperature, powder feed temperature, roller speed and powder layer thickness (30–32).

The most common material used in SLS is PA-12 (30–32), other materials include poly (ethylene terephthalate), polypropylene and thermoplastic polyurethane (33–36). The fabrication of parts made from composite materials has also been investigated, where glass carbon, potassium titanium whiskers and carbon black have been incorporated into the PA-12 polymer matrix (37–41). The feedstock material used in SLS comprises of both virgin and used powder, termed “refreshed powder”. Often a high percentage of virgin powder (30 – 50 %) is replenished into the build (32).

SLS fabricates components as prototypes and in low volume production (42), therefore many studies investigate the mechanical properties of SLS components. It has been reported that the mechanical properties are influenced by the processing parameters (43–49).

An early study examines effect of build orientation and processing parameters on the mechanical properties of PA-12 SLS components (43). The build orientation affected the mechanical properties whereby the Young’s modulus, fracture strength and elongation at break varied for different build orientations. However, the trends identified for each build orientation were similar.

It was reported that the processing parameters affected the energy density, consequently this affected the density and mechanical properties of the final component. The energy density is a measure of the energy supplied to the powder particles per unit area of the powder bed surface. This is determined by the laser power, beam speed and hatch spacing (43,45). In general, parts that had a lower energy density were weak and exhibited anisotropic behaviour. As the energy density increased, the parts were stronger and exhibited isotropic behaviour (43). The energy density has also been found to influence the microstructure which in turn affected mechanical properties (44).

Other parameters such as refresh rate, layer thickness and hatch pattern influenced the part strength (45). The mean strength was determined using the Taguchi method using L_{16} modified orthogonal array. As the refresh rate and part bed temperature increased, the mean strength of the part increased. However, as the layer thickness and hatch pattern spacing increased, the mean strength decreased (45).

The relationship between the beam speed and mechanical properties were also investigated, results showed that as the beam speed increased, the mechanical properties decreased (46). This was due to the degree of particle melt, i.e. the proportions of melted and unmelted regions (46). Likewise, Majewski et al also report the degree of particle melt influenced the mechanical properties (47).

The effect of ageing on the mechanical properties of parts produced by SLS and IM was also investigated (49). In this study, ageing was induced by keeping specimens in dry, humid and wet conditions and testing them at different temperatures. In dry conditions, IM samples had similar strengths throughout a given time period. However, samples produced by SLS showed an increase in strength over time. In wet conditions, IM samples experienced a decrease in strength and stiffness. Whereas samples produced by SLS exhibited a consistent strength and small decrease in Youngs Modulus. It was noted that PA-12

used in SLS had better moisture and water resistance than commercially available injection moulded grade PA-12 (49).

As shown, parts fabricated by SLS are influenced by many factors, including the processing parameters, part orientation and storage conditions, meaning it is likely that the mechanical properties vary between builds.

The thermal properties of PA-12 powder and parts used in SLS have also been investigated. PA-12 powder can be supplied by different manufacturers, e.g. Duraform PA, Innov PA and PA2200 to name a few (43,44,50,51). Of which, Duraform PA is the most common.

The data in Table 1.6.1 demonstrates the thermal properties of the different grades of PA-12 powder.

Table 1.6.1 – Reported values of the peak melting temperature T_M, peak crystallisation temperature T_C and enthalpy of fusion for different grades of PA-12 powder.

Reference	**Powder**	**Peak T_M [℃]**	**Peak T_C [℃]**	**Enthalpy of fusion [J/g]**
J. Kurth et al	Duraform®	187.26	-	-
F. Sillani et al	Duraform®	180.80 (onset)	151.10 (onset)	103.0
Wang et al	Duraform®	176.00	149.00	-
S. Dadbakhsh et al	PA2200	180.10 (onset)	154.40 (onset)	92.1
D. Pharm et al	PA2200	186.49	149.67	118.91
C. Cai et al	EOS	188.90	142.90	100.8

The data in Table 1.6.1 shows that the peak melting temperature of PA-12 powder varied between suppliers. For example, the peak melting temperature of Duraform® varied by almost 5 ℃. The peak crystallisation temperature showed less variation, where the highest a lowest peak crystallisation temperature were 151.1 and 149.0 ℃.

Thermal properties such as the onset and peak melting temperature are important to investigate since the powder bed must be maintained at a certain temperature throughout the duration of the build. This temperature must not exceed the melting temperature of the polymer as this will cause the powder within the build chamber to melt.

The onset and peak crystallisation temperature can be used to determine the sintering window. The sintering window reflects the sintering processability. This is the difference between the onset melting temperature and onset crystallisation temperature. M. Vasquez et al define the sintering window as “the temperature range in which the material can be processed without being degraded” as the material will remain in the melt phase (52).

1.6.2 Multi Jet Fusion

Multi Jet Fusion (MJF) is a proprietary AM technique that falls into the subcategory of PBF (53,54). The technique was developed by HP in 2014 and became commercial in 2016 (31,55). In general, MJF deploys radiation absorbing inks which define the cross section of a part. An infrared radiation lamp then scans the surface to melt localised regions on the powder bed. This is controlled by a printhead that is programmed to receive commands from a central unit (56).

Often MJF is compared to High Speed Sintering (HSS), a process developed by Hopkinson et al. HSS that operates using a similar principle to MJF. In HSS, selected areas of the powder bed absorb sufficient energy to elevate the temperature in localised regions and melt polymer particles, while the surrounding areas absorb less energy so that the melting temperature of the material is not exceeded (57). In HSS there are a number of methods to melt selected areas of the powder bed, these include; using a powder that absorbs energy more readily than the support powder, the addition of a secondary material to promote energy absorption in selected areas of the powder bed and using a mask to restrict the incoming energy so that certain areas of the powder bed are exposed to the incoming radiation (57). MJF is a more restrictive processing technique than HSS and SLS in that the processing parameters are controlled by algorithms and the materials are supplied by the manufacturers. However, MJF can achieve printing speeds much faster than other polymer PBF techniques (58). This has been reported to be up to 10 times faster than MEX and SLS (31,59). Voxeljet are a company that offer HSS solutions for prototyping and production. Other PBF technologies have a similar operating principle to MJF such as Selective Absorption Fusion (SAF). This also uses an infrared absorption fluid called HAF™ to facilitate the adhesion of polymer particles.

More specifically, MJF works by depositing a thin layer of polymer powder of approximately 0.08mm thickness (60,61) onto a build platform using a blade (58) which moves in the X direction (31). Afterwards, an inkjet head (coupled with the IR lamp) scans the surface in the Y direction to selectively deposit a fusing agent (FA) in the areas which define the cross-section of the component. A detailing agent (DA) is deposited around the perimeter of the FA (31). The amount of FA and DA are controlled by HP algorithms (55). After, infrared lamp scans the surface to enable localised melting of polymer particles in areas containing the FA. This process is repeated until the build is complete. It has been reported that the printing time of one layer is 10.5s (61). The surrounding unfused powder acts as a support medium for the components, this omits the requirement for moulds. The design freedom offered by PBF techniques, such as MJF, allows for the fabrication of a range of components, including high

pressure hydraulic valves, fuel tanks and biomedical devices and even complex components such as lattices and auxetic structures (62–67).

Once the components have been fabricated, they are allowed to cool within the powder bed for a length of time. The cooling time is determined by the user and has previously been reported at 10, 16 hr or overnight (55,61,68), or until the core of the building unit reaches 45/50 ℃ (55,69). Afterwards, excess powder is removed by hand or using compressed air (55,68). Further excess power is removed by glass vacuum bead blasting or using a hard bristle brush (55,68).

The feedstock material is often recycled since a small amount is used to create the final product. The recycled powder is mixed with virgin powder to reduce material waste and maintain powder quality, this is known as “refreshed powder”. Generally, in MJF 20 % virgin powder is added with each processing cycle, and this is known as the “refresh rate” (55).

Polyamide-12 (PA-12) is the most common polymeric material used in PBF and in particular, MJF (70). PA-12 is a semi-crystalline thermoplastic polymer with good mechanical and physical properties. PA-12 typically exhibits a tensile strength of ~ 49 MPa (68) and melts in the region of 184 – 187 ℃. The combination of a relatively high onset of melting and low onset of crystallisation provides a wide sintering window to prevent crystallisation during the build whilst offering greater control of the sintering or fusion process (58,71). More recently, the powder feedstock material selection has expanded to glass filled PA-12, polyamide-11, thermoplastic polyurethane and polypropylene (61,72–74).

In addition to PA-12, the FA and DA are also important components in the build process. The main difference between the two agents is the presence of carbon black within the FA, in which carbon black

is used as a radiation absorbing material (RAM) to facilitate particle melting (31). The FA enables localised heating by containing carbon black which penetrates into the surface of the powder bed (56). The carbon black also acts as a colourant meaning components fabricated by MJF are dark in colour due to the pigmentation provided by carbon black. Whereas, the DA provides an evaporative cooling effect to lower the temperature of the build material to prevent melting and prevent thermal bleeding, this contributes to edge acuity (31,56). The DA is thought to absorb < 10 % of radiation in the range of 650 – 2500 nm and is capable of absorbing radiation below 650 nm, such that the DA absorbs at least some wavelengths in the visible spectrum and little to no radiation in the infrared region. In contrast, the active material within the FA absorbs energy in the IR region (56). The radiation energy absorbed by the FA is converted to thermal energy to promote transfer of thermal heat to the build material on the powder bed surface. In the areas containing the FA, the temperature is elevated above the melting point of the build material to facilitate fusion of powder particles (56).

Deconstruction of the FA and DA reveal the key constituents include water, 2-pyrrolidone (2-PYR), triethylene glycol and carbon black (only present within the FA) (58,75). Though, the quantity of each organic solvent in the FA and DA varies (75). The increased content of water present within the DA enables a localised cooling effect and inhibits heat transfer on the powder bed surface (58,75). Whereas, water is used in the FA to allow a homogeneous distribution of carbon black to penetrate through the deposited powder layer (75). Following water, 2-PYR has been reported as the next abundant solvent, said to be included due to its inert nature and high boiling point (251 ℃) (76). Some chemicals such as 1,2-benzisothiazolin-3-one are present < 0.1 % weight of the FA and DA. Although this quantity may appear small, these chemicals act as a biocide (56).

Previous work on MJF is dominated by studies that focus on the mechanical properties of the fabricated parts, such as modulus or tensile behaviour (31,48,55,60–63,66–68,77–80).

An earlier study by O'Connor et al showed that tensile specimens appeared to exhibit more isotropic behaviour, while the flexural strength exhibited anisotropic behaviour. For example, specimens built in the Z-direction showed a 40 % increase in flexural strength than specimens built in the X-direction (68). Palma et al showed that tensile samples built in the vertical orientation exhibited a reduced elastic modulus and hardness, when compared to those built in the horizontal direction (78).

Riedelbauch et al expanded this theme of work by investigating the mechanical properties of tensile samples built from aged or refreshed PA-12 powder. The mechanical properties showed that parts built in the ZXY direction had slightly higher mechanical properties than those built in the YXZ direction (55). From a processing perspective, ageing caused a decrease in the melt flowability and an increase in molecular weight and length, yet ageing did not appear to significantly influence the mechanical properties (55). In these studies, the print mode used (if specified) was "balanced", which offers a good compromise between the mechanical strength and Youngs' Modulus (68).

Although literature shows the observed trends in mechanical properties are inconsistent, it is clear that the build orientation or position of parts built within the powder bed influenced the mechanical properties. This could be linked to the difference in microstructure between different build orientations which affects crack propagation (81).

Additives such as glass beads can be incorporated into the polymer powder to reinforce fabricated components and enhance the mechanical properties. A study by O'Connor and D. Dowling showed that the addition of 40 % volume glass beads increased the tensile modulus by 85 %, while the tensile strength decreased. A similar trend was observed for the flexural strength and modulus (61). B. Guo et al also reported enhanced mechanical properties by the addition of 32 % volume glass beads in PA-12 (82). In both (61,82), the elongation at break decreased by the addition of glass beads. This was due to

poor adhesion at the polymer-glass bead interface and the glass beads causing premature fracture (61,82). Moreover, X. Liu et al investigated the mechanical strength of PA-12 and reinforced glass-fibre PA-12 after high temperature annealing (83). In this study, glass fibres were introduced into the polymer matrix in weight percentage fractions up to 30 %. Overall, glass fibres enhanced the mechanical properties and annealing remarkably enhanced the mechanical strength of both PA-12 and PA-12/glass fibre composites (83).

As mentioned, other polymers besides PA-12 are suitable for MJF such as polypropylene (PP), polyamide-11 (PA-11) and thermoplastic polyurethane (TPU). A study by J. Safka et al tested the mechanical properties of PP components built in different orientations. This study showed that build orientation had a significant effect on the tensile mechanical properties. In comparison to other manufacturing techniques such as SLS or injection moulding, the components fabricated by MJF were more rigid (74).

PA-11 was reported to have similar trends in tensile and flexural properties to PA-12, while the tensile and flexural properties for TPU were much lower than PA-11 (73). The influence of the refresh ratio on the mechanical properties of PA-11 was investigated by C. Pandelidi et al (72). Components manufactured using recycled PA-11 were reported to have inferior mechanical properties to those created using refreshed or new PA-11 powder (72).

The effect of ageing on the mechanical properties of PA-12 was also investigated. Riedelbauch et al demonstrated that thermally induced ageing of PA-12 did not have a significant impact on mechanical properties, up to 5 processing cycles (55). However, a difference between these two studies that investigate the mechanical properties of PA-11 and PA-12, is that Riedelbauch et al (55) sieved PA-12 between processing cycles to remove and break up agglomerates, whereas in the study by C. Pandelidi et al (72) PA-11 was not sieved. Therefore, powder handling may also influence the mechanical properties of the resulting component.

The thermal properties of recycled feedstock material, in particular PA-12, used in modern manufacturing methods such as SLS have been explored, yet this is limited for MJF. Although the operating principles of SLS and MJF are similar, the building conditions for SLS and MJF are different. In SLS components are manufactured in an enclosed nitrogen atmosphere using a CO_2 laser, which can provide harsh heating conditions. While in MJF, components are manufactured in atmospheric conditions using a lower intensity radiation source i.e. an infrared lamp. Therefore, the thermal history of recycled SLS and MJF powder will be different and further influence the final properties of the manufactured component.

Thermoanalytical studies evaluate the thermal history of parts manufactured by MJF (largely as a means of quality control). Analysis using differential scanning calorimetry (DSC) typically reveals a double or single melting peak, which are interpreted as partial or complete melting of polymer particles during the manufacturing process, respectively (48,60,84,85).

Many authors have reported an increase in melting temperature of SLS grade recycled PA-12, this has been linked to a rise in molecular weight (Mw) (86–89). F. Sillani et al suggest the increase in Mw is due to the post-condensation reactions that occur due to the constant removal of water in SLS part production, promoted by the nitrogen atmosphere (31). Moreover, the crystallisation temperature shifts to lower temperatures due to inhibited mobility of macromolecular chains as a result of chain extension (86). This work has been extended to comparing the thermal properties of recycled PA-12 powder to final SLS components produced from virgin, recycled and refreshed powder (31,51,60,84). In which, a higher proportion of recycled powder in manufactured components decreased the melting enthalpy. In this instance, the larger proportion of longer molecular chains hindered ordered chain folding upon crystallisation, thereby displaying a reduced crystallinity in parts made with refreshed powder (51).

Due to the high content of refreshed powder used in MJF, the thermal stability of the powder is a key factor in selecting a suitable build material. The thermal properties such as the melting temperature, enthalpy of fusion and crystallisation temperature are often compared. It was shown in studies that the thermal properties of recycled PA-11 and PP, did not vary greatly (20,22). This made them suitable powders for MJF. However, J. Riedelbauch et al found differences in the melting and recrystallisation behaviour of reused PA-12 powder (55). It was concluded that powder exposed to multiple processing cycles and parts made from recycled or refreshed powder have a higher melting enthalpy due to post-condensation (55). Moreover, the melting temperature of the powder increased slightly when exposed to multiple processing cycles due to post-polymerisation or post-crosslinking. On the contrary, F. Sillani et al suggest post-condensation does not occur in MJF because PA-12 is "end-capped", a result of MJF taking place in the presence of air (31).

This data shows that the thermal properties of virgin and used PA-12 powder varied. This may influence the interaction between the FA and DA with PA-12 dependant on the degree of ageing.

1.7 Project aims and objectives.

PA-12 is a polymer used in PBF techniques such as SLS and MJF. PBF is a manufacturing method that is used to create prototypes and functional parts in low-volume production. A key benefit offered by PBF is the design freedom which allows parts with a complex geometry to be created without the use of a mould. As such, the mechanical properties of parts created by SLS and MJF have been comprehensively studied. This has shown that the mechanical properties are influenced by the operating parameters as well as the orientation of the part in the powder bed. Additionally, the mechanical properties were influenced by the incorporation of fillers or additives into the polymer matrix.

However, the thermal properties that have been reported in literature are inconsistent. This shows that more data should be acquired for means of comparison to see how the thermal properties of different grades of PA-12 vary. Additionally, literature relating to MJF is limited to the characterisation of the thermal properties of virgin or refreshed PA-12 feedstock material. Few studies have investigated the FA and DA, in which the chemical constituents have been quantified.

The cooling behaviour is an important factor to consider as the parts cool for a length of time once the build is complete. The cooling time is determined by the user and has previously been reported at 10, 16 hr or overnight (55,61,68), or until the core of the building unit reaches 45/50 ℃ (55,69). In the AM process, a layer of polymer is deposited and then fused with an IR lamp. Immediately after the fusion process, the polymer layer will begin to crystallise before the next layer is deposited. Therefore, it is important to evaluate the crystallisation kinetics of PA-12. This is difficult to determine on a localised level since the cooling behaviour within the build is difficult to predict. However, there is value in determining the crystallisation kinetics of PA-12 to understand the morphology and rate of crystallisation. The Avrami theory can be used to determine the isothermal crystallisation kinetics of PA-12. Over the years, the Avrami model has been applied to a variety of polymers, there have also been modifications and adaptations of the Avrami model. However, it is thought that in MJF crystallisation is a mixture of isothermal and non-isothermal processes, or quasi-isothermal (90). In reality, isothermal conditions are difficult to maintain within the powder bed chamber. One reason for this is that the surface of the powder bed is not a controlled environment but is exposed to air, this will influence the cooling behaviour of the polymer at the surface of the build platform. Therefore, it is important to explore the isothermal and non-isothermal crystallisation kinetics of PA-12 over a variety of temperatures and cooling rates.

The FA and DA are key components used in MJF. The agents are deposited by an inkjet and penetrate into the PA-12 powder layer (56). Additionally, some of the constituents within the FA remain within the final part e.g. carbon black and 2-PYR (58,75). This suggests that the agents interact with PA-12. The influence of the FA, DA and their chemical constituents on the thermal behaviour and microstructure of PA-12 is yet to be understood in more detail. This will provide an insight to how MJF operates on a technical level and how MJF is unique in comparison to other AM techniques, with respect to the proprietary FA and DA. This was achieved by creating blends of PA-12/FA and PA-12/DA. The FA and DA systems were deconstructed into their primary chemical constituents and blends of PA-12/carbon black, PA-12/water, PA-12/2-PYR and PA-12/2-PYR/water were created. These blends were characterised using DSC, optical microscopy and infrared spectroscopy in order to understand the effect of these FA and DA system constituents on the thermal behaviour and microstructure of PA-12.

Furthermore, due to MJF having the capability for being an industrial process, powder usage and efficiency of materials is important to consider. Generally, in MJF 20 % virgin powder is added with each processing cycle (55). This shows that a large majority of the powder has been exposed to high temperature conditions used within MJF. This will have an impact on the thermal history of the powder, since polymer chains have been exposed to temperatures greater than the T_g of the polymer where polymer chains are thermally activated. Therefore, it is important to investigate the thermal properties of aged powder. Since recycled powder is a part of the feedstock material, the influence of the FA, DA and their chemical constituents on the thermal properties and microstructure of aged PA-12 was also evaluated.

CHAPTER 2 – MATERIALS, EXPERIMENTAL METHODS AND TECHNIQUES

2.1 Materials

The materials used in MJF were supplied by The MTC (Coventry, UK) and used as received. These were proprietary Hewlett Packard (HP) materials. Namely, HP 3D High Reusability polyamide-12 powder (PA-12 powder), by trade name V1R10Series, the fusing agent (FA), by trade name V1Q63Series, and the detailing agent (DA), by trade name V1Q64Series. Additionally, 2-pyrrolidone (CAS 616-45-5) (2-PYR) was supplied by Merk (Darmstadt, Germany).

2.2 Sample preparation

Blends of virgin and aged PA-12 powder with varying compositions of FA, DA, CB (recovered from the FA), water and 2-PYR were created.

Non-volatile constituents such as carbon black were present within the FA. To recover the carbon black, the FA was added to glass vials and was left in a fume cupboard over a period of time to enable the volatile constituents to evaporate. The mass carbon black was then determined (see section 2.2.1).

A pre-determined amount of recovered carbon black was mixed with the PA-12 powder to produce blends in the following compositions, 1, 5, 10 and 20 wt.% carbon black. These blends were prepared as a solid-solid dispersion (see section 2.2.2). This composition range was selected in accordance with other reported compositions, where AM components were fabricated at varying compositions in the range 1-10 wt.% carbon black in PA-12 (40,41).

To replicate the conditions encountered within MJF, an alternative preparation route was adopted (see section 2.2.3). This involved the dispersion of the liquid FA into PA-12 powder. The liquid FA was added in volumes that would yield the same wt.% carbon black compositions as the solid-solid dispersions.

Studies have shown that the FA and DA are primarily composed of water; however, in the FA and DA water is present in different quantities (75). To verify that water was not degrading PA-12, water was added to PA-12 in quantities equal to the volume of liquid FA used to create the PA-12/FA blends. The same procedure was used to create the PA-12/DA blends, where liquid DA was added to PA-12.

The FA and DA also contain different quantities of 2-PYR. Further blends of PA-12/2-PYR were created, in which liquid 2-PYR was added to PA-12 in compositions within the range of 0.10 – 8.72 wt.% 2-PYR. This was in accordance with the content of 2-PYR present within the PA-12/FA and PA-12/DA blends.

Blends of PA-12/2-PYR/water were also created, in which the 2-PYR and water were compositionally identical to that found in the FA and DA blends. These liquid dispersion blends were designated as liquid-solid dispersions.

The preparation of solid-solid and solid-liquid dispersions can be found in more detail in section 2.2.2 and 2.2.3. A summary of the pre-determined masses of PA-12 and volumes of FA, DA, water and 2-PYR can be found in Table 2.1.1.

To create the blends, 2 different batches of PA-12 powder were used. One of which was used to create the PA-12/FA, PA-12/DA, PA-12/CB and PA-12/water blends. The other was used to create the PA-12/2-PYR, PA-12/2-PYR/water blends and blends produced from aged PA-12 powder (see section 2.2.4).

2.2.1 Preliminary study to determine target compositions

The first stage of blend preparation involved determining the mass of carbon black present within the FA. This was achieved by using a disposable pipette to deposit 2 mL of FA into five glass vials. The vials containing the FA were left in a fume cupboard until the volatile material had evaporated and then were transferred to a desiccator (filled with silica gel) for a further 48 hrs to remove residual moisture. The mass of the vials was weighed using an Ohaus Analytical balance before and after drying until the mass was constant. The final mass was calculated by subtracting the mass before drying and after drying. The average recoverable mass was 1.175 g for 2 mL of FA. Therefore, the carbon black was present at a concentration of 0.586 g / mL within the FA.

2.2.2 Preparation of solid-solid dispersions

To create the PA-12/carbon black blends, a pre-determined volume of FA (see Table 2.1.1) was extracted into a micropipette and deposited into a glass vial. The vials were left to dry in a fume cupboard for 48 hrs before being transferred to a desiccator (filled with silica beads) for a period of 48 hrs. This allowed volatile materials to evaporate without the use of heat. After, a residue of carbon black was left at the bottom of the vial, this was manually crushed using a spatula and physically mixed with a pre-determined mass of PA-12 powder. Blends were prepared in the composition range of 1, 5, 10 and 20 wt.% carbon black. The blends were transferred into a desiccator for 48 hrs to remove any moisture from the sample, in particular the powder. The vials were weighed periodically until the weight was constant before being stored at room temperature.

2.2.3 Preparation of solid-liquid dispersions

To create the PA-12/FA blends, PA-12 powder was weighed and added to a glass vial, to which the FA was measured and added using a micropipette. The masses and volumes are shown in Table 2.1.1. These

calculations were based off a preliminary study (see section 2.2.1), which revealed that carbon black was present at a concentration of 0.586 g/mL within the FA. An example of how the volume of FA was calculated is shown below.

$$\left(\frac{PA12\ mass[g]}{100 - target\ composition\ [\%]}\right) \times target\ composition\ [\%] = \boldsymbol{FA\ mass[g]}$$

$$\frac{FA\ mass[g]}{0.586\ [g\ /\ mL]} = \boldsymbol{FA\ volume\ [mL]}$$

An example for solid-liquid dispersion 1 wt.% FA:

$$\left(\frac{3\ g}{100 - 1\ \%}\right) \times 1\ \% = \boldsymbol{0.0303\ g\ FA}$$

$$\frac{0.0303\ [g]}{0.586\ [g\ /\ mL]} = \boldsymbol{0.0517\ mL\ FA}$$

$$\boldsymbol{0.0517\ [mL]\ \approx\ 51.7\ \mu L\ FA}$$

To prepare the PA-12/DA blends, the same procedure was adopted where the mass of PA-12 powder and volume of DA were equal to the mass of PA-12 powder and volume of FA used to create the PA-12/FA blends.

According to the material safety data sheet of both agents (supplied by Hewlett Packard), the FA and DA are composed of 20 and 5 % 2-PYR, respectively. To create PA-12/2-PYR blends, liquid 2-PYR was added to PA-12 powder in compositions within the range of 0.10 – 8.72 wt.% 2-PYR, in accordance with the content of 2-PYR present within the PA-12/FA and PA-12/DA blends.

The wt.% of 2-PYR was determined by firstly using the percentage of the 2-PYR present in the agents to calculate the proportion of liquid volume of 2-PYR present in the FA and DA blends. After, the density of 2-PYR (1.12 g/mL) was used to determine the mass of 2-PYR present in each sample. The mass of 2-PYR was divided by the total mass of the sample (PA-12 and 2-PYR) to determine the wt.% 2-PYR. For example, in order to create the 1 wt.% FA blend, 51.7 μL of FA was required. Since 2-PYR is present in 20 % of the FA, 10.3 μL of the 51.7 μL was 2-PYR. In order to convert the volume of 2-PYR to the wt.% fraction, the volume of 2-PYR was multiplied by the density to calculate the mass of 2-PYR (=11.6 mg). After, the mass of 2-PYR divided by the sum of the mass of 2-PYR and PA-12 within the blend to determine the 2-PYR wt.%. In this case, the 1 wt. % FA contains 0.10 wt.% 2-PYR.

To create the PA-12/2-PYR/water blends that were compositionally identical to the FA and the DA, the same procedure was adopted to determine the volume of 2-PYR and water required to create the blends. The FA and DA are composed of 80 and 90 % water, respectively. Note, the composition of 2-PYR was identical to that of the PA-12/2-PYR blends.

Once the blends were created, they were left in a fume cupboard for 48 hrs to enable volatile constituents to evaporate. These blends were transferred to a desiccator with silica gel for a further 48 hrs to remove residual moisture. The use of heat in the drying process was avoided to limit the extent to which hydrolysis could occur to prevent unwanted chain reactions and the blends were dried at room temperature.

Table 2.1.1: A Table showing the mass of PA-12 and liquid volume of additives such as the Fusing Agent (FA), Detailing Agent (DA), carbon black, water and 2-pyrrolidone (2-PYR required to make the blends from virgin and aged PA-12 powder).

Additive	**Composition [wt.%]**	**PA-12 [g]**	**Liquid volume [µL]**
FA	1	3	51.69
	5	0.3	26.93
	10	0.3	56.86
	20	0.3	127.93
DA	1	3	51.69
	5	0.3	26.93
	10	0.3	56.86
	20	0.3	127.93
Carbon black	1	3	51.69
	5	0.3	26.93
	10	0.3	56.86
	20	0.3	127.93
Water		3	51.69
		0.3	26.93
		0.3	56.86
		0.3	127.93
2-PYR	0.1	3	2.58
	0.38	3	10.34
	0.5	3	13.47
	1.05	3	28.43
	1.97	3	53.87
	2.33	3	63.97
	4.07	0.3	11.37
	8.72	0.3	25.59

2-PYR/water (FA)	0.38	3	10.34/38.77
	1.97	3	53.87/202.0
	4.07	0.3	11.37/42.64
	8.72	0.3	25.59/95.95
2-PYR/water (DA)	0.1	3	2.58/43.94
	0.5	3	13.47/228.9
	1.05	3	28.43/483.3
	2.33	3	63.97/1087.4

2.2.4 Preparation of aged powder and aged powder blends

The Ohaus Analytical balance was used to weigh approximately 0.30g of PA-12 powder into labelled petri-dishes, the samples were transferred into the air ventilating Memmert UFE 400 oven at 170 ℃ for 0, 120, 168 and 216 hrs. The samples were removed from the oven and cooled to room temperature naturally. After, samples were transferred into labelled glass vials and moved into a desiccator filled with silica beads for 7 days. The samples were removed from the desiccator and sealed before being stored at room temperature away from sunlight until required.

To create PA-12 aged powder blends, PA-12 powder was weighed in petri-dishes using the Ohaus Analytical balance in accordance with the data in Table 2.2.1. The samples were transferred into an air ventilating Memmert UFE 400 oven at 170 ℃ for 7 days and then left to cool until they reached room temperature. In other studies relating to SLS, the ageing time has been linked to the number of processing cycles, in which “1 x recycled”, “2 x recycled” and “3 x recycled” PA-12 powder was correlated to powder collected from the build chamber that had been exposed to high temperature conditions for 20 – 40, 80 – 100 and 120 – 150 hrs, respectively (87). Whereas, in MJF the build time is often shorter meaning that PA-12 powder within the build chamber is held at high temperatures for shorter periods of time (31,55). Therefore, the thermal history of recycled SLS and MJF powder is different and this will further influence the final properties of a manufactured component. An ageing time of 7 days (or 168 hrs) was chosen since this represents the upper limit of processing cycles in powder bed fusion techniques and will likely cause changes in the thermal properties of PA-12 powder. A temperature of 170 ℃ was chosen since it was sufficiently below the melting temperature of PA-12 powder and on the basis that the temperature does not exceed 185 ℃ in MJF (91). The samples were transferred into labelled sample vials which were then placed into a desiccator filled with silica beads for 7 days. After thermal ageing, the blends were created as per section 2.2.2 and section 2.2.3. The samples were sealed and placed away from sunlight until required.

2.3 Experimental methods and techniques.

2.3.1 Differential scanning calorimetry (DSC)

A Mettler Toledo DSC 1 (Mettler-Toledo, Greifensee, Switzerland), calibrated with indium and zinc standards, was used to record the thermal response of the PA-12 powder and the blends described in section 2.2.2, 2.2.3 and 2.2.4 (166). A standard procedure was adopted in which the samples were weighed into 40 μL aluminium DSC pans sealed with aluminium DSC lids (166). Samples masses were in the region of 6 ± 0.5 mg (166). All experiments were carried out under nitrogen supplied at a flow rate of 50 mL/min (166). Samples were heated from 25 to 220 °C at 10 °C/min. The glass transition temperature, peak melting temperature, last trace of crystallinity and the heat of fusion were determined from the glass transition region and the melting region, illustrated in Figure 2.1.1. Prior to cooling, samples were stored at an upper isotherm of 220 °C for a period of 5 minutes to ensure complete melting and eliminate residual crystals, they were then cooled to 25 °C at a rate of 10 °C/min. The onset crystallisation temperature, peak crystallisation temperature and the heat of crystallisation were determined from the crystallisation region. A subsequent heat and cool were performed using the same conditions and parameters.

The degree of crystallinity of PA-12 and PA-12 blends was determined using the enthalpy of fusion for 100 % crystalline PA-12, $\Delta H_f^{100\%}$ = 209.3 J/g (58). Where X_c is the degree of crystallinity, ΔH_f is the enthalpy of fusion, $\Delta H_f^{100\%}$ is the enthalpy of fusion for a 100 % crystalline polymer and f is the filler weight percentage (92). In the PA-12 blends, the filler weight percentage was taken relative to the carbon black in the PA-12/FA and PA-12/CB blends and 2-PYR in the PA-12/DA, PA-12/2-PYR and PA-12/2-PYR/water blends. In the PA-12/water blends the standard calculation was used to determine the degree of crystallinity for PA-12, since water was thought to have evaporated from the blend during the drying process.

For PA-12:

$$X_C = \left(\frac{\Delta H_f}{\Delta H_f^{100\%}} \right) \times 100$$

Equation 1

Where ΔH_f is the enthalpy of fusion, $\Delta H_f^{100\%}$ is the enthalpy of fusion of a 100% crystalline material and X_C is the degree of crystallinity (%).

For PA-12 blends:

$$X_C = \left(\frac{\Delta H_f}{(1 - f)\, \Delta H_f^{100\%}} \right) \times 100$$

Equation 2

Where ΔH_f is the enthalpy of fusion, $\Delta H_f^{100\%}$ is the enthalpy of fusion of a 100% crystalline material, f is the percentage content of filler, and X_C is the degree of crystallinity (%).

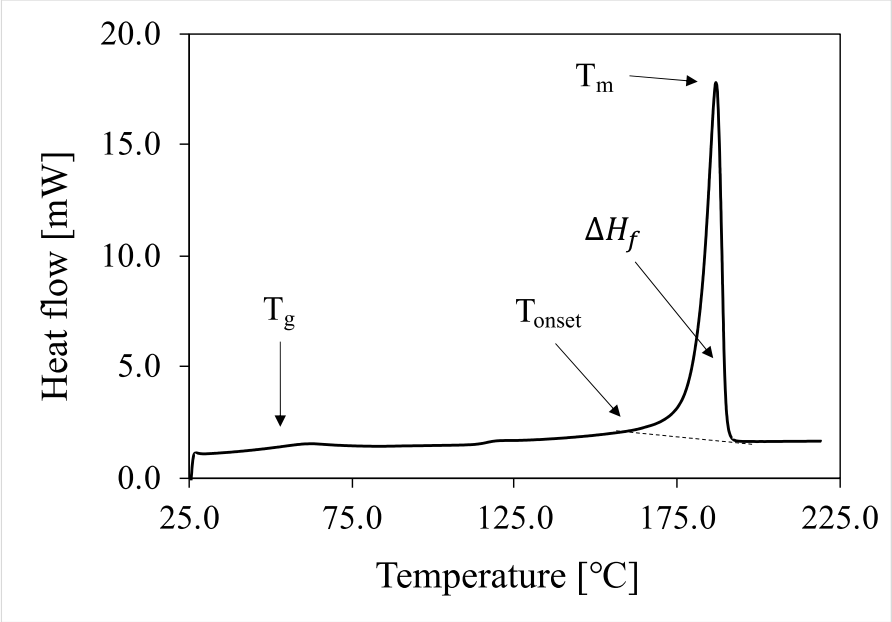

Figure 2.1.1: An example of a DSC trace of a dynamic heating run, showing melting parameters such as the glass transition temperature (T_g), onset melting temperature (T_{onset}), peak melting temperature (T_m) and the enthalpy of fusion (ΔH_f). The dashed line represents the baseline from which the onset of melting and enthalpy of fusion were determined.

Isothermal crystallisation was performed by heating samples from 25 – 220 ℃ at a rate of 10 ℃/min, where they were maintained at an upper isotherm of 220 ℃ for period of 5 minutes to erase the thermal history and eliminate residual crystals. Samples were then cooled rapidly at a rate of – 70 ℃/min to the desired isothermal crystallisation temperature, this ranged between 160 – 168 ℃, where they were maintained at the selected crystallisation temperature for 300 minutes. A rapid cooling rate was chosen in accordance with literature, this was also the upper limit of the DSC heating and cooling rate (20,21,93). After isothermal crystallisation, the samples were heated from the selected isothermal crystallisation temperature to 220 ℃, at a rate of 10 ℃/min. This stage was used to record the melting parameters, such as the peak melting temperature, to determine the equilibrium melting temperature of PA-12 (T_m^0). This was determined using the Hoffman-Weeks linear extrapolation method. Samples were then maintained at an upper isotherm of 220 ℃ for 2 minutes where they were cooled back to 25 ℃ at a rate of 10 ℃/min.

Non-isothermal crystallisation was performed by heating samples from 25 – 220 ℃ at a rate of 10 ℃/min, where they were maintained at an upper isotherm of 220 ℃ for period of 5 minutes to erase the thermal history and eliminate residual crystals. After, they were cooled to 25 ℃ using cooling rates of 5, 10, 15, 20, 25, 30, 35, 40 ℃/min. A subsequent heat at 10 ℃/min from 25 – 220 ℃ was used to observe the effect of cooling rate on the melting properties. Finally, the samples were cooled at a rate of at 10 ℃/min from 220 – 25 ℃.

2.3.1.1 Isothermal crystallisation: data processing

Isothermal crystallisation is observed by an exothermic peak on a graph of heat flow vs time. At the beginning of the process, there is an initial time period in which crystallisation has not yet started, this is referred to as the induction time or induction period. The beginning of the crystallisation process, t_0, is determined from the point at which the exothermic peak diverges from a baseline that is drawn from the induction period to the point at which the curve becomes flat and returns to the baseline. The end point of crystallisation (t_{end}) is determined when the exothermic curve returns to baseline. Between the regions of t_0 and t_{end} isothermal crystallisation models are implemented. An example of the crystallisation region between t_0 and t_{end} is shown in Figure 2.2.1.

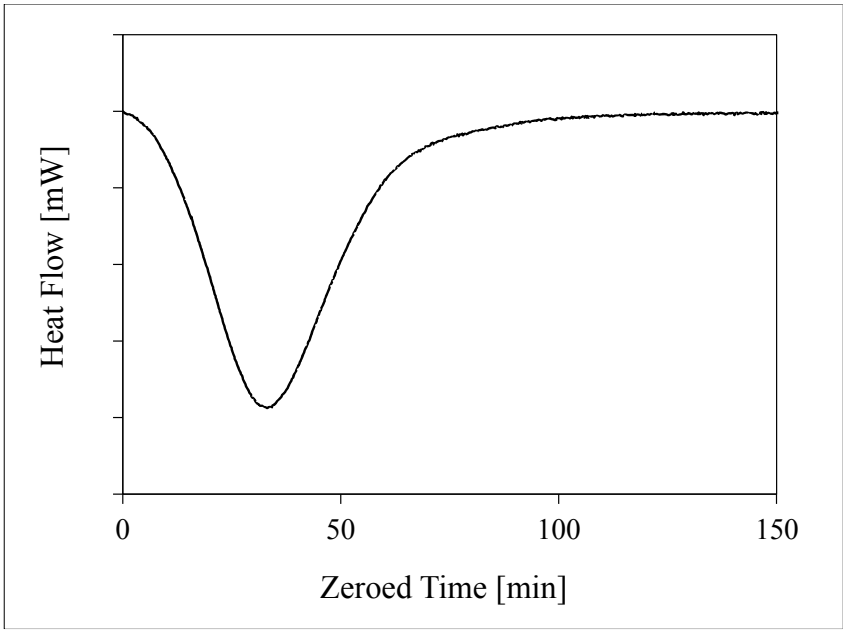

Figure 2.2.1: An example of a corrected isothermal crystallisation curve (endothermic, up), that has been limited between t_0 and t_{end} and corrected for time.

After raw data has been limited to the region between t_0 and t_{end}, a time correction was used to remove the induction period and ensure crystallisation begins at 0 s (referred to as "zeroed" or "corrected" data). This was done by subtracting the time at t_{end} by t_0. The trapezium rule was used to determine the cumulative area of the isothermal crystallisation curve. This involved dividing the exothermic crystallisation curve into sections. The area of each section was determined and then added cumulatively. This process describes the fraction of polymer that has transformed from the melt into the crystalline state over time, otherwise known as the fractional or relative crystallinity. Figure 2.2.3 shows a graph of relative crystallinity vs time, from which the crystallisation half time is determined by extrapolating the time, *t*, at 50 % transformation ($t_{50\%}$). This is a common measure of the rate of crystallisation. The half time for crystallisation can also be calculated by $t_{1/2} = t_{50\%} - t_0$.

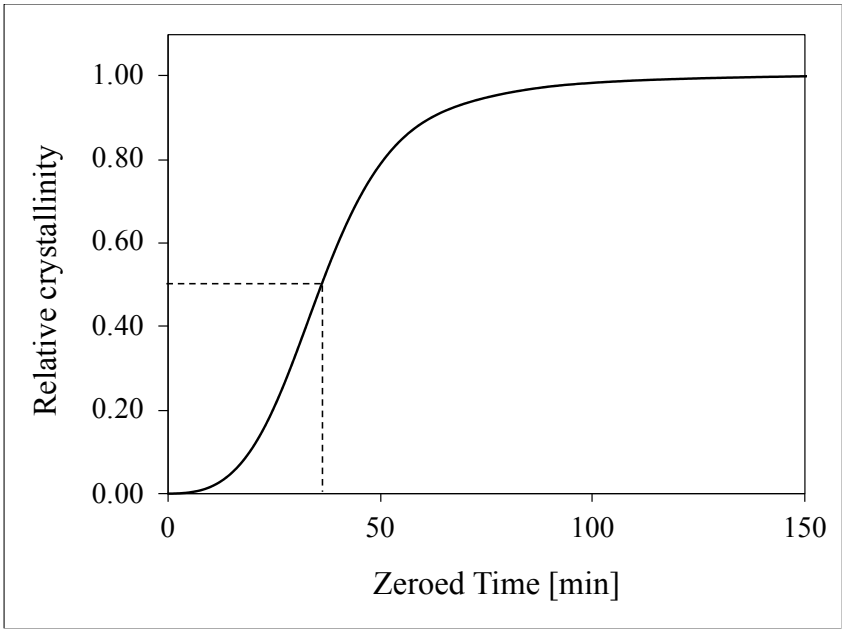

Figure 2.2.3: A graph of relative crystallinity vs time, showing the fraction of material that has transformed from the melt to a crystalline state over time. This graph has been generated from an isothermal crystallisation curve that has been limited between t_0 and t_{end} and corrected for time. The dashed line extrapolates the time at which 50 % transformation has taken place.

The Avrami equation shown below was used to analyse the crystallisation kinetics of PA-12 that was isothermally crystallised at different temperatures.

$$1 - X_t = exp(-kt^n)$$

Equation 3

This is also expressed in the double logarithmic form, from which a double log plot or Avrami plot is created:

$$ln[-ln(1 - X_t)] = ln\ k\ +\ n \ln t$$

Equation 4

Where, X_t is the relative crystallinity, k is the Avrami rate constant, t is the time and n is the Avrami exponent. In a plot of $ln[-ln(1-X_t)]$ vs ln t, the Avrami exponent and the Avrami rate constant are the gradient and intercept, respectively.

To obtain the Avrami rate and Avrami exponent from experimental data, the Avrami plot must be limited to only the linear portion of the data set. In accordance with the literature, the first 3 % and last 30 % of transformation were omitted, meaning the Avrami plot was limited to 3 – 70 % transformation to give the best linearity (20). This also removes the effects of secondary crystallisation since the Avrami equation focuses on primary crystallisation. A straight-line graph was produced, from which the gradient and intercept were used to determine the Avrami exponent, n and Avrami rate constant, k, respectively. The parameter, R^2, describes the linearity of the straight line and is a measure of how well the model describes experimental data, this should be above 0.990. An example of the linear region of an Avrami plot is shown in Figure 2.2.4. In addition to the Avrami model, other models were used and the relevant parameters were obtained by a double logarithmic plot.

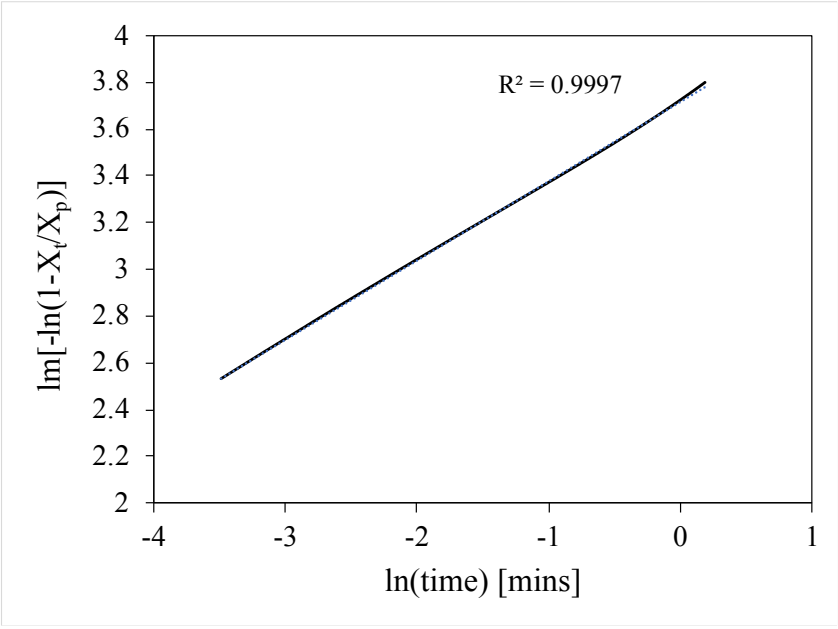

Figure 2.2.4: An example of an Avrami plot of [-ln(1-X_t)] Vs ln(t), for data limited between a relative crystallinity of 3 and 70 %.

2.3.2 Thermogravimetric analysis

Thermogravimetric analysis (TGA) measures the thermal degradation of a material in a controlled atmosphere of nitrogen or air by measuring the mass of a sample over a temperature range using a sensitive microbalance. To measure degradation of a sample in an inert atmosphere, nitrogen is used. However, to measure degradation products that may arise from oxidation, an oxygen atmosphere can also be used.

A NETZSCH STA 449C Jupiter was used to measure the mass of PA-12 powder over a temperature range. A sample of PA-12 powder was weighed (~ 5.2 mg) and sealed in an aluminium crucible. The sample was heated from 25 ℃ to 600 ℃ using a rate of 10 ℃/min in a controlled $20:80, O_2:N_2$ atmosphere.

An atmosphere of $20:80, O_2:N_2$ was chosen since MJF takes place under atmospheric conditions (23). In other studies, an atmosphere of $5:95, O_2:N_2$ was chosen since this represents conditions used in SLS (52,94).

2.3.3 Fourier transform infrared spectroscopy

A Nicolet 8700 attached with an Specac Attenuated Total Reflection (ATR) golden gate accessory, diamond crystal mounted in tungsten carbide and Smart Oribit accessory was used to record spectra of PA-12 powder, PA-12 powder blends, and samples of PA-12 and blends that had been extracted from DSC aluminium pans. The DSC samples were subjected to a standard heat and cool at a rate of 10 ℃/min, as per section 2.3.1. The spectra were recorded within the wavenumber range of 400 – 4000

cm^{-1}, using an optical velocity of 0.6329 cms^{-1} and 2 levels of zero filling. To define peak position and improve the signal quality, each sample was subjected to 250 scans at resolution of 2 cm^{-1}.

Before the spectra were collected, a background scan was recorded to remove effects of atmospheric water vapour and CO_2 from the sample data. The samples were then placed on the diamond crystal and fixed in place using a 80 cNm screw to eliminate trapped air. The samples were fixed in between the diamond crystal and the Sapphire Anvil. All spectra were recorded at ambient temperature. Between each sample, the diamond crystal mounted in tungsten carbide was cleaned with acetone to prevent cross contamination.

The resulting spectra were analysed using Omnic Software to determine shift in peak wavenumber, if any, of characteristic peaks such as the N-H and C=O band and to monitor the formation or disappearance of peaks. For polyamides, the N-H band (3100 – 3500 cm^{-1}) is of interest because it participates in hydrogen bonding (95,96).

The carbonyl index was determined in aged PA-12 powder and aged PA-12 extracted from DSC aluminium pans, following the work of W. Dong and P. Gijsman (10). This was defined as the ratio of the peak area of the oxidation band (carbonyl C=O, 1690 – 1754 cm^{-1}) and the reference band (CH_2, 1445 – 1484 cm^{-1}). Where the carbonyl band is susceptible to oxidative degradation and the CH_2 scissor bond is not and therefore does not change during oxidation.

2.3.4 Particle size analysis

The particle size of 4 samples of PA-12 powder was analysed using the HELOS H0972. Prior to analysis samples were dispersed in ethanol and sonicated using a Sucell sonicator for 15 s.

2.3.5 Scanning electron microscopy

The surface and shape of PA-12 powder was observed using Scanning Electron Microscopy (SEM). PA-12 powder was mounted to a SEM aluminium stub (of 30 mm diameter) using circular double-sided carbon adhesive discs. A Polaron SC7640 was used to sputter coat the sample in gold for 2 minutes. The JEOL 6060 was used to capture micrographs of PA-12 powder at magnifications ranging from 160 – 180 x at a 10 kV accelerating voltage.

2.3.6 Optical microscopy

Micrographs of recrystallised PA-12 and PA-12 blends were captured at a magnification of 500x. Samples were prepared by spreading $\sim 1\ mg$ of PA-12 powder and PA-12 powder blends (as described in section 2.2) between 2 circular glass discs (of diameter 16 mm). These were placed in a Linkam THMS600 hot-stage controlled by a Linkam LK600 controller. The hot-stage was mounted on a Leitz optical microscope. Digital images were captured using a Pixelink digital camera. Samples were heated to 220 °C and stored at an upper isotherm of 220 °C for two minutes prior to cooling back to 25 °C at a rate of 0.5 °C/min.

3.0 CHAPTER 3 – CHARACTERISATION OF POLYAMIDE-12

The aim of this work was to use a variety of characterisation techniques to determine the key characteristics of PA-12. DSC and TGA were used to determine the thermal properties of the polymer including the melting, recrystallisation and thermal degradation behaviour. This was important to consider since MJF relies on the thermal properties of PA-12 to create functional components. FTIR was used to identify the main functional groups within PA-12 powder. Particle Size Analysis was used to determine the average particle size and range of particle sizes of PA-12 powder used in MJF. This was used to provide an insight to powder processability. The data was compared to literature and used as a benchmark for further studies.

3.1 Characterisation of polyamide-12 powder

3.1.1 Differential scanning calorimetry

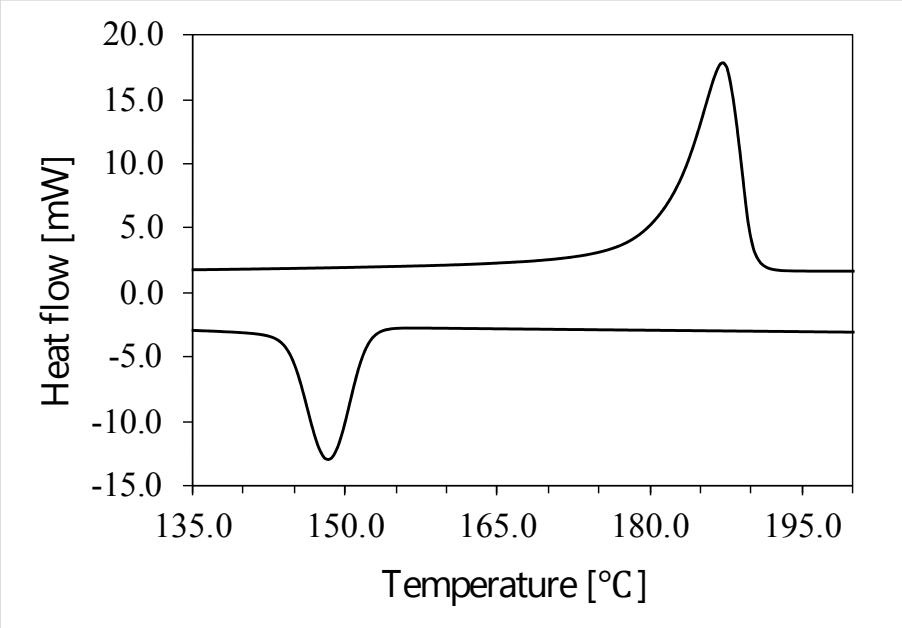

Figure 3.1.1: DSC thermogram (endo up) displaying the melting and recrystallisation behaviour of PA-12 powder (batch 1) used in MJF, using a heating and cooling rate of 10 ℃/min between 25 - 220 ℃.

The relationship between the structure, processing and properties of a polymer is highlighted by Chatham et al (23). This is referred to as the relationship between the "printability triad" and the "printed parts triad", in which, the chemical and morphological structure of a polymer define the intrinsic and extrinsic powder properties. This will dictate the behaviour of a polymer during processing. This is known as the printability triad. An understanding of these properties are required in order to optimise the processing technique. In turn, this creates a part with a particular microstructure that influences the final properties of the manufactured part. This is known as the printed parts triad.

For example, in SLS a wide variety of polymers are available and the processing parameters can be changed according to the material, since different materials have different melting and recrystallisation behaviour. This enables the user to have greater control over the printability triad and printed parts triad by selecting the material and the processing parameters. Whereas, in MJF (a HP technology), the materials available are limited and the processing parameters are controlled by HP algorithms that are designed for use with PA-12 powder supplied by HP. Therefore, it can be assumed that the relationship between the "printability triad" and the "printed parts triad" optimised.

In PBF techniques heat is used to fuse the powder particles in localised areas by heating a polymer to its melting temperature. According to F. Sillani et al, HP claim that MJF is 10x faster than other AM techniques such as SLS and FDM (31). S. Rosso et al, claim that the scanning speed in MJF is 10.5s, when used in balanced mode. This includes one rolling step and two injection passes. Whereas, in SLS the laser scan speed is 2000 mm/s (91). However, the parameters such as the scan speed in SLS are variable parameters. For example, in the work of F. Sillani et al, the scan speed used was 10 m/s (31). Other values of scanning speed include, 1500 mm/s (97), 6000 mm/s (51) 4000 mm/s and 5000 mm/s (98). After the polymer has been melted, it begins to crystallise. Once the build is complete, the build chamber is left to cool and the parts are removed. In MJF, parts are removed after being left to cool

overnight or once the core temperature of the powder chamber is below 50 ℃ (55,61). Therefore, it is important to investigate the thermal properties of the polymer. Investigating the thermal properties will reveal the thermal history of the polymer and provide and understanding of how the heating and cooling rate affects polymer melting and crystallisation.

DSC was used to record the melting and recrystallisation behaviour of PA-12 (batch 1). Heat 1 was used to record the thermal history of the polymer and cool 1 was used to record the recrystallisation properties at a controlled heating and cooling rate of 10 ℃/min. In PBF techniques, such as SLS and MJF, PA-12 powder is spread onto a build platform before it is melted, therefore the melting properties recorded on heat 1 can be related to PBF. Since MJF is a "closed" system controlled by HP algorithms, a standardised rate of 10 ℃/min was used to perform DSC experiments. This heating and cooling rate has also been used in other studies (55,58). The effect of heating rate on the melting behaviour of PA-12 is discussed later.

An example of a melting and recrystallisation curve of PA-12 powder used in MJF is displayed in Figure 3.1.1. The melting and crystallisation region of 4 samples of PA-12 powder (batch 1) showed an average glass transition temperature (T_g), peak melting (T_m) and crystallisation temperature (T_c) of 47.3 ± 0.4, 186.8 ± 0.6 and 148.6 ± 0.7 °C. Additionally, the average enthalpy of fusion and degree of crystallinity were 105.9 ± 0.7 J/g and 50.6 ± 0.4 %. This demonstrates minimal sample variation in the thermal behaviour of PA-12 powder.

The melting and recrystallisation behaviour of 3 samples of PA-12 powder from batch 2 were also recorded and averaged. This data is presented in Table 3.1.1. The melting parameters, such as the onset melting temperature, peak melting temperature and last trace of crystallinity of powder from batch 2

was comparable to batch 1. However, the degree of crystallinity of powder from batch 2 decreased when compared to batch 1, where $X_{c,\ batch\ 1}$ = 50.1 % and $X_{c,\ batch\ 2}$ = 42.0 %. The degree of crystallinity for batch 2 was comparable to the literature (55,58,60). The recrystallisation parameters, such as the onset, peak and end crystallisation temperature of batch 2 was also comparable to batch 1. However, the degree of crystallinity on cooling decreased, when compared to batch 1. Overall, this data shows that the degree of crystallinity determined from the enthalpy of fusion and enthalpy of crystallisation of powder from batch 2 was lower than batch 1.

The melting and recrystallisation behaviour of virgin PA-12 powder (batch 1) was compared to the literature. This data is displayed in Table 3.1.1. In general, there were variations in the melting and recrystallisation temperatures.

The onset melting temperature of virgin PA-12 powder (batch 1) was lower than Galati et al, Sillani et al and Xu et al (31,58,60). The peak melting temperature was comparable to Riedelbauch et al (55) and Xu et al (60) but lower than M. Galati et al (58). The degree of crystallinity was comparable to Sillani et al (31) but greater than M. Galati et al (58), Riedelbauch et al (55) and Xu et al (60).

The onset crystallisation temperature was greater than Galati et al (58), Sillani et al (31) and Xu et al (60). The peak crystallisation temperature was lower than Galati et al (58) and Reidelbauch et al (55) but greater than Xu et al (60).

Therefore, the data in Table 3.1.1 shows that there were variations in the melting and recrystallisation behaviour of PA-12 in the literature, despite all powders being labelled as HP MJF grade PA-12 virgin powder. This can be due to differences in heating and cooling rate, which affect the melting and recrystallisation behaviour of a material. A lower heating rate will typically cause the melting peak to shift to lower temperatures, become narrower and more defined, as seen in Figure 3.1.3. A lower cooling rate will typically cause the crystallisation peak to shift to higher temperatures, become narrower and more defined, as seen in Figure 3.1.4. Other studies also use a heating and cooling rate of 10 ℃/min (31,55,58). In studies by Xu et al (60), a lower heating and cooling rate of 5 ℃/min was used. The peak

melting temperature of PA-12 obtained in this experimental work was slightly lower temperature than in studies (31,55,58). In Table 3.1.1, the data corresponding to literature (31,55,58) shows a variation in the peak melting temperature of PA-12 powder on heat 1 by ~3 ℃, where the heating rate was 10 ℃/min. Furthermore, by comparing literature, the greatest variations in melting and recrystallisation behaviour were the onset melting temperature, last trace of crystallinity, degree of crystallinity and onset crystallisation temperatures. For example, the onset melting temperature reported by Galati et al was 183 ℃ (58). Whereas Xu et al report the onset melting temperature of 173 ℃, showing a difference of 10 ℃ (60). These variations are due to the parameters such as the onset melting temperature being subjective.

The melting behaviour of PA-12 on heat 2 is displayed in Figure 3.1.2. Heat 2 shows the material specific properties with a consistent thermal history, after the thermal history from processing has been erased. A double melting peak was observed, displaying 2 peak melting temperatures (labelled a and b in Figure 3.1.2). The peak melting temperature of peak *a* and *b* were 170.50 ℃ and 177.67 ℃. The double melting peak is due to melt-recrystallisation, which occurs when lower heating rates are used (99). Therefore, the main melting peak was assigned to peak *b*, at 177 ℃. This was comparable to Galati et al who reported a peak melting temperature of 177 ℃ (58). In the work reported by Reidelbauch et al, the presence of a shoulder peak at lower temperatures was also observed, however, this was not commented on (55).

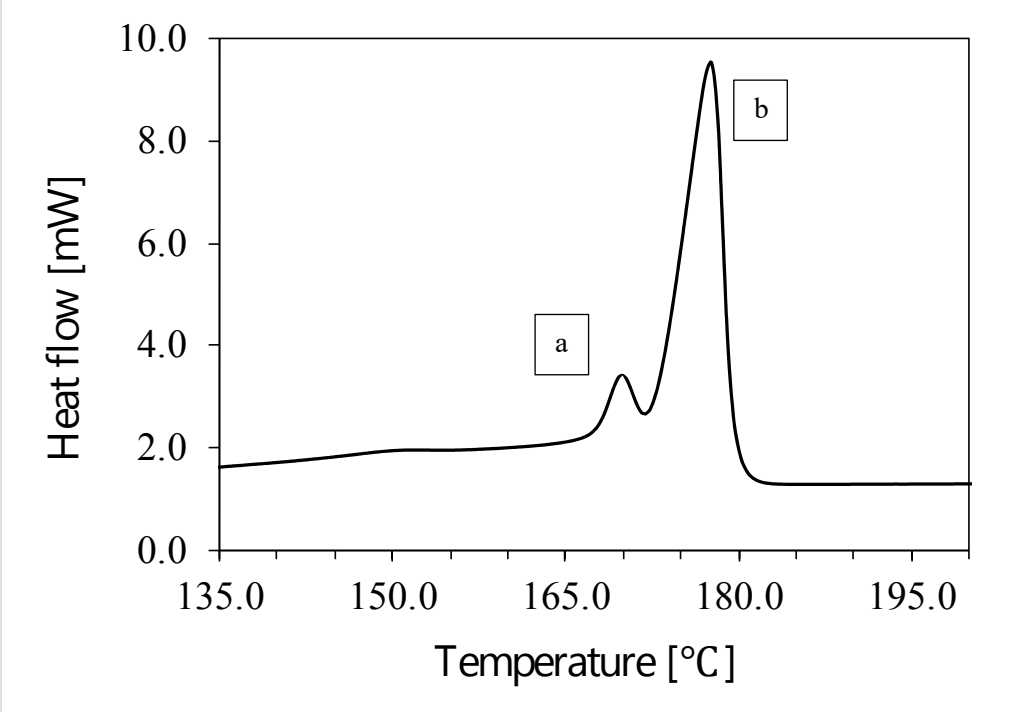

Figure 3.1.2: DSC thermogram (endo up) displaying the melting behaviour of PA-12 powder (batch 1) used for MJF on heat 2, performed using a heating rate of 10 °C/min between 25 - 220 °C. Labels "a" and "b" are assigned to the lower temperature and higher temperature melting peak, respectively.

Table 3.1.1: Melting and crystallisation parameters for heat 1 and cool 1 of PA-12 powder (averaged from 4 samples of PA-12 powder) using a heating and cooling rate of 10 K/min between 25 - 220 ℃, compared to melting and crystallisation parameters of virgin PA-12 powder obtained from the literature. Where T_P - Peak Melting/Crystallisation Temperature, T_E - Last Trace of Melting/End Crystallisation Temperature, T_O - Onset of Melting/Crystallisation, X_c – Degree of Crystallinity and ΔH is the heat of fusion/crystallisation.

	Melting					Crystallisation			
	T_O (℃)	T_P (℃)	T_E (℃)	ΔH (Jg^{-1})	X_c (%)	T_O (℃)	T_P (℃)	T_E (℃)	ΔH (Jg^{-1})
Batch 1	170.0	186.8	193.2	104.9	50.1	156.6	148.6	140.3	60.5
Batch 2	170.5	188.2	193.8	87.9	42.0	158.1	148.5	141.0	49.3
M. Galati et al (58)	183.0	189.0		82.0	39.2	147.0	141.0		41.0
J. Riedelbauch et al (55)		187.8		97.4	46.5		142.6		
F. Sillani et al (31)	180.5			110.3	52.7	148.6			47.9
Z. Xu et al (60)	173.6	185.4		82.6	39.5	156.1	151.2		40.0

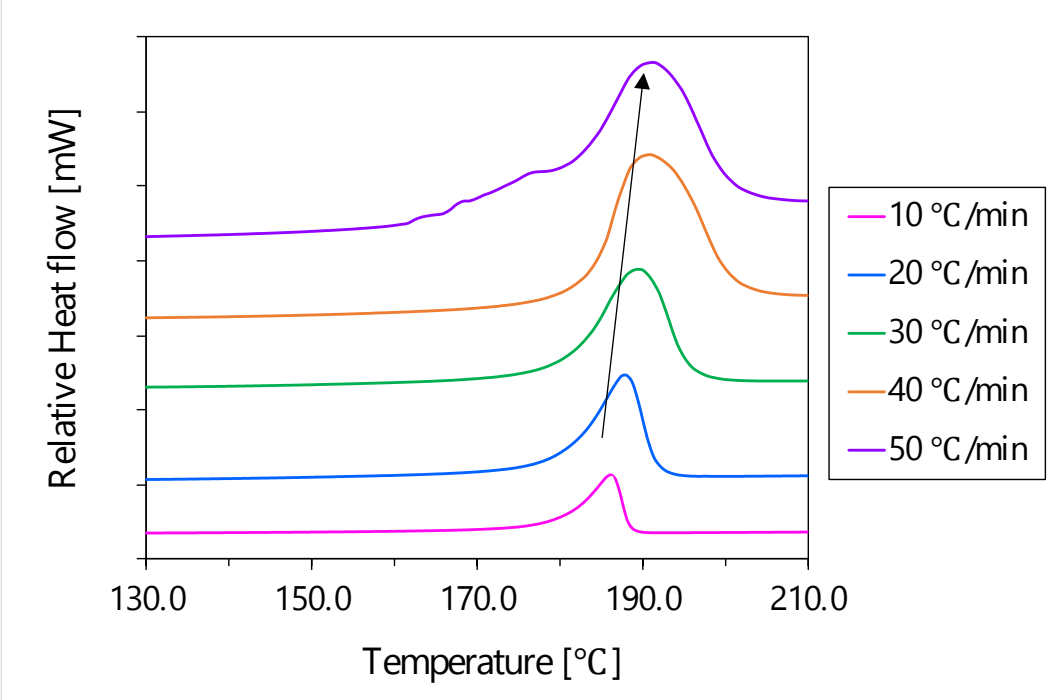

Figure 3.1.3: DSC curve (endo up) displaying the melting behaviour on heat 1 of PA-12 powder (batch 1) between 25 - 220 °C, using heating rates of 10, 20, 30, 40 and 50 °C/min.

Table 3.1.2: Melting behaviour of PA-12 at various heating rates. Where T_P - Peak Melting, T_E - Last Trace of Melting and T_O - Onset of Melting.

Heating rate [°C/min]	T_O [°C]	T_M [°C]	T_E [°C]	Melting region [°C]
10	170.00	186.80	193.20	23.20
20	169.33	187.67	197.00	27.67
30	160.13	189.50	206.00	45.87
40	158.90	191.20	214.00	55.10
50	154.50	192.83	216.00	61.50

The melting curve of PA-12 powder subjected to various heating rates is displayed in Figure 3.1.3 and the data is shown in Table 3.1.2. The heating rate had a significant influence on the melting behaviour of PA-12. As the heating rate increased, the onset melting temperature shifted to lower temperatures while the peak melting temperature and the last trace of crystallinity shifted to higher temperatures. The peak melting temperature of PA-12 at a heating rate of 10, 20, 30, 40 and 50 °C/min was 186.8, 187.7, 189.5, 191.2 and 192.8 °C, respectively. The melting region was determined by subtracting the last trace of crystallinity from the onset melting temperature. As the heating rate increased, the melting region increased and caused the melting peak to broaden. The change in melting behaviour with heating rate was a result of thermal lag. This was caused by poor thermal conductivity of the polymer, where the polymer takes time to melt. A heating rate of 10 °C/min was chosen as a standard heating and cooling rate in line with the literature (55,58). Additionally, the curve produced at 10 °C/min minimised the thermal lag and produced a curve that was distinct.

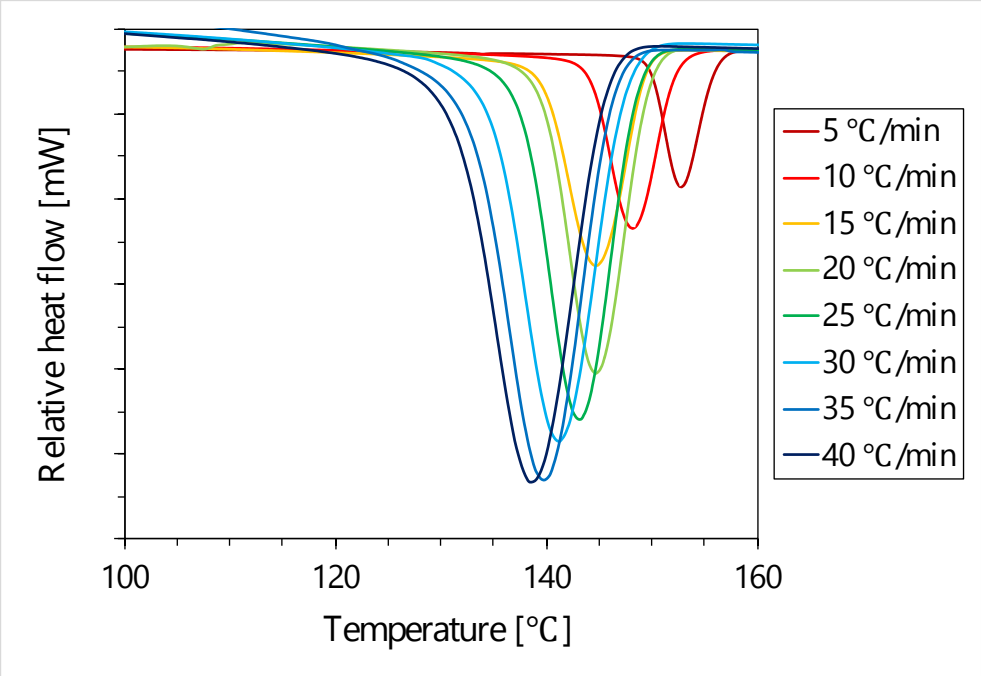

Figure 3.1.4: DSC thermogram (endo up) displaying the cooling behaviour on cool 1 of PA-12 powder (batch 1) between 220-25 °C, using cooling rates of 5, 10, 15, 20, 25, 30, 35, 40 °C/min.

Table 3.1.3: Crystallisation behaviour of PA-12 at various cooling rates. Where T_P - Peak Crystallisation Temperature, T_E - End Crystallisation Temperature, T_O – Crystallisation and X_c – Degree of Crystallinity.

Cooling rate [℃/min]	T_O [℃]	T_C [℃]	T_E [℃]	Crystallisation region [℃]
5	160	152.79	141.99	18.01
10	156.76	148.08	136.3	20.46
15	153.74	144.75	129.27	24.47
20	153.16	144.67	130.27	22.89
25	152.58	143.13	126.18	26.4
30	152.76	141.25	121.98	30.78
35	150.88	139.80	118.35	32.53
40	150.47	138.67	117.61	32.86

The cooling curve of PA-12 powder subjected to various cooling rates is displayed in Figure 3.1.4 and the data is shown in Table 3.1.3. The cooling rate had a significant influence on the crystallisation behaviour of PA-12. As the cooling rate increased, the onset crystallisation temperature, the peak crystallisation temperature and end crystallisation temperature shifted to lower temperatures. The peak crystallisation temperature of PA-12 at a cooling rate of 5, 10, 15, 20, 25, 30, 35 and 40 ℃/min was 152.8, 148.1, 144.8, 144.7, 143.1, 141.2, 139.8 and 138.7 ℃, respectively. This trend was comparable to H. W. B. Teo et al, when studying non-isothermal crystallisation of PA-12 used in MJF (100). The crystallisation region was determined by subtracting the end crystallisation temperature from the onset crystallisation temperature. As the cooling rate increased, the crystallisation region increased, causing

the crystallisation peak to broaden. A cooling rate of 10 ℃/min was chosen as a standard cooling and cooling rate in line with literature (58). Additionally, a cooling rate of 10 ℃/min produced a distinct cooling curve.

In PBF techniques, the supercooling window is considered a desirable processing temperature window in which the build chamber is maintained. A high temperature environment is desirable to minimize the effects of shrinkage and warping due to crystallisation (23). Additionally, a larger supercooling window offers more control of the ability to sinter which may lead to better consolidation of powder layers (58). The supercooling window is determined by subtracting the onset crystallisation temperature from the onset melting temperature, an example is shown in Figure 3.1.5. The supercooling window was affected by the heating and cooling rate, where the onset melting and onset crystallisation temperature shifted to lower temperatures with increased heating and cooling rate (see Table 3.1.2 and 3.3). The supercooling window decreased as the rate increased. The supercooling window for a heating or cooling rate of 10, 20, 30 and 40 ℃/min was 13.2, 16.2, 7.4 and 8.4 ℃. A similar analysis was performed by Teo et al on PA-12 used in MJF (100). In their work, the supercooling window was determined using the peak melting and crystallisation temperature of PA-12 and was found to vary with rate. However, it was reported that the supercooling window was significantly affected by the cooling rate in comparison to the heating rate. Whereby, the peak meting temperature varied ~185 ℃, whilst the peak crystallisation temperature changed with cooling rate. The chosen heating and cooling rates used were between 0.2 to 10 ℃/min, which was lower than in this experimental work.

The supercooling window was determined using different methods; by the onset melting and crystallisation temperature and the peak melting and crystallisation temperatures. The onset melting and crystallisation temperature, although subjective, provides an accurate measure of the supercooling window with respect to MJF since the powder will remain at a high temperature until it is melted/sintered by the application of heat areas containing the FA. The peak melting and crystallisation temperature is also beneficial since this will provide material specific information as the peak melting and crystallisation temperatures are defined.

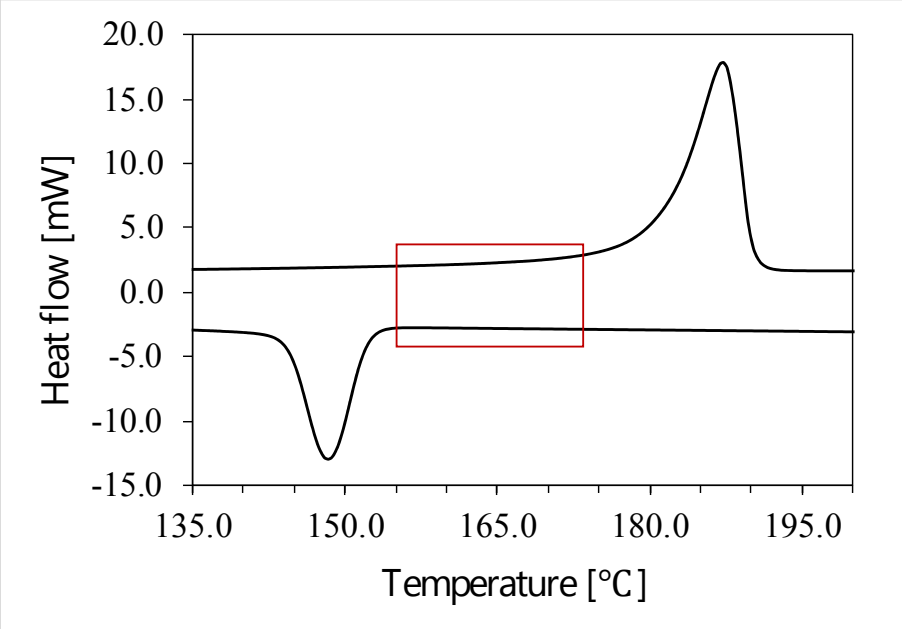

Figure 3.1.5: DSC thermogram (endo up) displaying the melting and cooling behaviour on heat 1 and cool 1 of PA-12 powder batch 1, using a heating and cooling rate of 10 °C/min. The red box illustrates the supercooling window.

3.1.2 Thermogravimetric analysis

The mass loss degradation of PA-12 powder was recorded over a temperature range of $25 - 600$ °C and is displayed in Figure 3.1.6. The polymer maintained 100 % mass until a temperature of ~320 °C. After, the mass gradually decreased within the temperature region of $320 - 400$ °C. A significant decrease in mass was observed between $400 - 500$ °C. The mass continually decreased between $500 - 600$ °C, where at 600 °C the mass decreased to 4.9 %. In other work on MJF parts produced from "neat" PA-12, a significant mass loss step was also observed between 320 – 500 °C (82).

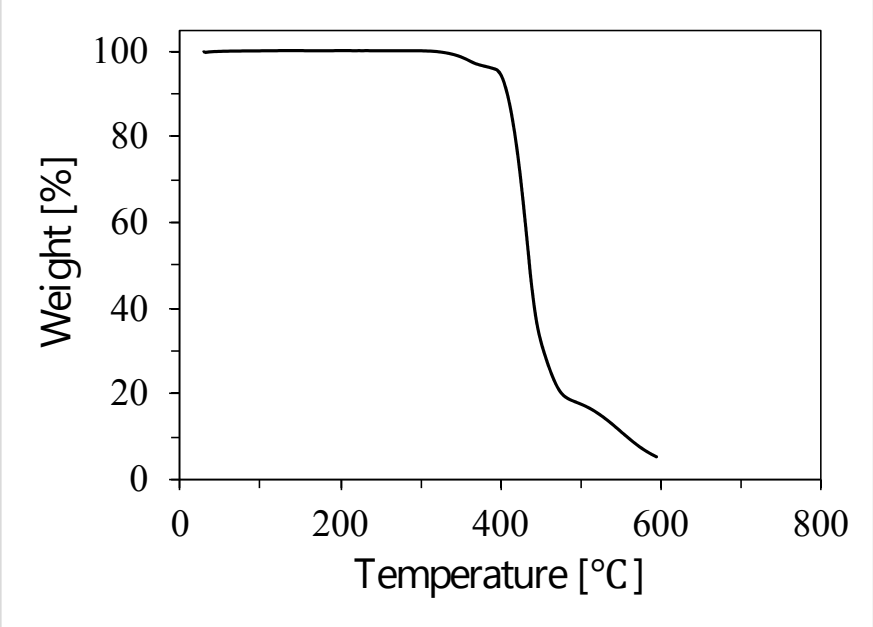

Figure 3.1.6: TGA and DSC trace of PA-12 powder (batch 1) between 25 – 600 ℃, using a heating rate of 10 ℃/min under a 20:80 O_2/N_2 atmosphere.

The temperature at 1 and 50 % mass were determined by extrapolating the curve at 1 and 50 % weight to the corresponding temperature, this was recorded at temperatures of 322 ℃ and 436.3 ℃, respectively. The TGA of a MJF component is shown in the literature (58), where a 50 % mass loss was recorded at a higher temperature of ~ 450 ℃ using a comparable heating rate. This could be due to the presence of the FA and DA used in MJF, which has been detected in printed parts (75).

The temperature corresponding to the 1 and 50 % mass loss will vary depending on heating rate, where a lower heating rate will shift the onset of degradation to lower temperatures. Vasquez et al note that in commercial processes, the mass loss is likely to occur at much lower temperatures suggesting that a low heating rate is used in commercial processes (52). In other PBF techniques, such as SLS, the build time is much slower than in MJF, however this is dictated by the laser scanning speed. The build time for components manufactured by MJF is quicker than SLS, where according to HP, the build time for MJF is up to 10x quicker than SLS or FDM (59). Therefore, the heating rate can be expected to be greater, this suggests less polymer degradation will occur at higher temperatures.

Other factors to consider that can affect mass loss degradation of PA-12 in MJF is the presence of the FA and DA, which are jetted on the powder bed surface during the component fabrication, in which, the FA and DA may interact with the polymer and change the physical properties of the polymer. Scherer et al investigated the mass loss of the FA and DA by TGA (75). It was shown that degradation took place in two-steps. The first step involved the degradation of components such as triethylene glycol, 2-pyrrolidone which occurred between 100 – 450 ℃ in a nitrogen atmosphere. The second step was a heating phase from 800 – 950 ℃ in an oxygen atmosphere. In an oxygen atmosphere, the DA did not show mass loss. Whereas, in the FA, the carbon black or pyrolysis products from the first step were oxidised. Additionally, within the temperature range of the second step all components had evaporated or completely decomposed without the formation of char by pyrolysis. In MJF the build temperature does not exceed 185 ℃ therefore it is likely that some components will be retained in the final part (31,91). This was confirmed by Scherer et al (75).

In both SLS and MJF, the powder is held at high temperatures for extended periods of time within the build chamber, this can cause degradation of powder. The powder bed temperature in SLS has been reported at 175 ℃, whereas in MJF the overall temperature is controlled by HP algorithms. It has been reported that the build temperature does not exceed 185 ℃ (31,91). Therefore, thermal degradation can occur during processing. Other types of degradation are likely to be present in MJF, such as thermo-oxidative degradation since manufacturing takes place in an ambient atmosphere. This results in polymer chain degradation which causes a decrease in molecular weight and/or chain formation by post-polymerisation reactions which cause an increase in molecular weight (55,101). Other mechanisms caused by degradation include crosslinking. Wudy et al studied the influence of degradation on PA-12 powder during SLS (11). Under multiple conditions, such as an oxygen, vacuum and a nitrogen atmosphere during the first processing hours, mechanisms such as cross-linking dominated. As the processing time increased chain scission dominated, especially under an oxygen atmosphere. It was clear that the use of aged powder reduced the mechanical properties of the final parts. The mechanism

of thermo-oxidative degradation of PA-6,6 was linked to the mechanical properties by Pliquet et al, where different reaction pathways led to the production of aldehydes, carboxylic acids, primary amides and imides (102).

To prevent degradation or ageing, thermocouples can be used to monitor the temperature distribution on the powder bed surface or in the build chamber (103). The use of thermocouples may also give an indication of the heating rate or cooling rate of PA-12 used in MJF by monitoring the change in temperature throughout the duration of the build.

3.1.3 Fourier transform infrared spectroscopy

The FTIR spectrum of PA-12 powder was recorded and is shown in Figure 3.1.7. The peak assignments for PA-12 are displayed in Table 3.1.4. Analysis of the fingerprint region displayed an Amide V band at ~725 cm^{-1}. Kinoshita et al and Schroeder denote this peak to the gamma formation of PA-12 where chains twist slightly to allow hydrogen bonding (104,105). The peak assignments of PA-12 from batch 1 and 2 were comparable to O'Conner et al, for a PA-12 part manufactured by MJF (61,68). In polyamides the N-H band (3100 – 3500 cm^{-1}) is of interest because it participates in hydrogen bonding (95,96). Therefore, further studies using FTIR in this work will focus on the N-H stretching vibrations.

Table 3.1.4: FTIR peak assignments for PA-12 powder.

Wavenumber [cm^{-1}]		O' Connor et al (68)	Peak assignment
Batch 1	Batch 2		
3292.9	3293.1	3279	Hydrogen bonded N-H stretching
2917.4	2917.7	2918	CH_2 asymmetric stretching
2849.1	2849.5	2850	CH_2 symmetric stretching
1633.5	1633.3	1639	C=O stretching
1540.4	1540.9	1545	C-N stretching, C=O in plane bending
1367.4	1367.7	1370	CH bend, CH2 twisting
1269.0	1268.8	1269	C-N stretching, C=O in plane bending
1124.3	1124.6	1122	C-C stretching
944.8	943.5	944	CONH in plane
719.4	719.6	720	CH_2 rocking

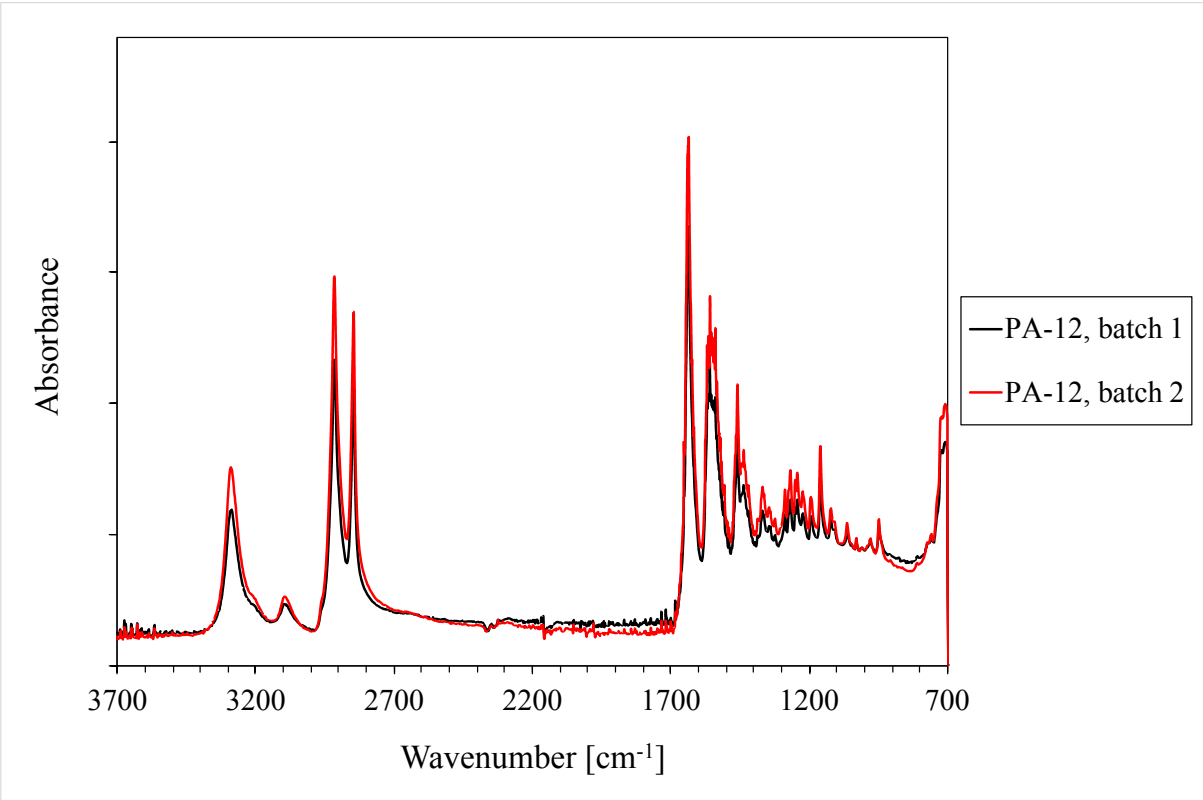

Figure 3.1.7: FTIR spectrum of PA-12 powder between 700 – 4000 cm^{-1}, normalised to the same baseline.

3.1.4 Particle size analysis

In PBF techniques, the particle size and particle size distribution are important to investigate since they affect the entire manufacturing process from powder processability, such as powder flowability, to the dimensional accuracy and performance of a manufactured component. This is performed by Particle Size Analysis (PSA). Goodridge et al reported an optimum powder size between 45 – 90 μm for PBF techniques (106).

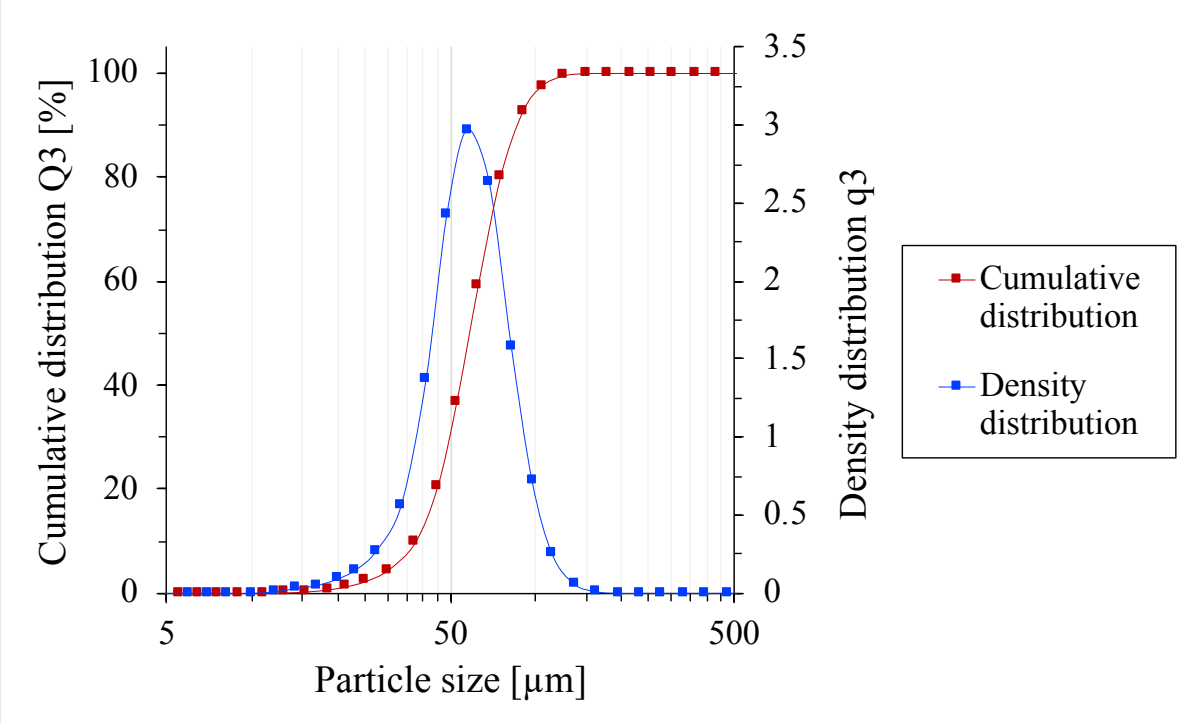

Figure 3.1.8: Particle size analysis of PA-12 powder (batch 1) displaying the particle size relative to the cumulative distribution and the density distribution.

The particle size distribution was determined by the density distribution curve shown in Figure 3.1.8. The particle size varied between 11.96 – 164.32 μm and followed a Gaussian distribution. The average particle size was determined by the peak maxima of the density distribution curve, showing an average particle size of 58.48 μm, thereby falling in the optimum range stated by Goodridge et al. Other literature has reported a slightly higher average particle size of 60 μm for PA-12 powder used in MJF, though the state of the powder was not known (e.g. virgin, refreshed or recycled) (66,77,85). Meanwhile, an average particle size of 54.8 μm was reported by Xu et al for PA-12 used in MJF, this was lower than the average particle size of PA-12 (batch 1). The literature shows that there is slight variability of average particle size between batches of PA-12 powder (60).

Table 3.1.5: D_{50} for PA-12 powder used in SLS and MJF.

	Powder state	SLS		MJF	
		Optical microscopy	Laser diffraction	Optical microscopy	Laser diffraction
		[μm]	[μm]	[μm]	[μm]
Experimental	Virgin				60.51
Sillani et al (31)	Virgin	62.8	52.2	65.1	67.3
	Recycled	69.7	52.4	67.3	54.8
Z. Xu et al (60)	Virgin		58		55.4

The Volume Mean Distribution (VMD) or D_{50}, was also determined. This is the diameter at which half of the sample population is below x μm and half are above. This data is displayed in Table 3.1.5. The average D_{50} from 4 samples of PA-12 powder (batch 1) was 60.5 μm. Other studies explore the particle size (D_{50}) for PA-12 powder used in MJF and SLS, this data is shown in Table 3.1.5. Sillani et al (31) report the D_{50} of virgin and recycled powder PA-12 powder used in SLS and MJF determined by laser diffraction and optical microscopy. In SLS, the D_{50} of virgin and recycled PA-12 powder (3D Systems Duraform) was 52 μm, determined by laser diffraction. The D_{50} of virgin and recycled SLS powder was $\sim$ 62 and $\sim$ 69 μm, determined by optical microscopy. In MJF grade PA-12, the D_{50} for virgin and recycled was $\sim$ 58 and $\sim$ 54 μm, determined by laser diffraction. The D_{50} of virgin and recycled powder was $\sim$ 65 and $\sim$ 67 μm, determined by optical microscopy. In general, for both PBF techniques the values obtained by laser diffraction were lower than optical microscopy. Xu also characterised the particle size of "raw" PA-12 powder used in SLS and MJF by a laser particle analysis. The D_{50} for SLS and MJF PA-12 powder was $\sim$ 58 and $\sim$ 55.4 μm (60). This was lower than the D_{50} obtained in this study. Overall, the literature shows that the D_{50} values vary slightly with MJF powder batch, material refresh status and characterisation technique.

3.2 Characterisation of a MJF component

3.2.1 Differential Scanning Calorimetry

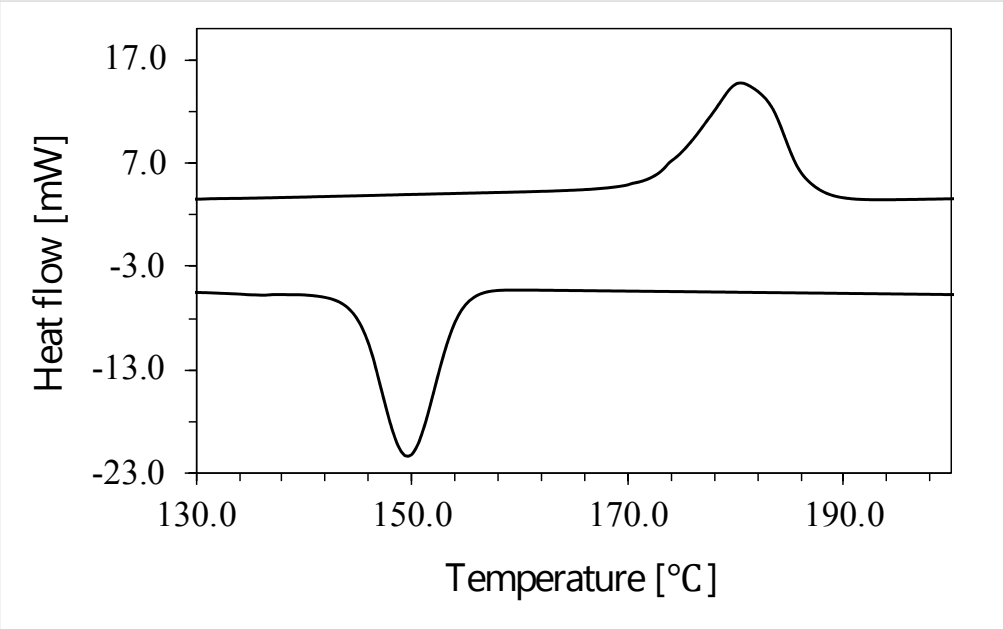

Figure 3.2.1: DSC thermogram (endo up) displaying the melting and crystallisation behaviour of a MJF component, performed using a heating and cooling rate of 10 ℃/min between 25 - 220 ℃.

The melting and recrystallisation behaviour of a MJF component was recorded on heat 1 and cool 1. This is displayed in Figure 3.2.1. The powder state i.e., virgin, recycled or refreshed, is unknown for this component. The melting behaviour showed an onset melting temperature, peak melting temperature and last trace of crystallinity of 166.2, 180.5 and 193.3 ℃. The enthalpy of fusion was 58.5 J/g and the degree of crystallinity was 27.9 %. The recrystallisation behaviour showed an onset and peak crystallisation temperature of 159.8 and 149.8 ℃. The enthalpy of crystallisation was 54.62 J/g and the degree of crystallinity was 26.10 %.

This data shows that the melting and recrystallisation behaviour for a PA-12 part manufactured by MJF is different to PA-12 powder. In comparison to heat 1 of PA-12 powder, the peak melting temperature of a MJF part decreased by 6.3 ℃. This is due a difference in thermal history of a MJF part and PA-12 powder. The difference in melting properties may also arise from the addition of the FA or DA used in MJF, which are retained in the part (75). The quantity of the FA and DA is unknown for MJF and is controlled by HP algorithms. Though the estimated processing parameters for a MJF build in fast mode is 0.058 mm^3 FA/mm^3 part and 0.062 mm^3 DA/mm^3 part (107).

A comparison of melting and recrystallisation behaviour of parts manufactured by MJF reported in the literature is shown in Table 3.2.1. In a study by Cai et al, the onset melting temperature and peak melting temperature were reported at 172.7 and 179.6 ℃. The onset recrystallisation temperature and peak recrystallisation temperature were reported at 153.5 and 149.1 ℃ (84). The peak melting and crystallisation temperature were comparable to that displayed in this section. The melting and recrystallisation behaviour of a part manufactured by MJF were also reported by O'Connor et al and showed a higher peak melting temperature of 183.9 ℃ and a lower peak crystallisation temperature of 147.1 ℃. The degree of crystallinity determined by the enthalpy of fusion and crystallisation were 32 and 26 %, respectively (27). In studies by O'Connor et al and Cai et al (27,84) the parts were printed in balanced mode and the heating and cooling rate was 10 ℃/min. Though the powder feedstock material was different in both studies. A refreshed feedstock material containing 20 % new and 80 % recycled powder was used by Cai et al to create components using MJF (84). In the work by O'Connor et al, the condition feedstock material was unreported (27). The differences in melting and recrystallisation properties may therefore be due to the condition of the feedstock material. This has been studied in more detail by Riedelbauch et al (55).

In parts fabricated from other PBF techniques, such as SLS, a bimodal melting peak is often observed, where the main melting peak is positioned at a lower temperature than the second melting peak. The

double melting peak is associated with incomplete melting of PA-12 particles during the SLS process (51,60,91). The lower temperature melting peak indicates complete melting of polymer particles, while the higher temperature melting peak indicates unmolten particle cores (84). The absence of the double melting peak in MJF components suggests complete melting of PA-12 powder during the part fabrication. This is likely due to the FA which contains carbon black to promote higher heating of powder particles by absorbing infrared radiation (58). Interestingly, Xu et al reported a double melting peak for a part fabricated by MJF, this was attributed to the presence of 2 crystal phases from a melted outer section of the particle and unmelted particle core of PA-12 powder (60). This could be due where in the powder bed the part is fabricated as different locations are exposed to different heating and cooling mechanisms.

The double melting peak phenomenon was discussed by Cai et al, who compared their work to S. Dadbakhsh et al in relation to the parts fabricated with refreshed feedstock powder. In SLS components a double melting peak was reported by S. Dadbakhsh et al, who claimed that the height of the higher temperature shoulder peak in SLS parts increased when the feedstock material contained a greater proportion of used powder. This was due to a polycondensation reaction that occurred when powder had been exposed to multiple processing cycles, leading to an increase in molecular weight in the used particles. The used particles therefore have a higher melting temperature than virgin particles due to an increase in molecular weight. Consequently, the proportion of unmolten particle cores in components was greater in components made from refreshed powder than virgin powder, where both states of powder are exposed to the same input energy during sintering. This was used to explain the presence of the second melting peak at higher temperature. It was also reported that the shoulder peak intensity increased proportionally with the amount of used powder within the feedstock.

However, the absence of the double melting peak in MJF components fabricated with refreshed feedstock material in the work of Cai et al contradicted the work by Dadbakhsh et al, in relation to the proportion of used powder in components. In this study, the MJF components contained a larger proportion of used powder (80 % used powder) than the SLS components (50 % used powder). This

would lead the reader to believe that the melting behaviour of MJF components should have a larger higher temperature shoulder peak than the SLS components, according to Dadbakhsh et al. Instead, Cai et al associated the absence of the double melting peak with the presence of the FA in MJF components. Where the higher thermal absorption capability of the FA caused the powder layer to be fully melted, despite containing a large proportion of used powder (51,84).

In the work by Sillani et al, it was reported that SLS grade PA-12 experienced polycondensation upon powder reuse. Whereas, in MJF the reaction mechanism is thought to be "end-capped" where the chain end cannot react further thereby does not experience chain extension like SLS powder (31). This would also provide an alternative explanation for the absence of the shoulder peak in the work of Cai et al, where a larger content of used powder was incorporated into the feedstock material.

The degree of crystallinity determined using the enthalpy of fusion of a MJF part was lower than PA-12 powder. The decrease in the degree of crystallinity was due to a change in the crystal phase which was a result of melting and recrystallisation of the polymer (84). Cai et al used XRD to determine the crystal phase of PA-12 in both the powder and a part manufactured by MJF. In their work, the printed parts were crystallised and cooled down within the powder bed under atmospheric pressure and over a long period of time (usually overnight), causing the cooling rate to be slow (84). This was related to the work of Dadbakhsh et al who claimed that the action of slow cooling could induce the formation of the stable γ phase (51). The formation of the stable γ phase was used to explain the sharp decrease in the degree of crystallinity from the powder to the part (84). The two phases also have been reported to melt at different temperatures, where the melting temperature of the α phase and γ phase are 175 and 182 ℃ (91). This is consistent with the peak melting temperature of the MJF part, shown in Table 3.2.1.

Table 3.2.1: Melting and crystallisation parameters for heat 1 and cool 1 of a MJF par*t using a heating and cooling rate of 10 K/min between 25 – 220 ℃, compared to melting and crystallisation parameters of MJF PA-12 parts obtained from literature. Where T_P - Peak Melting/Crystallisation Temperature, T_E - Last Trace of Melting/End Crystallisation Temperature, T_O - Onset of Melting/Crystallisation, X_c – Degree of Crystallinity and ΔH is the heat of fusion/crystallisation.

	Melting					**Crystallisation**			
	T_O (℃)	T_P (℃)	T_E (℃)	ΔH (Jg^{-1})	X_c (%)	T_O (℃)	T_P (℃)	T_E (℃)	ΔH (Jg^{-1})
MJF part	166.2	180.5	193.3	58.5	27.9	159.8	149.8		
Z. Xu et al (60)	171.8	179.4		62.80		159.3	155.3		53.90
C. Cai et al (84)	172.7	179.6		55.40		153.5	149.1		46.8
O'Connor et al (27)		184.0			32.00		147.0		26.00
B. Sagbas et al (69)					23.41				
S. Rosso et al (91)		182.7		65.90	31.50				

3.2.2 FTIR of a MJF component

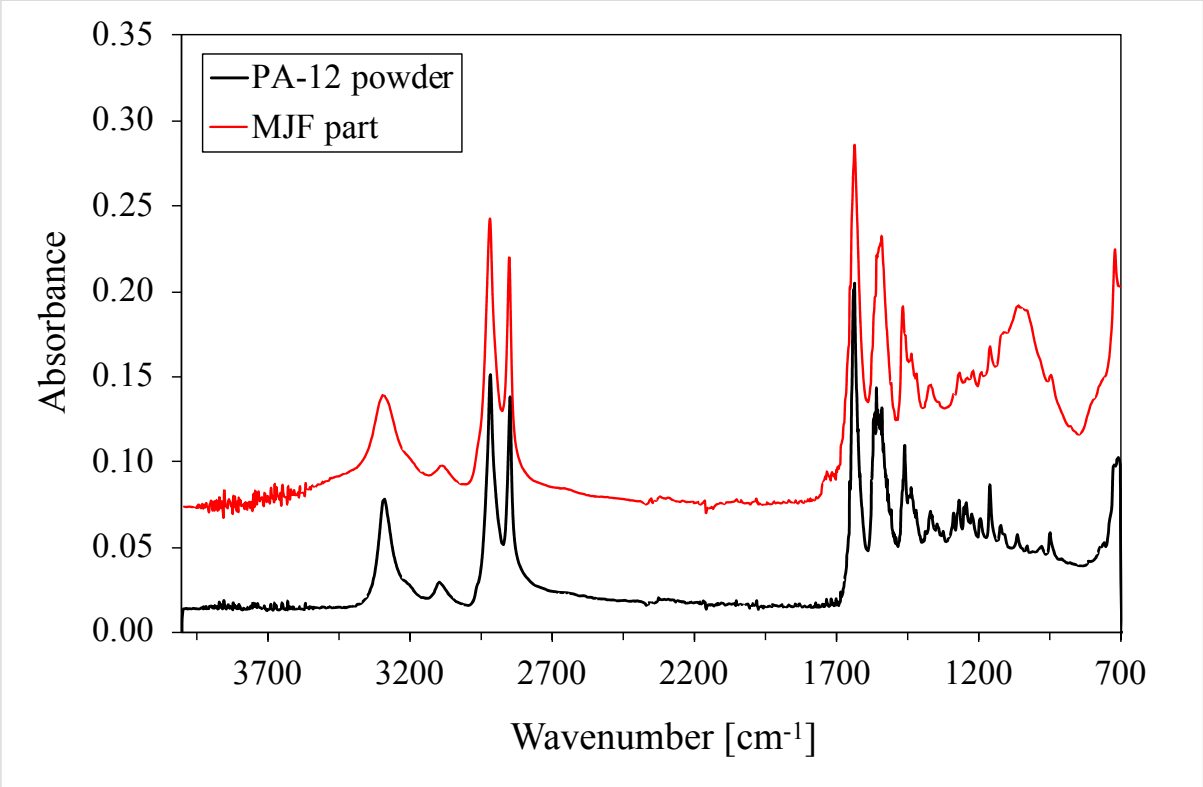

Figure 3.2.2: FTIR spectrum of a MJF component and PA-12 powder between 700 – 4000 cm^{-1}.

The infrared spectrum of PA-12 powder and a PA-12 part manufactured by MJF is displayed in Figure 3.2.2 and the peak assignments are shown in Table 3.2.2. The peaks were comparable to the literature (58,61,68,84) and to the FTIR spectra of PA-12 powder, as per section 2.4.3.

There were slight differences between the FTIR spectra of the PA-12 part and PA-12 powder. For example, the overall absorbance of a part manufactured by MJF was greater than PA-12 powder. Galati et al used FTIR to characterise the FA and DA and reported that the spectrum of the FA had shifted to a higher absorbance than the spectrum of the DA due to the presence of carbon black in the FA (58). In which the carbon atoms within the carbon black convert incident infrared radiation into heat energy on

the powder bed surface in areas where the FA has been jetted (58). Therefore the larger absorbance is due to the carbon black within the FA being retained in the part. Additionally, in (58) a large band between 3000 – 3500 cm^{-1} was assigned to hydroxyl groups due to the presence of bonded water within the agents. The presence of water in the FA and DA was also reported by Scherer et al (75). However, the FTIR spectrum of a MJF part shows the absence of the band assigned to the hydroxyl group. This suggests that during component manufacture in MJF, the water present in the FA and DA had evaporated due to the high temperature of the powder bed. This is unsurprising since the temperature of the powder bed reaches 185 ℃ which is above the boiling point of water. Moreover, the organic solvents within the agents degrade or evaporate between 100 – 400 ℃ (75,91). This suggests that some organic solvents may be retained in the part.

In MJF the FA, which contained graphitic carbon black, was retained in the component. This was quantitifed by the colour of the end product (58,84). Therefore, it is likely that other products from the FA and DA were retained within the component. This was confirmed by Scherer et al. Their work showed that many other compounds from the FA and DA were also present in a part fabricated by MJF (75). This is due to both the FA and DA being jetted on the powder bed surface. Therefore, the presence of other molecules may be likely in the spectrum of a PA-12 part (see Figure 3.2.2). This will account for spectral differences between the PA-12 powder and a part fabricated by MJF. Such differences can be found in the region of 800 – 1300 cm^{-1}. Peaks within this region were related to the C-O or C-N groups. Overall, this shows that the components from the agents which are jetted on the powder bed surface are retained in the final parts.

A small peak at 1732.9 cm^{-1} was also observed. This peak is related to carbonyl containing compounds, which absorb IR radiation within the region of 1710-1760 cm^{-1}. Ketones resonate at a frequency of ~1715 cm^{-1}, aldehydes at ~1725 cm^{-1}, aliphatic carboxylic acids at ~1750 cm^{-1} and esters at ~1735 cm^{-1} (10). In other work, the thermal degradation of PA-6,6 was studied, in which, peaks within the

carbonyl containing region were observed after thermo-oxidative degradation (102). A band at 1735 cm^{-1} was assigned to the formation of imides as a result of oxidation (102). Therefore, the peak at 1732.9 cm^{-1} could be associated with the presence of esters or imides. A potential explanation for the formation of degradation products arises from the high temperature of the powder bed surface and the prolonged time exposed to higher temperatures during component fabrication. Under these conditions, the polymer chains are more susceptible to thermo-oxidative degradation. This can cause powder to degrade during the component manufacture. Additionally, the powder state (i.e. virgin, refreshed or recycled) was unknown. Therefore, an alternative explanation for degradation products may be from recycled or refreshed feedstock material being present in the final part, in which used powder used to create the component has already been exposed to high temperatures for prolonged periods of time as a result of thermal cycling.

Table 3.2.2: FTIR-ATR peak assignments for a MJF component.

Wavenumber [cm^{-1}]	Peak assignment
3292.27	Hydrogen bonded N-H stretching vibration
2917.43	CH_2 asymmetric stretching vibration
2849.3	CH_2 symmetric stretching vibration
1365.6	C=O stretching vibration
1540.57	C-N stretching, C=O in plane bending
1465.47	CH_2 reference band
1372.39	CH bending, CH_2 twist
1267.12	C-N stretching, C=O in plane bending
1159.1	CONH in plane
719.63	CH_2 rocking

3.3 Conclusions for characterisation of PA-12 and of an MJF component

A variety of characterisation techniques were used to explore the properties of PA-12 powder and of a MJF component. The characterisation techniques included DSC, TGA, FTIR and particle size analysis. The data obtained in this section was compared to literature and used as a benchmark for further studies.

The thermal properties of PA-12 powder from batch 1 and batch 2 was characterised using DSC. The data showed that the peak melting temperature of powder extracted from batch 1 and batch 2 were 186.8 ℃ and 188.2 ℃, respectively. The peak crystallisation temperature of powder extracted from batch 1 and batch 2 were 148.6 ℃ and 148.5 ℃, respectively. The peak melting temperature was comparable to literature, whereas the peak crystallisation temperature varied in comparison to literature. TGA showed that PA-12 experienced a 1 % and 50 % mass loss degradation at 322 ℃ and 436 ℃, respectively. This suggests that in MJF it is unlikely that mass loss degradation of PA-12 occurs since the temperature of the powder bed does not reach such high temperatures beyond the melting point of PA-12.

The FTIR spectra of PA-12 extracted from batch 1 was comparable to O'Connor et al (61, 68). Since this was virgin PA-12 powder, it is expected that PA-12 was consistent between batches and that PA-12 powder was not contaminated with the agents used within MJF.

Particle size analysis showed that the average particle size of PA-12 powder was 58.5 μm. This was within the optimum range of 45 to 90 μm stated by Goodridge et al (106).

Meanwhile, the thermal properties of an MJF component showed a lower peak melting temperature. Additionally, a single melting peak suggested that PA-12 was fully melted during manufacturing. The FTIR spectrum of a PA-12 component showed the presence of additional carbonyl containing compounds, this indicated that the MJF component was made from refreshed or aged powder. Overall, this data shows that the properties of an MJF component and PA-12 powder were different. It is likely that this is due to the presence of the FA and DA used in MJF and the ageing state of PA-12 powder.

CHAPTER 4 – ISOTHERMAL CRYSTALLISATION OF POLYAMIDE-12

The aim of this work was to determine the equilibrium melting temperature and the isothermal crystallisation kinetics of PA-12 by using a variety of kinetic models. The Hoffman-Weeks construction was used to determine the equilibrium melting temperature of PA-12. This was achieved by isothermally crystallising PA-12 at a range of temperatures and re-heating the polymer to observe the melting temperature. This was important to consider since MJF relies on the complete melting of PA-12 to create functional components. The isothermal crystallisation kinetics were studied using the Avrami model and the Tobin model by constructing a double logarithmic plot to determine the rate constant and exponent. Non-linear regression was also used to determine the kinetic parameters, such as the rate constant and exponent, by performing a set of iterations and producing the kinetic parameters with the lowest standard error. The Differential Avrami model was also used and described the limit of primary crystallisation. The isothermal crystallisation kinetics were important to consider since the parts within the powder bed temperature experience different cooling mechanisms based on their position within the powder bed.

4.1 Hoffman-Weeks construction to determine the equilibrium melting temperature

The equilibrium melting temperature (T_m^0) of a polymer is defined as "the melting point of an assembly of crystals, each of which is so large that size (i.e. surface) effects are negligible, with the provision that each such large crystal is in equilibrium with the normal polymer liquid" (108). Another definition is as follows, "the melting temperature of an infinite stack of extended chain crystals…" (109). Both definitions convey that T_m^0 is the melting temperature of a group of crystals of infinite size.

Hoffman-Weeks analysis was used to obtain T_m^0. This involved recording the observed melting point of a polymer as a function of isothermal crystallisation temperature. This data was used in a plot of peak melting temperature vs isothermal crystallisation temperature to yield a straight-line slope. T_m^0 was

determined by extrapolating the melting temperature from the intersection of the slope obtained from experimental data and a slope of $T_m = T_c$.

The relationship between the melting temperature, T_m^0 and isothermal crystallisation temperature is displayed in the following equation:

$$T_m = T_m^0 \left(1 - \frac{1}{2\beta}\right) + T_c/2\beta$$

Equation 5

In the equation above, the thickening coefficient $\beta = \sigma_e l/\sigma l_e$, where σ is the lateral surface free energy, l is the lamellar thickness and the subscript e is the equilibrium conditions where no annealing on heating takes place. When crystallisation takes place under equilibrium conditions, β = 1. This corresponds to a slope of 0.5 in the Hoffman-Weeks construction (110).

The thickening coefficient $\beta = l/l^*$, where l is the lamellar thickness at the time of melting and the l^* is the thickness of a critical nucleus at T_C (111). When β = 1 no reorganisation occurs on melting of the polymer. When crystallisation occurs under equilibrium conditions β = 1, this corresponds to slope 0.5 (110).

T_m^0 is used to determine the degree of undercooling (ΔT), this represents the driving force of polymer crystallisation. Where the crystallisation process is composed of primary nucleation and crystal growth mechanisms (109).

$$\Delta T = T_m^0 - T_c$$

Equation 6

The observed peak melting temperature of PA-12 following isothermal crystallisation was recorded as the peak maximum of the endothermic melting peak. Additionally, the last trace of crystallinity was recorded as the point at which the curve returned to baseline, as illustrated in Figure 4.1.1. Both the peak melting temperature and the last trace of crystallinity were plotted in the Hoffman-Weeks construction. The rationale for using both the peak melting temperature and the last trace of crystallinity was that the peak melting temperature represents the bulk of the sample, where the majority of the crystals have melted. Consequently, on crystallisation residual crystals may act as nucleation sites on cooling. Whereas the last trace of crystallinity is the point where all crystals have melted.

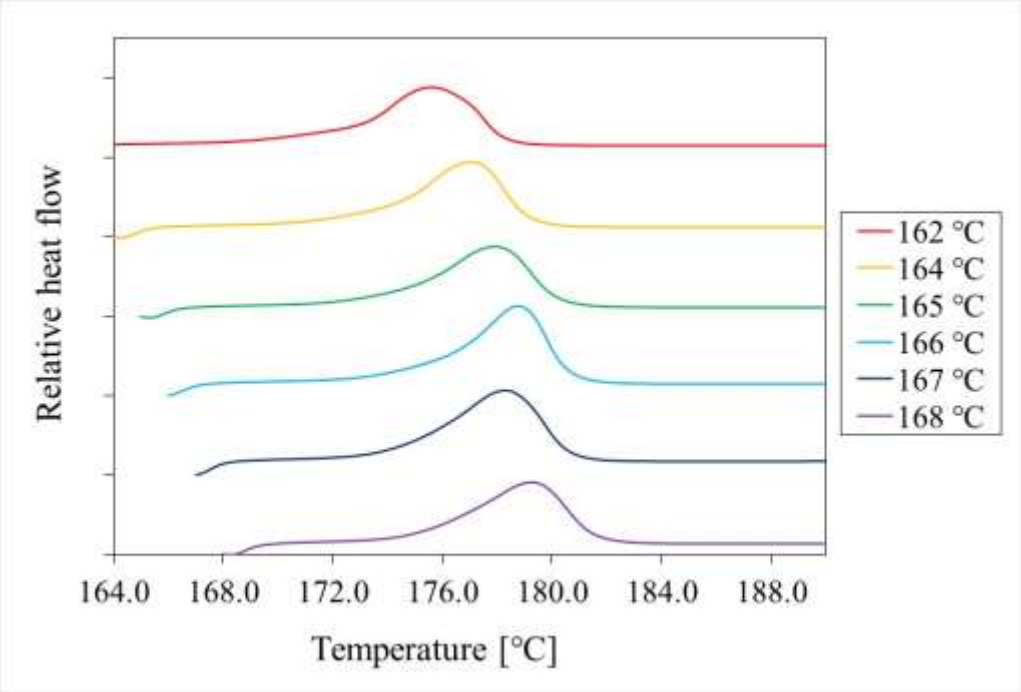

Figure 4.1.1: Melting endotherm of PA-12 samples as a function of isothermal crystallisation at different temperatures, where T_m is the observed peak melting temperature and T_E is the last trace of crystallinity.

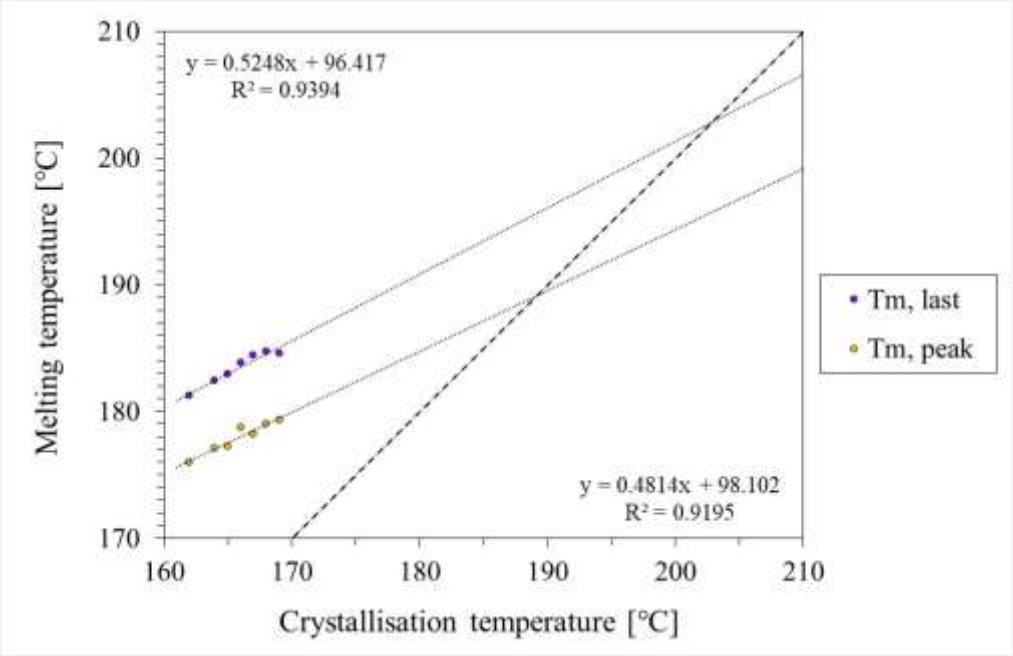

Figure 4.1.2: Hoffman-Weeks construction for the determination of the equilibrium melting temperature of PA-12, using the observed melting temperature (Tm(obs)) and the last trace of crystallinity (TE) of experimental data which passes through a line of $T_m = T_c$.

The melting curve was recorded following isothermal crystallisation at various temperatures, as displayed in Figure 4.1.1. The data showed that as the isothermal crystallisation temperature increased, the peak melting temperature and the last trace of crystallinity increased. The minimum and maximum recorded peak melting temperature was 176.0 and 179.3 ℃. The minimum and maximum recorded last trace of crystallinity was 181.2 and 184.6 ℃. This shows that at higher isothermal crystallisation temperatures, or at a low degree of undercooling, the crystals are thicker and more stable, therefore melting at a higher temperature (108).

Table 4.1.1 Equilibrium melting temperature and gradient obtained by the peak melting temperature and the last trace of crystallinity using the Hoffman-Weeks construction.

	T_m^0 [℃]	Gradient
Peak melting temperature	188	0.52
Last trace of crystallinity	205	0.48

The Hoffman-Weeks construction was used to determine T_m^0 from the experimental peak melting temperature and the last trace of crystallinity. This is shown in Figure 4.1.2. T_m^0 obtained using the peak melting temperature and last trace of crystallinity were 188 and 205 ℃, respectively. The gradient was 0.52 and 0.48, respectively. This data is shown in Table 4.1.1. The gradient was close to 0.5 (or $\beta = 1$), suggesting that no recrystallisation occurred and that lamella thickening had occurred on re-heat after isothermal crystallisation (112).

In this work, T_m^0 (determined by the peak melting temperature) was lower than reported values of PA-12 used in SLS (20,90). In work by Amado et al, the T_m^0 of PA-12 (DuraformPA ®) was 192.4 ℃. This was determined from an isothermal crystallisation temperature range of 166 – 170 ℃. In work by Zhao et al, the T_m^0 of PA-12 (PA2200) was 193.2 ℃. This was determined from an isothermal crystallisation temperature range of 160 – 168 ℃. In Chapter 3.0 it was shown in that the heating rate influenced the peak melting temperature of PA-12. In each study (20,90), the heating rate on melting following isothermal crystallisation was 10 ℃/min, which is comparable to the heating rate used in this work. Therefore, the difference between results is likely to be a result of PA-12 grade and different isothermal temperature ranges used across studies. Furthermore, this demonstrates that lower heating rates did not influence the reorganisation process on melting for multiple grades of PA-12 powder used in PBF. If lower heating rates influenced reorganisation of the crystal, a double melting peak would be observed.

Although the Hoffman-Weeks approach is a common method to determine T_m^0, there are experimental limitations that influence the degree of undercooling. These difficulties are described by Hoffman et al as the "nucleation controlled character of the growth process". In particular, these limitations arise when the degree of undercooling is very small, since crystallisation is extremely slow and may not be measurable using DSC (108). A critical review of using Hoffman-Weeks was carried out by Marand et al (109), where the following conclusions were made:

- The linear method to determine T_m^0 invariably underestimates T_m^0, when carried out for lamellar crystals exhibiting a constant thickening coefficient.
- The underestimation of T_m^0 increases with a decrease in lamellar thickening coefficient.
- Linear extrapolation leads to an overestimation of the lamellar thickening coefficient.

In relation to PBF techniques, T_m^0 and the degree of undercooling will influence crystallisation during the manufacturing process. Schmid et al linked T_m^0 to the energy input and the powder bed temperature. It was suggested that for powders with a high T_m^0 and manufacturing process with a low powder bed temperature, the energy input required to melt the polymer is greater (113). In PBF techniques, such as SLS, the processing parameters are controlled by the user meaning they can be changed according to the T_m^0 of powder. Whereas in MJF the processing parameters are set by the manufacturer (Hewlett Packard) and the user has no control. However, the determination of T_m^0 still holds significance, such that heating the polymer above T_m^0 during part fabrication will ensure all traces of crystallinity have been removed. If crystalline fractions were to remain, these will act as nucleation points.

Additionally, the degree of undercooling can be used to determine the crystallisation mechanisms with respect to crystal size and perfection. In PBF techniques, the cooling process is thought to be a mixture of isothermal and non-isothermal due to variations in temperature across the powder bed. This will have an influence on the spherulites formed during crystallisation. Parts that are built first, relative to *z*-height

in a fully packed build, will be exposed to a higher temperature for a longer period of time, in comparison to those built last (23). Typically, exposure to a high temperature for long periods of time increases the spherulite size. This suggests that parts built first will have a different crystalline morphology. Moreover, the build orientation will also affect the rate of crystallisation, as discussed by Kruth et al. In their work, it was suggested that a low crystallisation rate (or a low degree of undercooling) relative to the vertical build speed will limit the formation of intra-layer crystals (114). As a result, users of MJF must be mindful of how the build position can influence the micro-scale morphology since the processing parameters cannot be changed by the user.

4.2 Analysis of primary crystallisation kinetics by differential scanning calorimetry

PA-12 powder was isothermally crystallised within the temperature range of 162 to 168 ℃, the crystallisation exotherms are displayed in Figure 4.2.1. The DSC exotherms were modified to omit the induction period, such that they were limited to t_0 and t_{end}, where t_0 is the onset time of crystallisation and t_{end} is the end of crystallisation where the curve returns to a steady baseline. This is referred to as the “corrected time”. The data was corrected to ensure all exotherms were zeroed and were comparable on a relative scale.

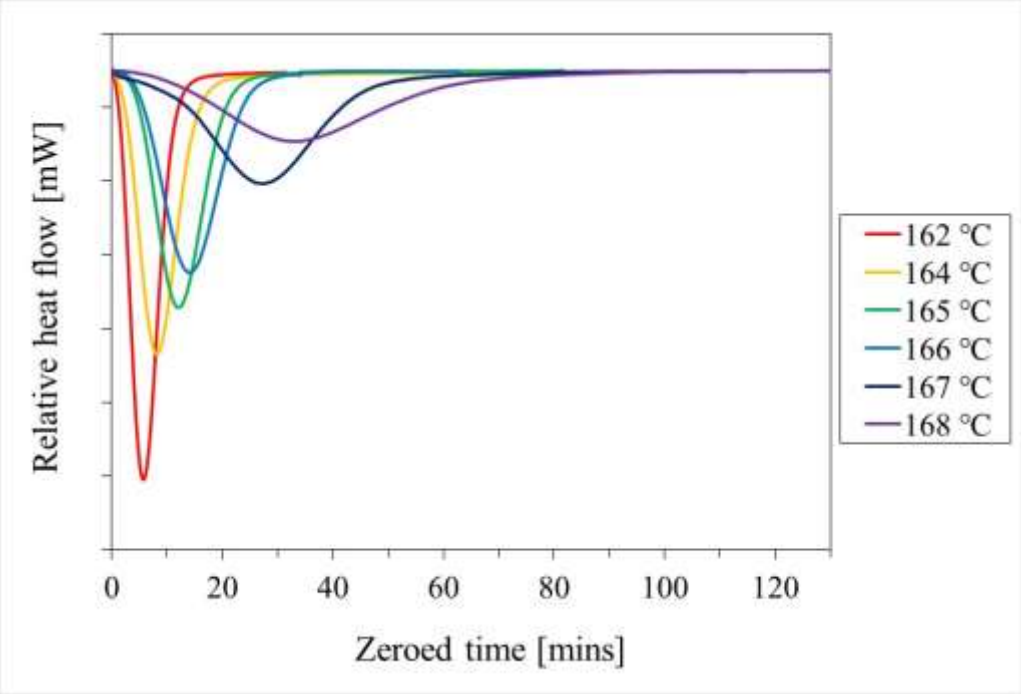

Figure 4.2.1: DSC crystallisation exotherms of PA-12 isothermally crystallised at temperatures ranging from 162 – 168 ℃, where time has been limited to the region between t_0 and t_{end} and zeroed.

The isothermal crystallisation temperature had a significant effect on the crystallisation behaviour of PA-12, as shown in Figure 4.2.1. An increase in isothermal crystallisation temperature decreased the peak heat flow and increased the time taken to reach complete crystallisation.

The half time of crystallisation was determined extrapolating the time at peak heat flow (using the corrected time). It was clear that as the isothermal crystallisation temperature increased, the half time of crystallisation increased. The half time of crystallisation at 162 ℃ was 5.75 mins and at 168 ℃ was 33.10 mins. This also gives an indication of the rate of crystallisation and suggests that at higher crystallisation temperatures, the rate of crystallisation decreases (93). The trends stated are consistent with Zhao et al, when evaluating the crystallisation kinetics of PA-12 used in SLS (grade PA2200) (20).

In Chapter 2, it was mentioned that the induction time was removed from experimental data, leaving a corrected time period of t_0 to t_{end}. This is a subjective measure showing that primary crystallisation process between t_0 and t_{end} is limited by human error. This can affect the isothermal crystallisation analysis. Mandelkern et al suggest that the induction time is concept created by users as a result of insensitivity of the DSC instrument (115). The lack of sensitivity of the DSC can affect isothermal crystallisation exotherms. For example, at a lower crystallisation temperature, the crystallisation rate is high. Therefore, the onset of crystallisation occurs quickly because of a high nucleation rate. This will cause the induction point to be missed because crystallisation starts on cooling to the desired isothermal crystallisation temperature from the melt. At higher crystallisation temperatures nucleation can occur during the induction time, however this is not detected due to the lack of sensitivity of the instrument.

A temperature range of 162 – 168 ℃ was selected for isothermal crystallisation and was deemed a suitable crystallisation range in line with literature (20). Below T_c = 162 ℃, the induction time was missed and the sample started crystallisation on cooling to the selected isothermal crystallisation temperature. Above T_c = 168 ℃, the sample did not completely crystallise after 300 mins. An isothermal crystallisation temperature of 163 ℃ was omitted from this work since the induction time was missed on every repeat. This was due to experimental error.

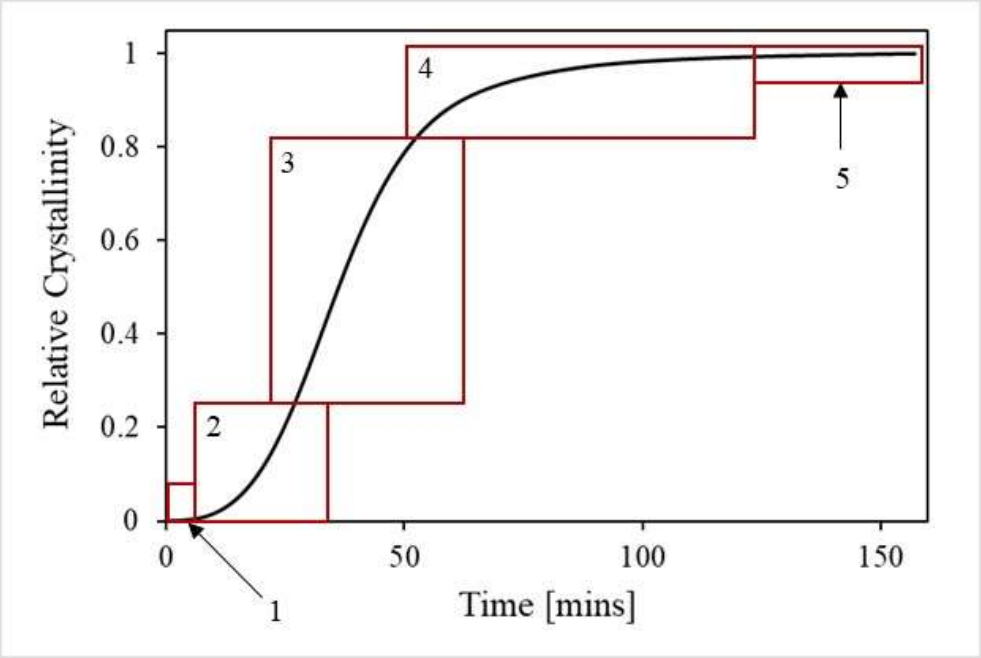

Figure 4.2.2: Phase transition of crystallisation during isothermal crystallisation, split into key sections.

Each isothermal crystallisation curve was integrated using the trapezium rule to enable the phase transition on crystallisation to be determined, as per Chapter 2. A characteristic sigmoidal shaped curve was produced showing the relative crystallinity. This is the transformation of the melt phase into the crystalline phase over a time period. This can be split into sections or phases to explain the process of crystallisation, shown in Figure 4.2.2. Phase 1 is the induction period, where the transformation is extremely small. Phases 2 – 4 are the main stages of crystal formation and growth. Phase 2 is where transformation is slow and nucleation is favoured, nuclei grow until they reach a critical size. Phase 3 is where transformation is rapid and the rate of nucleation and growth is at a maximum. Phase 4 is where the transformation slows down since the melt volume has significantly reduced and most of the polymer has transformed into the crystalline phase. At this point, nucleation stops and the crystals formed continue to grow until impingement occurs. Phase 5 is where the polymer has fully transformed and secondary crystallisation occurs. This is often a slow process and causes the crystal perfection to increase. However, it has been noted that secondary crystallisation may also occur in phase 4 (116). Although the crystal perfection is expected to increase during secondary crystallisation, this is difficult

to monitor due the insensitivity of the DSC. However, models have been developed to observe the secondary process in polymers that exhibit prominent secondary crystallisation, such as poly(3-hydroxybutyrate-co-3-hydroxyvalerate) (117). McFerran et al also used models, such as the Avrami model, to obtain Avrami parameters relevant to secondary crystallisation of PA-12 used in automotive multilayer tubing (93).

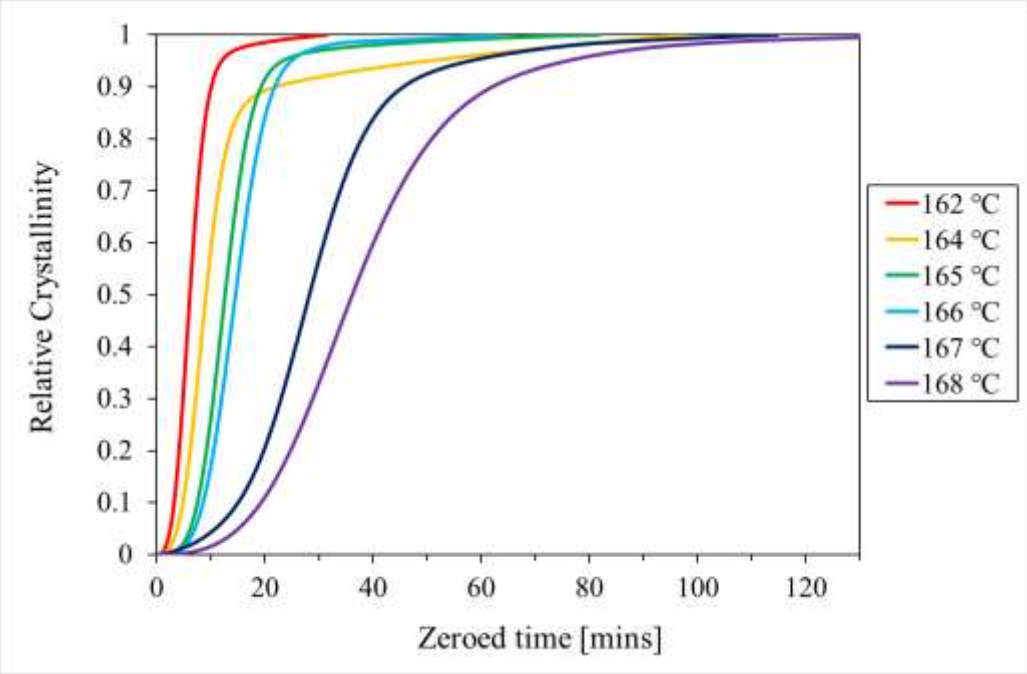

Figure 4.2.3: Relative crystallinity (or fraction transformed) of material over time at different isothermal crystallisation temperatures. Time was corrected within the region of t_0 and t_{end}, and zeroed.

The relative crystallinity (X_t) was significantly impacted by the isothermal crystallisation temperature, as shown in Figure 4.2.3. Isothermal crystallisation between 162 – 166 ℃ exhibited a similar style curve up to $X_t \approx 0.85$. In which, slow transformation occurred up to $X_t = 0.05$. Transformation was rapid between X_t of 0.05 to 0.80. After $X_t = 0.80$, the transformation was slow and the curve plateaued to $X_t = 1$. Isothermal crystallisation at 167 and 168 ℃ also exhibited a similar style curve. In which,

transformation was slow up to X_t of 0.20. Transformation was rapid between X_t = 0.20 to 0.70. At X_t greater than 0.70, transformation was slow and the curve plateaued to X_t = 1.

The Intermediate portion of the relative crystallinity curve (generally between 0.1 – 0.8) was steep for samples crystallised T_C = 162 – 166 ℃, this suggests the bulk of the material crystallised quickly within this region. Whereas, for T_C = 167 and 168 ℃ the intermediate region followed a smooth sigmoidal shape curve. This suggests that crystallisation was slower. The region in which the curve transforms into a plateau is sharp for T_C = 162 – 166 ℃. However, for samples T_c = 167 and 168 ℃, the curve smoothly transforms into a plateau. This is due to secondary crystallisation.

Interestingly, at T_C = 167 ℃ the transformation within the region of X_t up to 0.1 was quicker than expected. This may be due to impurities such as dust within the sample that can act as a site for heterogeneous nucleation. Additionally, at T_C = 164 ℃ the curve transformed into the plateux at X_t greater than 0.80 and did not reach X_t = 1 until a much later time, in comparison to T_C = 162 – 166 ℃.

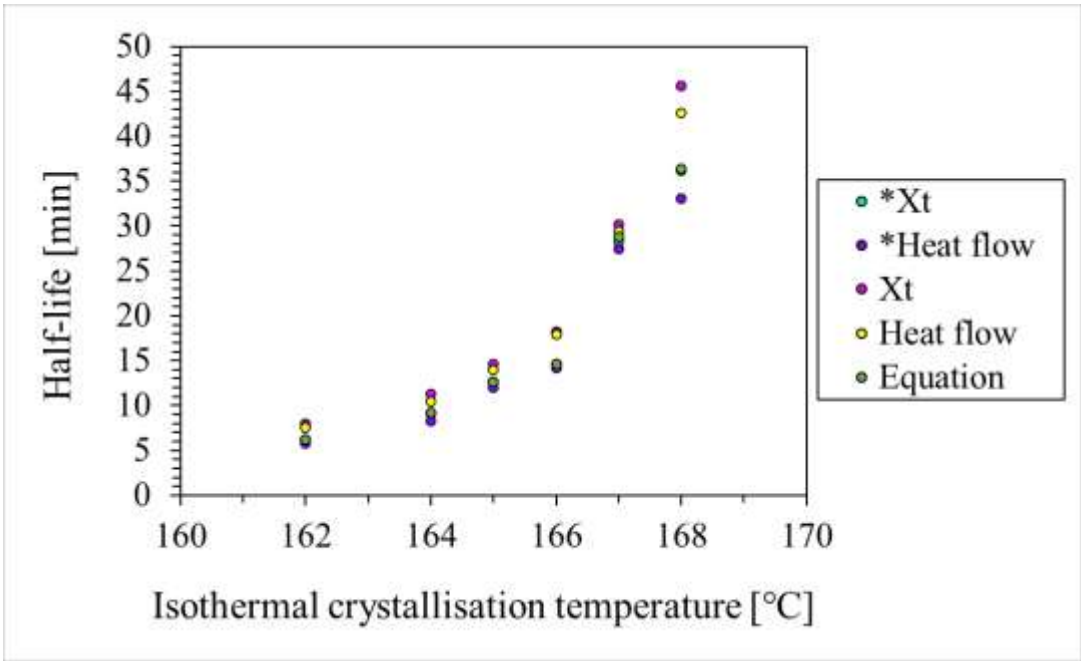

Figure 4.2.4: Crystallisation half-time as a function of isothermal crystallisation temperature, determined by the point at 50 % transformation (X_t), the heat flow (HF) and using equation $t = \left(\frac{\ln(2)}{K}\right)^{1/n}$;* marks the crystallisation half-life determined from data of corrected time.

This section will focus on the crystallisation half-time, determined using different methods. This included at 50 % transformation (X_t), the peak minima of the heat flow curve (HF), both determined from the corrected and uncorrected time and using equation $t = \left(\frac{\ln(2)}{K}\right)^{1/n}$.

Figure 4.2.4 and Table 4.2.1 shows the half-time for crystallisation determined by different methods. The corrected and uncorrected data for crystallisation half-life omits and includes the induction time, respectively. Figure 4.2.4 shows the crystallisation half-time at X_t = 0.5 as a function of isothermal crystallisation temperature. The crystallisation half-time was obtained by extrapolating the time at X_t = 0.5 in a graph of X_t vs time. The crystallisation half-time showed an exponential increase with isothermal crystallisation temperature. From the corrected data, the shortest crystallisation half-time was 6.15 mins at T_c = 162 ℃ and the longest crystallisation half-time was 36.18 mins at T_c = 168 ℃. From uncorrected data, the shortest and longest crystallisation half-time at T_c = 162 ℃ and T_c = 168 ℃

were 8.01 and 45.65 mins respectively. For T_c = 168 ℃ there was a large variation in crystallisation half-time, as shown in Figure 4.2.4. This was due to the difference in crystallisation half-time between the zeroed and non-zeroed data. This difference was due to the induction time, where the induction time was the greatest for T_c = 168 ℃. The X_t for non-zeroed data was equal to X_t (zeroed) plus the induction time.

The crystallisation half-time was also determined by extrapolating the time at the peak heat flow. This method was used in the non-isothermal crystallisation of polyamide-66/glass fibre/carbon black composites (118). The crystallisation half-time showed an exponential increase with isothermal crystallisation temperature, as displayed in Figure 4.2.4. From data that had been corrected shortest and longest crystallisation half-time were 5.75 mins at T_c = 162 ℃ and 33.10 mins at T_c = 168 ℃, respectively. From uncorrected data, the shortest and longest and shortest crystallisation half-time were 7.60 mins at T_c = 162 ℃ and 42.57 mins at T_c = 168 ℃, respectively.

The relationship between the rate parameter, *K*, determined by conventional Avrami analysis, and the crystallisation half-time is presented in the equation below (93):

$$t = \left(\frac{\ln(2)}{K}\right)^{1/n}$$

Equation 7

The crystallisation half-time was determined using the above equation. Figure 4.2.4 shows that the crystallisation half-time increased exponentially with isothermal crystallisation temperature. The shortest half-time was 6.17 mins at T_c = 162 ℃ and the longest half-life was 36.37 mins at T_c = 168 ℃.

The crystallisation half-time was measured at 50 % transformation (X_t), the heat flow (HF), determined from the zeroed time and non-zeroed time and using equation $t = \left(\frac{\ln(2)}{K}\right)^{1/n}$. The different methods to determine the crystallisation half-time showed an exponential increase with isothermal crystallisation temperature. In general, at lower isothermal crystallisation temperature between 162 – 165 ℃, there was less variation in crystallisation half-time obtained by the different methods. At higher isothermal crystallisation temperatures between 166 – 168 ℃, there was a greater variation in crystallisation half-time obtained by the different methods. This is due to the influence of the induction time, which increased with isothermal crystallisation temperature, where X_t for uncorrected data was equal to the time taken for crystallisation plus the induction time. Where the induction time increased, this had a larger impact on the half time of crystallisation when comparing corrected and uncorrected data.

Table 4.2.1: showing the values of crystallisation half-life as a function of isothermal crystallisation temperature (T_c), determined by the point at 50 % transformation (X_t), the heat flow peak minima (HF) and using equation *.

T_c [℃]	Induction time [mins]	Uncorrected [mins]		Eq*.	Corrected [mins]		$t_{1/2} + t_{induction}$	
		HF [mW]	$X_t = 0.5$		HF [mW]	$X_t = 0.5$	HF max [mW]	$X_t = 0.5$
162	1.85	7.60	8.01	6.17	5.75	6.15	7.60	8.00
164	2.18	10.47	11.32	9.19	8.29	9.13	10.47	11.31
165	1.92	13.98	14.58	12.68	12.06	12.66	13.98	14.58
166	3.67	17.89	18.27	14.60	14.23	14.60	17.90	18.27
167	1.90	29.39	30.16	28.83	27.49	28.26	29.39	30.16
168	9.47	42.57	45.65	36.37	33.10	36.18	42.57	45.65

*$t = \left(\frac{\ln(2)}{K}\right)^{1/n}$

Figure 4.2.5 shows the trend of induction time with isothermal crystallisation temperature. The induction time increased exponentially with isothermal crystallisation temperature. The induction time at T_c = 162 and 168 ℃ was 1.85 and 9.47 mins, respectively. However, T_c = 167 ℃ did not fit this trend, the induction time for T_c = 167 ℃ was 1.90 mins. This is consistent with the curve shown in Figure 4.2.3, where the beginning of the transformation X_t less than 0.1 increased more rapidly than expected. Typically, this portion would remain flat for a longer period of time before increasing.

The Induction time, as stated by Mandelkern (115), is “more apparent than real”. This suggests that the induction time is a subjective measure. This suggests there are errors when determining the induction time. This is true since it is up to the user to determine the induction time based on visual judgement.

For isothermal crystallisation temperatures between $T_g > T_c > T_m^0$ a plot of crystallisation half-time vs isothermal crystallisation temperature will exhibit a bell-shaped curve. This curve shows that at lower degrees of undercooling crystallisation is controlled by nucleation, whereas at higher degrees of undercooling crystallisation is controlled by growth (119). Therefore, at a temperature close to T_g and T_m crystallisation is at its slowest. The optimum crystallisation temperature for isothermal crystallisation is determined by the peak of the bell-shaped curve.

The temperature range explored in this work was not large enough to determine the optimum temperature for isothermal crystallisation. In this experimental work, the DSC could not accurately record isothermal crystallisation below 162 ℃, despite using a cooling rate of 70 ℃/min from the melting temperature to the selected isothermal crystallisation temperature. At a temperature below 162 ℃, the induction time was missed and the sample crystallised on cooling to the isothermal crystallisation temperature. In order to expand the isothermal crystallisation at lower temperature, a cooling rate quicker than 70 ℃/min is required.

Other studies have explored isothermal crystallisation of PA-12 powder used in PBF techniques (21,90,120). In (21), the isothermal crystallisation temperature range was 158 – 170 ℃ and the cooling rate from the melt to the selected isothermal crystallisation temperature was 40 ℃/min for PA2200 (EOS). In this work, a lower cooling rate was successful in determining the isothermal crystallisation kinetics of PA-12. In (120), the isothermal crystallisation temperature range was 160 – 168 ℃ and the cooling rate from the melt to the selected isothermal crystallisation temperature was 60 ℃/min for PA2200 (EOS). In (90), the isothermal crystallisation temperature range was 166 – 170 ℃ and the cooling rate from the melt to the selected isothermal crystallisation temperature was 40 ℃/min for DuraformPA®. This shows that the isothermal crystallisation temperature range varied between studies.

Interestingly, the FLASH DSC can use much higher heating or cooling rates, such as 1000 $℃s^{-1}$. Therefore, the FLASH DSC can be used to expand the isothermal crystallisation temperature range to much lower temperatures, close to the T_g of PA-12. Paolucci et al used FLASH DSC to quantify isothermal crystallisation of PA-12 powder (PA2200, EOS) that had been annealed at different temperatures and time within the range of 80 – 140 ℃. In this temperature range a variety of nucleation mechanisms were dominant and caused a bimodal dependence of the crystallisation rate (121).

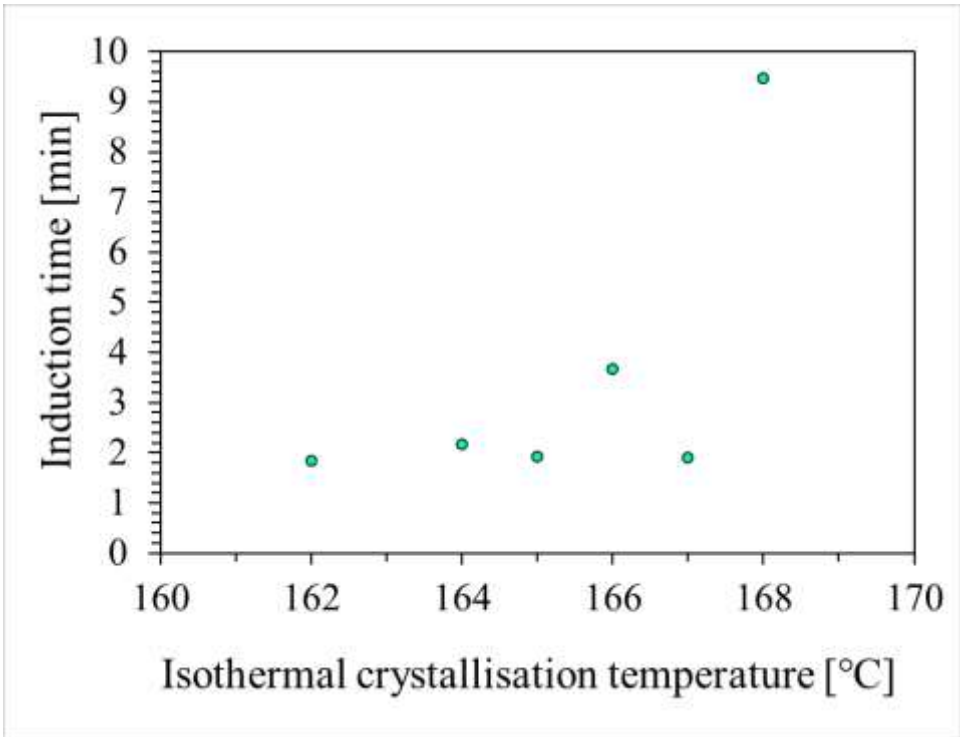

Figure 4.2.5: Variation of induction time with isothermal crystallisation temperature

4.3 Analysis of primary crystallisation using the Avrami model

This section will focus on using the Avrami and Tobin model on experimental DSC data to obtain parameters such as the exponent, n, rate constant, k. The models were used on data in Figure 4.3.1 where the data was limited to $X_t = 0.03 – 0.70$. This was selected on the basis that the curve gave good linearity and this was also in accordance with literature (120).

4.3.1 Analysis of primary crystallisation using the Avrami model

The isothermal crystallisation kinetics of PA-12 was analysed using the Avrami model, according to the double logarithmic plot shown below (124).

$$ln[-ln(1 - X(t))] = n\ ln(t)\ +\ ln(K)$$

Equation 8

Where X_t is the weight fraction of the crystallisation material at time, t, n is the Avrami exponent, and K is the Avrami crystallisation rate parameter. In a plot of ln[-ln(1-X(t))] vs log (t), the slope and intercept yield n and K.

Figure 4.3.1 displays the unlimited Avrami plot of PA-12 isothermally crystallised between 162 – 168 ℃. Each plot shows initial linear character and flattens towards the later stages of crystallisation. The plateaux at later stages suggests that secondary crystallisation is present, this occurs after impingement at the later stages of crystallisation.

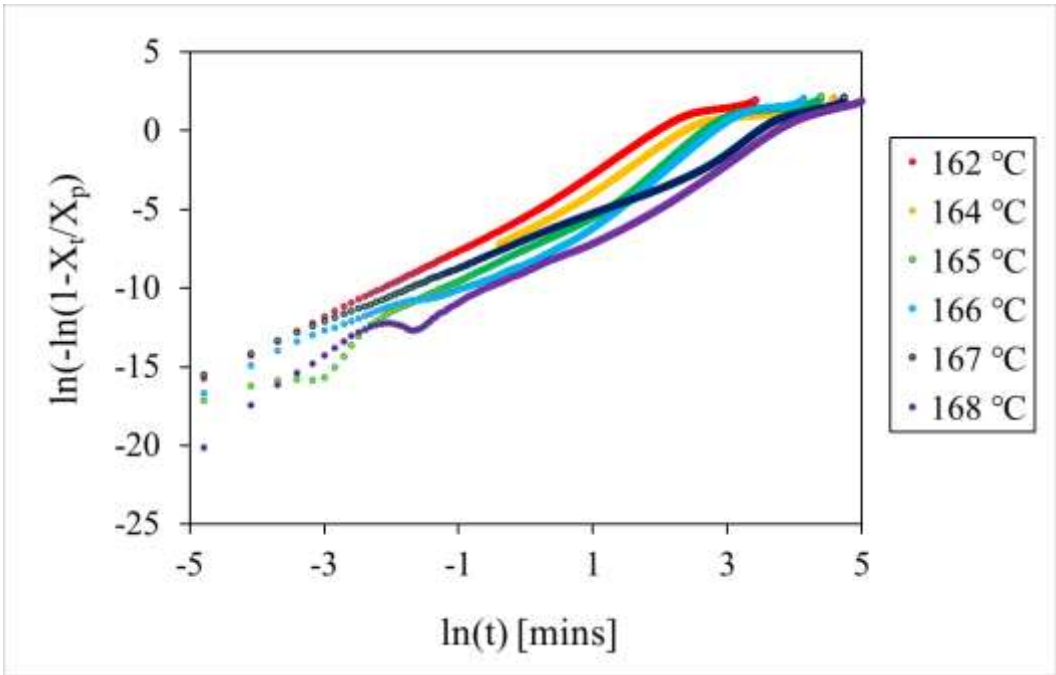

Figure 4.3.1: Avrami plot for the isothermal crystallisation of PA-12 from $X_c = 0 – 1$.

Figure 4.3.2 shows the limited Avrami plot. In the region of X_t = 0.03 – 0.70 the graphs exhibited a linear trend. From which, *n* and K were determined, these values are displayed in Table 4.3.1.

The Avrami exponent, *n*, ranged from 2.73 – 3.63. The non-integer values suggest a complex mode of nucleation and growth in the primary phase. The Avrami exponent is greater than 2, this indicates that growth is expected to be three dimensional. In other work on the crystallisation kinetics of SLS grade PA-12, isothermal crystallisation was studied between 160 – 168 ℃. The data showed that *n* increased from 2.24 – 2.90 with crystallisation temperature. This demonstrated that crystal growth was a mixture of two-dimensional and three-dimensional (20). Greater values of *n* (n ≈ 2 – 3) were obtained in this experimental work and literature that studied the crystallisation kinetics of PA-12 (20,21,93). In (93) polymer stabilizers and carbon black were incorporated into the polymer matrix. In studies (20,21) PA2200 EOS powder was used in the virgin and refreshed state, respectively. In these studies *n* varied between 2 – 3, which is consistent with this experimental work. Kalkar et al studied the crystallisation kinetics of Poly(phenylene sulfide)/TLCP Composites. Non-integral values of *n* were produced, it was suggested that this was a result of a combination between athermal and thermal nucleation mechanisms (122).

The variation in the Avrami rate constant with crystallisation temperature is presented in Table 4.3.1. The data shows that the rate decreased with increasing isothermal crystallisation temperature. In studies (20,21,93), the rate also decreased with increasing isothermal crystallisation temperature. These trends are influenced by the crystallisation half-time, where a sample crystallised closer to T_m (i.e., at a lower degree of undercooling) caused the rate of crystallisation is slower.

The value of R^2 was used to estimate the accuracy of parameters obtained from the experimental data using the double logarithmic plot. The R^2 values were in excess of < 0.9913, showing a good quality of fit. The lowest and highest values for R^2 were 0.9913 and 0.9998 for T_c = 167 and 168 ℃, respectively.

Overall, the Avrami model was successful in describing the isothermal crystallisation kinetics of PA-12 by providing reasonable *n*, *k* and R^2 parameters that were comparable to literature.

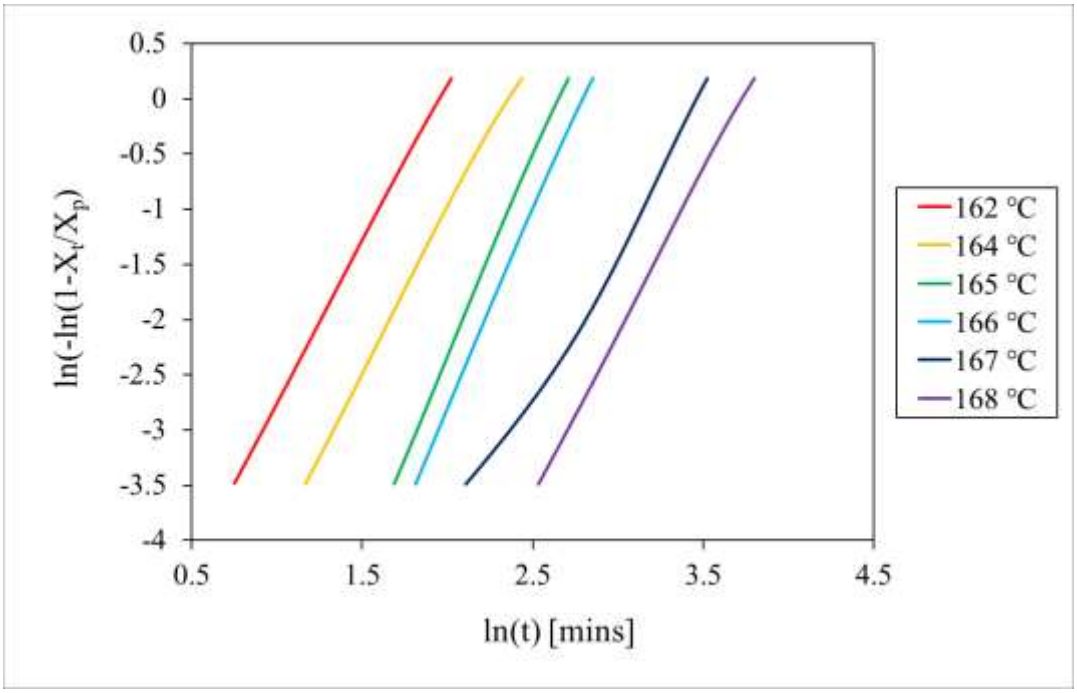

Figure 4.3.2: Avrami plot for limited data between a relative crystallinity of 0.03 and 0.7 between isothermal crystallisation temperature of 162 – 168 ℃.

Table 4.3.1: Table of Avrami parameters, showing the Avrami exponent, n, the Avrami crystallisation rate, K_a, and R^2.

Isothermal crystallisation temperature [°C]	n	K_a [min^{-1}]	R^2
162	2.90	3.52E-03	0.9998
164	2.93	1.04E-03	0.9989
165	3.63	6.90E-05	0.9994
166	3.55	5.11E-05	0.9996
167	2.73	7.17E-05	0.9913
168	2.95	1.72E-05	0.9997

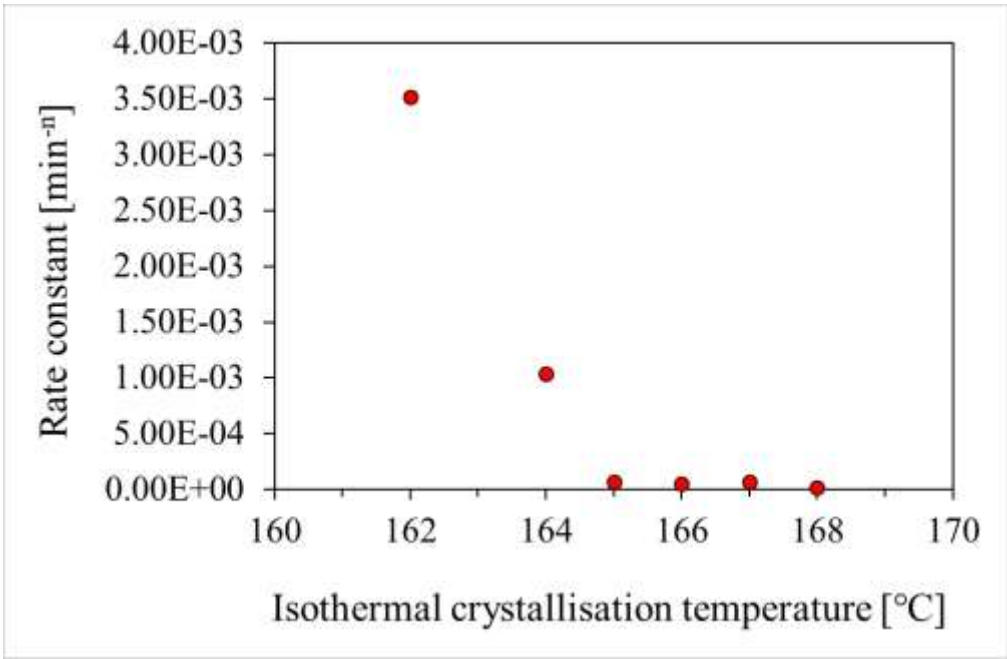

Figure 4.3.3: Variation of the Avrami crystallisation rate constant, K, determined by the intercept from a double logarithmic Avrami plot, with isothermal crystallisation temperature.

4.4 Analysis of primary crystallisation using the Tobin model

The isothermal crystallisation kinetics of PA-12 was analysed using the Tobin model, according to the double logarithmic plot shown below (124).

$$ln\frac{X(t)}{1-X(t)} = ln\,K_t + n_t\,ln(t)$$

Equation 9

In which, X_t is the weight fraction of the crystallisation material at time, t, n_t is the Tobin exponent, and K_t is the Tobin crystallisation rate parameter. In a plot of ln[X(t)/1 – X(t)] vs ln (t), the slope and intercept yield n_t and K_t.

The data presented in Table 4.4.1 shows the Tobin parameters. Overall, the values of n_t were higher than that obtained using the Avrami model. The lowest and highest values of n_t were 3.15 and 4.23 for T_c = 167 and 165 ℃, respectively. In the Tobin model, n_t does not need to be an integer, therefore it can be non-integer values are expected. The Tobin model is used to account for the later stages of crystallisation where impingement occurs, whereas the Avrami model is appropriate for the early stages of crystallisation (124). Comparing the values of n_t and n_a, the values of n_t were consistently greater than n_a. Other studies, that explore the crystallisation kinetics of Poly(ethylene-co-glycidyl methacrylate) and syndiotactic polypropylene also report that n_t was larger than n_a (123,124).

The Tobin rate constant decreased exponentially as the isothermal crystallisation temperature increased. This trend is displayed in Figure 4.4.1. The rate obtained using the Avrami model was greater than the rate obtained using the Tobin model.

The parameter R^2 was used to assess the fit of the model to the experimental data. The R^2 values ranged from 0.9793 – 0.9988. The lowest and the greatest R^2 values were 0.9793 and 0.9988 for T_c = 168 and 164 ℃, respectively. This suggests that the Tobin model provided a good fit to experimental data.

Overall, the Tobin model was successful in describing the isothermal crystallisation kinetics of PA-12 by providing reasonable n, k and R^2 parameters.

Table 4.4.1: Table of Tobin parameters for the isothermal crystallisation of PA-12 within the temperature range of 162 – 168 °C, showing the Tobin exponent, n_t, Tobin rate constant K_t and R^2.

Isothermal crystallisation temperature [°C]	n_t	K_t [min^{-1}]	R^2
162	3.39	2.12E-03	0.9974
164	3.44	4.98E-04	0.9988
165	4.23	2.20E-05	0.9983
166	4.13	1.55E-05	0.9981
167	3.15	2.55E-05	0.9972
168	3.45	4.24E-06	0.9793

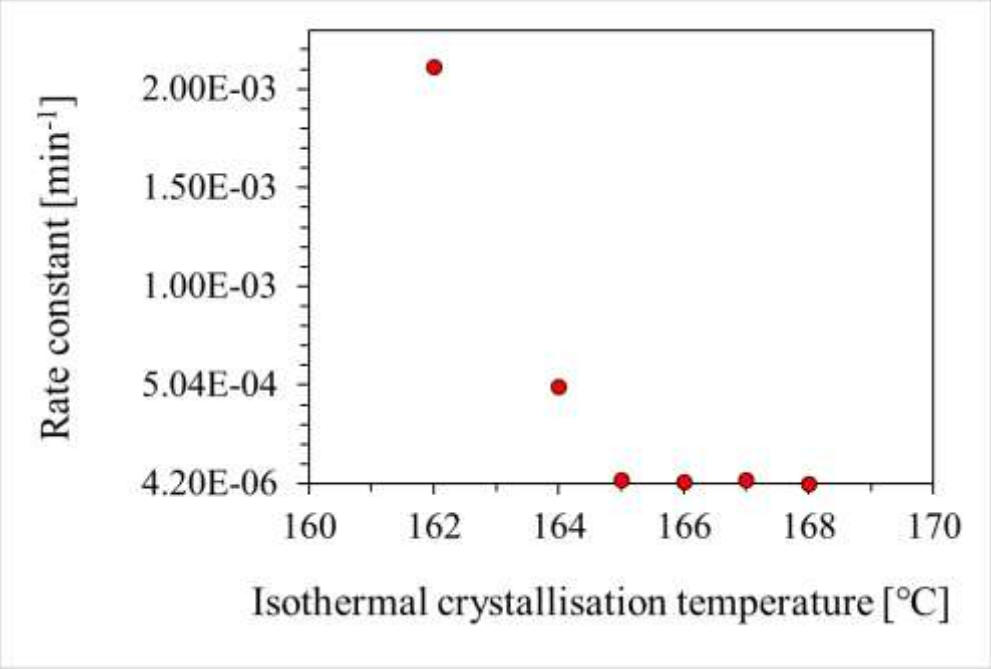

Figure 4.4.1: Variation of the Tobin crystallisation rate constant, K_t, determined by the intercept from a double logarithmic Tobin plot, with isothermal crystallisation temperature.

4.5 Differential Avrami analysis

Differential Avrami analysis produces the parameters n_a, k_a, $t_{1/2}$ based on primary crystallisation, where n_a is the Avrami exponent, k_a is the primary rate constant and $t_{1/2}$ is the half-time of crystallisation (125). The software uses the modified Avrami equation shown below.

$$n_a = -t\,(d\theta(t)/dt)/[(\theta_P(t) - \theta(t))\,ln(1 - \theta(t)/\theta_P(t))]$$

Equation 10

Where n_a is the Avrami exponent, t is time and θ_P is fractional crystallinity of primary crystallisation.

Experimental isothermal crystallisation data was transferred directly into the differential Avrami software. The software determined the limit of primary crystallisation, known as $\theta_P(t)$. Additionally, the area for each exotherm and the error associated with the differential analysis was also reported in the software. The differential Avrami analysis produced data to obtain a plot of of n_a vs $\theta(t)$, a plot of relative crystallinity vs time and n_a, k_a, $t_{1/2}$.

A series of iterations were performed on $\theta_P(t)$ to generate instantaneous values of n_a and produce a value of n_a. The instantaneous values of n_a are observed in a plot of n_a vs $\theta(t)/\theta_P(t)$, where n_a varied until a steady baseline is reached. The value of n_a at the steady baseline was used in the equation $k_a = ln(2)/(t_{0.5})^{na}$ to determine the rate constant.

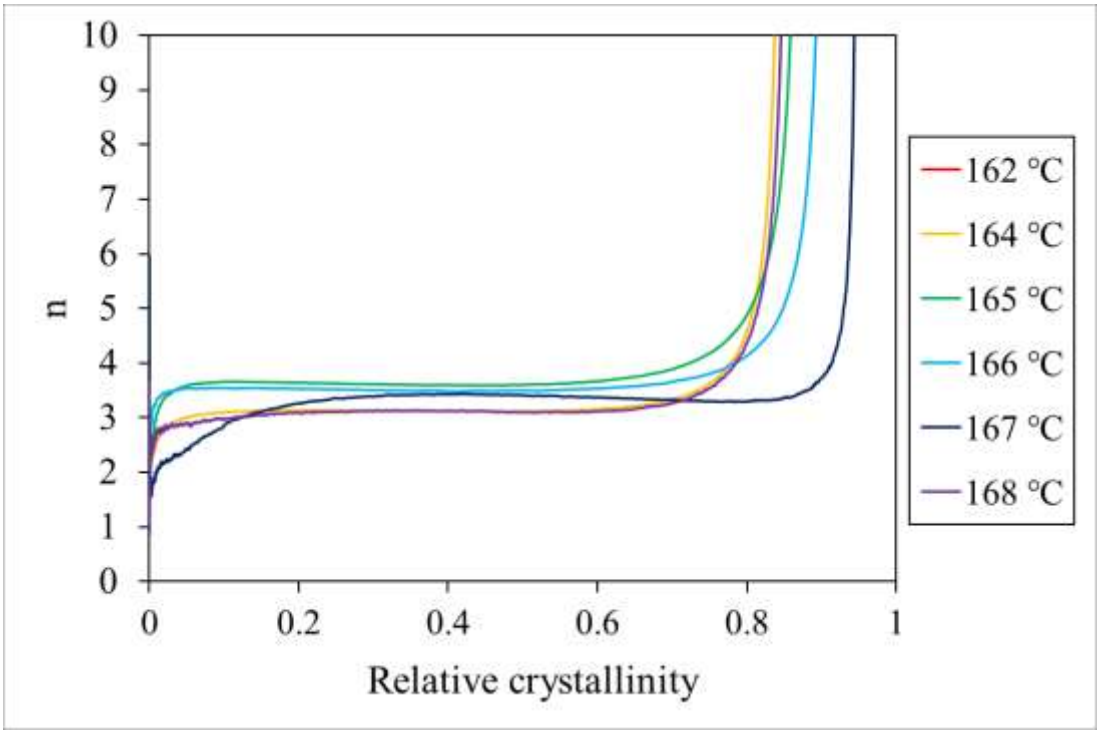

Figure 4.5.1 – Variation of n_a with relative crystallinity according to differential Avrami analysis.

Figure 4.5.1 shows the variation of n_a with relative crystallinity according to differential Avrami analysis. This was produced from a set of iterations on $\theta_P(t)$ that resulted in instantaneous values of n_a. The data shows a small variation in n_a at the beginning of crystallisation. A baseline is established between a relative crystallinity of 0.1 – 0.8. After n_a increased dramatically. The value of n_a was 2 – 4 for all crystallisation temperatures in the region of the steady baseline.

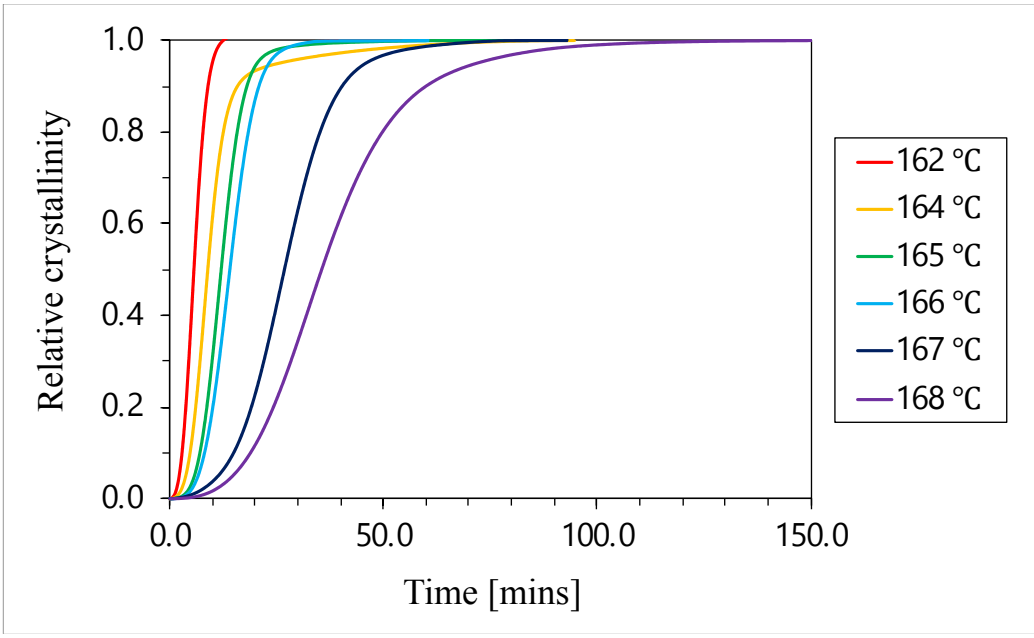

Figure 4.5.2 – Differential Avrami analysis: relative crystallinity (or fraction transformed) of material over time at different isothermal crystallisation temperatures.

A plot of relative crystallinity vs time is displayed in Figure 4.5.2. A sigmoidal shaped curve was produced, similar to conventional Avrami analysis. The graph showed that the onset of crystallisation increased as the crystallisation temperature increased, where the onset of crystallisation is less than X_c = 0.1. Additionally, the shape of each curve was smoother and the time taken to reach X_c = 1 increased. Interestingly, the curve for 164 ℃ shows a different trend at the later stages of relative crystallinity. The point at which the plateaux develops was reached at an earlier time than expected, this suggests that impingement occurred at an earlier stage of crystallisation. The same trend was displayed by conventional Avrami analysis.

Table 4.5.1 shows the differential Avrami parameters as a function of isothermal crystallisation temperature. The crystallisation half-time, $t_{1/2}$, increased with isothermal crystallisation temperature, in agreement with conventional Avrami data. At T_c = 162 ℃, the crystallisation half-time was 5.52 mins, at T_c = 168 ℃, the crystallisation half-time increased to 57.53 mins. The Avrami rate decreased with increasing crystallisation temperature. The Avrami exponent, n_a, was a non-integer value showing a

complex mode of nucleation and growth in the primary phase. A trend was not identified and the average value of n_a, = 3.27. Whereas the average value obtained by conventional Avrami analysis was n_a, = 3.12. This shows that Differential Avrami Analysis produced a slightly larger value for n_a.

The parameter, $X_{P,inf}$ is the relative crystallinity at the end of primary crystallisation. Therefore, $X_{P,inf}$ can be used as guide as to where secondary crystallisation begins, assuming the primary and secondary crystallisation are two independent processes. The data shows that $X_{P,inf}$ decreased as the isothermal crystallisation temperature increased. This suggests that secondary crystallisation occurs earlier into crystallisation as the isothermal crystallisation temperature increased. This is unsurprising since at higher temperatures crystallisation is slower.

Table 4.5.1 – Table of differential Avrami parameters, where $t_{1/2}$ is the crystallisation half-time, $X_{P,inf}$ is the relative crystallinity at the end of primary crystallisation, n_a is the Avrami exponent, and K is the rate.

Isothermal crystallisation temperature [°C]	$t_{1/2}$ [min]	$X_{p,inf}$ [%]	n_a	K [min^{-1}]	error
162	5.52	0.95	2.82	5.60E-03	0.006
164	8.14	0.85	3.13	1.00E-03	0.009
165	11.37	0.88	3.62	1.00E-03	0.021
166	13.52	0.91	3.51	1.00E-03	0.019
167	26.3	0.95	3.38	0.00E+00	0.045
168	33.12	0.87	3.10	0.00E+00	0.016

Figure 4.5.3 displays the relative crystallinity vs time for experimental data and differential Avrami software. The quality of fit of the differential curve was assessed against experimental data. The best and worst quality were T_c = 168 °C and T_c = 167 °C.

In general, the data showed that at $X_c < 0.8$ there was a good quality of fit. At $X_c > 0.8$ the quality of fit was poor. This is because the limit for primary crystallisation ($X_{P,inf}$) was reached. After $X_{P,inf}$ is reached, impingement occurs and the crystallisation mechanisms become more complex.

For experimental data (Chapter 4.2) the Avrami parameters were obtained between a relative crystallinity of 0.03 – 0.70. Within this region, the relative crystallinity for differential data shows a good quality of fit with experimental data. This suggests that the Avrami parameters should be similar. However, there was variation of n_a and and k. The variation is due to differences in mathematical equations.

Although differential Avrami data shows a good quality of fit to the experimental Avrami data, there are limitations associated with the differential Avrami method. For example, the de-sloping mechanism was implemented by the software, however, this can be further manipulated by the user which can lead to subjective error. In this work, the automatic de-sloping mechanism was used and further modifications were not made. Future work should investigate the effect of manual de-sloping on the curve.

Another function in the software is called “array”. This function characterises the smoothness of the curve of n_a vs relative crystallinity. In this work, the array was set 9 for each data set. In order to explore the effect of the level of array on the curve, the setting was increased to 15. However, this increased the error of the parameters obtained. The array was also set to values below 9, though this also increased the error of the parameters obtained. Therefore, an array of 9 was used since this produced parameters with the lowest error.

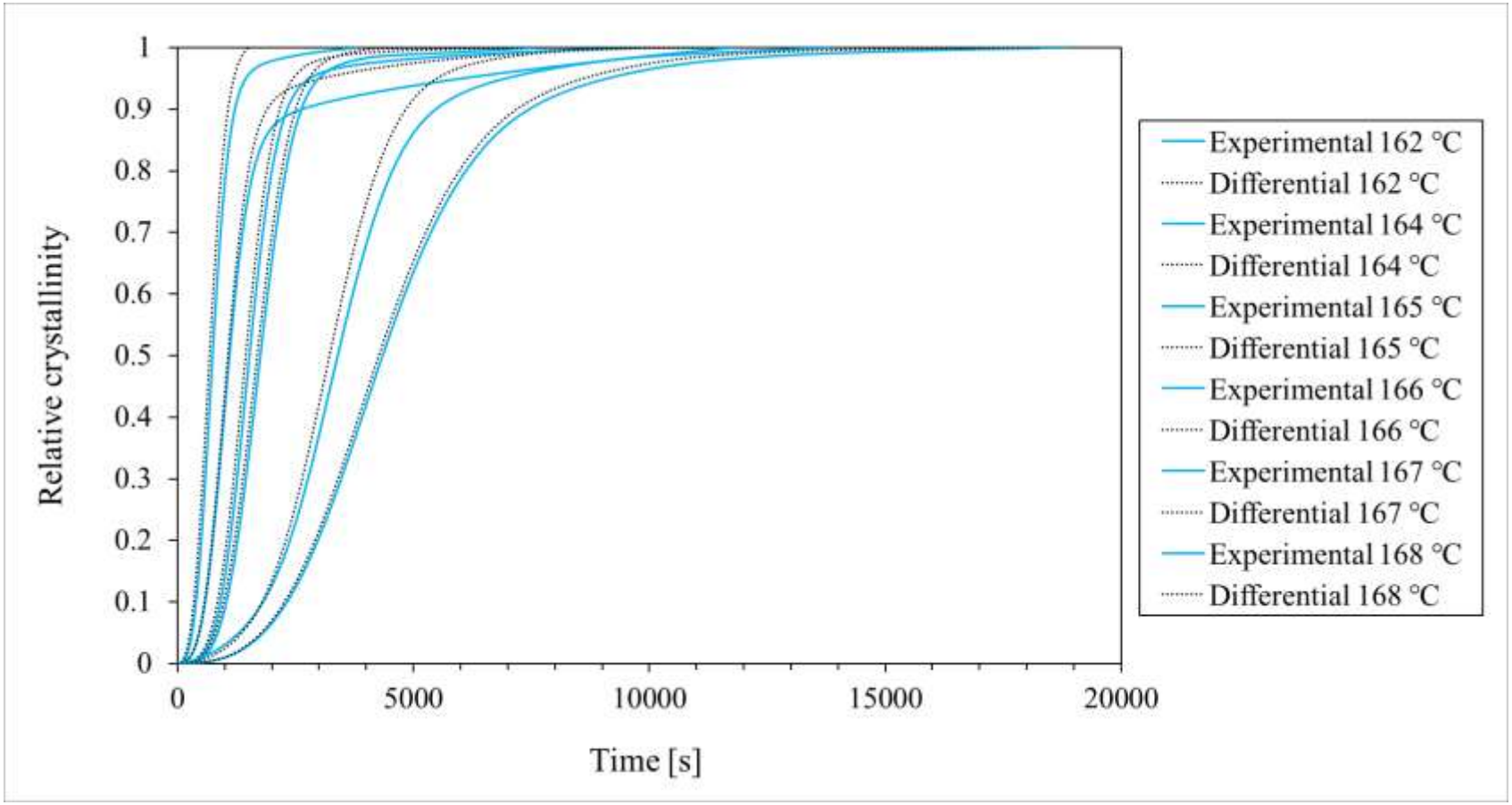

Figure 4.5.3 – Relative crystallinity vs time for isothermal crystallisation 162 – 168 ℃ obtained by the experimental curve and using differential Avrami software. For experimental data, time was zeroed.

4.6 Non-linear regression of models

In addition to using the conventional approach to obtain isothermal crystallisation kinetic parameters, non-linear regression (NLR) was also used. The experimental data of relative crystallinity vs time was transferred into SPSS software and the mathematical models were applied on the data. After a set of iterations, the relevant parameters were produced. A lower limit was set for the output in order to produce lower error. The Avrami and Tobin model were imposed on experimental data.

4.6.1 Avrami

The Avrami model produced values of n_a, K_a, R^2 and standard error. The limits for n_a and K_a were $n_a \geq 1$ and $K_a \geq 0$. These parameters were chosen since n_a should theoretically be an integer a value above 1 and K_a is positive.

Table 4.6.1 – Table of Avrami parameters, obtained using non-linear regression, where k_a is the Avrami rate, n_a is the Avrami exponent, the standard error of K_a and n_a and R^2, as a function of isothermal crystallisation temperature.

Isothermal crystallisation temperature [°C]	K_a [min^{-1}]	n_a	Standard error		R^2
			K_a	n_a	
162	1.39E-01	2.58	0	0.006	0.998
164	8.80E-02	1.98	0	0.011	0.962
165	6.90E-02	3.12	0	0.007	0.997
166	6.00E-02	3.18	0	0.005	0.999
167	3.10E-02	2.73	0	0.004	0.997
168	2.30E-02	2.50	0	0.003	0.997

The list of Avrami parameters obtained by NLR is displayed in Table 4.6.1. The Avrami rate showed a temperature dependant trend, where K_a decreased with increasing isothermal crystallisation temperature. At T_c = 162 ℃ the rate was 0.139 min^{-1} and at T_c = 168 ℃ the rate decreased to 0.023 min^{-1}. The standard error of the rate was 0.

The Avrami exponent, n_a, varied between 1.98 (T_c = 164 ℃) and 3.18 (T_c = 166 ℃) and displayed no trend. The average value of n_a = 2.68. The non-integral value suggests a complex mode of nucleation and growth. The Avrami exponent was greater than 2, this suggests that the growth is expected to be three dimensional. This data agrees with n_a reported by conventional analysis. The standard error associated with n_a ranged between 0.003 – 0.011, this was higher than the standard error associated with K_a.

The parameter R^2 ranged from 0.962 – 0.99, where the lowest T_c = 164 ℃ produced the lowest R^2 and T_c = 166 ℃ produced the highest R^2. The R^2 was relatively high, this suggests that the Avrami model adequately described the crystallisation kinetics of PA-12.

4.6.2 Tobin

The Tobin model produced values of n_t, K_t, R^2 and standard error. The limits for n_t and K_t were $n_t \geq 1$ and $K_t \geq 0$. These parameters were chosen since n_a should theoretically be an integer a value above 1 and K_a is a positive.

The list of Tobin parameters, obtained by NLR is displayed in Table 4.6.2. The rate showed a temperature dependant trend, where K_t decreased with increasing isothermal crystallisation temperature.

At T_c = 162 ℃ the rate was 0.166 min^{-1} and at T_c = 168 ℃ the rate decreased to 0.028 min^{-1}. The standard error of the rate was 0.

The Tobin exponent, n_t, varied between 2.66 (T_c = 164 ℃) and 4.82 (T_c = 166 ℃), displaying no trend. The average value of n_t = 3.92. Non-integral values of n_t are expected for the Tobin model. The standard error associated with n_t ranged between 0.001 – 0.009, this was higher than the standard error associated with K_t. The difference between the average Tobin and Avrmai exponent was 1.24, therefore, $n_t \cong n_a + 1.2$. In other reports, the Tobin exponent obtained using NLR was also larger than the Avrami exponent (119).

The parameter R^2 ranged from 0.982 – 1, where the lowest T_c = 164 ℃ produced the lowest R^2 and T_c = 166 ℃ produced the highest R^2. This shows that the Tobin model adequately described the crystallisation kinetics of PA-12.

Overall, Tobin parameters obtained using NLR had a lower standard error and greater R^2 than the Avrami parameters obtained using NLR. The Tobin model has received large amounts of criticism from authors claiming that it fails to accurately describe the isothermal crystallisation kinetics due to its complex derivation (119,126). However, the R^2 values suggest the Tobin model can adequately describe the crystallisation kinetics of PA-12.

Table 4.6.2 – Table of Tobin parameters, obtained using non-linear regression, where k_a is the Tobin rate, n_t is the Tobin exponent, the standard error of K_t and n_t and R^2, as a function of isothermal crystallisation temperature.

Isothermal crystallisation temperature [℃]	K_t [min^{-1}]	n_t	Standard error		R^2
			K_t	n_t	
162	1.66E-01	3.39	0	0.005	0.999
164	1.09E-01	2.66	0	0.009	0.982
165	8.00E-02	4.63	0	0.005	0.999
166	7.00E-02	4.82	0	0.005	0.999
167	3.60E-2	4.16	0	0.004	0.999
168	2.8E-02	3.87	0	0.001	1

4.7 Modelling of relative crystallinity using n and k determined using non-linear regression

The parameters *n* and *k*, or equivalent determined by the Avrami and Tobin model obtained using NLR were used to model relative crystallinity with time, as shown in Figure 4.7.1. This enabled the models to be compared to experimental data (as per section 4.2) by assessing the visual quality of fit.

The Avrami model was in good agreement with experimental data up to $X_c < 0.8$. After the model showed a continual increase in crystallinity before quickly transforming into a plateau at X_c of 0.9 and reaching complete crystallisation. Whereas experimental data showed that at X_c of 0.80 – 1.0 crystallisation was slow and complete crystallisation was reached at a much later time. Overall, T_c = 168 ℃ had the poorest quality of fit.

Generally, the deviations between the model and the experimental data were observed at the later stages of crystallisation (after impingement was achieved) where crystallisation is much slower. At this point, secondary crystallisation also influences the crystallisation process.

Overall, the Avrami model showed a good fit to experimental data, especially in the intermediate stages of crystallisation where $X_c = 0.2 – 0.8$. This is unsurprising, since the Avrami model is known to predict the primary crystallisation process. These conclusions agree with the R^2 returned by NLR, where $R^2 = 0.962 – 0.99$.

The Tobin was in good agreement with experimental data. The deviations between the model and experimental data were minimal and were observed mainly before X_c of 0.1 and after X_c of 0.9. This is within the region of the onset of crystallisation and end of crystallisation. Deviations are likely to occur at the onset due to rapid crystallisation. Whereas at the end of crystallisation deviations are likely to occur due to slow crystallisation, effects of impingement and secondary crystallisation. The Tobin model accounts for impingement such that non-integer values are commonly obtained for n_t. This can explain the good agreement between the Tobin model and experimental data. These conclusions correlate with R^2 returned by NLR, where $R^2 = 0.982 – 0.1$.

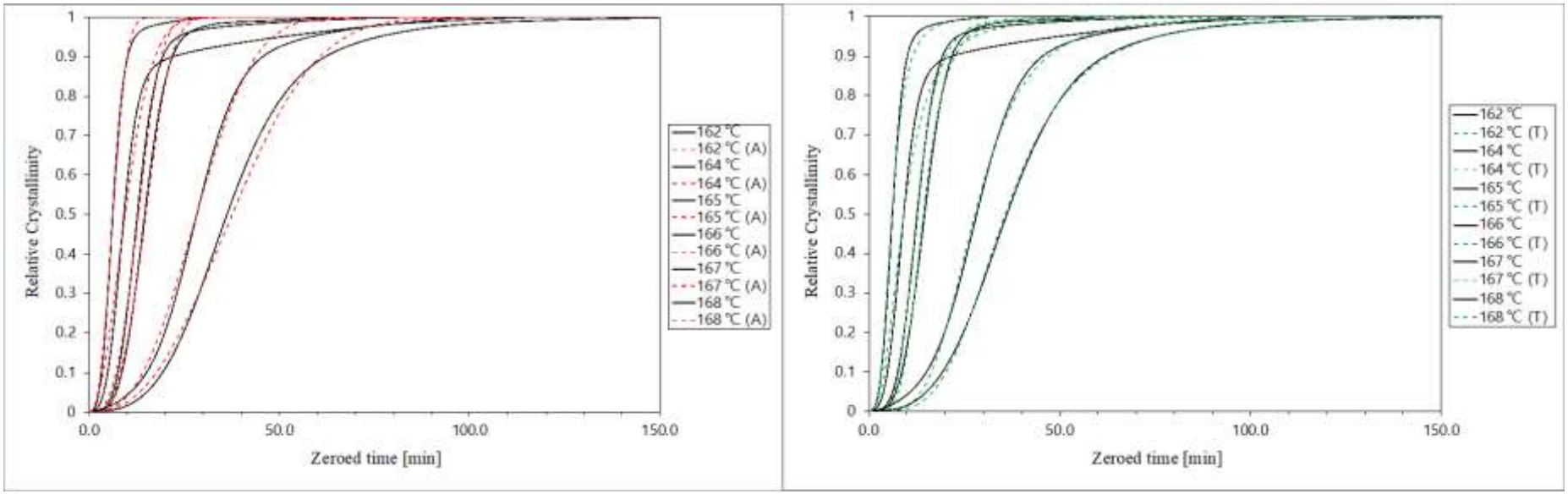

Figure 4.7.1 – Graph of relative crystallinity vs time for experimental data and from parameters obtained using non-linear regression for the Avrami (A) and Tobin (T).

4.8 Modelling of relative crystallinity using applied values of *n* to resolve for *k* determined using non-linear regression

NLR was used to apply values of *n* and resolve for *k* and R^2 for a range of isothermal crystallisation temperatures, where *n* = 1, 2, 3, and 4. This follows the work of Verhoyen et al (128). The rationale of applying *n* on experimental data was to observe how the rate was affected by *n* and to assess the quality of fit of integer values on data according to the Avrami equation. The same method was used on experimental data where *n* = 1, 2, 3, and 4. The data is shown in Table 4.8.1.

Table 4.8.1 – Rate constant, k, and R^2 from imposed integer values of n, according to the Avrami equation for a range of isothermal crystallisation temperatures T_c.

T_c [°C]	***n* = 1**		***n* = 2**		***n* = 3**		***n* = 4**	
	k [min^{-1}]	R^2	*k* [min^{-1}]	R^2	*k* [min^{-1}]	R^2	*k* [min^{-1}]	R^2
162	0.146	0.893	0.019	0.992	0.003	0.996	0	0.984
164	0.085	0.927	0.008	0.962	0.001	0.952	7.94E-05	0.937
165	0.071	0.881	0.005	0.982	0	0.997	2.43E-05	0.993
166	0.063	0.858	0.004	0.98	0	0.999	1.39E-05	0.995
167	0.032	0.877	0.001	0.988	2.92E-05	0.996	9.64E-07	0.986
168	0.024	0.888	0.001	0.992	1.32E-05	0.994	3.38E-07	0.981

The parameters *k* and R^2 for imposed *n* values at different temperatures is displayed in Table 4.8.1. The general trend showed that for imposed integers of *n*, the rate constant decreased as the isothermal crystallisation temperature increased. For example, at *n* = 1 the rate constant *k* decreased from 0.146 to

0.025 min^{-1} at T_c = 162 to 168 ℃. At n = 2 the rate constant k decreased from 0.138 to 0.023 min^{-1} at T_c = 162 to 168 ℃. When the Avrami exponent increased to n = 3 and n = 4 the rate constant k decreased considerably. For example, at n = 3 the rate constant k decreased from 0.003 to 1.32E-05 min^{-1} at T_c = 162 to 168 ℃. At n = 4 the rate constant k decreased from 0 to 3.38E-07 min^{-1} at T_c = 162 to 168 ℃.

Figure 4.8.1 shows a graph of relative crystallinity vs time for experimental data (as per section 4.2) and NLR using imposed values of n. For n = 1 a sigmoidal curve was not produced and the quality of fit was poor. The model shows that crystallisation begins immediately and slows down as time increases. Additionally, the curve becomes more pronounced as the isothermal crystallisation temperature increased. In many cases, the data stops before complete crystallisation is reached. This shows that n = 1 does not adequately describe the crystallisation of PA-12.

For n = 2, a sigmoidal graph was produced and the quality of fit was adequate. The model shows that the onset of crystallisation increased as the isothermal crystallisation temperature increased. However, as the isothermal crystallisation temperature increased the quality of fit in the mid-region was poor. As crystallisation continued and X_c = 1 was reached but the quality of fit was poor.

For n = 3 and n = 4, the relevant parameters were inputted into the Avrami equation to regenerate a curve of relative crystallinity vs time. However, due to the rate constant being extremely small, the curve could not be regenerated since X_t was also extremely small. An example is shown in Figure 4.8.2.

Interestingly, the greatest R^2 values were obtained for n = 3 yet the a graph of relative crystallinity vs time could not be regenerated. This is consistent with the data in section 4.3.1, where although a trend of n with isothermal crystallisation temperature was not observed, the average n = 3.12. This suggests that an integer value of n between 2 and 3 may best describe the isothermal crystallisation kinetics of PA-12.

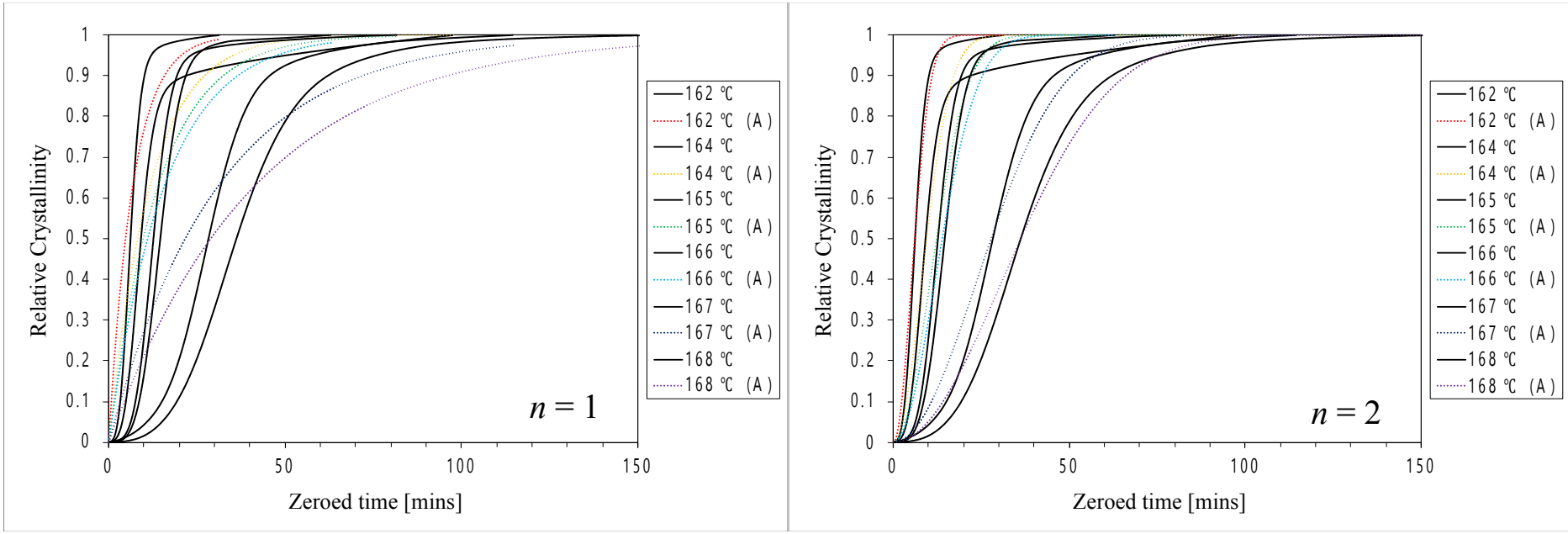

Figure 4.8.1 – Graph of relative crystallinity vs time for experimental data and from parameters obtained using non-linear regression for the Avrami (A) model, with applied values of n.

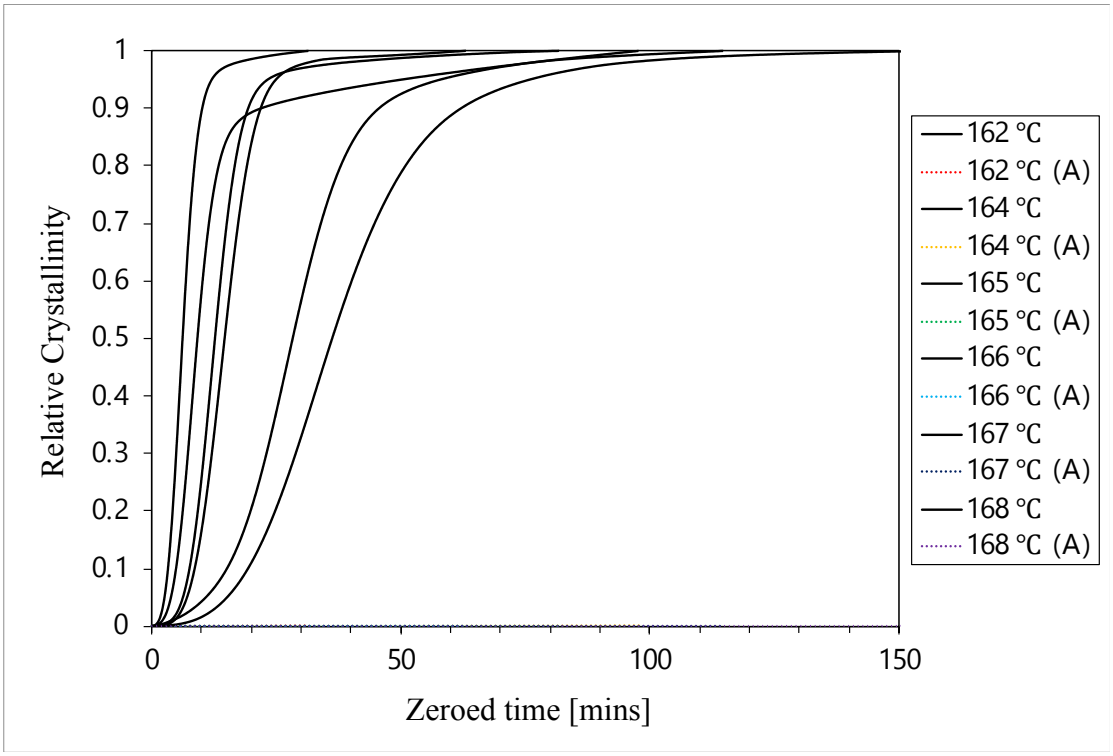

Figure 4.8.2 – Graph of relative crystallinity vs time for experimental data and from parameters obtained using non-linear regression for the Avrami (A) model, with an applied value of n = 3.

4.9 Discussion of the isothermal crystallisation kinetics of PA-12

Conventional analysis and NLR were used to evaluate the crystallisation kinetics of PA-12 according to the Avrami and Tobin model. The models were evaluated based on R^2 and the quality of fit of NLR data to experimental data in a graph of relative crystallinity vs time. A value for R^2 was produced for both conventional analysis and by NLR.

The conventional approach was used for the Avrami and Tobin model. The Avrami model produced R^2 within the range 0.9913 – 0.9998 and the Tobin model produced R^2 within the range 0.9793 – 0.9988. This suggests that both the Avrami model and Tobin model provided a reasonable fit and were

successful in describing the isothermal crystallisation kinetics of PA-12. Typically, $R^2 > 0.99$ is deemed reasonable. This suggests that the Avrami model had a more reasonable fit than the Tobin model.

The R^2 returned NLR was evaluated. The R^2 for the Tobin model was the produced the highest R^2, followed by the Avrami model. In the Tobin model, R^2 ranged between 0.982 – 1. This was closely followed by the Avrami model where R^2 ranged between 0.962 – 0.997.

On comparing R^2 for conventional and NLR data, R^2 for the Avrami model using conventional analysis was greater than NLR. Whereas, R^2 for the Tobin model using conventional analysis was lower than NLR. The difference in R^2 is due to the different methods used to determine the kinetic parameters, where the conventional approach is based on a set of calculations performed by the user. Whereas, in NLR a set of iterations is performed on the software to produce R^2 according to the limits set by the user and lowest standard error.

The quality of fit of NLR data was compared to experimental data in a graph of relative crystallinity vs time. This was achieved by inputting the parameters obtained by NLR into the kinetic equations to regenerate a curve of relative crystallinity vs time. The data showed that the Tobin model had the best quality of fit, followed by the Avrami model. The Avrami model had a good quality of fit at earlier stages of crystallisation However, the most deviation was displayed at later stages of crystallisation. This was typically where impingement occurred. In a graph of relative crystallinity vs time, impingement was observed as a distinctive change in gradient before the curve proceeds to reach a relative crystallinity equal to 1. In this region, the Tobin model had a greater quality of fit. This is because the Tobin model accounts for impingement. The Avrami model deviated slightly in these regions, since the Avrami model only accounts for primary crystallisation.

The Tobin model is a direct extension of the Avrami model that accounts for impingement. The R^2 data and the quality of fit suggests that the Tobin model adequately describes the crystallisation kinetics of PA-12.

For NLR, the R^2 and the quality of fit was used to evaluate how well the models described the crystallisation kinetics of PA-12. Both the R^2 and the quality of fit showed that the Tobin model adequately described the crystallisation kinetics of PA-12, this was closely followed by the Avrami model.

Although NLR is a common method to explore isothermal crystallisation kinetics, it has limitations. Such that the models may under or overestimate the crystallisation parameters based on the limits set by the user, if any. Therefore, there are points that must be considered. For example, in addition to assessing the overall quality of the fit, the fit of data in key regions is also important. The Avrami model accounts for primary crystallisation, hence the quality of fit within linear portion in a graph of relative crystallinity vs time is important to consider. For this data, this region was between $X_t = 0.03 – 0.70$. An extension of this work would Involve performing NLR without limits and using the parameters to generate a curve of relative crystallinity vs time.

CHAPTER 5 – NON-ISOTHERMAL CRYSTALLISATION KINETICS OF POLYAMIDE-12

Non-isothermal crystallisation is thought to be more complex than isothermal crystallisation kinetics. This is due to non-isothermal crystallisation being a dynamic process, where the cooling rate is constant and the temperature changes throughout crystallisation. The non-isothermal crystallisation kinetics were studied using the Jeziorny-modified Avrami model and the Caze model. These models were selected because they use different methods to determine the non-isothermal crystallisation kinetics of PA-12. Often, industrial processes proceed under non-isothermal conditions. Therefore, understanding non-isothermal crystallisation kinetics has relevance to industrial processes. For example, in MJF the IR lamp facilitates fusion of PA-12 powder particles where the FA has been applied. Once the lamp has scanned the surface, the cooling process begins. Furthermore, once the build is complete the powder chamber is left to cool over a period of time before the parts are removed.

5.1 Analysis of primary crystallisation kinetics by differential scanning calorimetry

Non-isothermal crystallisation was performed using a number of cooling rates between 5 and 40 °C/min, at 5 °C/min intervals. To analyse the non-isothermal crystallisation kinetics of PA-12, a temperature correction was required in order to convert the temperature scale into a time scale. This is shown in the equation below.

$$t = \frac{T_{c,onset} - T_c}{\phi}$$

Equation 11

Where t, is the time, $T_{c,\,onset}$ is the temperature at the onset of crystallisation, T_c is the temperature at time, t, and ϕ is the cooling rate.

The raw data of relative heat flow vs temperature that was extracted from the DSC is shown in Figure 5.1.1 and Table 5.1. This data shows that the onset, peak and end crystallisation temperature were affected by the cooling rate. The onset, peak and end crystallisation temperature shifted to lower temperatures as the cooling rate increased. Moreover, the crystallisation exothermic peak broadened as the cooling rate increased. This shows that crystallisation occurred over a larger temperature range as the cooling rate increased. Additionally, the peak heat flow moved to lower temperatures. Teo et al also note a decrease in crystallisation temperature and decrease in the degree of crystallinity as the cooling rate increased (100).

The trends above are explained by the temperature dependence of crystallisation. At lower cooling rates, crystallisation occurs slowly and the sample has more time to crystallise. This allows crystallisation to occur at higher temperatures, when compared to higher cooling rates (100).

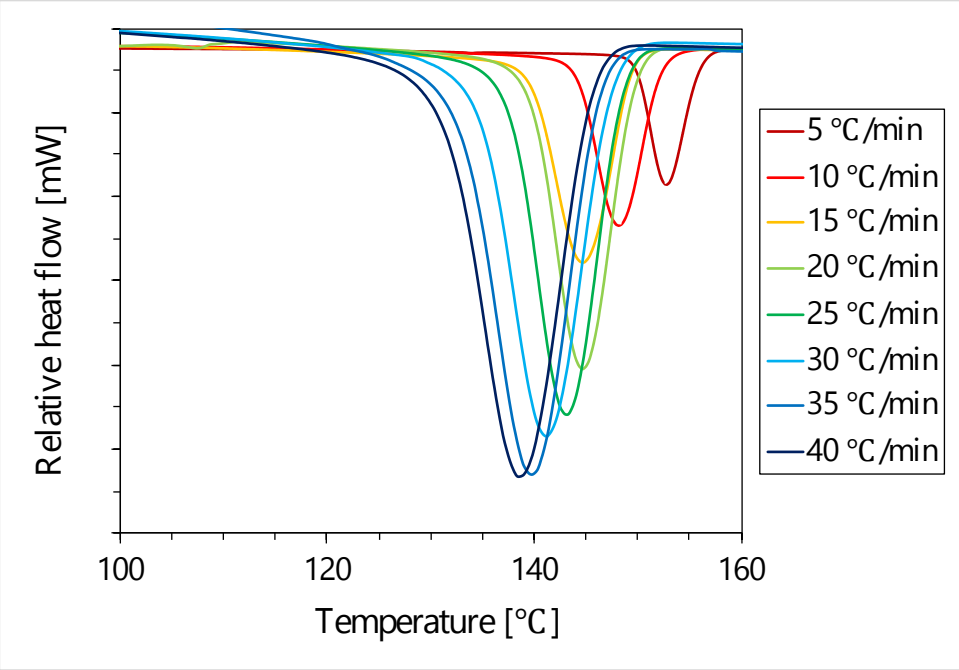

Figure 5.1.1 – Non-isothermal crystallisation of PA-12 at different cooling rates, where heat flow is normalised to the same baseline.

Table 5.1.1: The cooling parameters of PA-12 at different cooling rates, showing the onset crystallisation temperature, $T_{c,onset}$, peak crystallisation temperature $T_{c,peak}$, end crystallisation temperature $T_{c,off}$, enthalpy of crystallisation, ΔH_c and degree of crystallinity, X_c.

Cooling rate [°C/min]	$T_{c,onset}$ [°C]	$T_{c,peak}$ [°C]	$T_{c,off}$ [°C]	ΔH_c [Jg^{-1}]	X_c [%]
5	163.00	152.79	100.00	120.57	57.61
10	161.67	148.08	116.67	115.29	55.08
15	154.00	144.75	112.88	114.77	54.84
20	156.67	144.67	122.33	112.56	53.78
25	153.33	143.33	120.83	115.06	54.97
30	153.00	141.25	113.75	114.03	54.48
35	155.84	139.8	121.42	109.24	52.19
40	153.33	138.67	112.67	117.42	56.10

Once the temperature had been converted to time, the data was corrected such that the time between t = 0 min and t_{onset} was removed. This allowed the time taken for crystallisation at different cooling rates to be compared on a zero timescale or at the onset of crystallisation, as shown in Figure 5.1.2. At lower cooling rates, the peak was broad and the time taken for crystallisation increased. This suggests that slower cooling rates enhanced the crystal structure of PA-12 by allowing more time for crystallisation.

For a sample of PA-12 cooled at 5 °C/min the bulk of the material had crystallised in ~ 3 mins. However, the sample required another ~ 2.5 mins for the curve to return to the induction baseline. This slow region of crystallisation is due to secondary crystallisation. This was also observed for samples cooled at a rate of 10 and 15 °C/min. However, for faster cooling rates at 35 and 40 °C/min the exothermic peak was sharp and the curve quickly returned to baseline.

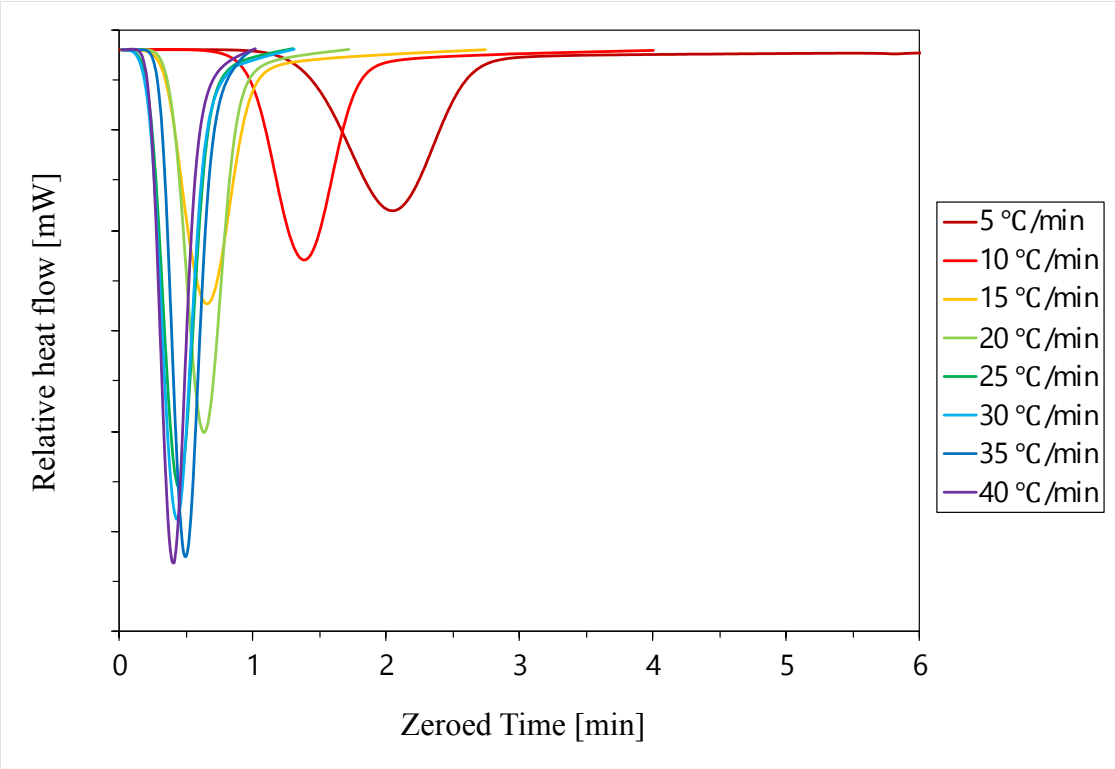

Figure 5.1.2 – Non-isothermal crystallisation of PA-12 at different cooling rates, showing the time taken for crystallisation, where heat flow has been normalised to the same baseline and time is normalised so the onset of crystallisation for each sample is marked at t = 0 mins.

Figure 5.1.3 shows a graph of relative crystallinity vs time. A sigmoidal shaped curve was displayed for each cooling rate. The curves initially show a flat region, after which the curve rapidly increased demonstrating that the rate of crystallisation increased. The curve then plateaus; this is where impingement occurs (129). The rate of crystallisation decreases and eventually stops because the temperature has dropped below the T_g.

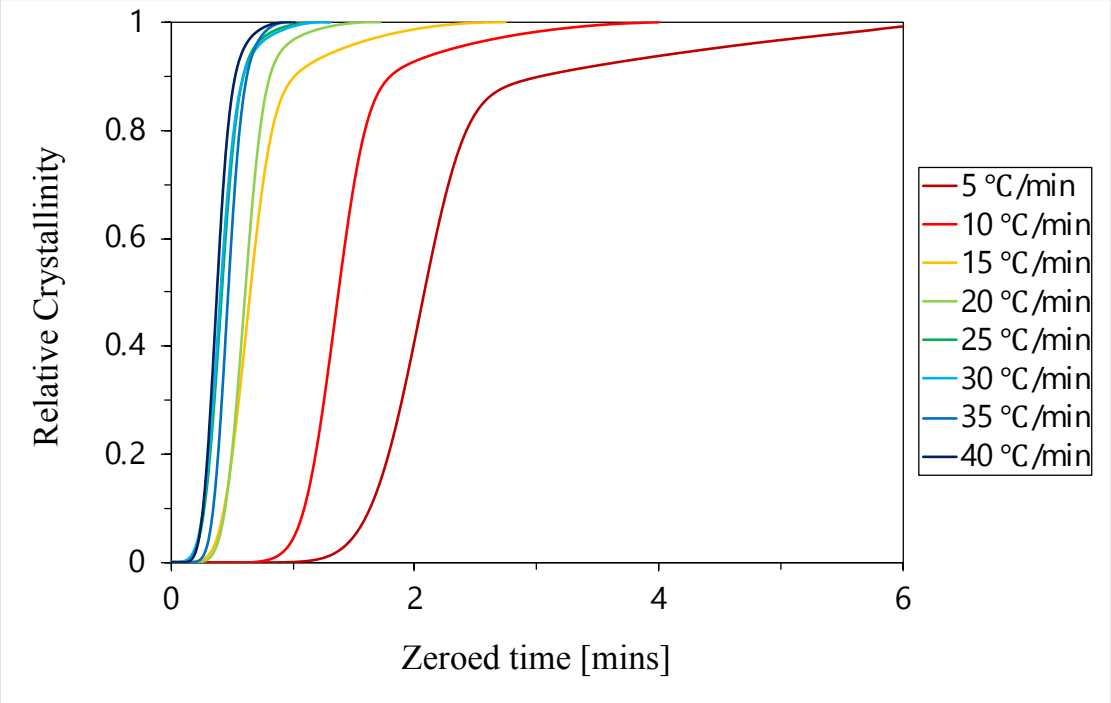

Figure 5.1.3 – Relative crystallinity vs time, as a function of cooling rate for PA-12.

5.2 Jeziorny-modified Avrami model

Jeziorny modified the Avrami equation to account for the constant cooling rate in non-isothermal crystallisation (93). The rate parameter as describe by Jeziorny is shown below.

$$log\ Z_c = log\ \frac{Z_t}{\phi}$$

Equation 12

Where ϕ is the cooling rate, Z_c is the Jeziorny rate that has been corrected using the cooling rate and Z_t is obtained from a graph of log [-ln (1 – X_t)] vs log (time), this is displayed in Figure 5.2.1.

Figure 5.2.1 shows a double logarithmic plot according to log [-ln (1 – X_t)] vs log (time). The Avrami exponent *n* and the Avrami rate *K* were determined from the slope and intercept, respectively. The curve shows a linear region and a flat region. This suggests that a 2-stage crystallisation process is present, whereby the linear portion represents primary crystallisation and the flat region represents secondary crystallisation. This trend was also reported by McFerran et al, where spherulite impingement showed crystal growth during secondary crystallisation (93). The cooling rates used by McFerran et al were identical to the cooling rates used within this experiment. The lowest and highest cooling rates were 5 and 40 ℃/min. Interestingly, Figure 5.1.5 shows that at lower cooling rates the flat region of the curves was larger. This suggests that there is more secondary crystallisation, since at lower cooling rates crystallisation takes place over a longer period of time. It has been noted by Vefwoyen et al, when studying the crystallisation of Polyethylene Terephthalate that secondary crystallisation occurs when the primary crystallisation process is almost complete. In this work, at very high cooling rates (greater than 10 K/s) no crystallisation was observed. At lower cooling rates "global crystallinity" was due to primary crystallisation. Therefore, secondary crystallisation can occur at cooling rates lower than 10 K/s (126). In this experimental work, primary crystallisation was observed between cooling rates of 5 to 40 ℃/min. According to (126) secondary crystallisation can occur once primary crystallisation is complete. Therefore, (126) suggests that secondary crystallisation can be present. N. McFerren et al obtain parameters for non-isothermal secondary crystallisation of PA-12 between 5 to 40 ℃/min demonstrating that secondary crystallisation was present (93).

The 'vrami parameters for primary crystallisation were obtained between X_t = 0.03 – 0.70, the parameters are displayed in Table 5.2.1. The double logarithmic plot limited to X_t = 0.03 – 0.70 is displayed in Figure 5.2.2. The data in Table 5.2.1 shows that the Avrami exponent, *n*, was not an integer value and decreased with increasing cooling rate. The Avrami exponent ranged from 4.42 to 7.68 and the average *n* value was 6.03. This is considerably larger than values of *n* obtained by isothermal crystallisation and is due to non-isothermal crystallisation being a dynamic process. A non-integral *n* value greater than 2 suggests the growth of 3D spherulites is formed by athermal nucleation (134). In

Jeziorny's original work on poly(ethylene terephthalate), *n* increased with cooling rate and ranged from 2.35 to 2.65 for cooling rates between 8.5 and 17 K/min. This trend was directly related to the increasing effect of athermal nucleation (134). Moreover, J. Li et al 124tudied the non-isothermal crystallisation kinetics of a PA-6 and multi-walled carbon nanotube composite materials. It was reported that $n \approx 4$ demonstrates very complicated crystallisation mechanisms, though it was not reported in what way the mechanism is complicated (135). The term "very complicated crystallization mechanism" may be used to explain values of *n* greater than 4, where in the original Avrami theory *n* is integer values of 1, 2, 3 and 4.

The Jeziorny rate, Z_c, showed a dependency with cooling rate in that the Jeziorny rate increased with cooling rate. The Jeziorny rate, Z_c, at 5 and 40 ℃/min were 0.294 and 1.134 min^{-1}. This is unsurprising since the time taken for crystallisation decreased as the cooling rate increased. Likewise, the crystallisation half-time, extrapolated at $X_c = 0.5$, decreased as the cooling rate increased. N. McFerran at al also reported a similar trend (93).

For the primary crystallisation process, the R^2 values were in excess of > 0.99. This justifies the Avrami exponent and rate modified by Jeziorny showing confidence in the data obtained. Therefore, the Avrami model modified by Jeziorny adequately described the crystallisation kinetics of PA-12.

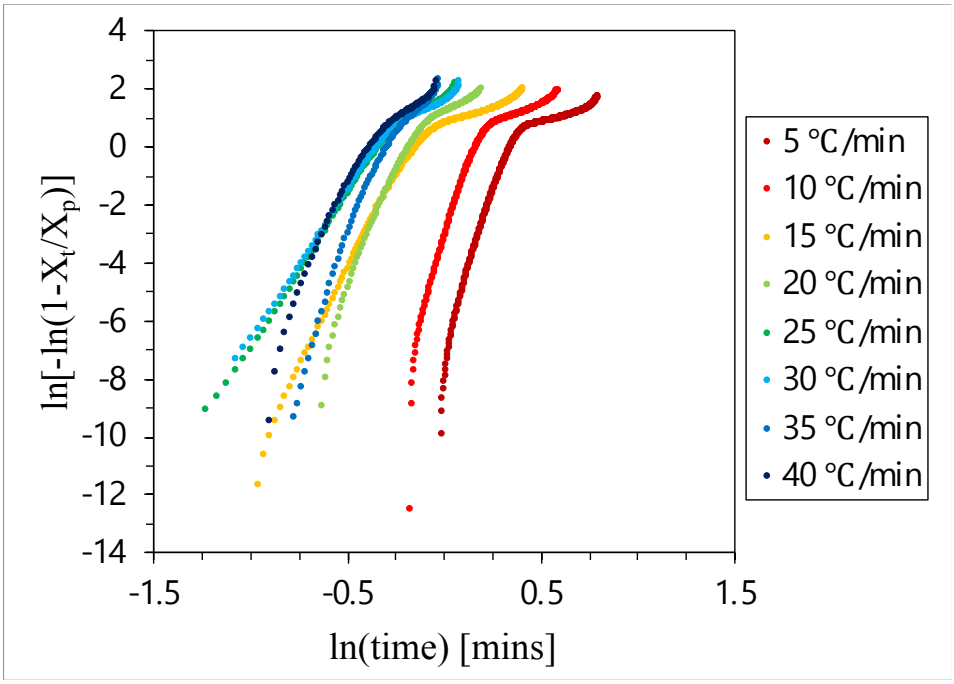

Figure 5.2.1 – Unlimited Avrami plot for PA-12 crystallised in non-isothermal conditions.

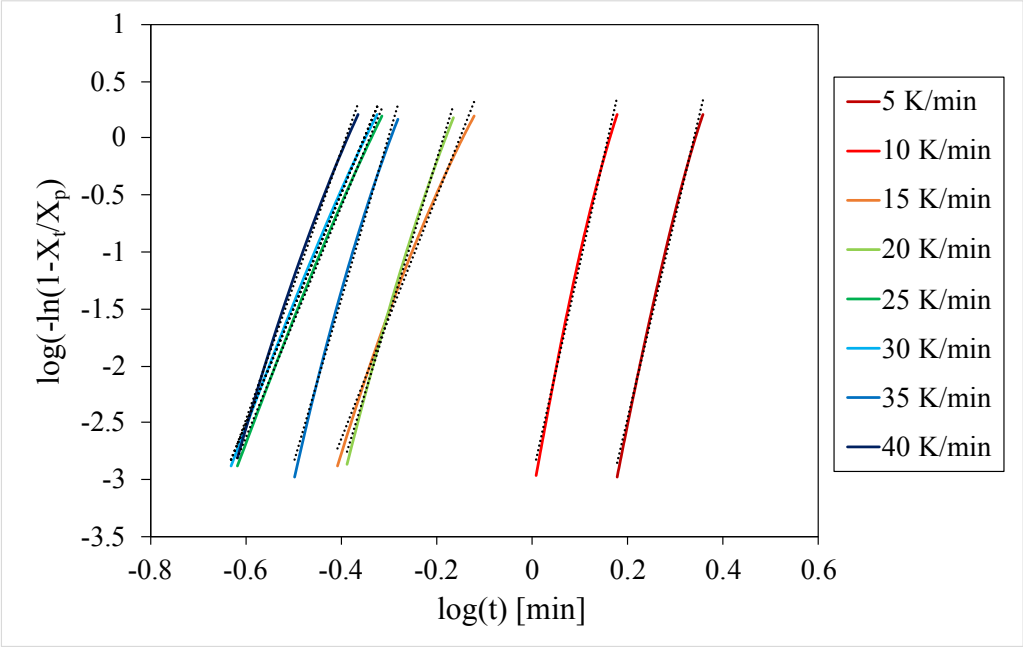

Figure 5.2.2 – Limited Avrami plot (between $X_t = 0.03 – 0.70$) for PA-12 crystallised in non-isothermal conditions.

Table 5.2.1 – The Avrami parameters, modified by Jeziorny, showing the crystallisation half-time (determined from $X_c = 0.5$), $t_{0.5}$, the Avrami exponent, n, Avrami rate, Z_t, the rate modified by Jeziorny, Z_c, and R^2, as a function of cooling rate.

Cooling rate [°C/min]	$t_{0.5}$ [min]	n	$\ln Z_t$	K_t [min^{-1}]	$\ln Zc$	Zc [min^{-1}]	R^2
5	2.08	7.86	-6.13	0.00	-1.225	0.294	0.9957
10	1.38	8.29	-3.02	0.05	-0.302	0.740	0.9938
15	0.65	4.81	1.69	5.42	0.113	1.119	0.9937
20	0.62	6.10	2.64	14.07	0.132	1.141	0.9958
25	0.42	4.50	3.34	28.33	0.134	1.143	0.9985
30	0.41	4.42	3.59	36.21	0.120	1.127	0.9985
35	0.48	6.33	4.94	140.33	0.141	1.152	0.9937
40	0.38	5.91	5.03	153.55	0.126	1.134	0.995

It has been mentioned in Chapter 4 that PA-12 exhibits secondary crystallisation in isothermal crystallisation, this was also observed in non-isothermal crystallisation and was demonstrated by the flat region in Figure 5.2.1. The parameters of n_2, $Z_{c,2}$ and R^2 were determined within the region of X_t = 0.95 – 0.98, these are displayed in Table 5.2.2. The Avrami exponent ranged between 1 – 2, this was significantly smaller than the Avrami exponent obtained for primary crystallisation. The low values of Avrami exponent was due to spherulite impingement where the spherulite growth transforms into one dimension space extension. The rate Zc_2 was also smaller than that obtained for primary crystallisation and was again due to spherulite impingement causing the further rate of crystallisation to decrease. The R^2 values ranged from 0.9968 – 1, showing that the data was in good agreement with a linear trendline.

Overall, the Jeziorny-modified Avrami model was successful in describing the crystallisation kinetics of PA-12. A clear distinction between the primary and secondary crystallisation process was observed. The rate parameters were temperature dependant and values of *n* were in the primary crystallisation stage were larger than the secondary crystallisation stage.

Table 5.2.2 – Table of Avrami parameters, modified by Jeziorny for the secondary crystallisation of PA-12, showing the Avrami exponent, n, Avrami rate, Z_t, the rate modified by Jeziorny, Z_c, and R^2, as a function of cooling rate.

Cooling rate [°C/min]	n_2	$\ln Z_{t,2}$	$Z_{t,2}$ [min^{-1}]	$\ln Zc_2$	Zc_2 [min^{-1}]	R^2
5	1.21	-0.71	0.49	-0.142	0.868	0.9948
10	1.09	0.18	1.20	0.018	1.019	0.9985
15	0.95	0.78	2.17	0.052	1.053	0.9979
20	1.32	1.22	3.39	0.061	1.063	0.9988
25	1.43	1.67	5.30	0.067	1.069	0.9968
30	1.25	1.56	4.74	0.052	1.053	0.9992
35	2.40	2.03	7.59	0.058	1.060	1
40	1.90	2.07	7.93	0.052	1.053	0.9974

5.3 Caze model

The Caze method determines an average Avrami exponent, $n_{average}$, over a range of non-isothermal crystallisation conditions. The Caze method however does not apply when the matrix is reinforced with an efficient nucleating agent (137). The average Avrami exponent is obtained plotting a graph of

temperature vs log cooling rate for the onset crystallisation temperature ($T_{c,onset}$), peak crystallisation temperature ($T_{c,peak}$) and end crystallisation temperature ($T_{c,end}$). According to the Caze model, the crystallisation temperatures should vary linearly with cooling rate.

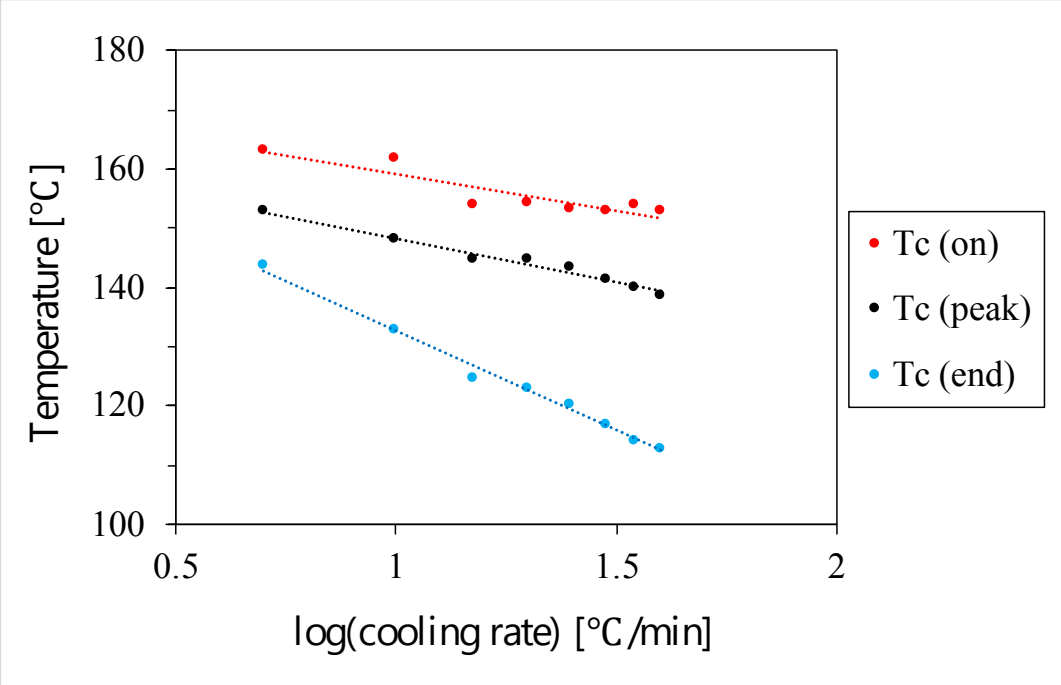

Figure 5.3.1 – Graphs of the onset crystallisation temperature ($T_{c,\,on}$), peak crystallisation temperature ($T_{c,\,peak}$), and end crystallisation temperature ($T_{c,off}$) as a function of cooling rate.

Figure 5.3.1 shows the temperature vs cooling rate for $T_{C,onset}$, $T_{C,\,peak}$ and $T_{C,\,end}$. Each curve shows a negative correlation, where $T_{C,onset}$, $T_{C,\,peak}$ and $T_{C,\,end}$ decreased as cooling rate increased. The $T_{C,onset}$, $T_{C,\,peak}$ and $T_{C,\,end}$ at 5 °C/min were 163.00, 152.79 and 115.71 °C, respectively. At 40 °C/min $T_{C,onset}$, $T_{C,\,peak}$ and $T_{C,\,end}$ were 152.67, 138.67 and 112.67 °C, respectively.

From the graph in Figure 5.3.1 the constants A, B_i, B_{ii} were obtained from the gradient and intercept values; A = - 14.93, B_i = 171.44 and B_{ii} = 166.34. These are displayed in Table 5.5.1. As such $n_{average}$ was determined by:

$$n_a = \frac{T_{C,peak}(gradient) \times \ln\frac{3-\sqrt{5}}{3+\sqrt{5}}}{B_i - B_{ii}}$$

Equation 13

Using the constants, $n_{average}$ = 5.64. For a more detailed method on how A, B_i, B_{ii} and $n_{average}$ are derived, see literature (137). This was higher than that obtained by Liu et al where $n_{average}$ = 1.96 for nylon-12,12 and McFerran et al where $n_{average}$ = 0.292 for PA-12 (93,129). Interestingly, McFerran et al comment on the limitations on the Caze model. Aside from discounting secondary crystallisation, the parameter $T_{C,end}$ is subjective which makes it difficult to assign. Moreover, the secondary crystallisation process occurs over a longer period of time which can decrease $T_{C,end}$ and lead to inaccurate estimations. Additionally, where a lower value of $T_{c,end}$ is recorded, the value of $n_{average}$ decreases.

The Caze model produced $n_{average}$ = 5.64. This correlates with the Avrami model by Jeziorny, where relatively high values of *n* were obtained. In other work using the Avrami model modified by Jeziorny, it was reported that $n \approx 4$ demonstrates very complicated crystallisation mechanisms (135). The term "very complicated crystallization mechanism" may be used to explain values of non-integer *n* greater than 4, where in the original Avrami model *n* is integer values of 1, 2, 3 and 4.

Table 5.3.1 – Showing the gradient and intercept of a graph of $T_{C,onset}$, $T_{C, peak}$ and $T_{C, end}$ vs log(cooling rate).

	Gradient	Intercept
$T_{C, onset}$	-12.332	171.44
$T_{C, peak}$	-14.934	163.2
$T_{C, end}$	-33.722	166.34

5.4 Discussion of the non-isothermal crystallisation kinetics of PA-12

The aim of this chapter was to evaluate the non-isothermal crystallisation and the non-isothermal crystallisation kinetics of PA-12. The non-isothermal crystallisation was considered because MJF is an industrial process and crystallisation of PA-12 is expected to be both isothermal and non-isothermal. This provides a greater understanding of the cooling mechanisms that are experienced in the powder bed.

Non-isothermal crystallisation of PA-12 was evaluated by observing the crystallisation behaviour of PA-12 at different cooling rates. The cooling rate had a significant influence on PA-12 in that as the cooling rate increased, the peak crystallisation temperature shifted to lower temperatures. For example, the peak crystallisation temperature at 5 and 40 ℃/min was 152.8 ℃ and 138.7 ℃, respectively. Additionally, the onset of crystallisation and the end crystallisation temperatures also shifted to lower temperatures. At lower cooling rates, the time taken to reach the end of crystallisation increased. This was due to the temperature dependence of crystallisation, where the sample has more time to crystallise allowing crystallisation to occur at higher temperatures.

A range of non-isothermal crystallisation models were selected to analyse the non-isothermal crystallisation kinetics of PA-12. These included the Jeziorny-modified Avrami model and the Caze model. The models were selected because they use different methods to obtain information on the non-

isothermal crystallisation kinetics. The Jeziorny-modified Avrami model was selected since it largely replicated the Avrami model and produced an Avrami exponent and rate constant. The Jeziorny-modified Avrami model produced large *n* values ranging from 4.42 to 7.68, suggesting 3D spherulitic growth. The average *n* was 6.03. The large *n* values were a result of non-isothermal crystallisation being a dynamic process. The rate constant was modified to account for the constant cooling rate. The Jezionry rate constant increased as the cooling rate increased indicating that non-isothermal crystallisation was quicker as the cooling rate increased.

The Caze model was used to determine the average Avrami exponent by plotting a graph of the onset crystallisation temperature, peak crystallisation temperature and end crystallisation temperature against the logarithm of the cooling rate. This model provided a quick way to determine an average Avrami parameter across a large range of cooling rates. An average Avrami exponent of 5.64 was obtained. This was similar to the average Avrami exponent obtained using the Jeziorny-modified Avrami model. However, the disadvantage with the Caze model is that it only provides information on the Avrami exponent and does not provide additional information on the rate constant. Overall, the Jeziorny-modified Avrami model provided a greater insight into the crystallisation kinetics of PA-12.

CHAPTER 6 – CHARACTERISATION OF POLYAMIDE-12 BLENDS

The aim of this work was to evaluate the effect of the FA, DA and their chemical constituents on the thermal properties and chemical properties of PA-12. Blends of PA-12 and FA, DA, CB, water, 2-PYR and 2-PYR/water were created. The thermal properties of the blends were evaluated and compared to PA-12. This allowed the effect of the FA, DA and their chemical constituents on the thermal and chemical properties of PA-12 to be studied. In MJF, the agents are jetted on to the surface of PA-12 during manufacture and penetrate the layer of PA-12. Therefore, the agents can influence the thermal properties of PA-12 by affecting the melting and recrystallisation behaviour by their interaction with PA-12.

The chemical properties were assessed using FTIR, where the spectra of the blends were compared to PA-12 by identifying the functional groups. FTIR was used to determine if the agents were present in the PA-12 powder blends and how the agents and their chemical constituents interacted with PA-12. Additionally, the DSC samples were extracted and assessed using FTIR.

The morphology of PA-12 and PA-12 blends was analysed using optical microscopy. This was used to determine how the agents and their chemical constituents affected the spherulite size of PA-12.

The use of DSC, FTIR and optical microscopy provided an understanding into what makes MJF unique in comparison to other AM techniques.

6.1 Visual inspection of PA-12 blends

The colour of PA-12 powder used in MJF is white, however it has been reported that the colour of components manufactured by MJF is grey/black. It is thought that the grey/black colour of the components is from the carbon black within the FA (58). The FA has been reported to contain ~ 5 % carbon black (75). In order to investigate the effect of the agents on the colour of PA-12, the blends

were visually examined and any changes in colour from the addition of the FA, DA, carbon black, water, 2-PYR and 2-PYR/water were reported.

In the PA-12/FA blends, the liquid FA was deposited onto PA-12 powder, following a similar procedure to MJF. The colour of the PA-12/FA blends is displayed in Figure 6.1.1. The addition of the FA had a significant effect on the colour of PA-12 powder. As the composition of FA increased, the colour of the powder changed from white to grey to black, this was due to the greater content of FA (and consequently carbon black) present within the blend. This shows that the darker colour of MJF components is a result of the addition of the FA. Since colour pigmentation increased as the content of FA increased, the colour of the powder or of a MJF component could indicate the composition of FA used within the build process.

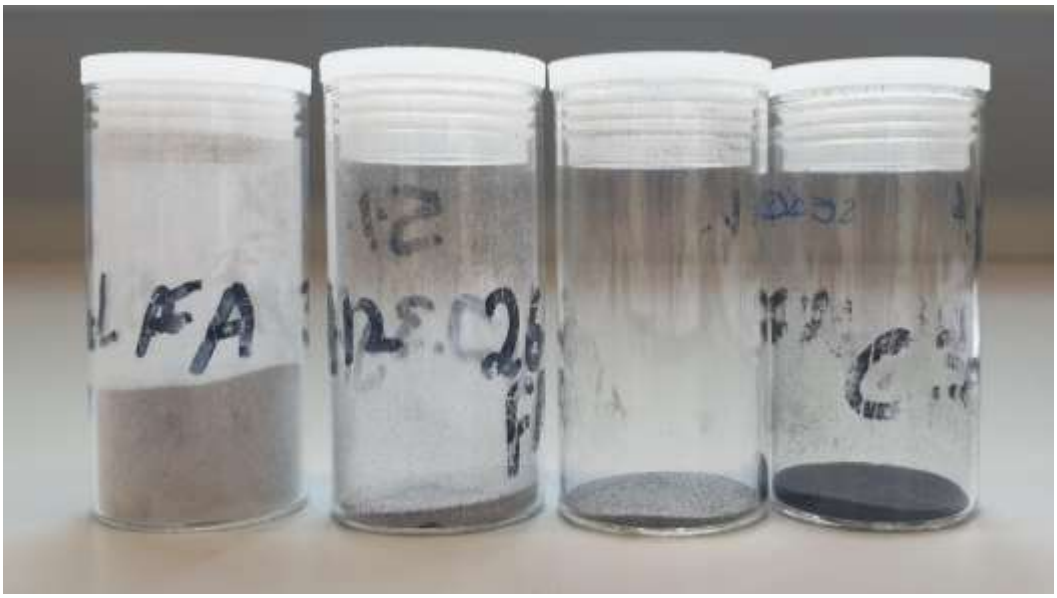

Figure 6.1.1: PA-12/FA blends (left to right) 1, 5, 10 and 20 wt.% FA.

In the PA-12/DA blends, the liquid DA was deposited onto PA-12 powder, following a similar procedure to MJF. The colour of the powder did not change with increasing composition of DA and all samples appeared white.

In the PA-12/water blends, water was deposited into PA-12 powder. The colour of the blends did not change with increasing content of water and the samples appeared white.

In the PA-12/CB blends, the carbon black was recovered from the FA and dispersed within the polymer matrix in the form of solid particles. The colour of the powder appeared white, while carbon black was visible within the blend as individual black particles. As the composition of carbon black increased, the quantity of black particles visible within the blend increased. This was due to the greater quantity of carbon black present within the sample.

In the PA-12/2-PYR blends, 2-PYR was added in accordance with the composition of 2-PYR in the FA and DA blends. The colour of the blend did not change with composition of 2-PYR and the samples appeared white.

In the PA-12/2PYR/water blends, 2-PYR and water was added in accordance with the quantity of 2-PYR and water found in the FA and DA. In the blends that were compositionally identical to the FA and DA, the colour of the blends did not change with increasing content of 2-PYR and water, and the powder samples appeared white.

Overall, the FA had a significant effect on the colour of PA-12 blends, where the FA coated the powder in a grey/black colour. In the PA-12/CB blends, the recovered carbon black did not change the colour

of the powder, however, was retained in the powder and was visible as independent black particles. Meanwhile, solvents such as a 2-PYR and water did not have an effect on the colour of PA-12. This was consistent with the colour of the PA-12/DA blend which does not contain carbon black.

6.2 Thermal characterisation of PA-12 blends using differential scanning calorimetry

The FA and the DA have a significant role in MJF, where the FA facilitates particle fusion in localised areas of the powder bed surface by absorbing IR radiation, and the DA provides an evaporative cooling effect to lower the temperature of the build material to prevent thermal bleeding (31). Despite having very different roles in the manufacturing process the FA and DA are largely made up of the same chemicals (75). A major difference between the agents is the quantity of each chemical present as well as the addition of carbon black in the FA. Both agents are jetted onto the powder bed surface during component fabrication and the PA-12, FA and DA are exposed to an IR lamp which heats the powder bed surface.

The aim of this work is to evaluate the effect of the FA and DA, and their constituent components on the thermal properties such as melting and recrystallisation of PA-12. This was achieved by creating blends of PA-12/FA and PA-12/DA at varying compositions of FA and DA. The FA and DA were deconstructed into their key components according to the HP Safety Data Sheet and additional blends were created, including PA-12/carbon black (CB), PA-12/water, PA-12/2-PYR and PA-12/2-PYR/water. Further details on the blend preparation can be found in Chapter 2.2. Herein, the melting and recrystallisation behaviour of heat 1 and cool 1 are discussed, unless otherwise stated.

6.2.1 Melting behaviour of polyamide-12 blends

The melting behaviour of PA-12 powder from batch 1 and batch 2 were similar, as shown in Chapter 3.1. However, the degree of crystallinity was greater in batch 1, when compared to batch 2. Since the PA-12/FA, PA-12/DA, PA-12/water and PA-12/CB blends were created from powder from batch 1, the melting behaviour of PA-12 (batch 1) was used as a basis for comparison to evaluate the effect of the agents on the thermal behaviour of PA-12. The same procedure was followed for the PA-12/2-PYR and PA-12/2-PYR/water blends, which were created from PA-12 powder (batch 2).

The blends were heated at a controlled rate of 10 ℃/min from 25 – 220 ℃, where they were stored at an upper isotherm of 220 ℃ for 5 minutes. The melting peak was evaluated from which the onset melting temperature, peak melting temperature, last trace of crystallinity, enthalpy of fusion and degree of crystallinity were recorded. This data is displayed in Table 6.2.2 and Figure 6.2.1.

In the PA-12/FA blends, the FA had a significant effect on the melting behaviour of PA-12, in that a depression T_g and peak melting temperature were observed with increasing composition of FA. The T_g of 1, 5, 10 and 20 wt.% FA blends were 43.2, 38.2, 35.6, and 34.4 ℃, respectively. The peak melting temperature of 1, 5, 10 and 20 wt.% FA blends were 185.5, 183.2, 179.8, 173.8 ℃, respectively. A peak melting temperature decrease of up to 13 ℃ was recorded, when compared to the peak melting temperature of PA-12 powder (T_M = 187 ℃). Furthermore, the onset melting temperature and last trace of crystallinity were affected by the presence of the FA and shifted to lower temperatures as the composition of the FA increased. This suggests the FA was acting as a plasticiser by shifting the T_g to lower temperatures and promoted melting of the crystalline regions. The presence of graphitic carbon in the FA has been shown to “promote higher heating of powders” that have been exposed to the FA due to the “sympathetic vibration of the carbon atoms that convert incident infrared emission into heat

energy" (58). Moreover, the enthalpy of fusion, and consequently degree of crystallinity, increased as the composition of the FA increased showing evidence of post-crystallisation.

The melting region was determined by calculating the difference between the last trace of crystallinity and the onset melting temperature of the blend. The FA had a significant effect on the melting region in that the melting region increased as the composition of the FA increased. The melting region for the 1, 5, 10 and 20 wt.% FA was 28.3, 29.7, 34.4 and 41.6 ℃, respectively. This was accompanied by a change in shape and position of the melting endotherm with the addition of FA, in that the endothermic melting peak became increasingly broad as the composition of the FA increased. Since the melting region increased and shifted to lower temperatures, the peak melting temperature also decreased. This suggests that the lamellar were less thermodynamically stable by the addition of the FA and this promoted melting of the crystalline phase. This demonstrated that the FA moderated the melting behaviour of the PA-12 powder.

On heat 2, a depression in peak melting temperature was also observed. This suggested that the components within the FA were retained within the polymer and permanently affected the melting behaviour of PA-12. Additionally, the melting behaviour displayed a double melting peak. This was due to melt-recrystallisation and reorganisation of polymer chains on heating (99).

In the PA-12/DA blends, the DA had a significant effect on the melting behaviour of PA-12, in that a depression in T_g and peak melting temperature were observed with increasing composition of the DA. The T_g of 1, 5, 10 and 20 wt.% DA blends were 48.4, 43.2, 41.1 and 38.5 ℃, respectively. The peak melting temperature of 1, 5, 10 and 20 wt.% DA blends were 187.3, 185.0, 182.5 and 179.0 ℃, respectively. The extent of the peak melting temperature depression observed in the PA-12/DA blends was less than the melting temperature depression observed in the PA-12/FA blends, where the peak melting temperature decreased by a maximum of 9 ℃ in the PA-12/DA blends. Moreover, the onset

melting temperature and last trace of crystallinity in the PA-12/DA blend also decreased with increasing composition of DA. Meanwhile, the enthalpy of fusion, and degree of crystallinity was comparable to PA-12. Additionally, the melting region increased as the composition of the DA increased. This demonstrated that the DA moderated the melting behaviour of the PA-12 powder.

On heat 2, a depression in peak melting temperature was also observed. This suggested that the components within the DA were retained within the polymer and permanently affected the melting behaviour of PA-12. Additionally, the melting behaviour displayed a double melting peak due to melt-recrystallisation and reorganisation of polymer chains on heating (99).

The FA and DA has a significant effect on the melting behaviour of PA-12. In order to quantify which chemical or chemicals within the FA and DA affected the melting behaviour of PA-12, the FA and DA were deconstructed into their key components and further blends were created.

Since the FA and DA are water-based dispersions containing a minimum of 70 % water, separate blends of PA-12/water were created in order to evaluate the effect of water on the melting behaviour of PA-12.

In the PA-12/water blends, the melting behaviour of PA-12 was unaffected by the addition of water and the T_g and peak melting temperature were comparable to PA-12. The T_g of the 1, 5, 10 and 20 wt.% water blends were 49.8, 51.3, 50.8 and 47.2 ℃. The peak melting temperature of the 1, 5, 10 and 20 wt.% water blends were of 187.0, 186.8, 186.3 and 186.3 ℃, respectively. The average T_g and peak melting temperature was 49.8 and 186.6 ℃. Moreover, the enthalpy of fusion and degree of crystallinity were comparable to PA-12.

In other work, the effect of water conditioning on PA-12 manufactured by SLS was examined, where PA-12 was immersed in water at high temperatures. The results indicated that the degree of crystallinity increased after water conditioning (138). However, this work indicated that the degree of crystallinity

was unaffected by the addition of water. The difference is due to the temperature conditions of PA-12 and water. In (138) conditioning took place at temperatures above the T_g of PA-12, where the mobility of polymer chains in the amorphous regions was enhanced. In this work, water was added to PA-12 in varying volumes and the samples were left to dry at room temperature for a total time period of 96 hrs. Due to the hygroscopic nature of PA, water can migrate into the amorphous regions and consequently affect the T_g. However, the T_g of the PA-12/water blends was unaffected. This shows that during the drying period, water had evaporated. Therefore, the addition of water did not affect the melting behaviour of PA-12 at ambient conditions.

On heat 2, the melting behaviour was comparable to PA-12 (heat 2). Additionally, the melting behaviour displayed a double melting peak due to melt-recrystallisation and reorganisation of polymer chains on heating (99).

In MJF, the time taken to process one layer of 80 μm powder thickness is 10.5 s, in which simultaneous fusion of PA-12 particles and evaporation of water takes place by the use of an IR lamp and elevated powder bed temperature (61,78). Therefore, in MJF components it can be expected that water is also not retained within the component since it is evaporated by the elevated temperature of the powder bed surface.

In the PA-12/CB blends, the melting behaviour was unaffected by the addition of carbon black and the T_g and peak melting temperature were comparable to PA-12. The T_g of the 1, 5, 10 and 20 wt.% CB blends was 48.2, 48.9, 46.7 and 47.5 ℃, respectively. The peak melting temperature of the 1, 5, 10 and 20 wt.% CB blends was 187.3, 187.7, 187.7 and 186.8 ℃, respectively. The blends showed an average T_g and peak melting temperature of 47.8 and 184.4 ℃. The enthalpy of fusion, and consequently degree of crystallinity, increased with composition of CB showing evidence of post-crystallisation.

On heat 2, the melting behaviour was comparable to PA-12 (heat 2) and the degree of crystallinity was unaffected by the addition of carbon black, such that it was comparable to PA-12 (heat 2). Additionally, the melting behaviour displayed a double melting peak due to melt-recrystallisation and reorganisation of polymer chains on heating (99).

In other studies which report the melting behaviour of PA-12 and carbon black components manufactured by SLS, carbon black and PA-12 in the form of a solid-solid powder dispersion also did not influence the melting behaviour of PA-12 powder, with respect to the peak melting temperature (41,139).

In PA-12/2-PYR blends, the 2-PYR had a significant impact on the melting behaviour of PA-12 powder in that a depression in T_g and peak melting temperature was observed with increasing content of 2-PYR. The T_g of the 0.10, 0.38, 0.50, 1.05, 1.97, 2.33, 4.07 and 8.72 wt.% 2-PYR blend was, 48.9, 51.3, 46.1, 39.8, 46.7, 45.6, 34.8 and 33.0 ℃, respectively. The peak melting temperature of the 0.10, 0.38, 0.50, 1.05, 1.97, 2.33, 4.07 and 8.72 wt.% 2-PYR blend was 185.8, 185.8, 185.3, 184.5, 185.7, 185.3, 181.8 and 176.3 ℃, respectively. Furthermore, the onset of melting and last trace of crystallinity also shifted to lower temperatures with increasing content of 2-PYR. The data in Table 6.2.2 shows that within the region of 0.10 – 2.33 wt.% 2-PYR, the overall decrease in the peak melting temperature was less pronounced. In these blends, the small volume of 2-PYR was insufficient to cause a change in melting behaviour of PA-12. This meant that the distribution of 2-PYR and its interaction with PA-12 was limited by the small content of 2-PYR present. On the contrary, a significant decrease in melting behaviour of the blends was observed when 2-PYR was present at compositions greater than 4.07 wt.% 2-PYR. The enthalpy of fusion and degree of crystallinity remained constant and were unaffected by the increasing content of 2-PYR. Additionally, melting region increased with composition of 2-PYR.

This data suggests the 2-PYR component (common to the FA and DA) was behaving as a plasticizer to lower the T_g and promoted the melting of the crystalline phase. Other models such as the Gordon-Taylor equation and Fox equation are used to predict the change in T_g in polymer blends. These models have been discounted since they are based on the T_g and weight fraction of more than one polymer component within the blend (140,141). The Kelly-Bueche equation incorporates the effect of plasticizers on the T_g of a polymer based on the plasticizer being completely miscible with the host polymer. Additionally, it is thought that the plasticizer and host polymer interact via weak Van Der Waal forces (142). Therefore, the Kelly-Bueche equation also cannot be used to model the T_g of the PA-12/2-PYR since it is based on weak intermolecular forces.

According to the HP Material Safety Data Sheet, the FA and DA contain 2-PYR in a fraction of 20 and 5 %, respectively. It has been reported that water may enhance the distribution of carbon black within the FA (75). Therefore, water may also enhance the distribution of solvents within the agents.

In the PA-12/2-PYR/water blends, the combined effect of 2-PYR and water on the melting behaviour of PA-12 was investigated. The blends were created according to the ratio of 2-PYR and water in the FA and DA. The HP Material Safety Data Sheet shows that the FA contained 70-80% water and 20% 2-PYR, while the DA contained 80-90% water and 5% 2-PYR. Despite the ratio of 2-PYR and water present in the FA and DA being different, the trends in melting behaviour were similar, in that a depression in T_g and peak melting temperature were observed.

In the PA-12/2-PYR/water blends where the content of 2-PYR and water was compositionally identical to that of the FA, the 2-PYR/water had a significant effect on the melting behaviour of PA-12, in that a depression in both the T_g and peak melting temperature were observed with increased content of 2-PYR. The blends containing 0.38, 1.97, 4.07 and 8.72 wt.% 2-PYR blends displayed a T_g of 48.9, 47.9, 38.9 and 35.0 ℃. The peak melting temperature of these blends were 187.8, 186.0, 183.2, 179.2 ℃,

respectively. The enthalpy of fusion and degree of crystallinity remained constant and was unaffected by the addition of 2-PYR and water.

In the PA-12/2-PYR/water blends where the content of 2-PYR and water was compositionally identical to that of the DA The T_g of the PA-12/2-PYR/water blends, the 2-PYR/water had a significant effect on the melting behaviour of PA-12, in that a depression in both the T_g and peak melting temperature were observed with increased content of 2-PYR. The blends containing 0.10, 0.50, 1.05 and 2.33 wt.% 2-PYR displayed a T_g of 49.2, 48.6, 47.5 and 47.2 ℃. The peak melting temperature of these blends were 189.0, 187.5, 186.0 and 186.0 ℃. The enthalpy of fusion and degree of crystallinity remained constant and was unaffected by the addition of 2-PYR and water.

Additionally, in both blends the melting region decreased with increasing composition of 2-PYR/water.

On heat 2, a depression in peak melting temperature was also observed. This suggested that the 2-PYR was retained within the polymer and permanently affected the melting behaviour of PA-12. Additionally, the melting behaviour displayed a double melting peak due to melt-recrystallisation and reorganisation of polymer chains on heating (99).

The melting behaviour of the PA-12/2-PYR/water blends displayed a systematic decrease in T_g and peak melting temperature, analogous to the PA-12/2-PYR blends. This showed that the 2-PYR behaved as a plasticizer by enhancing mobility in the amorphous phase and promoted melting of the crystalline phase.

It was clear that the melting properties of PA-12 were affected by the addition of the FA, DA, CB, water and 2-PYR due to the observable changes in the T_g and melting point. This suggests that the polymer chain can react with the components within the agents such as 2-PYR to influence the molecular weight of PA-12. These reactions would rely on the N-H and C=O group at the end of the polymer chains. An

increase in molecular weight will typically cause the T_g and melting temperature to increase due to restricted polymer chain mobility (168). Since the T_g and the melting temperature decreased with the addition of 2-PYR, it is unlikely that the molecular weight of the polymer chain increased. Furthermore, the blending was carried out at room temperature in the absence of a catalyst. The heating rate used in this experiment was 10 ℃/min, which is relatively quick to allow such reactions to occur. It is conceivable that these reactions would occur in the DSC. Although, if they were to occur this would be on a small scale and not detected by the DSC. Under these conditions where an increase in molecular weight is possible, polymer chain extension would occur in the amorphous regions and cause the T_g to increase but the melting point would remain unaffected (168). However, the PA-12 blends exhibit a decrease in T_g and melting point, when compared to the T_g and melting point of PA-12.

6.2.2 Crystallisation behaviour of polyamide-12 blends

The blends were cooled at a controlled rate of 10 ℃/min from 220 – 25 ℃. The crystallisation peak was evaluated from which the onset crystallisation temperature, peak crystallisation temperature, last trace of crystallinity, enthalpy of crystallisation and degree of crystallinity on cooling were recorded. This data is displayed in Table 6.2.3 and Figure 6.2.3.

In the PA-12/FA blends, the FA had a significant effect on the recrystallisation behaviour of PA-12 in that a decrease in the peak crystallisation temperature with increasing composition of FA was observed. In the 1 and 5 wt.% FA blends, the peak crystallisation temperature shifted to higher temperatures, compared to PA-12 powder. The peak crystallisation temperature of the 1 and 5 wt.% FA blend were 149.3 and 148.8 ℃; the peak crystallisation temperature of PA-12 was 147.8 ℃. Interestingly, in the 10 and 20 wt.% FA blend, the peak crystallisation temperature shifted to lower temperatures, compared to PA-12. The peak crystallisation temperature for the 10 and 20 wt.% FA blend were 147.01 and 141.80

℃. Moreover, the onset crystallisation temperature also followed the same trend. The enthalpy of crystallisation and degree of crystallinity on cooling increased as the content of FA increased.

In the PA-12/DA blends, the DA had a significant effect on the recrystallisation behaviour of PA-12 in that a decrease in the peak crystallisation temperature with increasing composition of DA was observed. In the 1, 5 and 10 wt.% DA blend, the peak crystallisation temperature was comparable to PA-12. The peak crystallisation temperature of the 1, 5 and 10 wt.% DA blends were 147.7, 149.0 and 147.5 ℃. Whereas the peak crystallisation temperature of the 20 wt.% DA blends shifted to a lower temperature, when compared to PA-12. The peak crystallisation temperature of the 20 wt.% DA blend was 144.8 ℃. The same pattern was observed for the onset crystallisation temperature. The enthalpy of crystallisation and the degree of crystallinity on cooling were unaffected by the addition of DA and were comparable to PA-12.

At first thought, the respective shift of peak crystallisation temperatures to higher temperatures in the 1 and 5 wt.% FA blend can be associated the carbon black within the FA acting as a nucleating agent (40). Whereas the shift in peak crystallisation temperature to lower temperatures in the 10 and 20 wt.% FA blend and in the DA blends suggest that a component within the agents delayed the onset of crystallisation. However, the melting behaviour must also be considered since the peak melting temperature was affected by the addition of the FA and DA. Therefore, the degree of supercooling was calculated in order to evaluate the effect of the agents on the crystallisation behaviour of PA-12. The degree of supercooling was determined by subtracting the peak crystallisation temperature from the peak melting temperature. In both blends, the degree of supercooling decreased as FA and DA content increased, suggesting that the FA and DA in fact facilitated crystallisation of PA-12.

The FA and DA were deconstructed into their key components and further blends of PA-12/water, PA-12/carbon black, PA-12/2-PYR and PA-12/2-PYR/water were created and their crystallisation behaviour was recorded.

In the PA-12/water blends, the recrystallisation behaviour was unaffected by the addition of water and was comparable to PA-12. The peak crystallisation temperature of the 1, 5, 10 and 20 wt.% water blends were 148.0, 149.0, 148.5 and 148.8 ℃, respectively. The onset crystallisation temperature was also unaffected by the addition of water. The average onset crystallisation temperature and peak crystallisation temperatures were 158.2 and 148.6 ℃. The enthalpy of crystallisation and degree of crystallinity on cooling were comparable to PA-12 and displayed no trend. This was due to water evaporating during the drying stage after the blends were created, leaving PA-12 in its original form.

In the PA-12/CB blends the recrystallisation behaviour was unaffected by the addition of carbon black and was comparable to PA-12. The peak crystallisation temperature for the 1, 5, 10 and 20 wt.% CB blends were 149.2, 148.2, 148.2 and 150.1 ℃, respectively. The onset crystallisation temperature was also unaffected by the addition of carbon black. The average onset crystallisation temperature and peak crystallisation temperatures of the blends were 157.5 and 148.8 ℃. The enthalpy of crystallisation and degree of crystallinity on cooling varied between samples displaying no trend but was comparable to PA-12.

A study by Athreya et al, compared the thermal properties of PA-12 and PA-12/CB (4 wt.% CB) extrusion-injection moulded and SLS fabricated components. In their work, the peak crystallisation temperature of the extrusion-injection moulded components shifted to higher temperatures than the SLS counterparts, suggesting CB behaved as a nucleating agent only in extrusion-injection moulded systems (40). This demonstrates that the processing technique used to create PA-12 and carbon black components influenced the thermal properties of the material. This could be due to the processing

technique influencing the interaction between carbon black and the polymer matrix, though this area of work in relation to MJF requires more investigation.

In the PA-12/2-PYR blends, the 2-PYR had a significant effect on the recrystallisation behaviour of PA-12 in that a decrease in the peak crystallisation temperature with increasing composition of 2-PYR was observed. The peak crystallisation temperature of the 0.10, 0.38, 0.50, 1.05, 1.97, 2.33, 4.07 and 8.72 wt.% 2-PYR blends were 149.2, 148.8, 148.7, 148.0, 149.0, 148.7, 146.0, 141.7 ℃, respectively. The onset crystallisation temperature also displayed the same trend. The largest decrease in crystallisation temperature was displayed in the 8.72 wt.% 2-PYR blend, where the peak crystallisation temperature decreased by 6.7 ℃, when compared to the peak crystallisation temperature of PA-12. The enthalpy of crystallisation and degree of crystallinity on cooling were unaffected by the addition of 2-PYR.

In the PA-12/2-PYR/water blends, the 2-PYR and/or water had a significant effect on the recrystallisation behaviour of PA-12 in that a decrease in the peak crystallisation temperature with increasing composition of 2-PYR and/or water was observed.

In the blends which were compositionally identical to the FA, the peak crystallisation temperature decreased as the composition of the 2-PYR increased. The peak crystallisation temperature of the 0.38, 1.97, 4.07 and 8.72 wt.% 2-PYR blends were 148.0, 146.8, 145.0 and 142.7 ℃, respectively. The onset crystallisation temperature also displayed the same trend.

In the blends which were compositionally identical to the DA, the peak crystallisation temperature decreased slightly, in comparison to PA-12. In the 0.10, 0.50, 1.05 and 2.33 wt.% 2-PYR blends were 148.5, 147.8, 147.7 and 147.7 ℃. The onset crystallisation temperature also displayed the same trend. The enthalpy of crystallisation and degree of crystallinity in both blends were unaffected.

In the PA-12/2-PYR/water blends, the systematic decrease in the onset crystallisation temperature and peak crystallisation temperature with increased composition of 2-PYR and/or water was analogous to

the PA-12/2-PYR blends, suggesting that that crystallisation behaviour was moderated by the addition of 2-PYR and not water.

As discussed, in the PA-12/FA and PA-12/DA blends the melting and recrystallisation behaviour were affected by the addition of FA and DA. This was also observed in the PA-12/2-PYR and PA-12/2-PYR/water blends, where both the melting and recrystallisation behaviour were affected by the addition of 2-PYR. In order to evaluate the effect of 2-PYR on the crystallisation behaviour of PA-12, the degree of supercooling was determined. The degree of supercooling decreased as the composition of 2-PYR increased, suggesting that 2-PYR facilitated crystallisation. Therefore, in the PA-12/FA and PA-12/DA blend, the recrystallisation behaviour was moderated by the 2-PYR (common to both the FA and DA).

Studies have reported that in addition to 2-PYR, water is a major constituent of the FA and DA. It has been reported that water is present in 65% and 83 % and 2-PYR is present in 18.7% and 3.7 % in the FA and DA, respectively (17). Furthermore, other studies show that water and 2-PYR interact via hydrogen bonding. This interaction arises from the NH and C=O groups that are present in 2-PYR which act as a proton donor and acceptor groups, respectively (31–33). Despite the potential for an interaction between water and 2-PYR, the thermal behaviour of the PA-12/2-PYR/water blends was comparable to the PA-12/2-PYR blends, indicating that the effect of 2-PYR in PA-12 was not moderated by the addition of water.

Overall, the melting and recrystallisation behaviour of PA-12 was affected by the addition of the FA and DA. This was due to the presence of 2-PYR and carbon black. In which, the 2-PYR acted as a plasticizer to shift the T_g to lower temperatures and promote melting of the crystalline phase. While carbon black increased the degree of crystallinity. Additionally, in the PA-12/FA and PA-12/DA blend, the melting behaviour on heat 2 was affected by the addition of the FA and DA, where the peak melting

temperature decreased with increasing content of FA and DA. This was also observed in the PA-12/2-PYR and PA-12/2-PYR/water blend. This suggests that 2-PYR was retained within the polymer matrix.

The changes in melting and recrystallisation behaviour were a result of the interaction between PA-12 and 2-PYR, where the N-H and C=O moieties, present in both materials, interact via hydrogen bonding. Trends owed to hydrogen bonding have been established in other PA-12 blends. S. Li et al evaluated the thermal behaviour of semi-crystalline nanostructured PA-12/polyketone (PK) blends (143). The thermal behaviour of PA-12/PK were analysed on cool 1 and heat 2. The crystallisation behaviour showed that the peak crystallisation temperature of PA-12 was affected by the addition of PK. At low concentrations of PK, the domains of PK may have acted as nucleation sites to increase crystallisation temperature by the hydrogen bond interactions between PA-12/PK (established using FTIR). On heat 2, the melting temperature of the blends were systematically lower than the homopolymer counterparts, showing a change in lamellar thickness causing crystals to become thermodynamically less sTable due to hydrogen bond interactions (143). Therefore, this suggests that the melting and recrystallisation behaviour of PA-12 was moderated by hydrogen bonding between PA-12 and 2-PYR.

In conclusion, the PA-12/FA blend displayed similar trends in thermal behaviour to the PA-12/DA blend. It was shown that water did not hydrolyse PA-12 and had evaporated under these sample preparation methods, this is also agrees with (78) where water has been reported to evaporate in MJF. Additionally, recovered carbon black did not cause changes in melting and recrystallisation temperatures but influenced the degree of crystallinity of PA-12. Meanwhile, 2-PYR had a significant effect on the melting and recrystallisation behaviour of PA-12. Therefore, the carbon black present within the FA and organic solvents within both the FA and DA contributed to the trends observed.

6.2.3 Processing window and stable sintering region (SSR) of polyamide-12 and polyamide-12 blends

The melting and recrystallisation behaviour of PA-12 was affected by the FA, DA and 2-PYR, as described in Chapter 6.2.1 and 6.2.2. Consequently, the processing window and stable sintering region (SSR) were also affected since they are determined by the thermal behaviour of PA-12.

The processing window is a metastable thermodynamic region that the powder bed surface must be kept within in order to delay crystallisation and is determined by subtracting the onset melting temperature from the onset crystallisation temperature (71). The SSR shows the temperature range in which particle fusion can occur without degradation (144). To determine the SSR, the temperature defining the last trace of crystallinity and 1 % mass loss are required. These are obtained using DSC and TGA (23).

The processing window for PA-12, PA-12/FA, PA-12/DA and PA-12/2-PYR blends is displayed in Table 6.2.1. The PA-12/FA, PA-12/DA and PA-12/2-PYR were chosen since it was shown in Chapter 6.2.1 and 6.2.2 that the thermal behaviour of PA-12 was affected by the addition of the FA, DA and 2-PYR. In the PA-12/FA blend, the processing window was comparable to PA-12, up to a composition of 5 wt.% FA. However, in the 10 and 20 wt.% FA blend, the processing window was negative. This is because of the onset melting temperature overlapping with the onset crystallisation temperature.

In the PA-12/DA blends, a similar trend was observed, where the processing window decreased with increasing composition of DA. At a composition of 20 wt.% DA the processing window was negative.

In the PA-12/2-PYR blends, the processing window decreased with increasing composition of 2-PYR.

Often, a large processing window is favoured to compensate for temperature fluctuations on the powder bed surface (23). This information suggests that in MJF, a lower composition of FA should be used to provide a greater processing window and allow greater control of crystallisation.

Figure 6.2.1 shows the SSR for PA-12, where the SSR for PA-12 was 127.83 ℃. The addition of the FA will cause the SSR to increase if the TGA data was to remain constant in the PA-12/FA blend, since the last trace of crystallinity of PA-12 decreased with the addition of FA. This would suggest that the temperature range in which particle fusion can occur without degradation is greater. However, this data is limited in that the TGA is not representative of a PA-12/FA blend. In order to make an accurate determination of the SSR for the PA-12/FA blend, the TGA data should be from a sample within the PA-12/FA blend. This is because data showed that the FA had a significant effect on the melting behaviour of PA-12. However, this provides an example of the SSR is affected by the melting temperature of a sample.

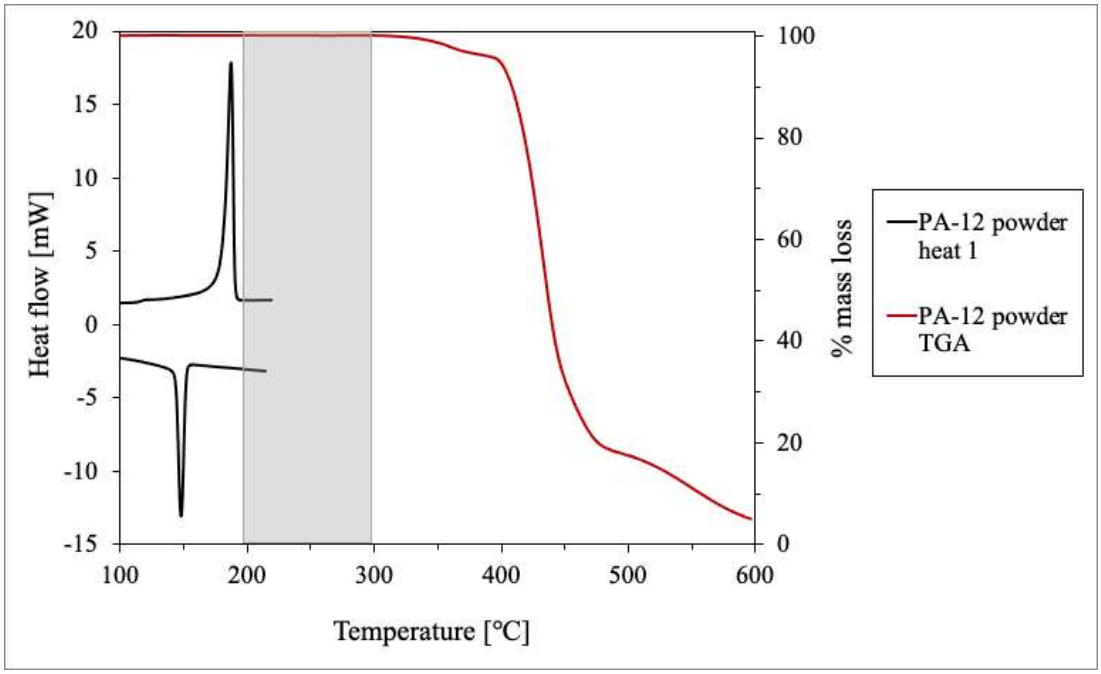

Figure 6.2.1 – The SSR of PA-12 powder, demonstrated by the grey box. DSC data recorded as endo up.

Table 6.2.1 – The processing window for PA-12, PA-12/FA, PA-12/DA and PA-12/2-PYR blends. Where T_M - Peak Melting Temperature and T_C – Peak Crystallisation temperature.

Sample	T_M [°C]	T_C [°C]	Processing window [°C]
PA-12	162.67	155.83	6.84
1 wt.% FA	164.69	157.73	6.96
5 wt.% FA	162.11	155.36	6.75
10 wt.% FA	151.83	153.76	-1.93
20 wt.% FA	139.89	147.61	-7.72
1 wt.% DA	172.10	155.19	16.91
5 wt.% DA	167.43	157.17	10.26
10 wt.% DA	161.02	156.53	4.49
20 wt.% DA	147.76	152.01	-4.25
0.10 wt.% 2-PYR	168.03	155.35	12.68
0.38 wt.% 2-PYR	164.00	156.47	7.53
0.50 wt.% 2-PYR	167.09	155.75	11.34
1.05 wt.% 2-PYR	166.55	154.81	11.74
1.97 wt.% 2-PYR	167.76	155.49	12.27
2.33 wt.% 2-PYR	168.03	154.95	13.08
4.07 wt.% 2-PYR	155.35	152.10	3.25
8.72 wt.% 2-PYR	152.79	147.79	5.00

Table 6.2.2 – The melting behaviour of PA-12 blends on heat 1 and heat 2 using a heating rate of 10 ℃/min (continued on the next page). Where T_M - Peak Melting Temperature, T_E - Last Trace of Melting, T_O - Onset of Melting, X_c – Degree of Crystallinity and ΔH is the heat of fusion.

Blend	wt.%	Heat 1					Heat 2				
		T_M (℃)	T_O (℃)	T_E (℃)	ΔH (Jg^{-1})	X_c (%)	T_M ((℃)	T_O (℃)	T_E (℃)	ΔH (Jg^{-1})	X_c (%)
FA	1.00	185.5	164.7	193.0	103.6	49.5	176.8	156.7	183.3	46.7	22.3
	5.00	183.2	162.1	191.8	108.3	51.7	174.8	153.6	181.5	51.7	24.7
	10.00	179.8	151.8	186.2	117.9	56.3	172.2	146.6	179.6	55.1	26.3
	20.00	173.8	139.9	181.5	121.9	58.2	166.5	139.5	173.8	60.5	28.9
DA	1.00	187.3	172.1	193.8	105.4	50.4	177.8	156.5	184.2	44.7	21.4
	5.00	185.0	167.4	192.3	109.3	52.2	177.2	156.6	183.9	43.3	20.7
	10.00	182.5	161.0	190.2	117.9	56.4	177.0	156.7	183.3	44.5	21.3
	20.00	179.0	147.8	189.0	129.8	62.0	176.7	155.2	183.9	47.3	22.6
CB	1.00	187.3	166.4	197.1	111.2	53.1	177.8	156.5	184.2	44.7	21.4
	5.00	187.7	165.7	196.0	116.1	55.5	177.2	156.6	183.9	43.3	20.7
	10.00	187.7	165.1	198.2	120.1	57.4	177.0	156.7	183.3	44.5	21.3
	20.00	187.3	164.1	195.8	132.2	63.2	176.7	155.2	183.9	47.3	22.6

Water	1.00	187.0	170.2	192.0	108.2	51.7	177.0	157.1	183.7	39.0	18.6
	5.00	186.8	170.4	192.9	111.5	53.3	177.8	157.8	184.2	47.5	22.7
	10.00	186.3	168.8	191.9	109.4	52.3	177.3	158.4	183.4	47.9	22.9
	20.00	186.3	172.4	192.8	95.1	45.4	177.3	160.3	184.9	41.6	19.9
2-PYR (FA)	0.38	185.83	164.0	192.85	109.0	52.1	177.00	162.9	183.41	44.6	21.3
	1.97	185.67	167.8	191.00	107.1	51.2	177.17	163.5	181.80	46.8	22.4
	4.07	181.83	155.4	187.20	109.3	52.2	173.67	157.7	179.23	49.3	23.5
	8.72	176.33	152.8	181.48	108.1	51.6	169.33	152.3	174.17	52.3	25.0
2-PYR (DA)	0.10	185.83	168.0	191.24	103.7	49.5	177.33	164.8	181.31	46.4	22.2
	0.50	185.33	167.1	190.83	101.5	48.5	176.83	163.1	180.85	44.8	21.4
	1.05	184.50	166.6	189.77	102.5	49.0	176.00	162.8	180.33	47.4	22.6
	2.33	185.33	168.0	191.11	104.9	50.2	177.17	163.3	181.18	48.1	23.0

Table 6.2.3 – The crystallisation behaviour of PA-12 blends on cool 1 using a cooling rate of 10 ℃/min (continued on the next page). Where T_P - Peak Crystallisation Temperature, T_O - Onset Crystallisation Temperature, T_E - End Crystallisation Temperature, ΔH - Heat of Crystallisation, X_C - Degree of Crystallinity.

Additive	wt.%	Cool 1				
		T_P (℃)	T_O (℃)	T_E (℃)	ΔH (Jg^{-1})	X_c (%)
PA-12		148.3	155.8	136.4	60.5	28.9
FA	1.00	149.3	157.7	138.9	55.1	27.4
	5.00	148.8	155.4	138.9	59.5	28.4
	10.00	147.0	153.8	136.5	61.2	29.3
	20.00	141.8	147.6	129.3	66.3	31.7
DA	1.00	147.7	155.2	139.1	53.5	25.6
	5.00	149.0	157.2	136.6	56.9	27.2
	10.00	147.5	156.5	136.8	58.9	28.2
	20.00	144.8	152.0	134.1	58.4	27.9
CB	1.00	149.2	158.9	135.8	52.7	26.3
	5.00	148.2	157.4	138.8	52.2	25.0

	10.00	148.2	157.6	136.6	53.5	25.6
	20.00	148.3	157.2	137.7	57.0	27.2
Water	1.00	148.0	156.3	139.9	45.7	21.8
	5.00	149.0	156.4	139.5	55.9	26.7
	10.00	148.7	156.1	141.5	56.5	27.0
	20.00	148.8	157.4	139.0	49.7	23.7
2-PYR	0.10	149.2	155.4	140.5	57.0	27.2
	0.38	148.8	156.5	141.7	56.1	26.8
	0.50	148.7	155.8	140.4	55.6	26.5
	1.05	148.0	154.8	139.6	57.1	27.3
	1.97	149.0	155.5	141.5	58.1	27.7
	2.33	148.7	155.0	140.7	58.3	27.9
	4.07	146.0	152.1	138.8	59.5	28.4
	8.72	141.7	147.8	131.5	61.1	29.2
FA (2-PYR + Water)	0.38	148.0	155.9	139.4	48.7	23.3
	1.97	146.8	155.9	138.5	49.3	23.6
	4.07	145.0	152.9	135.5	51.6	24.6
	8.72	142.7	150.4	133.8	53.7	25.6
DA (2-PYR + Water)	0.10	148.5	156.2	139.6	49.5	23.7
	0.50	147.8	155.1	140.8	48.5	23.2

1.05	147.7	155.3	140.6	47.4	22.6
2.33	147.7	154.8	139.4	49.3	23.6

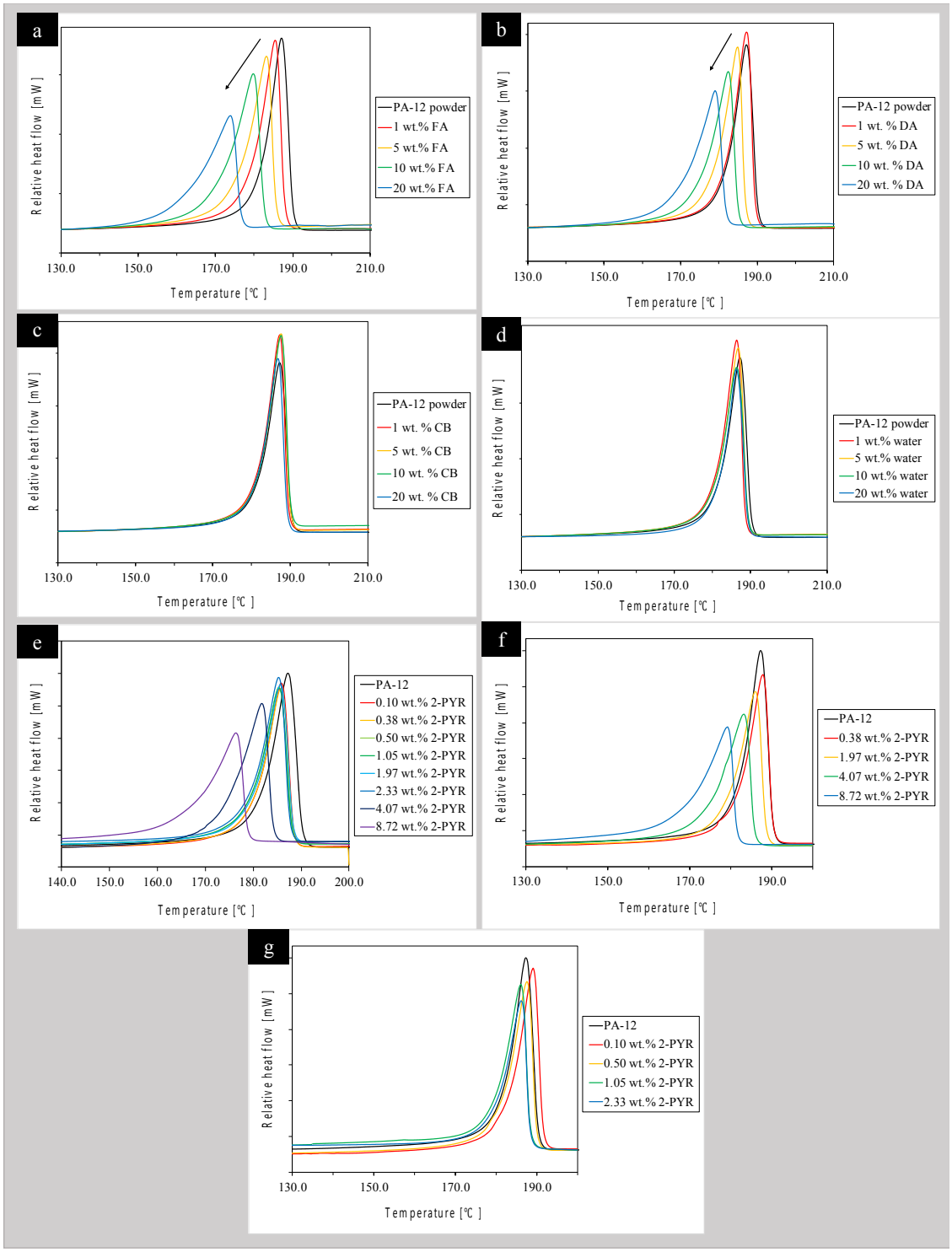

Figure 6.2.2 – The melting behaviour of PA-12 blends on heat 1, a) PA-12/FA, b) PA-12/DA, c) PA-12/CB, d) PA-12/water, e) PA-12/2-PYR, f) PA-12/2-PYR/water (FA) and g) PA-12/2-PYR/water (DA).

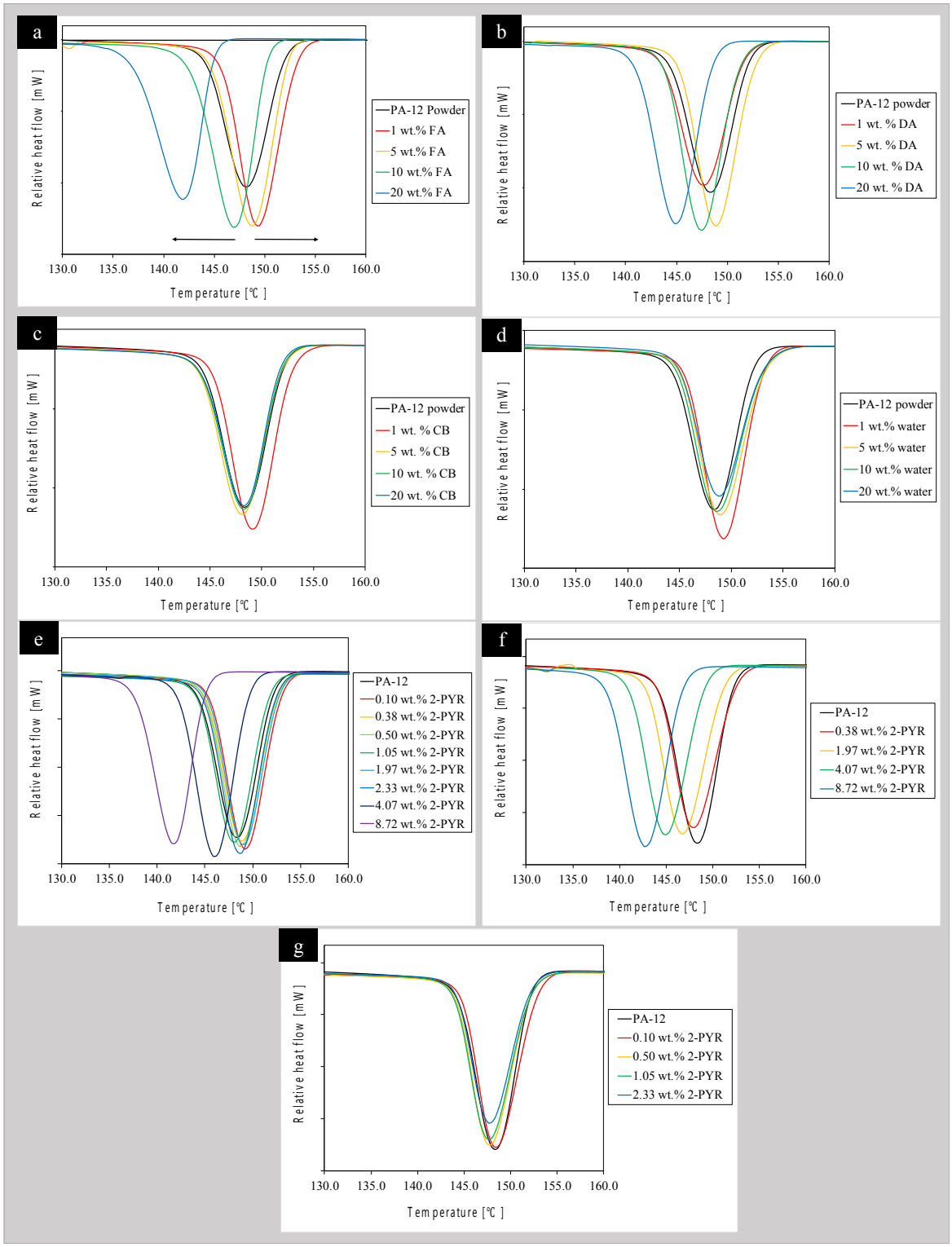

Figure 6.2.3 – The recrystallisation behaviour of PA-12 blends on cool 1, a) PA-12/FA, b) PA-12/DA, c) PA-12/CB, d) PA-12/water, e) PA-12/2-PYR, f) PA-12/2-PYR/water. and g) PA-12/2-PYR/water (DA).

6.3 FTIR of PA-12 powder blends

The FTIR spectra of PA-12 powder blends and blend samples that had been extracted from DSC pans were recorded and compared to PA-12. The samples that were extracted from DSC pans were subjected to a heat-cool-heat-cool cycle using a heating rate and cooling rate of 10 ℃/min during DSC analysis.

The aim of this work was to characterise PA-12 blends and observe the effect of agents and additives on the chemical structure of PA-12. This was achieved by comparing the spectra of the blends to virgin PA-12. The agents and additives include the FA, DA, carbon black, water, 2-PYR and 2-PYR/water.

6.3.1 Characterisation of PA-12 blends using FTIR

The peak wavenumber for characteristic peaks is shown in Figure 6.3.1. The data in Table 6.3.1 is comparable to PA-12 powder (see chapter 3.3) and FTIR data reported by H.J O'Conner et al for a PA-12 part manufactured by MJF (61,68).

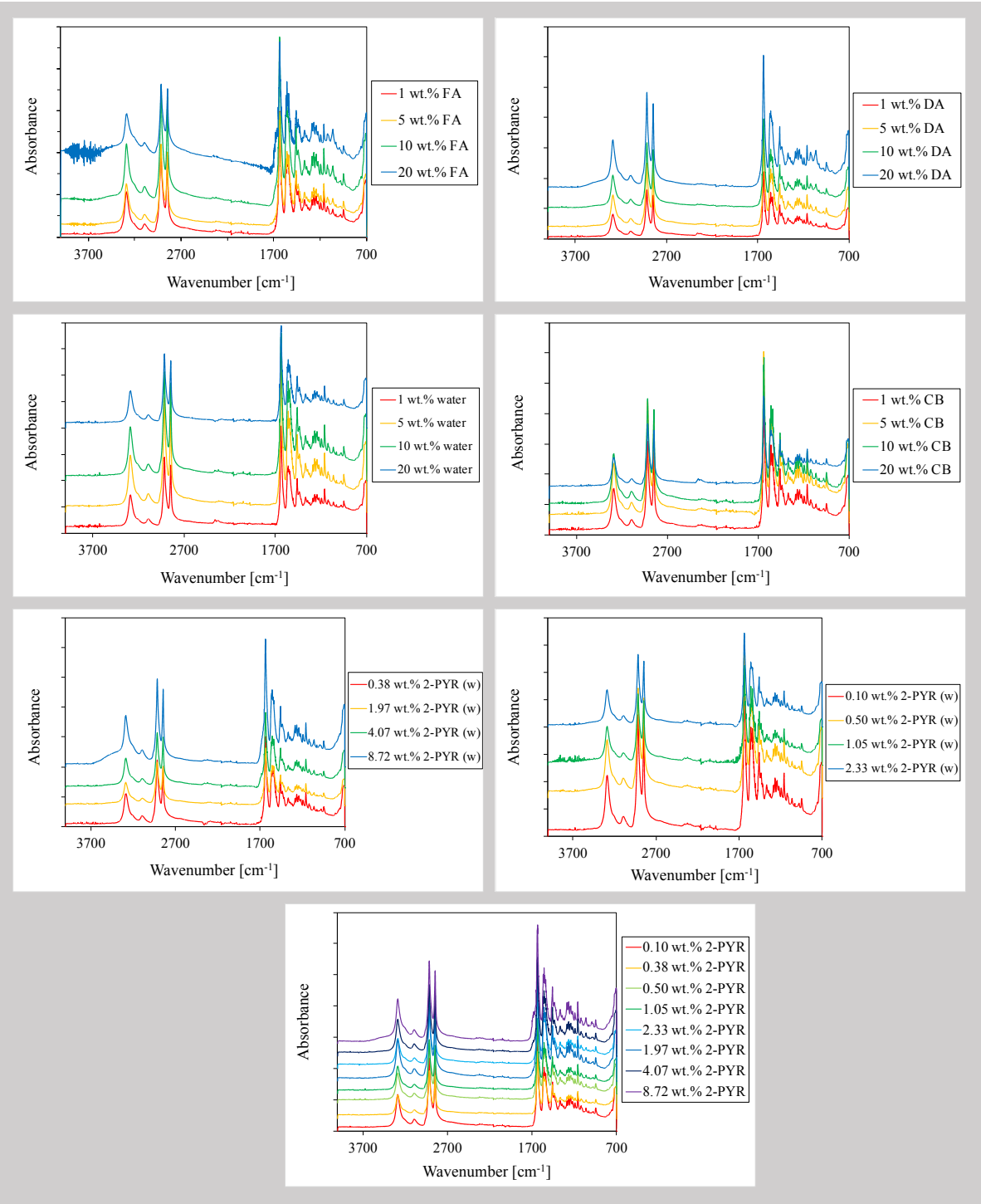

Figure 6.3.1: FTIR spectra of PA-12/FA, PA-12/DA, PA-12/2-PYR and PA-12/2-PYR/water powder blends at varying compositions of FA, DA, 2-PYR and water. All recorded spectra were normalised to the same baseline. All recorded spectra were overlaid to produce the graphs as shown. Where FA is the Fusing Agent, DA is the Detailing Agent, CB is carbon black, 2-PYR is 2-pyrrolidone and 2-PYR (w) is 2-pyrrolidone and water.

Figure 6.3.1 shows the FTIR spectra of PA-12 powder blends. The addition of the FA, DA, carbon black, 2-PYR and water did not have a significant influence on the spectra in that new strong peaks were not observed. On closer examination, slight differences were observed and these are discussed below.

In the PA-12/FA blends, the absorbance in the region of 3500 – 4000 cm^{-1} increased dramatically in the 20 wt.% FA blend, when compared to the 1, 5 and 10 wt.% FA blend. This could be a result of the colour of PA-12 powder after the addition of the FA. In the PA-12/FA blends, the orginally white PA-12 powder had been dyed black by the carbon black present within the FA (this was discussed in Chapter 6.1). The pigmentation of the powder in the 20 wt.% FA blend was much darker in comparison to the 1, 5, and 10 wt.% FA blend, this was due to the greater content of carbon black present and was associated with the greater content of FA used to create the blend. Therefore, the increase in absorbance in the region of 3500 – 4000 cm^{-1} can be due carbon black. In a study by Galati et al, the spectra of the FA and DA were recorded. The spectra of the FA showed a higher absorbance, this was associated with the graphitic carbon black present within the FA. This was due to carbon black promoting a "higher heating of powders" due to the "sympathetic vibration of carbon atoms that converts incident IR emission into heat energy" (58). Meanwhile, Jiang et al characterised poly(ethylene terephthalate) and carbon black blends produced using pristine carbon black and surface modified carbon black (145). The FTIR spectrum of pristine carbon black was recorded and distinguished peaks in the region of 3500 – 4000 cm^{-1} were displayed. The peaks were more distinguished than that shown in the FTIR spectrum of 20 wt.% FA blend. Since the peaks in the 20 wt.% FA blend were not defined, this suggests that the addition of carbon black did not specifically produce peaks in 3500 – 4000 cm^{-1} and that the change in absorbance was due to the addition of carbon black.

This being said, Figure 6.3.1 showed that the blends 1.05 wt.% 2-PYR (w), 5 wt.% FA and the 1 wt.% CB also exhibited similar spectral features between 3500 – 4000 cm^{-1}, in that the absorbance fluctuated and changed. However, the abosorbance was not as high in comparison to the 20 wt.% FA blend.

Therefore, the features between 3500 – 4000 cm^{-1} can also be attributed to a poor baseline. It is likely that this is due to poor signal quality which arises from poor contact between the powder sample and the crystal. Consequently, the penetration depth of the beam into the sample is reduced by the rough surface of the sample and leads to a reduced contact area. M. Galati et al linked a low transmittance and peak resolution in the spectra of MJF components to imperfect contact between the sample and crystal. This was due to the rough surface of a MJF component (58).

For this reason, the absorbance between 3500 – 4000 cm^{-1} in the 20 wt.% FA blend can be a result of a number of factors; i) Imperfect contact between the sample and the cystal and ii) The presence of carbon black intensifying the signal and iii) A poor baseline within in the region of 3500 – 4000 cm^{-1}. This agrees with the fact that other spectra showed similar features.

In order to improve the contact between the sample and the crystal, the screw can be set to a higher force. Additionally, this will improve the penetration depth of the beam into the sample. The penetration depth also depends on factors such as the wavelength, refractive indices of the crystal and sample, as well as the angle of the incident beam (167).

To explore the idea that carbon black readily absorbs IR radiation, the uncorrected spectra of the PA-12/FA and PA-12/CB blends were overlaid (see Figure 6.3.2). In the PA-12/FA blends, it was clear that the absorbance was modified by the addition of the FA to PA-12, where the abosrbance of the spectra systematically increased with increasing composition of the FA. The FTIR spectra of the FA and DA in their liquid form was recorded by M. Galati et al. The spectra of the FA and DA were identical, however the FA spectrum had shifted to a lower transmittance when compared to the spectum of the DA. This was due to the presence of graphitic carbon within the FA, which makes the FA appear black in colour.

In their work, the carbon within the FA justified the higher abosorbance of the FA, when compared to the DA, since the role of the FA is to convert incident IR radiation into heat energy (58). Therefore, in the PA-12/FA blends the systematic increase in absorbance with FA is due to the increased content of carbon black within the FA. This showed that the carbon black within the FA had a significant effect on the absorbance of PA-12, where the presence of carbon black increased the aborption of IR radiation. This is consistent with the action of a RAM (146). Additionally, this observation was justified by the grey/black appearance of the PA-12/FA blends.

Figure 6.3.2 shows the uncorrected spectra of the PA-12/CB blends. In the PA-12/CB blends, the carbon black did not have a significant influence on the absorbance, in that the absorbance of the spectra did not significantly increase with increased content of carbon black. Though, in the 20 wt.% CB blend a slight increase in absorbance was observed. However, this was insignificant in comparison to the increase in absorbance exhibited by the PA-12/FA blends.

Although carbon black was in the PA-12/FA and PA-12/CB blends, the absorbance was greater in the PA-12/FA blends. This difference is due to the interaction between carbon black and PA-12. In the PA-12/FA blends, the carbon black was dispersed as an ink over PA-12 powder and caused the colour of the powder to change from white to black. Whereas, in the PA-12/CB blends the carbon black was in the form of solid black particles that were dispersed within the white PA-12 powder. This shows that the interaction between the carbon black and PA-12 influenced the FTIR spectra of PA-12 and suggests that the interaction was enahnced when the carbon black was present as an ink within the FA and caused the aborbance to be greater. This is a beneficial feature of the FA in MJF, since the FA is deposited in localised areas on the powder bed promote melting and facilitate adhesion of polymer particles.

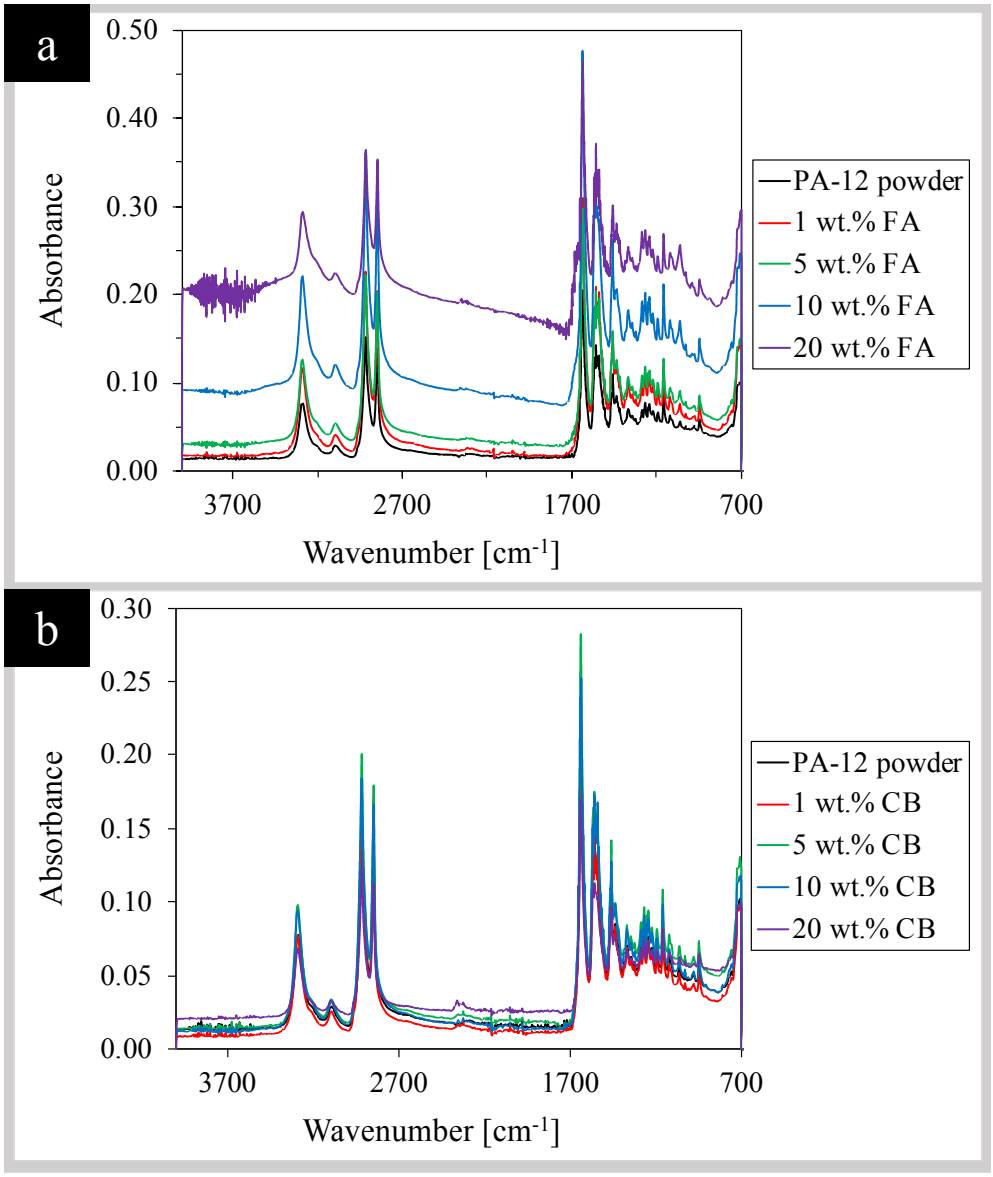

Figure 6.3.2: FTIR spectra of the PA-12/FA and PA-12/CB powder blends, where the data has not been corrected, where FA is the Fusing Agent and CB is carbon black.

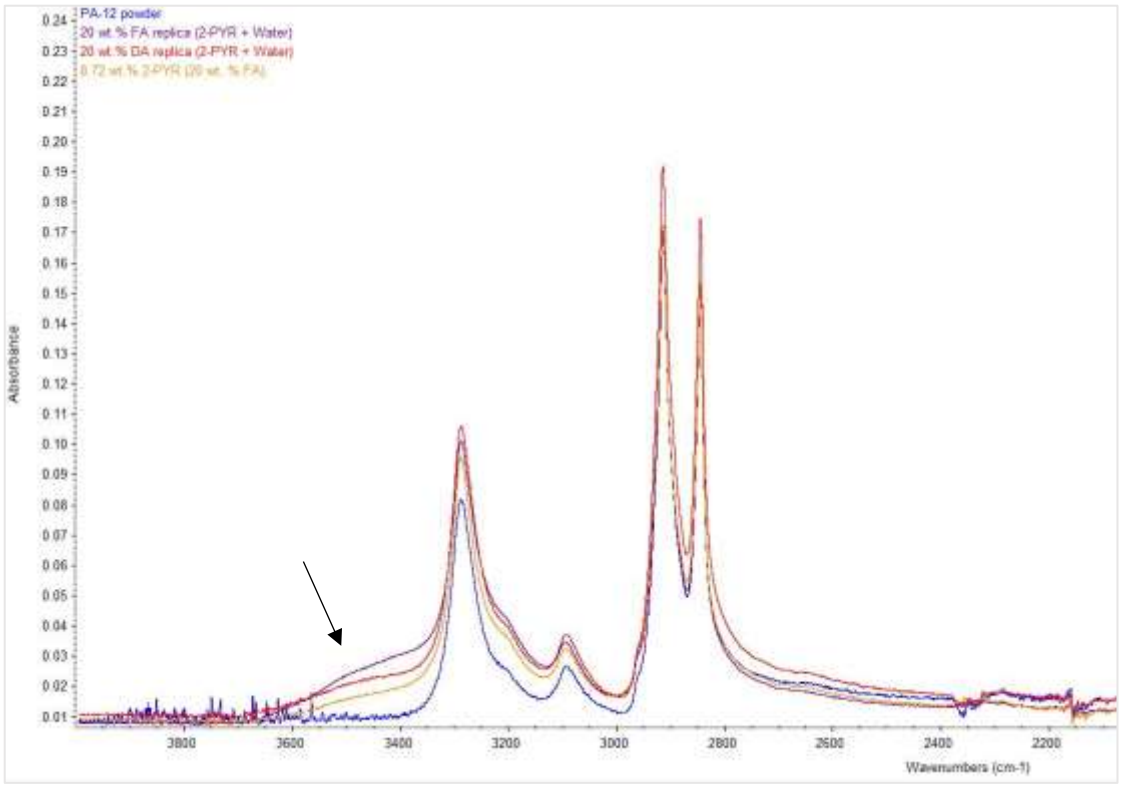

Figure 6.3.3: FTIR spectra of PA-12 and selected PA-12 powder blends between 2200 – 4000 cm^{-1}, where FA is the Fusing Agent, DA is the Detailing Agent and 2-PYR is 2-pyrrolidone. The arrow illustrates the free N-H stretch.

In the PA-12/2-PYR and PA-12/2-PYR/water blend containing 8.72 wt.% 2-PYR, a broad shoulder peak between 3550 – 3600 cm^{-1} was observed off the N-H stretch, this is illustrated by the arrow in Figure 6.3.3. This was assigned to free N-H stretch, Schroeder and Skrovanek had also assigned peaks at 3440 cm^{-1} and 3444 cm^{-1} in polyamide to the free N-H stretch, respectively (95,105). Interestingly, this was not observed in the spectrum of PA-12 powder, therefore this was due to the presence of 2-PYR within the blend. Moreover, this peak was also observed in the PA-12/FA and PA-12/DA blends (10 and 20 wt.% FA; 20 wt.% DA). This is unsurprising since 2-PYR was present in the FA and DA.

The molecular structure of 2-PYR is similar to PA-12 in that 2-PYR also contains N-H and C=O moieties. Therefore, 2-PYR can experience self-associative hydrogen bonding between N-H and C=O (147). Yet, it is possible that hydrogen bonding can occur between the N-H and C=O moieties between PA-12 and 2-PYR due to the similarities in the functional groups of PA-12 and 2-PYR. As such, this can leave free N-H moieties that are not hydrogen bonded. This suggests that the free N-H stretch is associated to the non-hydrogen bonded N-H moieties on both PA-12 and 2-PYR.

The FTIR spectra of samples that had been extracted from DSC pans after being subjected to a heat-cool-heat-cool cycle using a heating and cooling rate of 10 ℃/min between 25 – 220 ℃ were recorded.

The FTIR spectra of the blends are shown in Figure 6.3.4. The peak wavenumber for characteristic peaks is shown in Table 6.3.2. The data in Table 6.3.2 is comparable to PA-12 powder (see chapter 3.3) and FTIR data reported by O'Conner et al for a PA-12 part manufactured by MJF (61,68). This shows that the spectra of powder blends and blends extracted from DSC pans were similar.

Figure 6.3.4 shows the FTIR spectra of PA-12 powder blends. The addition of the FA, DA, carbon black, 2-PYR and water did not appear to have a significant influence on the spectra after a heat-cool-heat-cool cycle between 25 – 220 ℃. Moreover, the composition did not have a significant influence on the spectra. On closer examination, slight differences were observed and these are discussed below.

Figure 6.3.5 shows the FTIR spectra of selected blends between 1590 – 1750 cm^{-1}. A strong peak at ~1634 cm^{-1} was observed, this was assigned to the C=O stretch. On closer examination of this region, a small and wide peak at ~1690 cm^{-1} was observed. The peak at ~1690 cm^{-1} increased with 2-PYR composition, illustrated by the upwards arrow in Figure 6.3.5. In another study, the FTIR spectrum of 2-PYR in CCl_4 solution was recorded. A strong narrow band at 1699 cm^{-1} was observed and was

assigned to the amide-I band (C=O stretch) of 2-PYR (148). Therefore, the peak at ~1690 cm^{-1} was assigned to the amide-I band (C=O stretch) of 2-PYR. This data suggests that 2-PYR was retained in the polymer post-DSC thermal analysis. Further investigation showed that this peak was also present in the powder blends, suggesting that 2-PYR was retained from the powder blend to the DSC sample. Though, the appearance of this peak in the powder blends was distorted due to the poor contact between the powder and the crystal. The physical properties of 2-PYR show that the boiling point of 2-PYR is 251 ℃. Since the DSC samples were prepared by heating the polymer up to a maximum temperature of 220℃, it is unsurprising that 2-PYR was retained in the polymer since the boiling point of 2-PYR was not surpassed. In MJF, the temperature during the printing process does not exceed 185 ℃, therefore it is expected that 2-PYR will also be retained in refreshed powder where some of the DA has been applied in previous builds and in the final parts as a result of the FA and DA (91).

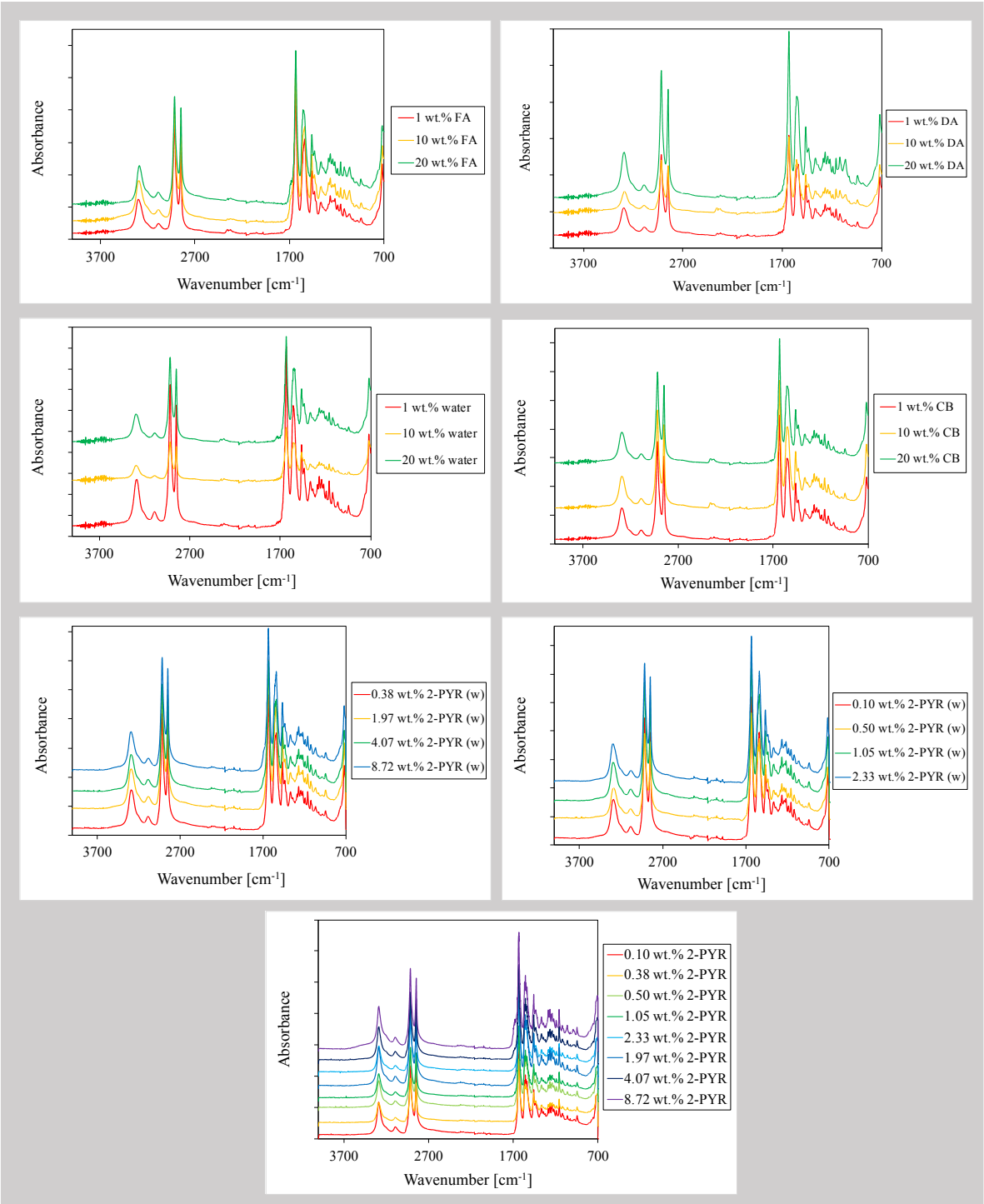

Figure 6.3.4: FTIR spectra of PA-12, PA-12/FA, PA-12/DA, PA-12/2-PYR and PA-12/2-PYR/water DSC blends at varying compositions of FA, DA, 2-PYR and water. All recorded spectra were overlaid to produce the graphs as shown. Where FA is the Fusing Agent, DA is the Detailing Agent, CB is carbon black, 2-PYR is 2-pyrrolidone and 2-PYR (w) is 2-pyrrolidone and water.

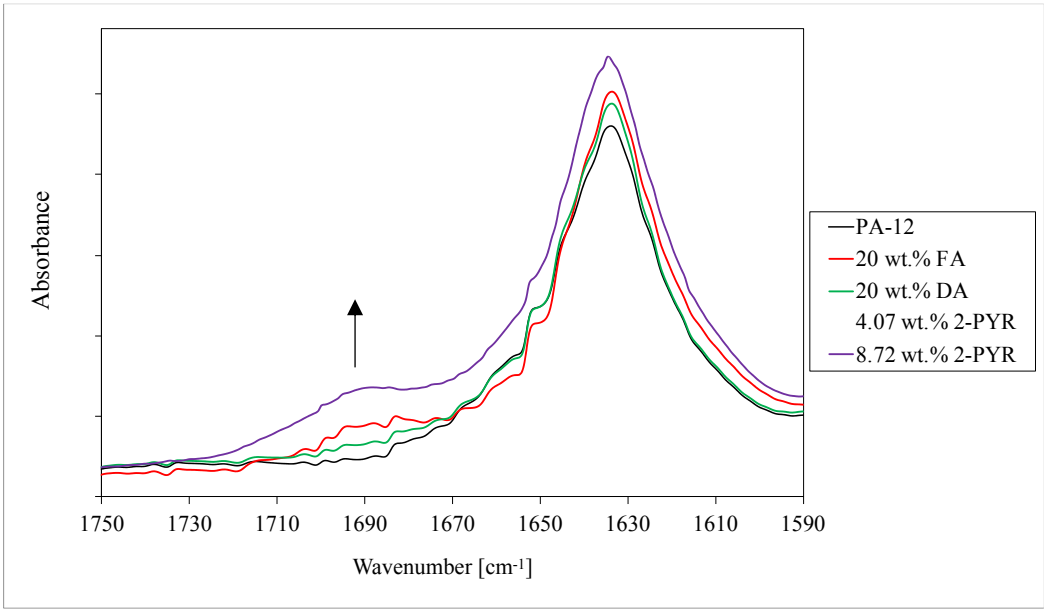

Figure 6.3.5: FTIR spectra of DSC samples of PA-12, PA-12/2-PYR, PA-12/FA and PA-12/DA blends showing the carbonyl (C=O) stretch at 1635 cm^{-1}. The upwards arrow indicates a peak at 1690 cm^{-1} that increased with composition of 2-PYR. All recorded spectra were normalised to the same baseline. Where FA is the Fusing Agent, DA is the Detailing Agent and 2-PYR is 2-pyrrolidone.

6.3.2 Peak shift of the N-H stretch

This section will focus on hydrogen bond interactions in the PA-12 powder blends by analysing the peak wavenumber of the N-H stretch. FTIR is a highly effective tool to investigate specific interactions between polymers, such as hydrogen bond interactions (95,96,105,149,150). These interactions are present within the amorphous and crystalline regions of the polymer and can also be formed in polymer blends or with the addition of additives to a polymer matrix.

In polyamides, the N-H moiety (absorbance band 3100 – 3500 cm^{-1}) participates in hydrogen bonding with the C=O moiety (absorbance band 1590 – 1670 cm^{-1}) (95,96). It has been reported in literature that the peak wavenumber of the N-H stretch in polyamide shifts to higher or lower wavenumbers when

polyamide forms hydrogen bonds with other molecules present within the polymer matrix (143). For this reason, the peak wavenumber of the N-H stretch for each blend was recorded in order to observe the effect of hydrogen bonding between PA-12 and the FA, DA, CB, water, 2-PYR and 2-PYR/water (151). Since the blends were created from PA-12 powder from 2 batches, the N-H peak wavenumber of PA-12 powder (batch 1) and PA-12 (batch 2) were recorded. The peak wavenumber of the N-H stretch in PA-12 (batch 1) and PA-12 (batch 2) were comparable.

The peak wavenumber of the N-H stretch in PA-12 powder blends is displayed in Figure 6.3.6. In the PA-12/FA and PA-12/DA blend, the peak wavenumber of the N-H stretch varied unsystematically. This was also observed in the PA-12/CB, PA-12/2-PYR/water and PA-12/water blends.

The blend that exhibited the largest shift to lower wavenumbers was the 20 wt.% FA blend, where the peak wavenumber decreased by 2.8 cm^{-1}, when compared to the peak wavenumber of PA-12. The blend which exhibited the largest shift to a higher wavenumber was the 5 wt.% CB blend, where the peak wavenumber increased by 0.26 cm^{-1}, when compared to the peak wavenumber of PA-12. Where the peak wavenumber of PA-12, 20 wt.% FA blend and 5 wt.% CB blend were 3290.4, 3287.6 and 3290.7 cm^{-1}, respectively.

Interestingly, a large decrease in peak wavenumber of the N-H stretch was also observed in the 1 wt.% CB blend, in comparison to the peak wavenumber of PA-12. The peak wavenumber of the 1 wt.% CB blend was 3288.4 cm^{-1} thus displaying an overall decrease of 2 cm^{-1}. This would suggest PA-12 and carbon black interacted by hydrogen bonding. This was unexpected since this was the blend with the lowest composition of CB in the PA-12/CB blends. Additionally, carbon black was recovered by a process in which volatile components were removed. This leads to the conclusion that the shift in peak wavenumber was due to sample variation or the presence of residual solvents or moisture within PA-12.

In the PA-12/2-PYR blends, the peak wavenumber of the N-H band was comparable to PA-12. This was unusual since 2-PYR contains N-H and C=O moieties demonstrating that 2-PYR can bond with PA-12. This data suggests 2-PYR did not form hydrogen bonds with PA-12 in the powder blend. It is possible that 2-PYR formed self-associative hydrogen bonds or that a proportion of 2-PYR was monomeric. This agrees with the findings in section 6.3.1 where the free N-H band was identified in Figure 6.3.3. However, a shift in peak wavenumber of the N-H band was identified for PA-12/2-PYR/water blends and not the PA-12/water blends. This suggests that in a multi-component system, where both 2-PYR and water are present, hydrogen bonds are formed leading to a shift in peak wavenumber. The hydrogen bonds can act between; 2-PYR:water, 2-PYR:2-PYR, water:water, 2-PYR:PA-12, water:PA-12 or 2-PYR:water:PA-12. This data suggests that water acts as a facilitator for hydrogen bonding in PA-12/2-PYR/water blends. This could be due to bond favourability. M. Davila et al study the interaction of 2-PYR and water in extensive detail in (147). This an interesting concept since a unsystematic shift in peak wavenumber was also reported in th PA-12/FA and PA-12/DA blends where both 2-PYR and water were present.

Overall, the data shows a shift in peak wavenumber with the addition of the FA, DA, CB and 2-PYR/water to PA-12 powder, this suggests that hydrogen bonds were formed. It is likely that the shift in peak wavenumber was due to 2-PYR and water (also common to the FA and DA) within the blend, since 2-PYR and PA-12 can form hydrogen bonds. The hydrogen bond interaction between PA-12 and 2-PYR arises from the similarity in functional groups, whereby 2-PYR also contains N-H and C=O moieties. Both PA-12 and 2-PYR also can bond to O-H in water.

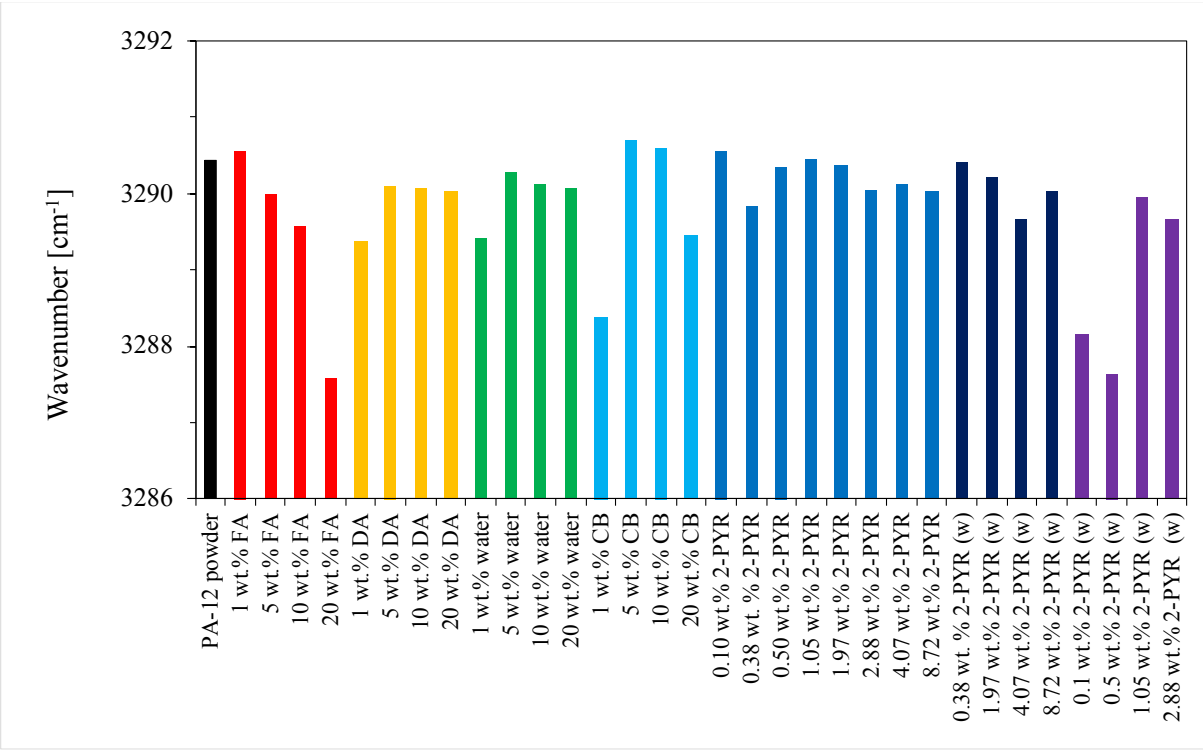

Figure 6.3.6: Bar chart showing the peak wavenumber of the N-H stretch for powder blends exhibiting a shift in peak wavenumber, when compared to the peak wavenumber of PA-12. Where FA is the Fusing Agent, DA is the Detailing Agent, CB is carbon black, 2-PYR is 2-pyrrolidone and 2-PYR (w) is 2-pyrrolidone and water.

This section will focus on the shift in peak wavenumber of the N-H stretch and hydrogen bond interactions in the PA-12 blends that were subjected to DSC analysis.

Figure 6.3.7 shows the peak wavenumber of the N-H stretch in the PA-12 blends. In the PA-12/FA and PA-12/DA blends, the peak wavenumber of the N-H stretch varied unsystematically with composition of FA and DA. This suggests that hydrogen bond interactions were present between the constituents of the FA and DA with PA-12. Interestingly, a shift in peak wavenumber of the N-H stretch was also observed in the PA-12/2-PYR blends. This suggests that the 2-PYR (also common to the FA and DA) and PA-12 interacted by hydrogen bonding. Since this was not observed in the powder PA-12/2-PYR blends this can be attributed to the reorganisation of the polymer chains during crystallisation. Similarly,

this was also observed in the PA-12/2-PYR/water blends. This data is justified by the peak at 1690 cm^{-1} related to the amide-I band (C=O stretch) that confirmed the presence of 2-PYR within the blends, demonstrating that 2-PYR and PA-12 can form hydrogen bonds.

The blend that exhibited the greatest increase in peak shift was the 1 wt.% FA blend, where the peak wavenumber increased by 6.7 cm^{-1}, when compared to the peak wavenumber of PA-12. The blend which exhibited the greatest decrease in peak shift was the 0.5 wt.% 2-PYR blend, where the peak wavenumber decreased by 4.33 cm^{-1}, when compared to the peak wavenumber of PA-12. Where the peak wavenumber of PA-12, 1 wt.% FA and 0.5 wt.% 2-PYR were 3292.9, 3299.6 and 3288.6 cm^{-1}, respectively.

In the PA-12/carbon black and PA-12/water blends, no significant shift in peak wavenumber was observed. In total, 3 FTIR spectra were recorded for each blend. In the PA-12/CB and PA-12/water blends, 1 of the 3 samples displayed a significant shift in peak wavenumber. This was classed as an anomalous result. In order to increase the reliability of this data, FTIR spectra need to be recorded again and the results are to be compared.

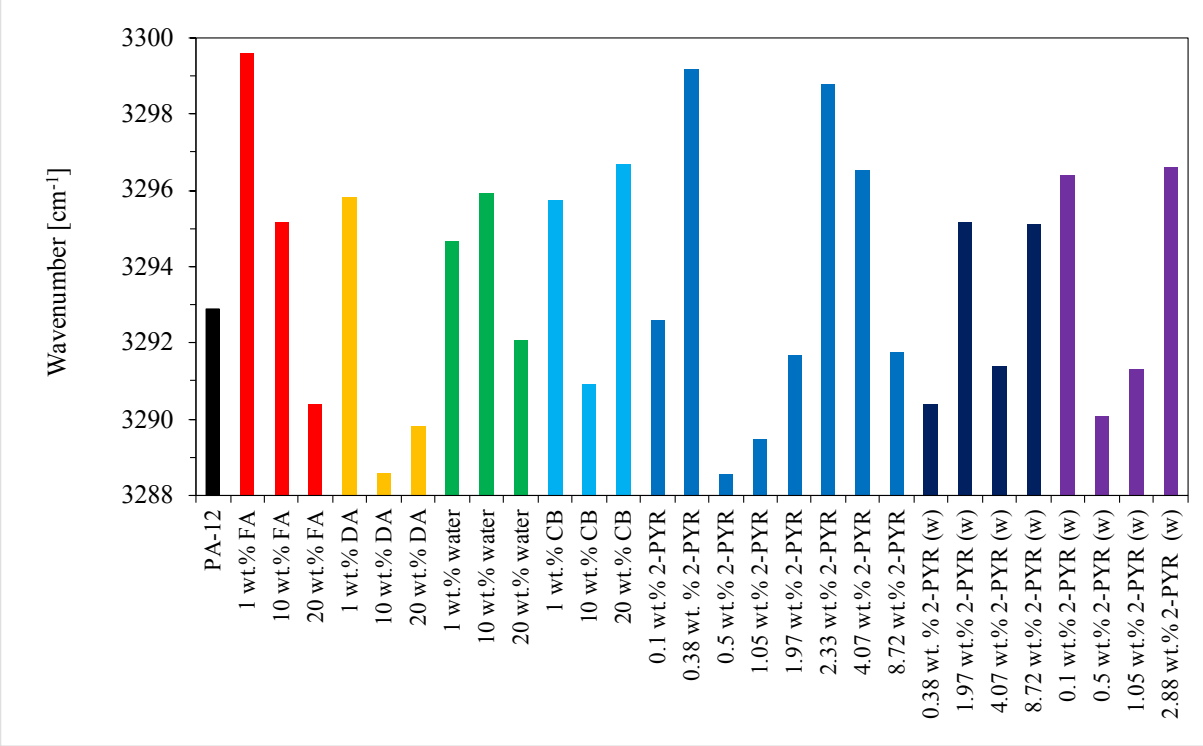

Figure 6.3.7: Bar chart showing the peak wavenumber of the N-H stretch for DSC samples of PA-12 blends exhibiting a shift in peak wavenumber, when compared to the peak wavenumber of PA-12. Where FA is the Fusing Agent, DA is the Detailing Agent, CB is carbon black, 2-PYR is 2-pyrrolidone and 2-PYR (w) is 2-pyrrolidone and water.

6.3.3 Deconvolution of the N-H stretch in PA-12/2-PYR blends

In section 6.3.1, it was shown that 2-PYR was retained in PA-12 by the peak at 1690 cm^{-1} (assigned to the C=O, 2-PYR). Additionally, in the powder PA-12/2-PYR/water blends and the DSC extracted PA-12/2-PYR blends, a shift in peak wavenumber was observed and suggested that 2-PYR interacted with PA-12 by hydrogen bonding. This data suggsts that 2-PYR influenced the properties of PA-12.

A study by M. Davila et al evaluated the interaction between 2-PYR and water in solution. It was noted that hydrogen bond interactions and dipolar interactions occur between 2-PYR and water exist (147). In their work, FTIR and Density Functional Theory (DFT) was used to investigate the structural changes

of 2-PYR that occur on mixing of 2-PYR and water as a result of hydrogen bonding. Selected peaks in the FTIR spectra were linked to selected bands in DFT analysis that represent particular molecular level characteristics of 2-PYR. This enabled the conformation of 2-PYR to be determined, with resepct to its form as a monomer or cyclic dimer. In their work, an intense band at 3221.9 cm^{-1} was assigned to the N-H stretch of 2-PYR and was related to the therotical value of a cyclic dimer obtained by DFT. This showed that in its pure liquid form 2-PYR was present as a cyclic dimer. Additionally, a band at 3482.8 cm^{-1} suggested that 2-PYR was present as a monomer and therefore nonassociated with other 2-PYR molecules. Deconvolution of the spectra using the Guassian-Lorentzian function within the region of 3000 – 3500 cm^{-1} resolved further peaks at 3100 cm^{-1} and 3311.9 cm^{-1} relating to overtones of the C=O stretch and the hydrogen bonded C=O of 2-PYR.

In Figure 6.3.8, the N-H stretch of selected powder blends is displayed. On the main N-H stretch, a shoulder peak is illustrated by an arrow; the shoulder peak was within the region of 3180 - 3240 cm^{-1}. In blends containing a large content of 2-PYR, the shoulder peak was more distinguishable. This demonstrates peak growth with composition of 2-PYR. Given that the shoulder peak was within the region of 3180 – 3248 cm^{-1}, this wavenumber region can be related to the 3221.9 cm^{-1} peak, as described by M. Davila et al (147).

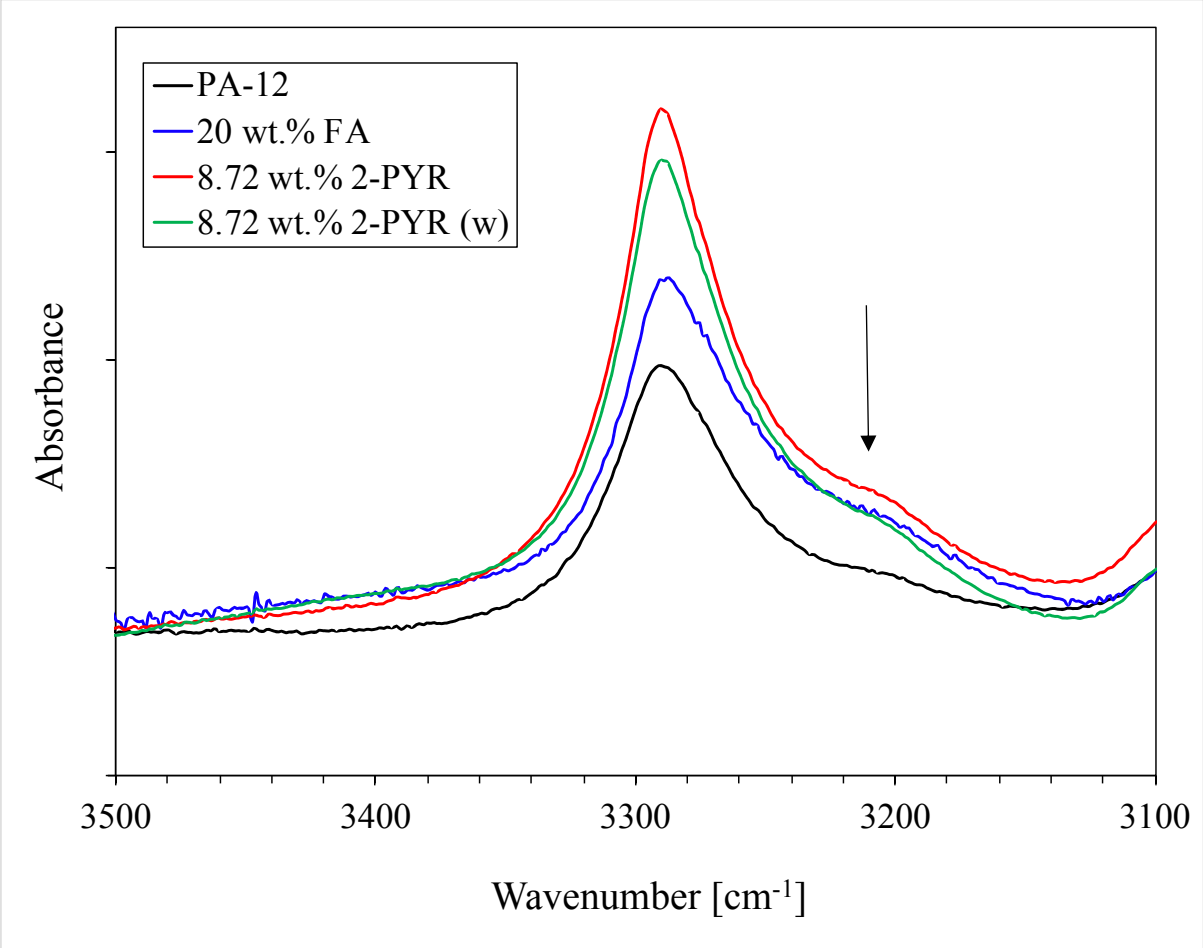

Figure 6.3.8: FTIR of selected powder blends. The arrow high shows the shoulder peak on the right-hand side of the N-H stretch.

In order to distinguish the peak at 3221.9 cm^{-1}, selected PA-12/2-PYR blends were deconvoluted using the Guassian-Lauritzen function (147).

Deconvolution of selected 2-PYR blends showed a peak at 3221 cm^{-1} or close to this value. The peak area and peak height were recorded. Figure 6.3.9 shows a plot of 2-PYR composition vs peak area and peak height of the ~3221 cm^{-1} peak. As a reminder to the reader, M. Davila et al associate a peak at 3221.9 cm^{-1} with 2-PYR in the cyclic dimer conformation. Figure 6.3.9 shows a positive linear correlation; as the composition of 2-PYR increased, the peak area and peak height of the ~3221.9 cm^{-1} peak increased. This data indicates that i) 2-PYR was present in the form of a cyclic dimer and ii) as the composition of 2-PYR increased the content of cyclic dimer also increased. Where 2-PYR is in the

form of a cyclic dimer, it is unable to form hydrogen bonds with PA-12, unless other configurations are adopted (147).

Although this data shows that 2-PYR was present as a cyclic dimer and the content of the cyclic dimer increased with composition of 2-PYR, it is unclear what fraction of 2-PYR within the blend adopted this configuration. This suggests 2-PYR may also be present as a monomer.

M. Davila et al showed that when 2-PYR is in the form of a monomer, a peak at 3482 cm^{-1} was observed (147). However, in this experimental work a distinguishable peak at 3482 cm^{-1} was not observed. This can be due to monomeric 2-PYR being undetected since it was present in a small quantity. This being said, in some PA-12/2-PYR blends a shoulder peak within the region of 3550 – 3600 cm^{-1} was observed (also mentioned in Chapter 6.3.1). The shoulder peak was assigned to free N-H. This could be associated with PA-12 or 2-PYR since both contain N-H that can either be bonded or free. Therefore, shoulder peak within the region of 3550 – 3600 cm^{-1} demonstrates the presence of free N-H in PA-12 and 2-PYR.

An extension of this work would involve deconvoluting all of the spectra for the 2-PYR blends to identify peaks at 3222 cm^{-1} and 3482.8 cm^{-1} and examine peak growth relative to 2-PYR content.

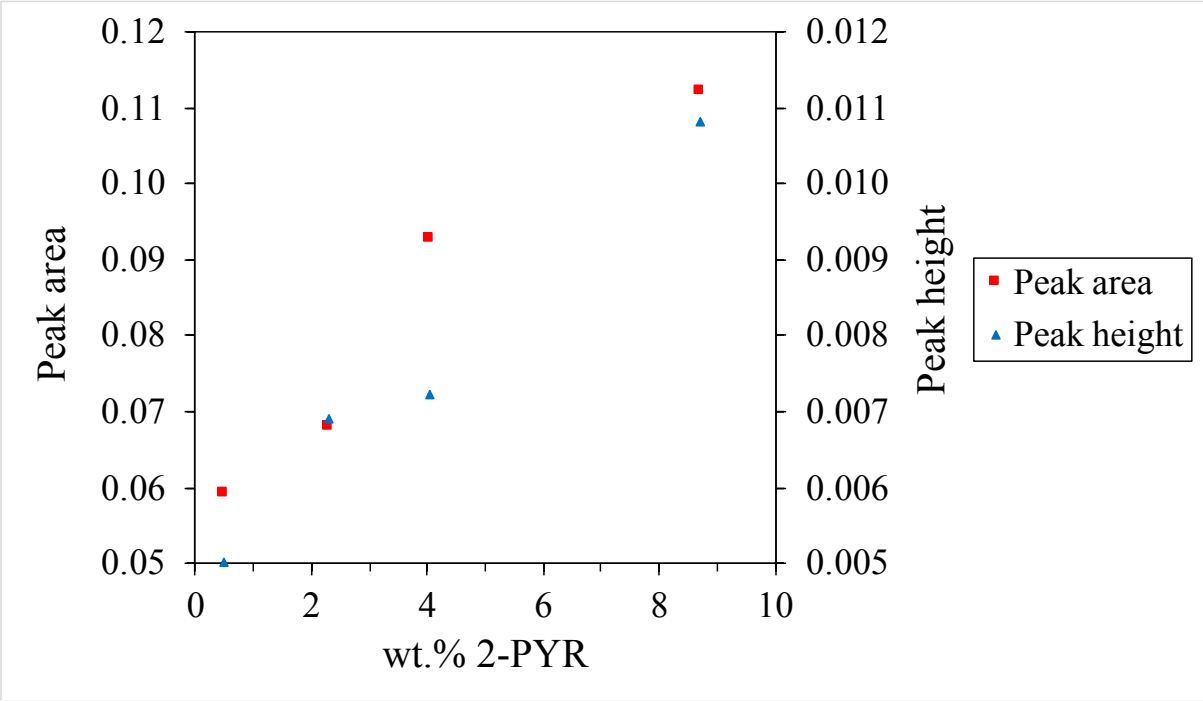

Figure 6.3.9: Graph of 2-PYR composition vs peak area and peak height of the 3222 cm^{-1} obtained by deconvolution using the Guassian-Lorentzian method for selected powder blends.

Table 6.3.1: Peak assignments for PA-12 powder and PA-12 powder blends (continued on next page).

Peak assignment	Hydrogen bonded N-H stretch	CH_2 asymmetric stretch	CH_2 symmetric stretch	C=O stretch	C-N stretch, C=O in plane bending	CH bend, CH2 twist	C-N stretch, C=O in plane bending	C-C stretch	CONH in plane
PA-12	3290.42	2915.92	2846.19	1634.77	1538.90	1368.05	1267.62	1121.48	947.88
1 wt.% FA	3290.55	2916.62	2846.68	1634.76	1538.89	1367.97	1267.51	1121.26	948.24
5 wt.% FA	3289.99	2916.05	2846.37	1634.73	1538.89	1367.9	1267.55	1121.66	947.96
10 wt.% FA	3289.57	2915.68	2846.02	1634.05		1367.89	1267.89	1120.97	947.87
20 wt.% FA	3287.57	2915.25	2845.94	1634.96	1538.84	1367.77	1267.45	1120.69	947.90
1 wt.% DA	3289.37	2916.29	2845.49	1634.07	1538.87	1368	1267.57	1121.44	948.25
5 wt.% DA	3290.1	2916.31	2846.54	1647.05	1538.86	1367.91	1267.6	1121.56	948.23
10 wt.% DA	3290.06	2916.01	2846.2	1637.09	1538.91	1367.93	1267.55	1121.08	947.99
20 wt.% DA	3290.02	2916.13	2846.26	1637.26		1367.98	1267.65	1120.8	948.07
1 wt.% CB	3288.38	2915.77	2846.04	1637.38		1368.31	1267.52	1121.56	947.77
5 wt.% CB	3290.69	2915.88	2846.16	1637.5		1368.15	1267.54	1121.6	948

10 wt.% CB	3290.59	2916.27	2846.52	1637.07	1538.88	1367.97	1267.59	1121.51	948.21
20 wt.% CB	3289.45	2915.81	2846.11	1637.44		1367.74	1267.57	1120.56	947.88
1 wt.% water	3289.41	2915.75	2846.08	1637.31	1539.07	1367.75	1267.49	1121.44	947.82
5 wt.% water	3290.28	2916.2	2846.39	1637.08	1538.9	1367.88	1267.53	1121.54	948.1
10 wt.% water	3290.12	2916.33	2846.55	1637.07	1538.88	1367.89	1267.56	1121.56	948.12
20 wt.% water	3290.12	2916.33	2846.55	1637.07	1538.88	1367.89	1267.56	1121.56	948.12
0.1 wt.% 2-PYR	3290.55	2916.15	2846.36	1637.12	1538.84	1367.94	1267.53	1121.57	948.07
0.38 wt. % 2-PYR	3289.83	2915.84	2846.15	1637.19	1538.94	1367.83	1267.55	1121.39	947.84
0.5 wt.% 2-PYR	3290.34	2916.33	2846.48	1637.06	1538.92	1367.93	1267.51	1121.38	948.08
1.05 wt.% 2-PYR	3290.45	2915.96	2846.24	1634.81	1538.86	1367.84	1267.58	1121.59	948.04
1.97 wt.% 2-PYR	3290.37	2916.33	2846.53	1637.06	1538.87	1367.88	1267.54	1121.57	948.09
2.88 wt.% 2-PYR	3290.04	2915.81	2846.06	1637.12		1367.69	1267.52	1121.42	947.98
4.07 wt.% 2-PYR	3290.02	2916.08	2846.29	1637.04	1538.93	1367.85	1267.51	1121.76	948.16
8.72 wt.% 2-PYR	3290.03	2916.36	2846.41	1637.04	1538.91	1367.94	1267.62	1121.79	948.29
0.38 wt. % 2-PYR(w)	3290.5	2916.26	2846.52	1637.16	1538.96	1368	1267.61	1121.6	948.19
1.97 wt.% 2-PYR (w)	3290.22	2917	2487.44	1637.06	1538.81	1368.03	1267.69	1121.99	948.38

4.07 wt.% 2-PYR (w)	3289.67	2915.64	2845.94	1637.18		1367.87	1267.54	1121.58	947.7
8.72 wt.% 2-PYR (w)	3290.02	2916.18	2846.28	1637.08	1538.95	1368.05	1267.7	1121.73	948.14
0.1 wt.% 2-PYR (w)	3289.97	2916.61	2846.76	1637.09	1538.84	1367.99	1267.56	1121.48	948.2
0.5 wt.% 2-PYR (w)	3287.63	2916.42	2846.77	1637.06	1538.89	1367.96	1267.56	1121.52	948.15
1.05 wt.% 2-PYR (w)	3289.95	2916.5	2846.55	1637	1538.92	1368.02	1267.47	1121.49	948.24
2.88 wt.% 2-PYR (w)	3289.66	2916.09	2486.25	1637.1	1539.13	1367.98	1267.55	1121.66	948.13

Table 6.3.2: Peak assignments for DSC samples of PA-12 and PA-12 blends (continued on next page).

Peak assignment	Hydrogen bonded N-H stretch	CH_2 asymmetric stretch	CH_2 symmetric stretch	C=O stretch	C-N stretch, C=O in plane bending	CH bend, CH2 twist	C-N stretch, C=O in plane bending	C-C stretch	CONH in plane
MJF component	3292.27	2917.43	2849.3	1365.6	1540.57		1267.12		
PA-12	3292.90	2917.44	2849.14	1633.47	1540.44	1367.36	1268.99	1124.31	944.79
1 wt.% FA	3299.6	2197.47	2849.37	1634.44	1539.8	1368.31	1268.74	1121.17	944
10 wt.% FA	3295.18	2916.99	24848.97	1633.83	1540.26	1367.34	1268.63	1120.98	943.51
20 wt.% FA	3290.40	2916.63	2848.39	1633.66	1557.13	1366.90	1268.33	1120.78	945.16
1 wt.% DA	3295.81	2917.35	2849.1	1634.07	1539.41	1367.5	1268.89	1121.31	944.65
10 wt.% DA	3288.6	2916.89	2848.69	1633.41	1557.52	1366.96	1269.23	1121.19	945.47
20 wt.% DA	3289.8	2916.87	2848.54	1633.45	1557.42	1366.75	1269.2	1120.91	945.18
1 wt.% CB	3294.66	2917.26	2849.02	1633.54	1548.58	1367.13	1268.96	1121.33	944.9
10 wt.% CB	3295.91	2917.36	2849.15	1633.74	1540.43	1367.37	1268.91	1121.34	944.58
20 wt.% CB	3292.05	2917.05	2848.89	1633.54	1557.42	1367.28	1269.22	1121.33	945.28

1 wt.% water	3295.74	2917.36	2849.13	1633.78	1540.4	1367.32	1268.81	1121.27	944.74
10 wt.% water	3290.94	2917.16	2848.98	1634.01	1557.41	1367.21	1268.99	1121.32	944.71
20 wt.% water	3296.68	2917.63	2849.48	1634.69	1540.03	1368.08	1268.37	1120.79	943.76
0.1 wt.% 2-PYR	3292.61	2917.4	2849.1	1634.45	1538.84	1367.76	1268.62	1121.15	944.83
0.38 wt. % 2-PYR	3299.19	2917.35	2849.14	1634.59	1539.15	1368.36	1268.63	1121.42	943.88
0.5 wt.% 2-PYR	3288.57	2196.96	2848.58	1634.15	1543.53	1367.5	1268.78	1121.33	945.67
1.05 wt.% 2-PYR	3289.47	2916.89	2848.6	1634.16	1541.34	1367.49	1268.78	1121.19	945.34
1.97 wt.% 2-PYR	3291.69	2917.16	2848.93	1634.39	1538.95	1367.6	1268.66	1121.24	944.49
2.88 wt.% 2-PYR	3298.8	2917.75	2849.47	1634.46	1538.79	1367.71	1268.42	1121.15	942.08
4.07 wt.% 2-PYR	3296.54	2917.51	2849.4	1634.53	1538.7	1367.94	1268.16	1121.56	943.55
8.72 wt.% 2-PYR	3291.76	2917.31	2849.11	1634.54	1539.02	1367.62	1268.29	1121.53	944.95
0.38 wt. % 2-PYR (w)	3290.38	2917.31	2848.9	1634.54	1538.9	1367.63	1268.81	1121.3	945.24
1.97 wt.% 2-PYR (w)	3295.18	2917.57	2849.33	1634.45	1539.19	1367.89	1268.66	1121.42	943.96
4.07 wt.% 2-PYR (w)	3291.39	2917.13	2848.76	1634.5	1538.98	1367.63	1268.57	1121.53	945.24
8.72 wt.% 2-PYR (w)	3295.14	2917.52	2849.16	1634.55	1539.09	1367.96	1268.39	1121.75	943.99
0.1 wt.% 2-PYR (w)	3296.38	2917.68	2849.37	1634.45	1539.15	1367.98	1268.5	1121.43	944.15

0.5 wt.% 2-PYR (w)	3290.09	2917.36	2849.01	1634.54	1538.93	1367.81	1268.72	1121.24	945.03
1.05 wt.% 2-PYR (w)	3291.32	2917.42	2849.15	1634.51	1539.11	1367.81	1268.65	1121.53	944.72
2.88 wt.% 2-PYR (w)	3296.61	2917.69	2849.46	1634.54	1539.21	1367.86	1268.55	1121.47	943.79

6.4 Optical microscopy of PA-12 blends

Figure 6.4.1 displays optical micrographs of blends created from virgin powder that were cooled at controlled rate of 0.5 ℃/min. A slow cooling rate of 0.5 ℃/min was used since it produced distinguished spherulites whilst enabling the nucleation effect provided by the agents to be observed, if any.

In this work the effect of the FA, DA, CB and 2-PYR on the microstructure of virgin PA-12 was observed using optical microscopy. The spherulites formed at different compositions of the FA, DA, CB and 2-PYR were compared.

Figure 6.4.1 shows the microstructure of PA-12. The spherulites were relatively large in diameter, ranging from ~ 30 – 50 μm. This was comparable that reported by H. Teo, where a cooling rate of 1 ℃/min produced spherulites of diameter 39.8 μm and dendrite thickness of 1.88 μm (100). In the work of H. Teo et al, the cooling rate was varied and the spherulite diameter and dendrite thickness were recorded. It was shown that as the cooling rate increased, the spherulite diameter and dendrite thickness decreased (100). Hence, it is unsurprising that a decrease in = cooling rate from 1 ℃/min to 0.5 ℃/min produced spherulites with a diameter larger than 39.8 μm. A decrease in cooling rate caused the spherulite size to increase as a result of crystallisation taking place over longer period of time. In turn, the crystallisation temperature shifts to higher temperatures. The nucleation model shows that nucleation is less frequent when the crystallisation temperature is higher. Therefore, at slow cooling rates nucleation is limited and the diameter of the nucleated crystals increases since crystallisation occurs over a longer time period, thereby favouring growth (100,152).

The presence of additives can also affect the spherulite size in semi-crystalline materials. This behaviour has been observed in PA-6 and clay composites manufactured by extrusion. The incorporation of clay into the polymer matrix caused the spherulite size to decrease (153). Moreover, the spherulites became less defined with the addition of clay. This was due to clay inducing heterogeneous nucleation by acting as an impurity within the polymer matrix. Greater magnification of crystallised composites revealed small crystalline bundles that consisted of closely packed lamellae and clay platelets (153).

A similar effect was also reported in PA-6/carbon black/organoclay nanocomposites produced by melt-compounding. The addition of carbon black and/or organoclay increased the nucleation density and resulted in the formation of a large number of small spherulites (154).

In other work, S. Athreya et al compared the microstructural properties of PA-12/carbon black composites produced by different manufacturing techniques such as extrusion-injection moulding (extrusion-IM) and SLS (40). The spherulite size of extrusion-IM and SLS fabricated components was compared using optical microscopy. In the extrusion-IM system, the spherulites had a narrow size range distribution, ranging from 5 -10 μm. However, in the SLS system, the range of spherulite sizes observed was greater, this was linked to the large particle size distribution of PA-12 used in SLS. Additionally, it was noted that the spherulite size can also be influenced by build direction, where the spherulite size distribution along the depth of the part was smaller in SLS fabricated components, when compared to their IM counterparts.

Literature has shown that the presence of additives or fillers into the polymer matrix influence the spherulite size. It has been demonstrated that the spherulite size decreases due to heterogeneous nucleation. Earlier, it was shown that a cooling rate of 0.5 ℃/min produced large and well-defined spherulites in PA-12. Therefore, a cooling rate of 0.5 ℃/min was selected to evaluate the nucleation effect induced by the addition of agents, if any.

The microstructure of 1 and 20 wt.% FA blend is displayed in Figure 6.4.1 (b and c), the dark regions represent carbon black and the surrounding area is the PA-12 matrix. As the composition of FA increased, a greater content of carbon black was dispersed within the polymer matrix. This showed that carbon black was retained within the polymer but rejected into the inter-spherulitic regions. This was also reported by C. Abbott et al (155). In the PA-12/FA blends, the spherulite size was significantly reduced by the addition of the FA, even at compositions as low as 1 wt.% FA. This suggests that the carbon black within the FA acted as a nucleating agent or impeded the radial growth of spherulites by acting as a physical barrier. The latter would have a significant effect at particularly large compositions of FA.

The microstructure of the 1 and 20 wt.% DA blends is displayed in Figure 6.4.1 (d and e). In the 1 wt.% DA blend, the spherulite size was comparable to PA-12. As the composition increased, the spherulite size decreased slightly. This demonstrated that a component within the DA impacted the spherulite size of PA-12 in high compositions.

The microstructure of the 1 and 20 wt.% CB blends is displayed in Figure 6.4.1 (f and g). The carbon black was dispersed within the polymer matrix as irregular shaped black particles. In the 1 and 20 wt.% carbon black blend, the spherulite size decreased in comparison to PA-12. Since carbon black was present as individual particles, it is possible that the presence of carbon black impeded the radial growth of spherulites by acting as a physical barrier. Additionally, it is possible that carbon black induced heterogeneous nucleation by acting as an impurity.

The microstructure of the PA-12/water blends is displayed in Figure 6.4.1 (h and i). In the PA-12/water blends, the spherulite size was unaffected by the addition of water and the spherulite size of the blends was comparable to PA-12. This suggested water evaporated during the drying process. This agrees with section 6.2 in that the thermal properties of PA-12 were not affected by the addition of water.

The microstructure of 0.38 and 8.72 wt.% 2-PYR blends is displayed in Figure 6.4.1 (j and k). In the 0.38 wt.% 2-PYR blend, the spherulite size was comparable to PA-12. In the 8.72 wt.% 2-PYR blend, the spherulite size decreased slightly. This was due to 2-PYR acting as a plasticizer to enhance chain mobility. This agrees with section 6.2, where the addition of 2-PYR caused the supercooling window to decrease suggesting that 2-PYR facilitated crystallisation by acting as a plasticizer. This data suggests that 2-PYR was retained within the polymer. Overall, the decrease in spherulite size caused by 2-PYR was insignificant to that of the FA, therefore, showing the FA had a greater impact on spherulite size than 2-PYR.

The microstructure of the PA-12/2-PYR/water blends is displayed in Figure 6.4.1(l and m). In the blend that was compositionally identical to the FA, generally the spherulite size comparable to PA-12. However, in larger compositions of 2-PYR and/or water, the spherulite size decreased slightly. By process of elimination, the spherulite size was impacted by the addition of 2-PYR since in the PA-12/water blends the spherulite size was unaffected by the addition of water. In the blend that was compositionally identical to the DA, the spherulite size was comparable to PA-12. This was due to the small content of 2-PYR present within the blend.

Overall, the PA-12/2-PYR/water blends displayed a similar trend to the PA-12/2-PYR blend, demonstrating that the 2-PYR influenced the spherulite size when present in larger compositions.

In conclusion, the data showed that the carbon black within the FA limited the growth of the spherulites by acting as a physical barrier to impede radial growth or induce heterogenous nucleation and that 2-PYR decreased the spherulite size slightly when present in large compositions by behaving as a plasticizer.

As shown, the microstructure was affected by the addition of agents or additives in the polymer blend. In manufacture, other factors may affect the microstructure of a component. For example, the processing parameters will impact the final microstructure of the component, in turn this also affects the mechanical properties.

A review article by C. Chatham et al shows that the entire manufacturing process influences the microstructure of final properties of a component. This includes the polymer structure, the chemical and physical properties of the polymer and the processing parameters. It was stated that a good understanding of the entire manufacturing process is required in order to manufacture a "successful" component (23). This demonstrates that the microstructure is important to investigate since this is affected by the cooling conditions in MJF and the presence of agents or additives within the polymer matrix. A study has shown that the cooling rate has a significant impact on the degree of crystallinity and final properties of a part manufactured by MJF. Whereby, an increase in the mechanical resistance was linked to the higher degree of crystallinity (85). Often, in PBF techniques such as MJF, components are left to cool overnight which leads to a slow cooling process (61,68).

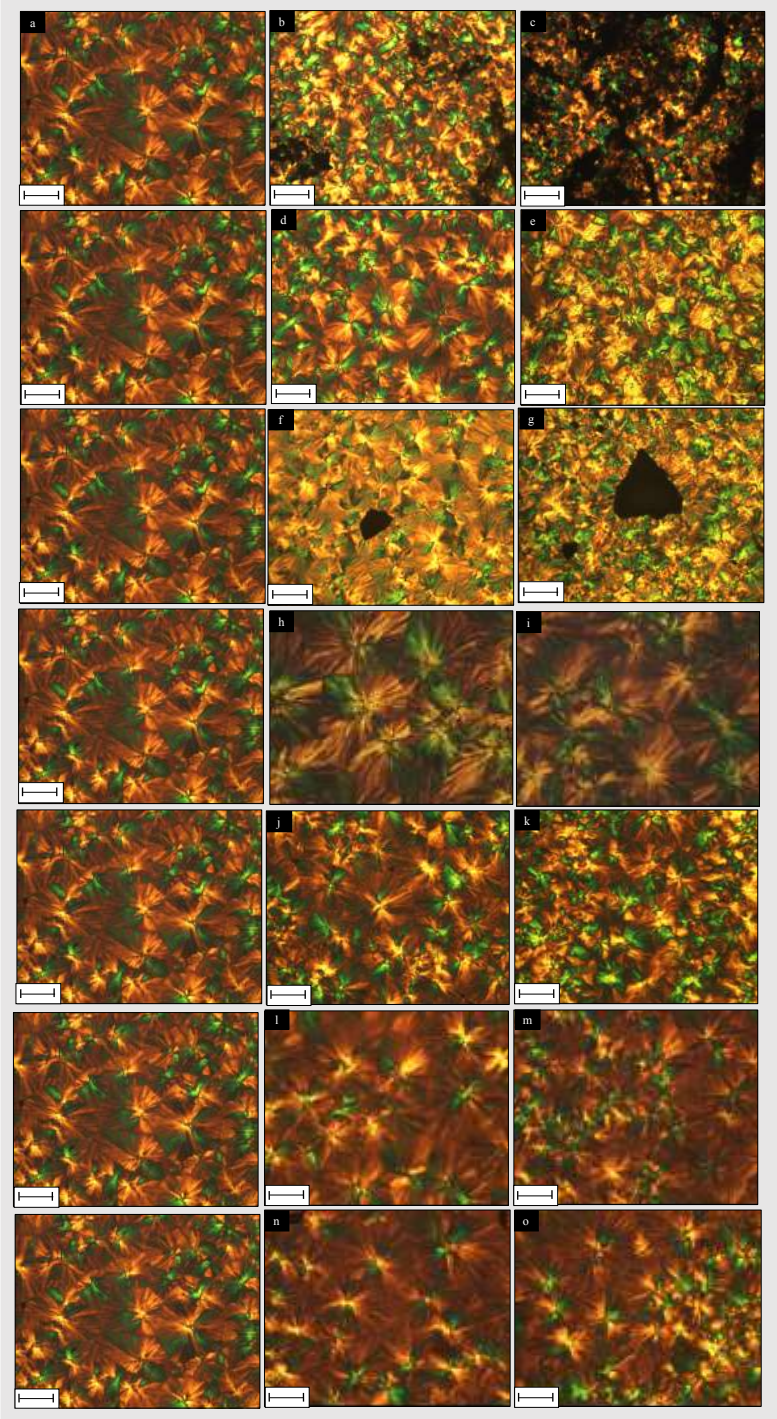

Figure 6.4.1 – Optical microscopy of PA-12 blends; a) PA-12, b) 1 wt.% PA-12/FA, c) 1 wt.% PA-12/FA, d) 1 wt.% PA-12/DA, e) 20 wt.% PA-12/FA, f) 1 wt.% PA-12/CB, g) 20 wt.% PA-12/CB, h) 1 wt.% PA-12/water, i) 20 wt.% PA-12/water, j) 0.1 wt.% PA-12/2-PYR, k) 8.72 wt.% PA-12/2-PYR, l) 0.38 wt.% PA-12/2-PYR(w), m) 8.72 wt.% PA-12/2-PYR(w), n) 0.10 wt.% PA-12/2-PYR(w) and o) 2.88 wt.% PA-12/2-PYR(w).

CHAPTER 7 – CHARACTERISATION OF AGED POLYAMIDE-12 BLENDS

The aim of this work was to replicate the studies mentioned in Chapter 6 on aged PA-12 powder. This was achieved by firstly subjecting PA-12 powder to different ageing conditions and analysing the thermal and chemical properties using DSC and FTIR. The morphology of aged powder was observed using optical microscopy. This provided a benchmark for further studies. The further studies included creating blends of PA-12 and FA, DA, CB, water, 2-PYR and 2-PYR/water using aged powder. The blends were created from PA-12 powder that had been subjected to the harshest ageing conditions. The thermal and chemical properties were analysed using DSC and FTIR. DSC allowed the thermal properties such as the melting and recrystallisation behaviour to be observed and compared to aged PA-12. FTIR allowed the functional groups to be identified and compared to aged PA-12. The morphology of aged blends was observed using optical microscopy and compared to aged PA-12. In MJF the PA-12 powder is often refreshed, where a large portion of used PA-12 powder remains within the build chamber. Therefore, it was important to consider the effect of the agents and their chemical constituents on aged PA-12 powder.

7.1 Characterisation of aged PA-12

7.1.1 Visual characterisation

PA-12 samples were stored in an oven at 170 ℃ for 5, 7 and 9 days. Figure 7.1 shows images of aged PA-12 powder and PA-12 powder after being subjected to DSC analysis.

It was clear that with increased ageing time, the visual appearance of the powder changed. Unaged virgin PA-12 appeared white in colour. After being subjected to 170 ℃ for 5 days, the powder was slightly discoloured (off-white). After 7 days, the powder appeared beige in colour. After 9 days, the powder was

orange in colour. The change in colour of the powder suggests that degradation occurred. The transition in colour between day 7 to day 9 was significant in comparison to day 5 to day 7. This suggests that after a certain time exposed to high temperatures, the powder quickly discoloured and showed signs of major degradation.

The insets of the image shown in Figure 7.1.1 shows samples that had been extracted from a DSC pan after being subjected to 3 heat-cool cycles at a heating a cooling rate of 10 ℃/min.

The colour of the DSC samples were darker as the ageing time increased. The extracted samples were darker in comparison to their powder counterpart. The DSC samples, in particular the 7 day and 9 day aged sample, were significantly darker than the powder counterparts. This was due to the sample being exposed to multiple heating and cooling cycles. Additionally, the edges of the DSC sample were darker than the centre, this was due to polymer build up at the edges of the pan from the meniscus formed in the polymer melt. The discolouration of aged samples was also observed by M. Pliquet et al for degraded PA-6,6 (102).

Overall, this data suggests that the colour of PA-12 powder changed significantly between 7 and 9 days under the given temperature conditions, suggesting degradation occurred. Moreover, after multiple heat-cool cycles, the aged powder experienced further discolouration suggesting that the material cannot be recycled extensively.

Figure 7.1.1 – Image of powder samples removed from an oven at 170 ℃ on day 5, 7 and 9. The inset images show samples extracted from a DSC that have been subjected to 3 heat-cool cycles between 25 – 220 ℃ using a heating and cooling rate of 10℃/min.

7.1.2 Thermal analysis

Thermal characterisation of PA-12 powder aged for 5, 7 and 9 days at 170 ℃ in an oven open to the atmosphere was performed by DSC. The powder was subjected to multiple heat-cool cycles in the DSC, from which, heat 1 was used to characterise the thermal history of the sample and heat 2 showed the material specific properties where the thermal history had been erased.

The influence of ageing on PA-12 powder had a significant effect on the T_g, in that the T_g shifted unsystematically to lower temperatures, when compared to virgin PA-12 powder. This is displayed in Figure 7.2.1. The T_g of the 5, 7 and 9 day aged powder were 39.0, 40.33 and 39.16 ℃ respectively. The average T_g was 39.50 ℃. According to Flory, degradation causes the T_g to decrease since the molecular weight of the material decreases (157). In this instance, if lower molecular weight products from chain scission do not diffuse out of the material, they may redistribute themselves within the polymer matrix to increase the

degree of crystallinity (158,159). The data shows that the T_g shifted to lower temperatures as the ageing time increased with no trend, this suggests that the polymer chains within the amorphous regions were more mobile.

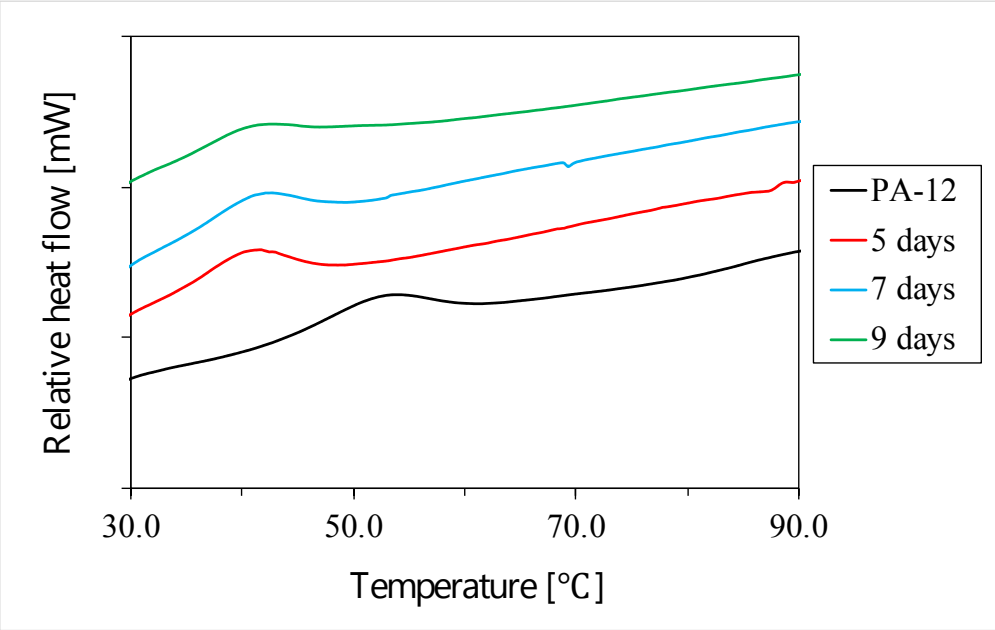

Figure 7.1.2 – Glass transition region of PA-12 artificially aged at 170 ℃ for 5, 7, and 9 days on heat 1.

The melting curve obtained from heat 1 is displayed in Figure 7.1.2. The ageing time had a significant effect on the thermal behaviour of PA-12 powder, in that the peak melting temperature increased and then decreased with ageing time. The peak melting temperature of PA-12 aged for 0, 5, 7 and 9 days were 187.2, 189.3, 189.0 and 184.8 ℃, respectively. The onset melting temperature and last trace of crystallinity also followed the same trend, this data is shown in Table 7.1. The respective increase in peak melting temperature suggests that the aged material had experienced post-crosslinking or post-polymerisation (55). This could be due to ageing taking place at a temperature above the T_g of the polymer meaning that the polymer chains had increased mobility. The decrease in melting temperature can be a result of thermal

degradation of polymer chains causing polymer chains to become shorter by chain scission reactions. In the 9 day aged sample, a double melting peak was observed, where the lower temperature melting peak returned to a baseline before the high temperature melting peak formed. The presence of 2 melting peaks can be due to melt-recrystallisation of the polymer or this could show the formation of different a crystal structure formed during ageing. The presence of 2 crystal structures was quantified using XRD. It was reported that PA-12 powder is present in the α crystal (48). M. Galati et al also use XRD to study the different crystal structures of PA-12 powder. It was reported that the 2 main peaks were observed. These were linked to the α crystal and γ crystal. The peak corresponding to the γ crystal was strongly prevalent in PA-12 refreshed powder. This was linked to rapid cooling associated with post-manufacture (58). It has also been reported that at temperatures above the glass transition temperature, the two crystal forms can interconvert. As the two crystal forms have different melting temperatures, it can be concluded that during this prolonged time period at a temperature above the glass transition temperature two crystals structures formed (160).

Since each sample of PA-12 was subjected to the same cooling conditions after ageing, the cooling rate would not influence the crystal structure of the powder. This leads to the idea that the double melting peak can be due to melt recrystallisation.

F. Sillani et al reported that the peak melting temperature of virgin and recycled PA-12 used in MJF differed by 1 ℃, suggesting that the thermal properties of PA-12 used in MJF were not affected by repeated heating and cooling cycles, unlike other PBF techniques such as SLS (31). The thermal behaviour of refreshed PA-12 was also characterised, though it was not stated which stage of the processing cycle the recycled powder was from. In comparison to virgin PA-12 powder the peak melting temperature and crystallisation temperature of refreshed powder increased slightly by approximately 2 and 1 ℃, respectively (31). This demonstrated that the thermal properties of PA-12 used in MJF were not affected by the refresh rate. In comparison to the experimental work in this section where the melting properties of PA-12 were affected by ageing, it is possible that PA-12 characterised by F. Sillani et al was subjected to less harsh conditions

and therefore was less susceptible to post-polymerisation and post-crystallisation mechanisms. This may be a reason F. Sillani et al suggest PA-12 is “end-capped” (31).

The enthalpy of fusion and consequently, the degree of crystallinity, increased and then decreased with ageing time. The increase in the degree of crystallinity can be linked to post-crystallisation of PA-12 powder due to being exposed to a high temperature (above the T_g of the polymer) for an extended time period. As described in (157–159), degradation can lead to the formation of shorter polymer chains in the amorphous regions. At temperatures above the T_g, polymer chains are mobile and can join the crystalline region which leads to an increase in the degree of crystallinity. However, the observed increase in melting temperature (heat 1) suggests that post cross-linking or post-polymerisation occurred which does not agree with literature (157–159).

Whereas, in the 9 day aged sample, the degree of crystallinity decreased. In relation to literature (157–159), shorter polymer chains formed by chain scission can enter the crystalline region and increase the degree of crystallinity. The observed decrease in melting temperature (heat 1) suggests that chain scission occurred, yet a decrease in the degree of crystallinity was observed. Therefore, this also does not agree with (157–159). In order to explore this further, PA-12 should be exposed to higher temperatures (above the T_g) of the polymer for longer than 9 days.

In terms of the melting properties of aged powder, P. Chen et al report a slight increase in melting temperature for recycled SLS grade PA-12 (VESTOSINT X1556). The degree of crystallinity obtained from heat 1 however decreased for recycled powder. It was suggested that the increase in the melting temperature was due to crystalline reorganisation (32). This is also different to the melting properties exhibited by MJF powder in this section of experimental work. The data suggests that powder used in MJF behaves differently to that used in SLS after ageing (or recycling).

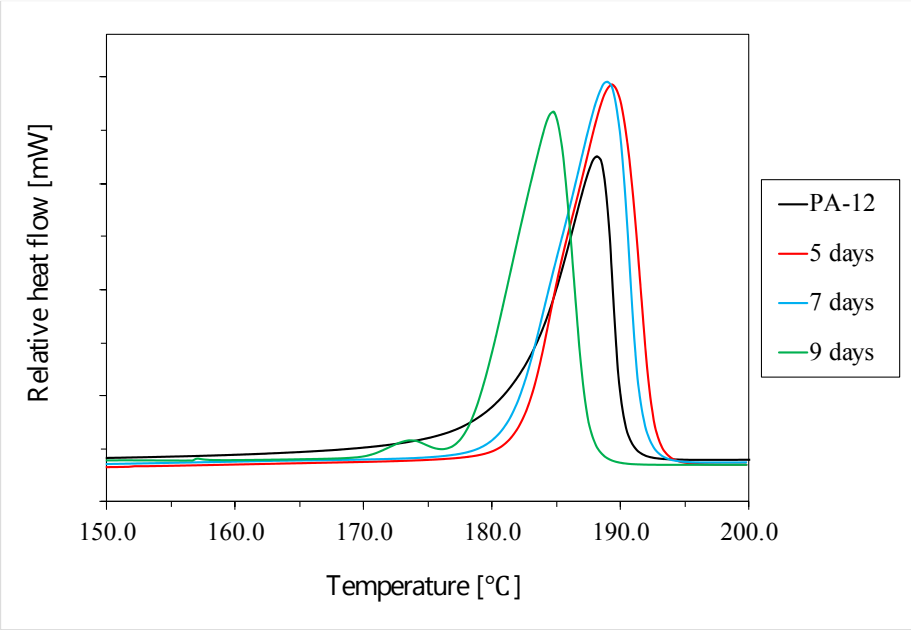

Figure 7.1.3 – Melting behaviour of PA-12 artificially aged at 170 °C for 5, 7, and 9 days on heat 1.

The cooling curves, displayed in Figure 7.1.4, show that ageing time had a significant effect on the cooling behaviour of PA-12 in that a decrease in peak crystallisation temperature was observed with ageing time. The peak crystallisation temperature of the 0, 5, 7 and 9 day aged PA-12 were 148.3, 145.8, 144.6 and 141.5 °C, respectively. Moreover, the onset crystallisation temperature followed the same trend. The decrease in crystallisation temperature is a result of post-crosslinking or post-polymerisation. Longer polymer chains experience limited mobility, as such the chain folding ability of the polymer is hindered and the crystallisation temperature shifts to lower temperatures. This agrees with the data for heat 1, whereby an increase in melting temperature for the 5 and 7 day aged sample was observed showing that polymer chains experienced post-crosslinking or post-polymerisation.

In the 9 day aged sample a decrease in melting temperature was observed, suggesting that the polymer chains had decreased in length. In turn, this can cause the crystallisation temperature to increase since the

chains are smaller and crystallise more easily. However, the crystallisation temperature of the 9-day aged sample decreased to a lower temperature than the 5 and 7 day aged samples which contrasts with the statement above. In order to correlate the molecular weight and the melting and recrystallisation temperature, gel permeation chromatography can be used.

The recrystallisation behaviour observed in aged PA-12 contrasts with a report by J. Riedelbauch et al, who noted an increase in peak crystallisation temperature when PA-12 powder was exposed to an increased number of processing cycles. The increase in crystallisation temperature was linked to the presence of residual agents which may act as impurities and consequently exhibit a nucleating effect (55). This is a more accurate representation of the behaviour of PA-12 powder used in MJF, since the powder was extracted from the build.

In SLS grade PA-12, a slight increase in the peak crystallisation temperature was reported for recycled PA-12 (32). The authors also report that the enthalpy of crystallisation decreased with aging due to an increased melt viscosity of aged powder. The increased in melt viscosity can hinder chain folding and the slow down the diffusion rate of chain segments to the nucleus, when compared to original PA-12 powder. These observations are different to that observed in this experimental work on aged PA-12 powder (Hewett Packard). This could indicate that PA-12 powder used in MJF behaves differently to SLS grade PA-12 powder (VESTOSINT X1556).

The degree of supercooling was determined by calculating the difference in peak melting and peak crystallisation temperature. Some studies determine the degree of supercooling using the onset melting temperature and the onset crystallisation temperature (32). By using the peak melting temperature and the

peak crystallisation temperature, this will accurately determine the degree of supercooling in that the onset temperatures can be somewhat subjective.

The degree of supercooling for aged powder increased in comparison to PA-12. However, the degree of supercooling for the for 5, 7 and 9 day aged powder was comparable. The degree of supercooling for 0, 5, 7 and 9 day aged powder was 39.7, 43.5, 44.3 and 43.3 ℃, respectively.

In terms of how ageing affected the crystallisation, an increase in the degree of supercooling suggests that crystallisation was hindered by ageing. This is associated with changes in molecular weight or cross-linking. A report by B. Holland and J.N. Hay investigates thermal degradation of nylon polymers. It was demonstrated that in PA-6 and PA-6,6, the formation of cross-links reduced the heat of recrystallisation and thus degree of crystallinity on cooling. Moreover, it was reported that PA-6,6 experienced an additional decrease in the degree of crystallinity in comparison to the degree of crystallinity of PA-6 due to a faster rate of crosslinking (8). This is due to the presence of additional functional groups in the polymer chain. In comparison to PA-12, the degree of crystallinity on cooling of aged PA-12 increased, where the degree of crystallinity of 0, 5, 7 and 9 day aged powder was 23.6, 28.6, 28.4 and 28.6 %. This suggests that post-crystallisation and not cross-linking occurred by ageing.

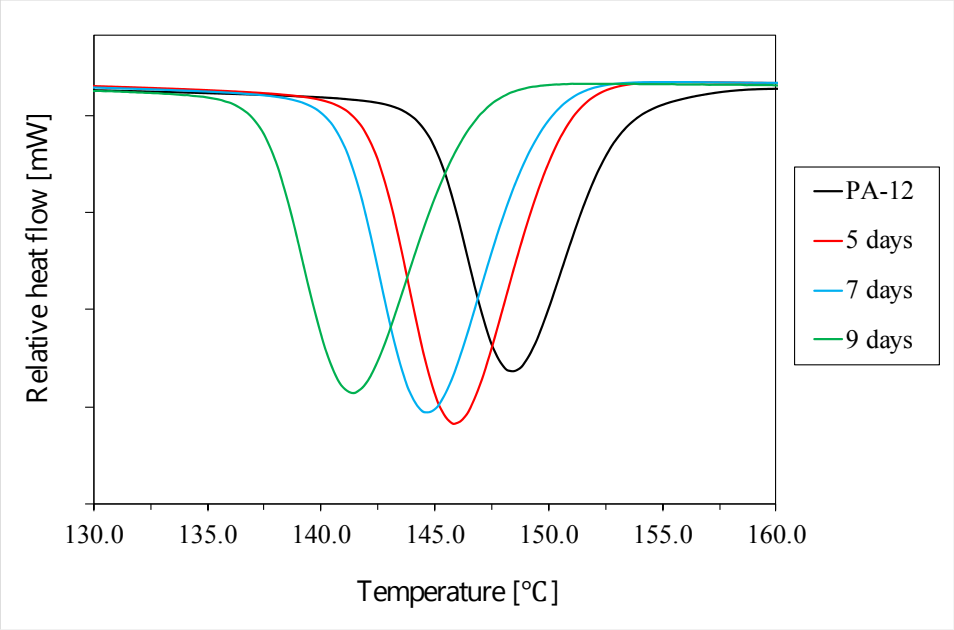

Figure 7.1.4 – Crystallisation behaviour of PA-12 artificially aged at 170 ℃ for 5, 7, and 9 days on cool 1.

The melting endotherm on heat 2 of aged polymer powder is displayed in Figure 7.1.5. The trend in melting temperature on heat 2 was the opposite to that observed on heat 1. On heat 1 ageing caused the melting temperature to shift to higher and then lower temperatures, compared to unaged PA-12. On heat 2, the peak melting temperature of PA-12 aged for 5, 7 and 9 days shifted to lower temperatures with increased aging time. The peak melting temperature PA-12 aged for 0, 5, 7 and 9 days were 179.7, 177,5, 177.5 and 173.5 ℃, respectively. The decrease in melting temperature of PA-12 on heat 2 in comparison to heat 1 is attributed to a transformation in crystal structure. G. Craft et al report that virgin PA-12 powder exists in the α monoclinic form and on melting these regions transform in to the γ (pseudo)hexagonal form due to faster cooling rates (161).

In other work, J. Riedelbauch et al reported an increase in peak melting temperature on heat 2 of PA-12 powder. This was attributed to non-reversible build up reactions in the polymer which suggest an increase in molecular weight (55). The difference between the experimental results and those reported by J.

Riedelbauch et al are likely due to the thermal history of the powder, which leads to different material specific thermal behaviour as a result of degradation mechanisms. In the work by J. Riedelbauch et al, the recycled powder was extracted from the build chamber in MJF and the exact condition of the powder was unclear. Whereas, in this experimental study, the thermal history of the powder is known.

A bimodal melting peak was observed on heat 2, where the low temperature melting peak did not return to a baseline. This was due to melt-recrystallisation and reorganisation of polymer chains on heating (99). In unaged PA-12, the melting endotherm on heat 2 showed a low temperature melting peak at ~ 170 ℃. The curve then then decreased below the baseline, suggesting an exothermic process occurred before the polymer melted at a higher temperature. In PA-12 powder that had been aged for 5 days, the same pattern was observed. In the 7 day aged powder, an exothermic transition was observed before the main melting peak. PA-12 powder that had been aged for 9 days also followed the same pattern. This demonstrates that as the PA-12 aged the thermal properties change with respect to thermal transitions.

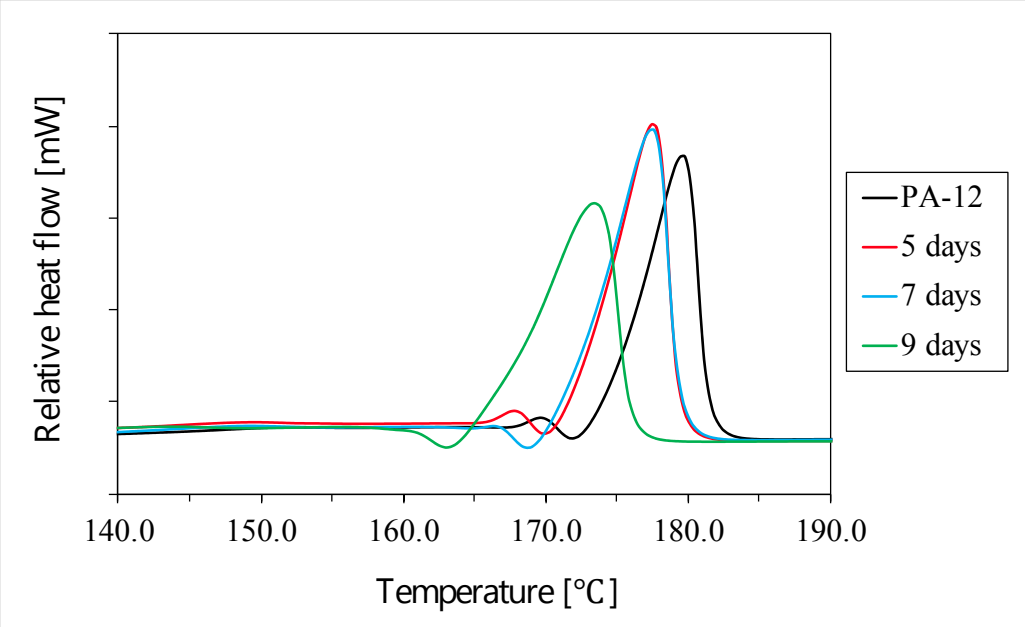

Figure 7.1.5 – Melting behaviour of PA-12 artificially aged at 170 °C for 5, 7, and 9 days on heat 2.

Table 7.1.1 – Table showing the melting and crystallisation parameters of unaged and aged PA-12. Where, T_O is the onset of melting or recrystallisation temperature, T_P is the peak melting or recrystallisation temperature, T_E is the last trace of crystallinity and end recrystallisation temperature, dH_f is the enthalpy of fusion, dHc is the enthalpy of recrystallisation and X_C is the degree of crystallinity.

	Ageing time [Days]	T_O [°C]	T_P [°C]	T_C [°C]	ΔH_f [J/g]	ΔH_c [J/g]	$X_{c,\ melt}$ [%]
Heat 1	0.00	170.50	188.17	193.83	87.88		41.99
	5.00	175.29	189.33	195.87	120.33		57.49
	7.00	175.77	189.00	194.40	116.14		55.49
	9.00	168.51	184.83	191.27	105.10		50.22
Heat 2	0.00	166.75	179.67	183.91	43.26		20.67

	5.00	164.67	177.50	182.45	49.36		23.58
	7.00	166.09	177.50	182.12	49.33		23.57
	9.00	159.41	173.50	179.32	50.66		24.20
Cool 1	0.00	158.10	148.50	141.03		49.32	23.56
	5.00	154.15	145.83	136.94		59.95	28.64
	7.00	153.25	144.67	135.52		59.53	28.44
	9.00	150.29	141.50	132.95		59.91	28.62

7.1.3 Optical microscopy

Optical microscopy was used to observe the effect of the ageing on the microstructure of PA-12 by cooling the samples from 220 ℃ to room temperature at a controlled cooling rate of 0.5 ℃/min.

The microstructure of unaged and aged PA-12 is shown in Figure 7.1.6. In a sample aged for 5 days at 170 ℃, the spherulite size was slightly larger than 0 day aged PA-12. In the 7 day aged sample, the spherulite size was comparable to PA-12 and in the 9 day aged sample the spherulite size was relatively large. This demonstrates that the spherulite size was not significantly impacted by ageing.

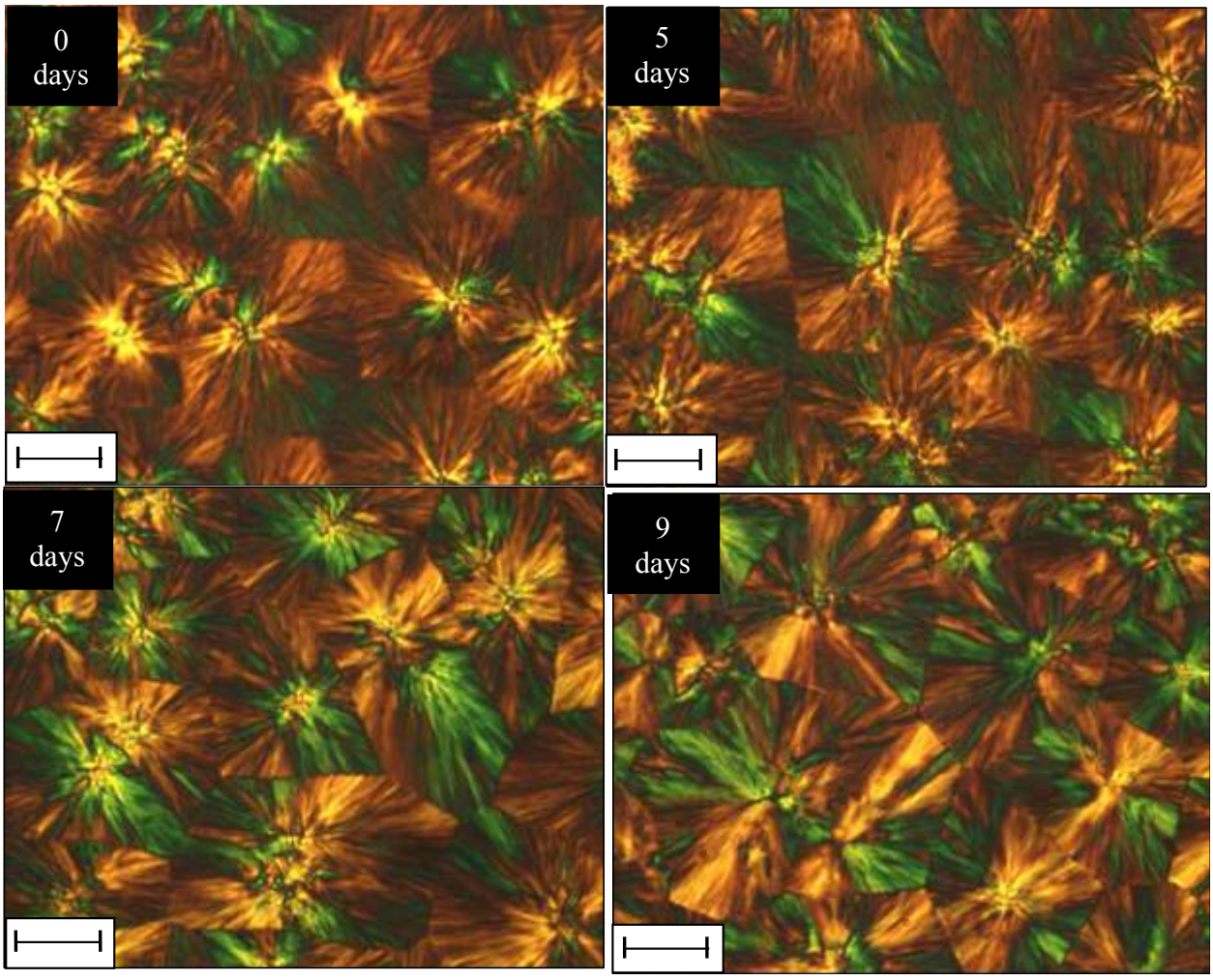

Figure 7.1.6 – Optical microscopy images of unaged and aged PA-12 at 500 x magnification. Scale bar to 50 µm.

7.1.4 Infrared spectroscopy

The FTIR spectra were recorded for aged PA-12 and blends created from aged PA-12. The FTIR spectra of aged PA-12 powder and aged PA-12 samples that were extracted from a DSC pan are displayed in Figure 7.1.7 and Figure 7.1.8. Table 7.1.2 shows the characteristic peaks. The peak assignments for PA-12 are

shown in Table 7.1.2. These were comparable to that reported by H.J O'Conner et al for a PA-12 part manufactured by MJF (61,68).

The FTIR spectra of PA-12 powder aged for 5 and 7 days was comparable to PA-12. This suggests that ageing did not lead to the formation of new peaks, despite visual characterisation showing discolouration. However, in the 9 day aged sample, a small peak at 1716.4 cm^{-1} was observed (see arrow in Figure 7.7). This was assigned to carbonyl containing compounds that had formed due to degredation products from thermooxidative degredation. In other work, degredation products of thermally aged polyamide-6,6 and polyamide-11 were explored (102,162). In both cases, oxidative species such as carboxylic acids were produced and were assigned to peaks at 1710 cm^{-1} and 1711 cm^{-1} (102,162). Mechanisms of the thermo-oxidation of PA-6,6 are highlighted in more detail in (102). The formation of new species arising from degradation is unsurprising since the visual characterisation of PA-12 powder showed significant discolouration from virgin state to the day 9 aged state, as displayed in Figure 7.1.1. Other degredation products of polyamide reported elsewhere inlcude, imides and aldehydes (102).

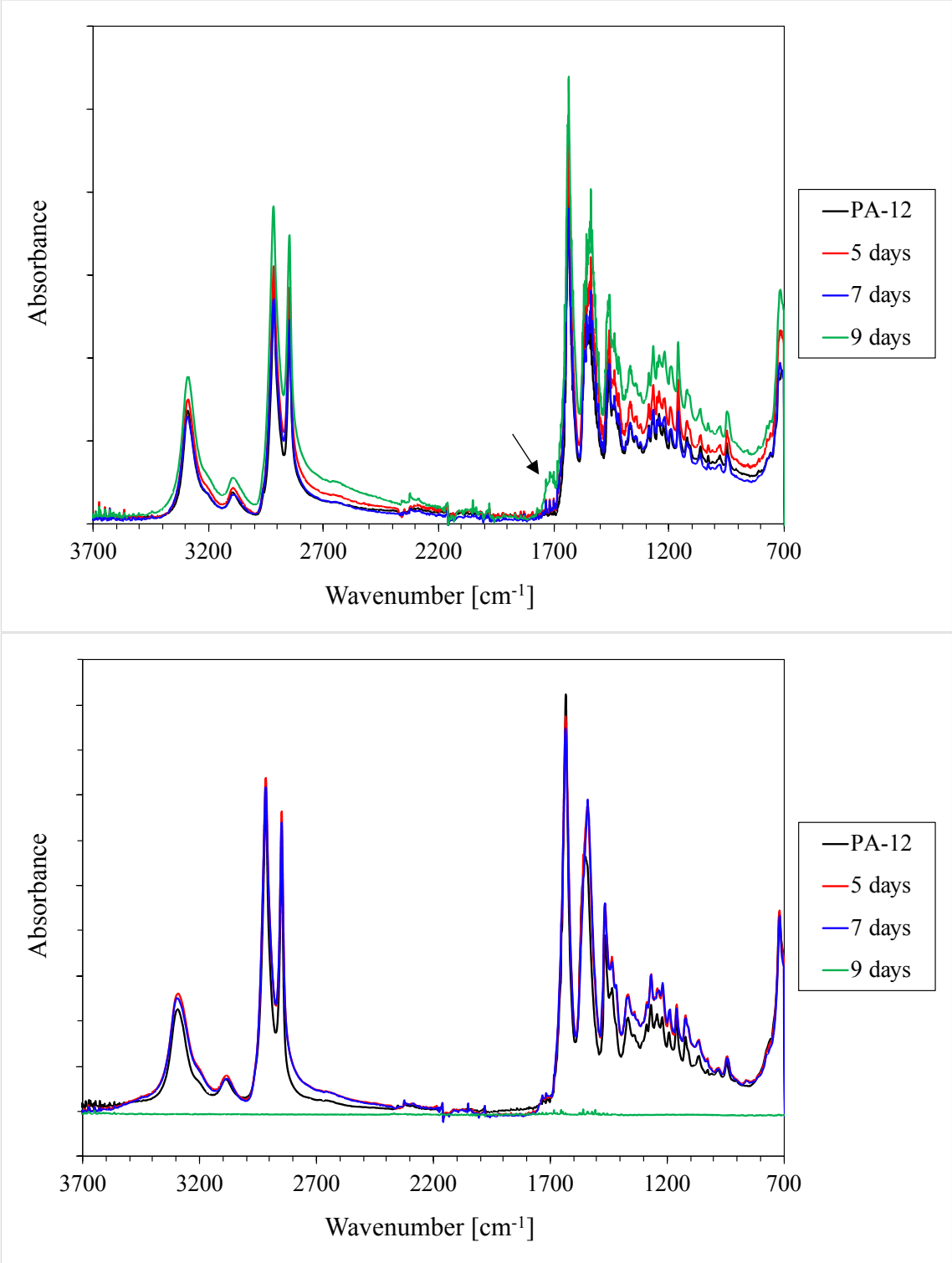

Figure 7.1.7 – FTIR-ATR spectra of PA-12 powder (top) and DSC samples (bottom) aged at 170 ℃ for 0, 5, 7 and 9 days.

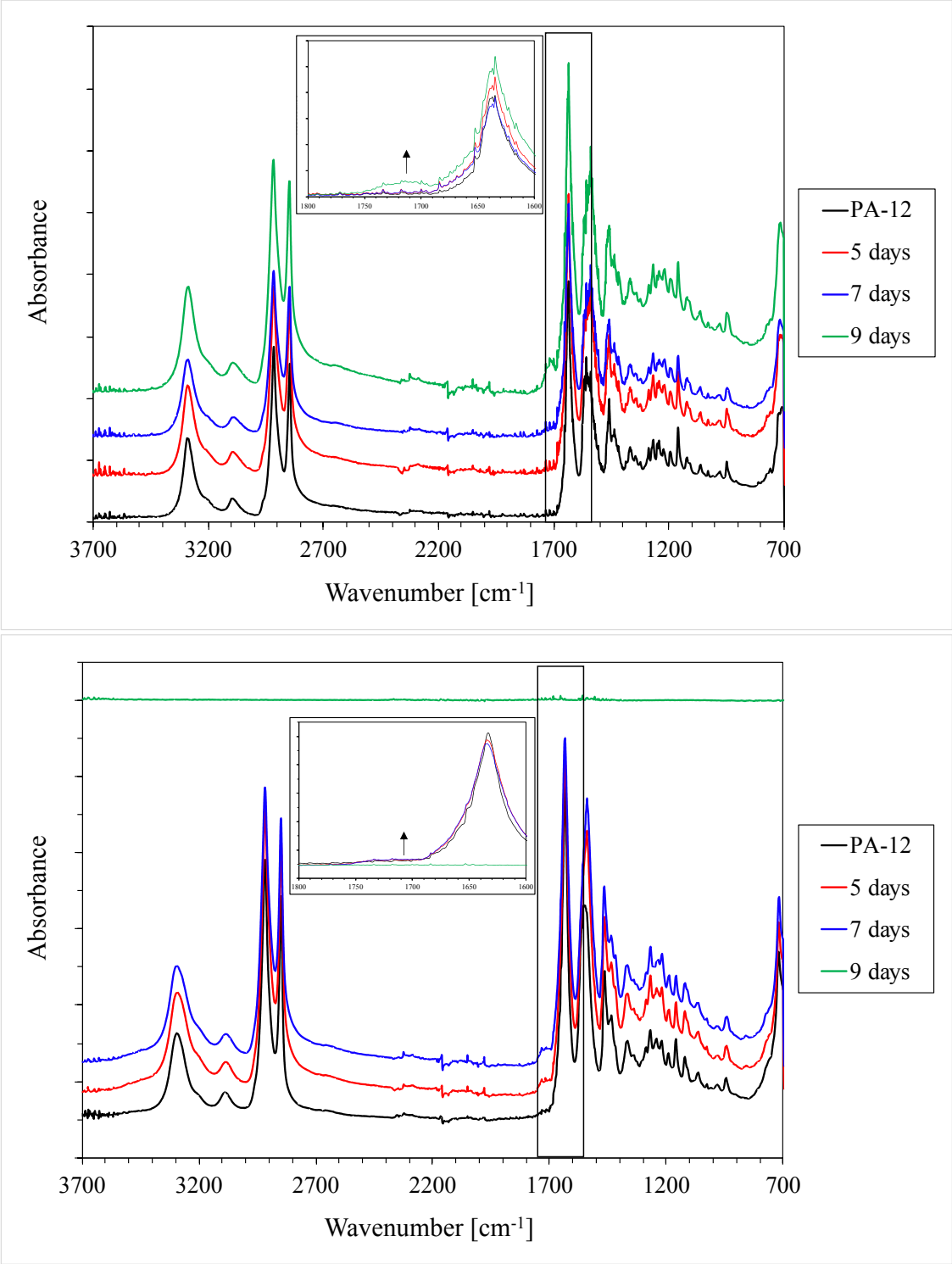

Figure 7.1.8 – Stacked FTIR spectra of aged PA-12 powder (top) and DSC samples of aged powder (bottom). The inset shows the carbonyl region between 1600 – 1800 cm^{-1}.

Figure 7.1.9 shows a peak related to the overtone of the amide II band at 3100 – 3070 cm^{-1}. M. Pliquet et al studied the thermal degredation of injection moulded PA-6,6. In their work, the amide II band progressively dissapeared with with increased ageing time. This was due to N-H deformation and C-N bond stretching (102).

In PA-12 powder that was thermally aged, the amide II band was not affected by ageing time and the peak was consistent for all samples. In aged PA-12 that was extracted from DSC pans, the overtone of the amide II band at 3100 – 3070 cm^{-1} was also not affected, suggesting N-H deformation did not occur. In (102), the time period allowed for thermal degredation to occur was up to 2000 hrs at 140 ℃, whereas in this work an upper limit of 9 days at 170 ℃ was used. Therefore, the dissapearance of the band at 3100 – 3070 cm^{-1} was not observed in this work due to ageing taking place over a shorter time period, despite ageing at a higher temperature. This shows that under conditions used in PBF techniques, where powder is exposed to less harsh conditions, the N-H band is resistant to degredation.

The spectra of unaged and aged PA-12 extracted from DSC pans were also obtained, as displayed in Figure 7.1.8. The spectra of samples aged at 170 ℃ for 5 and 7 days were comparable to PA-12. This suggests after multiple heat-cool cycles there were no major products from degradation, despite visual characterisation showing sample discolouration. The spectrum for a sample aged for 9 days displayed a poor unreadable signal and was therefore incomparable to PA-12. This is also displayed in Figure 7.1.8.

Interestingly, in DSC samples a weak shoulder peak emerged at 3400 – 3600 cm^{-1} was observed, this was assigned to the free amide moiety (102). This suggests reorganisation of the crystal structure after multiple heat-cool cycles. The free N-H band shows a population of N-H bonds within the polymer are not hydrogen bonded.

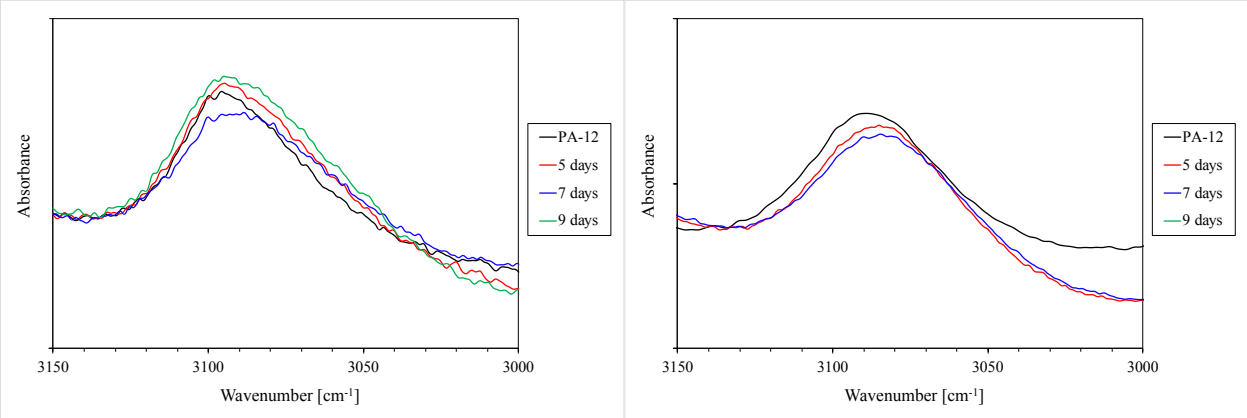

Figure 7.1.9 – The amide II band in aged PA-12 powder (left) and aged PA-12 samples subjected to DSC thermal analysis (right).

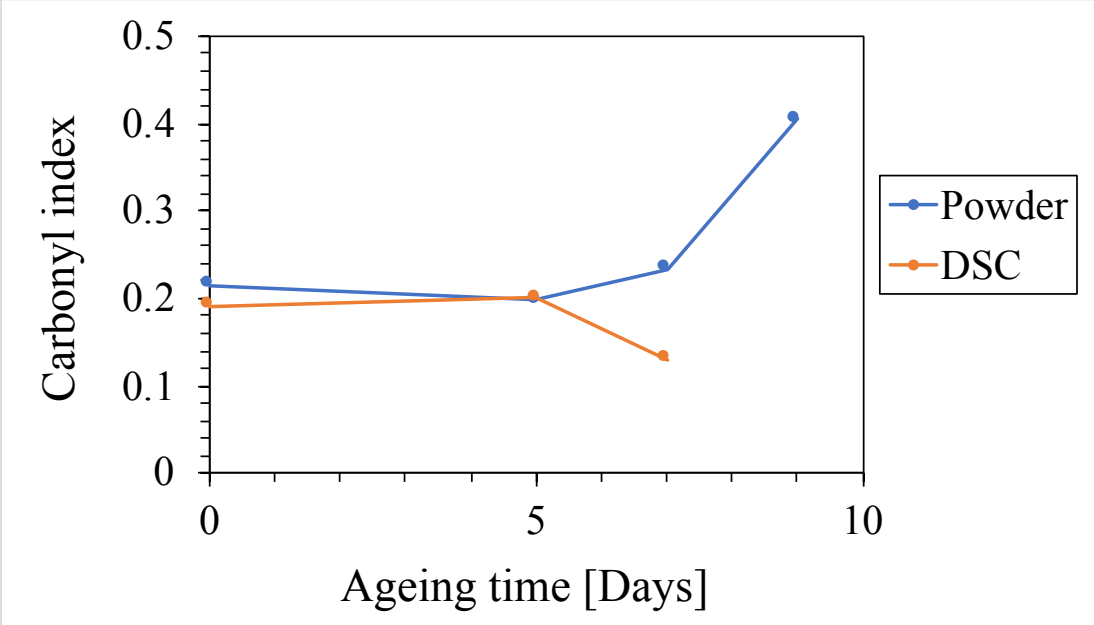

Figure 7.1.10 – The carbonyl index as a function of ageing time for PA-12 powder that had been aged at 170 ℃ for 5, 7 and 9 days (blue) and ages PA-12 that had been subjected to a multiple heating and cooling cycle in the DSC (orange).

The carbonyl index for both aged PA-12 powder and aged PA-12 samples that had been extracted from an aluminium pan is displayed in Figure 7.1.10. The carbonyl index was defined by the ratio of the oxidation band (C=O, 1710 – 1760 cm^{-1}) and the reference band (CH_2 scissor, 1458 – 1468 cm^{-1}), as per (10).

The carbonyl index for PA-12 powder increased with ageing time. A large increase was observed in the 9 day aged sample. This agrees with data, such that in the region of 1690 – 1754 cm^{-1} a peak at *ca.*1716 cm^{-1} that increased with ageing time, suggesting products from thermo-oxidative degradation were present. Meanwhile, the carbonyl index did not vary significantly for DSC extracted samples. The peak at *ca.*1716 cm^{-1} that is affected by oxidative degradation, was not present in DSC extracted samples (see the inset of Figure 7.1.8). This is interesting in that degradation is an irreversible process, therefore degradation products observed in powder are expected to be observed in DSC extracted samples. The reason why this may have not been the case can be due to reorganisation of the crystal structure after melt-recrystallisation.

In the work of W. Dong and P. Gijsman (10), the carbonyl index was reported for PA-6 films that were aged at 170 ℃ up to 300 hrs. The carbonyl index was greater than that reported in this study with aged PA-12. This is due to harsher ageing conditions and PA-6 containing more amide and carbonyl groups than PA-12, therefore making PA-6 more susceptible to degradation mechanisms.

Table 7.1.2 – Table showing peak assignments for characteristic wavelength of unaged and aged PA-12 powder and DSC samples.

Peak assignment		Hydrogen bonded N-H stretch	CH2 asymmetric stretch	CH2 symmetric stretch	C=O stretch	C-N stretch, C=O in plane bending	CH bend, CH2 twist	C-N stretch, C=O in plane bending	C-C stretch	CONH in plane	CH2 rocking
H. O'Conner et al	(68)	3297	2918	2850	1639	1545	1370	1269	1122	944	720
Powder	PA-12	3290.04	2916.50	2846.70	1634.73	1538.92	1367.91	1267.54	1121.33	948.19	719.40
	170 °C 5 days	3291.15	2916.39	2846.84	1634.70	1541.44	1368.18	1267.68	1121.91	947.97	716.97
	170 °C 7 days	3291.06	2916.56	2847.34	1634.68	1538.85	1368.19	1267.83	1120.81	947.87	717.39
	170 °C 9 days	3286.71	2917.37	2847.99	1634.63	1541.37	1367.96	1267.55	1121.09	947.75	716.07
DSC Samples	PA-12	3289.89	2917.47	2849.15	1634.28	1539.46	1367.83	1268.78	1121.40	945.38	719.26
	170 °C 5 days	3291.95	2917.11	2848.96	1634.29	1539.47	1368.33	1268.29	1121..13	943.37	719.22
	170 °C 7 days	3295.62	2917.60	2849.42	1634.30	1539.35	1368.40	1268.38	1121.03	942.78	718.00

7.2 – Melting and recrystallisation behaviour of aged PA-12 blends.

In MJF, PA-12 powder is often refreshed, a large proportion of powder is reused in subsequent builds to which virgin PA-12 powder is added. Therefore, the FA and DA are deployed onto the surface of used PA-12 powder as well as virgin PA-12 powder. The aged PA-12 blends were created as per section 2.3, using PA-12 powder aged at 170 ℃ in a ventilated oven for 7 days. All powders were produced using PA-12 powder (batch 2).

Following Chapter 6.2 which analysed the melting and recrystallisation behaviour of virgin PA-12 blends, the aim of this work is to analyse the melting and recrystallisation behaviour of aged PA-12 blends on heat 1 and cool 1. The melting behaviour was recorded on heat 1 in order to observe the thermal history of the sample. The recrystallisation behaviour was recorded on cool 1 in order to observe the effect of the agents and solvents on the recrystallisation behaviour of aged PA-12.

The blends were heated at a controlled rate of 10 ℃/min from 25 – 220 ℃, where they were stored at an upper isotherm of 220 ℃ for 5 minutes. The melting peak was evaluated, from which the onset melting temperature, peak melting temperature, last trace of crystallinity, enthalpy of fusion and degree of crystallinity were recorded. This data is displayed in Table 7.2.1 and Figure 7.2.1.

The melting behaviour of aged PA-12 (aged at 170 ℃ for 5, 7 and 9 days) is shown in Chapter 7.1. The data obtained for PA-12 powder aged at 170 ℃ for 7 days was used as a benchmark for comparison against aged PA-12 blends since the PA-12 blends were created from 7 day aged PA-12 powder.

In the aged PA-12/FA blends, the FA had a significant effect on the melting behaviour of aged PA-12. Generally, the T_g of aged PA-12/FA blends shifted unsystematically to slightly higher and lower

temperatures than aged PA-12. The T_g of the 1, 5, 10 and 20 wt.% FA blends were 39.83, 46.17, 40.50 and 42.50 ℃ respectively. The T_g of the aged 5 wt.% blend was greater than the aged 1, 10 and 20 wt.% FA, this is an anomalous result.

The melting behaviour of the aged PA-12/FA blends were affected by the addition of the FA. As composition of the FA increased, a peak melting temperature depression was observed. The peak melting temperature of the 1, 5, 10 and 20 wt.% FA blends were 187.5, 183.3, 180.3 and 174.7 ℃, respectively. This is consistent in the action of the FA acting as a plasticiser whereby the FA promoted melting of the crystalline region.

The onset melting temperature and last trace of crystallinity also shifted to lower temperatures as the composition of the FA increased. Moreover, the enthalpy of fusion (or degree of crystallinity) increased with the composition of FA, showing evidence of post-crystallisation.

The melting region, defined as the difference between the onset melting temperate and last trace of crystallinity, increased with composition of FA and both shifted towards lower temperatures as the composition of the FA increased. This suggests that with increasing composition of FA, the lamellar are thinner and less sTable, consequently melting at lower temperatures (23). Interestingly, for the 20 wt.% FA sample, the melting endotherm displayed a shoulder peak at lower temperature. This was due to melt-recrystallisation and reorganisation of polymer chains on heating (99).

This data shows that the FA acted as a plasticiser and enhanced the mobility of the amorphous regions and affected the crystalline regions by influencing the melting temperature and the degree of crystallinity.

In the aged PA-12/DA blends, the DA had a significant effect on the melting behaviour of aged PA-12. The T_g of aged PA-12/DA blends shifted unsystematically to slightly higher temperatures than aged PA-12. The T_g of the 1, 5, 10 and 20 wt.% DA blends were 46.83, 42.17, 41.50 and 42.83 ℃ respectively. This suggests that the DA immobilised the amorphous regions of aged PA-12. Interestingly, the 1 wt.% DA blend exhibited the largest increases in T_g, when compared to aged PA-12 powder. This was

unexpected since this blend contained the smallest amount of DA. The T_g of the 1 wt.% DA blend was close to the T_g of unaged PA-12 powder (47.3 ℃). This result could be due to sample variation.

As composition of the DA increased, a peak melting temperature depression was observed. The peak melting temperature of the 1, 5, 10 and 20 wt.% DA blends were 188.0, 187.0, 184.8 and 180.5 ℃, respectively. This data suggests that the DA behaved as a plasticiser and promoted melting of the crystalline region. The onset melting temperature and last trace of crystallinity also followed the same trend. Moreover, the enthalpy of fusion, or degree of crystallinity, increased slightly with the addition of the DA. However, the overall increase was considered insignificant, when compared to the degree of crystallinity of aged PA-12. The melting region increased with the addition of DA and the melting endotherm shifted to lower temperatures. This shows that the DA influenced lamellar thickness, whereby the lamellar were thinner and less sTable (23).

Similar to the unaged PA-12 blends, it was clear that the FA and DA influenced the melting behaviour of aged PA-12. To further investigate the effect of the FA and DA on the thermal properties of PA-12, the FA and DA were deconstructed into their key components and blends of aged PA-12/water, PA-12/CB, PA-12/2-PYR and PA-12/2-PYR/water were created.

In the aged PA-12/water blends, increasing volumes of water did not significantly influence the melting behaviour of aged PA-12. The T_g of the 1, 5, 10 and 20 wt.% water blends were 39.46, 48.83, 49.87 and 49.15 ℃, respectively. The T_g of the 7 day aged PA-12 powder was 39.50 ℃. Therefore, this data shows that the T_g of the 5, 10 and 20 wt.% water blend significantly increased, compared to aged PA-12 powder. In these blends, the shape of the T_g curve was different compared to virgin PA-12, aged PA-12, and 1 wt.% water. This behaviour is unusual in that water typically would cause the T_g to shift to lower temperatures by acting as a plasticizer due to the presence of polar groups (163). The onset melting temperature, peak melting temperature and the last trace of crystallinity were comparable to aged PA-12. The average peak melting temperature of the blends was 188.6 ℃, where the peak melting

temperature of aged PA-12 was 189.0 ℃. The melting region increased slightly with an increasing content of water. A maximum increase of 3 ℃ was observed. The enthalpy of fusion and the degree of crystallinity of the 1, 5 and 10 wt.% water blend were comparable to aged PA-12. Whereas the degree of crystallinity for the 20 wt.% water blend increased by 12 %. This was due to post-crystallisation. R. Seltzer et al studied the effect of water conditioning on the thermal properties of PA-12 composites fabricated by (138). In their work, PA-12 SLS samples were conditioned by submerging the samples in water at 90 ℃ (above the T_g of PA-12) for 80 days. An increase in the degree of crystallinity was reported for samples that had been conditioned. This was a result of 2 possibilities; firstly, hydrolysed molecules fold more easily, thus increasing the degree of crystallinity and rate of crystallisation (164); secondly, both hydrolysation and plasticization of the polymer matrix enhanced the chain mobility, causing the molecular structure to rearrange to create more thermodynamically favourable configurations.

In the aged PA-12/CB blend, the composition of carbon black did not significantly influence the melting behaviour of aged PA-12. The T_g of the 1, 5, 10 and 20 wt.% CB blends were 41.50, 42.30, 42.67, 45.17 ℃ respectively. The T_g of the 20 wt.% blend was greater than the 1, 5, and 10 wt.% blends. This may have been due to the presence of residual solvents present within the blend that had not evaporated during the drying process. The onset melting temperature, peak melting temperature and the last trace of crystallinity were comparable to aged PA-12. The average peak melting temperature of the blends was 188.8 ℃, where the peak melting temperature of aged PA-12 was 189.0 ℃. The melting region increased slightly with an increasing content of carbon black where a maximum increase of 4 ℃ was observed. The enthalpy of fusion and degree of crystallinity increased significantly with the addition of carbon black as a result of post-crystallisation. This could be due to the chemicals within the FA not being entirely evaporated from the carbon black, despite the drying process mentioned in Chapter 2.

In the aged PA-12/2-PYR blends, 2-PYR was added to aged PA-12 to create blends that were compositionally identical to the 2-PYR present in the FA and DA blends. The data shows that 2-PYR influenced the melting properties of aged PA-12. The T_g of aged PA-12/2-PYR blends shifted unsystematically to slightly lower and higher temperatures than aged PA-12. The slight shift in T_g showed that 2-PYR did not significantly influence the T_g of PA-12. The melting region of aged PA-12 was significantly influenced by the addition of 2-PYR when the 2-PYR was present in excess of 4.07 wt.% 2-PYR, from which the peak melting temperature shifted to lower temperatures. The peak melting temperature of the 0.10, 0.38, 0.50, 1.05, 1.97, 2.33, 4.07 and 8.72 wt.% 2-PYR blend was 187.3, 187.3, 187.6, 187.6, 187.5, 186.7, 186.0, 183.7 and 178.0 ℃, respectively. The onset melting temperature and last trace of crystallinity also displayed the same trend. The enthalpy of fusion and degree of crystallinity were comparable to aged PA-12. However, the enthalpy of fusion and degree of crystallinity for the 4.07 wt.% and 8.72 wt.% 2-PYR blend increased slightly, when compared to aged PA-12 showing evidence of post-crystallisation. The melting region increased with the addition of 2-PYR, when compared to the melting region of aged PA-12. This coupled with a decrease in melting temperature indicated that 2-PYR influenced the lamellar thickness, whereby lamellar were thinner and less sTable and therefore melted at lower temperatures. Again, this was significant when the 2-PYR was present in excess of 4.07 wt.% 2-PYR.

In the aged PA-12/2-PYR/water blends, 2-PYR and water was added to aged PA-12 to create blends that were compositionally identical to the 2-PYR and water present in the FA and DA blends.

In the blends that were compositionally identical to the FA, the melting properties were influenced, in that the T_g was comparable to aged PA-12 and the peak melting temperature shifted to lower temperatures when the composition (relative to 2-PYR) increased. The peak melting temperature of the 0.38, 1.97, 4.07 and 8.72 wt.% 2-PYR was 187.0, 183.2, 182.5 and 181.5 ℃, respectively. The onset melting temperature and last trace of crystallinity followed the same trend. The melting region increased and shifted to lower temperatures as the composition increased. Furthermore, the enthalpy of fusion, or the degree of crystallinity, increased as the composition (relative to 2-PYR) increased, showing

evidence of post-crystallisation. It is possible that the increase in the degree of crystallinity was due to the presence of water and the hydrogen bond interaction between water and 2-PYR.

In the blends that were compositionally identical to the DA, the melting properties were influenced, in that the T_g shifted to slightly higher temperature than aged PA-12 when the composition (relative to 2-PYR) increased. This suggests that the mobility of polymer chains in the amorphous regions was hindered.

The peak melting temperature shifted unsystematically to slightly lower temperatures than aged PA-12, where the peak melting temperature of the 0.10, 0.50, 1.05 and 2.33 wt.% 2-PYR (relative to the DA) was 172.6, 169.9, 172.8 and 169.51 ℃. The onset melting temperature and last trace of crystallinity also followed the same trends. The melting region remained constant at ~ 24 ℃ and was not affected by the composition but was greater than the melting region for aged PA-12. Since the melting region remained constant and the peak melting temperature was comparable to PA-12, it can be said that the lamellar thickness was not significantly affected by the composition. Moreover, the enthalpy of fusion, or the degree of crystallinity, was comparable to aged PA-12.

Since the trends of the PA-12/2-PYR/water blends were similar to the PA-12/2-PYR blends, the data suggests that 2-PYR influenced the melting properties of aged PA-12 by behaving as a plasticizer, influenced lamellar thickness and induced post-crystallisation and water did not significantly influence melting behaviour of PA-12.

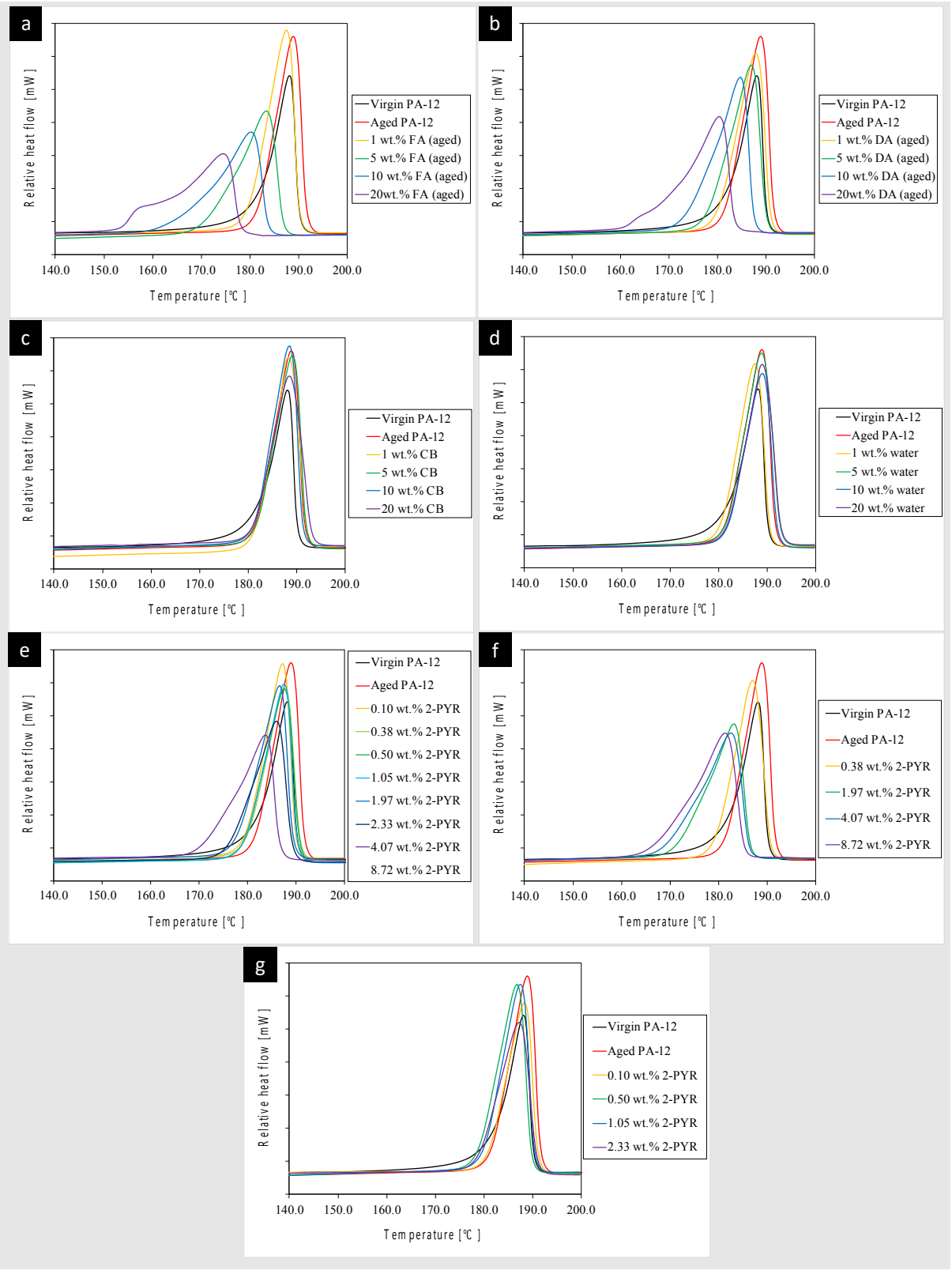

Figure 7.2.1 – The melting behaviour of aged PA-12 blends on heat 1, a) PA-12/FA, b) PA-12/DA, c) PA-12/CB, d) PA-12/water, e) PA-12/2-PYR, f) PA-12/2-PYR/water (FA) and g) PA-12/2-PYR/water (DA).

The blends were cooled at a controlled rate of 10 ℃/min from 220 – 25 ℃. The crystallisation peak was evaluated, from which the onset crystallisation temperature, peak melting temperature, enthalpy of crystallisation and degree of crystallinity were recorded. This data is displayed in Table 7.2.2 and Figure 7.2.2.

In the aged PA-12/FA blends, the FA had a significant effect on the crystallisation behaviour of PA-12. The recrystallisation behaviour was complex in that the peak crystallisation temperature increased and then decreased as the composition of the FA increased, when compared to the peak crystallisation temperature of aged PA-12. The peak crystallisation temperature of the 1, 5, 10 and 20 wt.% FA blends were 145.0, 147.0, 145.2 and 140.3 ℃, respectively. The onset crystallisation temperature also displayed the same trend. The initial increase in peak crystallisation temperature would suggest that at low compositions the FA acted as a nucleating agent. The decrease in crystallisation temperature would suggest that nucleation was hindered. To investigate this further, the degree of supercooling was evaluated. The degree of supercooling decreased with increasing composition of FA. This suggests that the FA facilitated nucleation. The enthalpy of crystallisation, and degree of crystallinity, increased slightly when the composition of the FA increased.

In the aged PA-12/DA blends, the DA influenced PA-12 in that the crystallisation temperature shifted to lower temperatures as the composition of the DA increased. The peak crystallisation temperature of the 1, 5, 10 and 20 wt.% DA were 144.7, 144.0, 143.3, 141.0 ℃, respectively. The onset crystallisation temperature displayed the same trend. The degree of supercooling decreased slightly as the composition of DA increased, suggesting the DA facilitated nucleation. The enthalpy of crystallisation, and degree of crystallinity, remained constant and was comparable to aged PA-12. This data suggests the DA influenced the crystallisation temperature more than the degree of crystallinity on cooling.

In the aged PA-12/water blends, the recrystallisation behaviour was not affected by the addition of water. The onset recrystallisation temperature and peak crystallisation temperature were comparable to PA-12. The average peak crystallisation temperature for aged PA-12/water blends was 144.8 ℃, the peak crystallisation temperature for aged PA-12 was 144.7 ℃. The enthalpy of crystallisation and degree of crystallinity of the 1, 5 and 10 wt.% water samples were comparable to aged PA-12. Whereas, the degree of crystallinity in the 20 wt.% water sample increased. This can be due to post-crystallisation if the water had not entirely evaporated during the drying stage. Alternatively, this can be an anomalous result. The degree of supercooling was also unaffected by the addition of water and was comparable to aged PA-12. This demonstrates that water did not affect the crystallization behaviour, in that water did not facilitate nor hinder crystallisation. However, in large quantities water increased the degree of crystallinity.

In the aged PA-12/CB blends, the recrystallisation behaviour was affected by the addition of carbon black. In the 1 wt.% CB blend, the onset crystallisation temperature and peak crystallisation temperature were comparable to aged PA-12. However, as the content of carbon black increased, the onset crystallisation temperature and peak crystallisation temperature shifted to higher temperatures. The onset crystallisation temperature for the 1, 5, 10 and 20 wt.% CB blend were 153.4, 155.6, 154.2 and 155.1 ℃, respectively. The peak crystallisation temperature for the 1, 5, 10 and 20 wt.% CB blend were 144.7, 147.8, 147.0 and 146.8 ℃, respectively. The shift in the onset crystallisation temperature and peak crystallisation temperature to higher temperatures suggests that carbon black facilitated nucleation by acting as a nucleation agent. This agrees with the degree of supercooling, which decreased as the composition of carbon black increased. Moreover, the enthalpy of crystallisation and degree of crystallinity on cooling increased as the content of carbon black increased. This is consistent with the action of a nucleating agent which induces heterogenous nucleation. However, the presence of carbon black can also influence crystallisation in that with increasing content of carbon black, the radial growth of spherulites is hindered. This data demonstrates that carbon black influenced the recrystallisation behaviour by facilitating nucleation and increasing the degree of crystallinity on cooling. In a study

exploring the effect of carbon nanotubes on the electrical conductivity and thermal properties of PA-12, it was suggested that an increase in the degree of crystallinity, determined by the enthalpy of crystallisation, was reported due to nanotubes being expelled to the amorphous phase (159). Despite the size of carbon black in the FA and DA not being of nanoscale, this can also be true in the PA-12/FA and PA12/CB blends, where the slight increase in the degree of crystallinity is due to the carbon black being rejected from the crystalline regions.

In the aged PA-12/2-PYR blends, the 2-PYR had a significant effect on the recrystallisation behaviour of PA-12 in that the crystallisation temperature decreased as the composition of 2-PYR increased. The peak crystallisation temperature of the 0.10, 0.38, 0.50, 1.05, 1.97, 2.33, 4.07 and 8.72 wt.% 2-PYR blend were 144.3, 144.0, 144.0, 144.0, 143.3, 142.8, 140.8 and 137.3 ℃, respectively. The onset crystallisation temperature also followed the same trend. The decrease in crystallisation temperature suggests that crystallisation was hindered as the composition of 2-PYR increased. However, the degree of supercooling decreased slightly indicating that 2-PYR facilitated nucleation. The enthalpy of crystallisation and the degree of crystallinity decreased slightly as the composition of 2-PYR increased.

In the aged PA-12/2-PYR/water blends that were compositionally identical to the FA, the peak crystallisation temperature decreased as the composition increased. The peak melting temperature of the 0.38, 1.97, 4.07 and 8.72 wt.% 2-PYR was 143.7, 141.2, 140.3 and 140.3 ℃, respectively. The onset crystallisation temperature also displayed the same trend. The degree of supercooling decreased, suggesting that crystallisation was facilitated. The enthalpy of crystallisation and degree of crystallinity was comparable to aged PA-12.

In the aged PA-12/2-PYR/water blends that were compositionally identical to the DA, the recrystallisation behaviour such as the onset and peak crystallisation temperature and the enthalpy of crystallisation were comparable to aged PA-12.

This data shows that in the PA-12/FA and PA-12/DA blends, similar trends in melting and recrystallisation behaviour were observed. The FA and DA were deconstructed and further blends were created to examine the effect of individual components on the melting and recrystallisation behaviour of aged PA-12 powder. This work demonstrated that 2-PYR and carbon black had a significant effect on the crystallisation behaviour of PA-12. Aged PA-12 was of interest since in PBF techniques, such as MJF, powder is often refreshed with each processing cycle and both virgin and aged powder is used to fabricate subsequent components.

Further deconstruction of the FA and DA showed that water did not influence the melting and recrystallisation behaviour of PA-12. However, water increased the degree of crystallinity, when present in large quantities. In the aged PA-12/CB blends, the carbon black affected the degree of crystallinity on melting and cooling. On recrystallisation, the onset and crystallisation temperature shifted to higher temperatures, showing that CB acted as a nucleating agent. This demonstrates that carbon black influenced the melting and recrystallisation behaviour of PA-12. Overall, 2-PYR had the greatest influence on the melting and recrystallisation behaviour of aged PA-12, where the melting and recrystallisation temperature decreased with increasing content of 2-PYR. The degree of supercooling also decreased with increasing composition of 2-PYR. This showed that 2-PYR behaved as a plasticizer to enhance mobility of polymer chains to promote melting of the crystalline phase. Similarly, on cooling 2-PYR facilitated crystallisation. The degree of crystallinity also increased slightly with the addition of 2-PYR, which is consistent with the action of a plasticizer. Interestingly, in the 3 component blends of aged PA-12/2-PYR/water the results were comparable to blends of aged PA-12/2-PYR. This showed that water did not significantly influence the system. This agrees with the trends identified in the aged PA-12/FA and aged PA-12/DA blends.

This shows that both 2-PYR and CB contribute to the melting and recrystallisation behaviour observed in the aged PA-12/FA blends, while only 2-PYR affects the melting and recrystallisation behaviour in aged PA-12/DA blends (due to carbon black not being present).

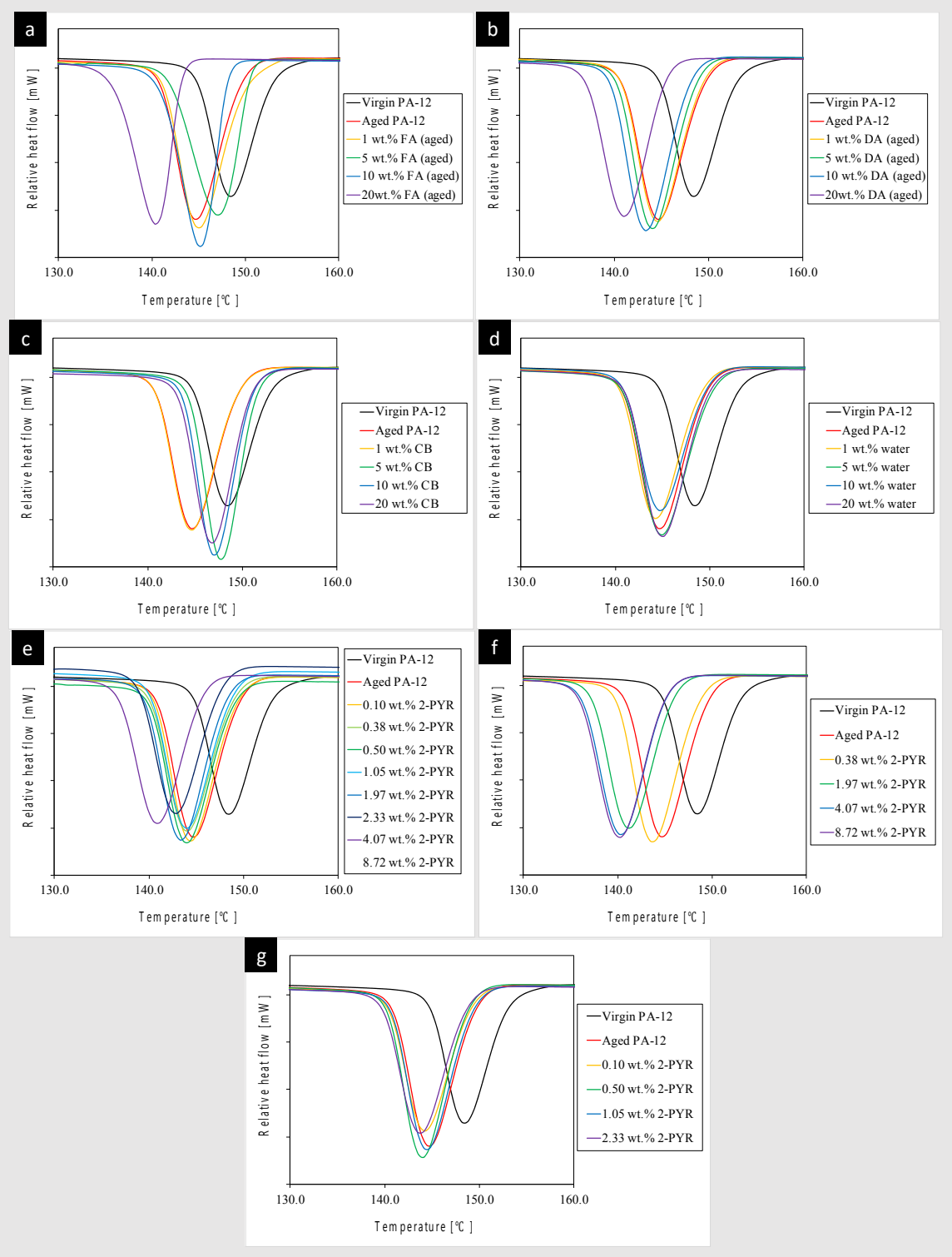

Figure 7.2.2 – The crystallisation behaviour of aged PA-12 blends on cool 1, a) PA-12/FA, b) PA-12/DA, c) PA-12/CB, d) PA-12/water, e) PA-12/2-PYR, f) PA-12/2-PYR/water (FA) and g) PA-12/2-PYR/water (DA).

Table 7.2.1 – Melting properties of aged PA-12 blends on heat 1 and heat 2. Where T_P - Peak Melting Temperature, T_E - Last Trace of Melting Temperature, T_O - Onset of Melting, X_c – Degree of Crystallinity and ΔH is the heat of fusion.

Blend	wt.%	**Heat 1**						**Heat 2**				
		T_g (°C)	T_P (°C)	T_O (°C)	T_E (°C)	ΔH (Jg^{-1})	Xc (%)	T_P (°C)	T_O (°C)	T_E (°C)	ΔH (Jg^{-1})	Xc (%)
PA-12 (7 day aged)		40.33	189.3	175.77	193.83	87.88	41.99	177.5	166.09	182.12	49.33	23.57
FA	1.00	39.83	187.50	172.35	193.87	121.76	58.17	176.50	164.25	181.40	53.43	25.53
	5.00	46.17	183.33	161.26	190.27	120.93	57.78	173.67	155.00	180.03	53.37	25.50
	10.0	40.50	180.33	154.57	188.14	121.10	57.86	171.00	150.09	177.05	56.13	26.82
	20.0	42.50	174.67	146.54	183.02	134.36	64.20	165.83	144.76	170.93	60.10	28.71
DA	1.00	46.83	188.00	171.07	195.11	117.69	56.23	177.17	162.96	182.68	51.60	24.65
	5.00	42.17	187.00	170.40	193.54	115.05	54.97	176.33	163.39	182.00	50.70	24.23
	10.0	41.50	184.83	165.38	191.13	120.28	57.47	174.67	159.79	179.62	53.03	25.34

	20.0	42.83	180.50	153.35	189.70	120.87	57.75	171.67	154.57	178.22	51.34	24.53
CB	1.00	41.50	188.33	173.21	197.07	119.79	57.23	177.33	163.49	182.72	53.09	25.37
	5.00	42.30	189.71	174.91	195.93	122.61	58.58	177.67	164.96	183.59	49.94	23.86
	10.0	42.67	188.67	174.63	195.68	134.19	64.11	177.17	164.05	182.62	54.98	26.27
	20.0	45.17	188.50	174.91	197.13	149.73	71.54	177.33	164.10	182.74	59.65	28.50
Water	1.00	39.46	187.50	174.15	193.83	121.20	57.91	176.67	162.69	182.04	53.54	25.58
	5.00	48.83	188.83	175.12	196.69	120.29	57.47	177.50	164.53	182.45	52.27	24.98
	10.0	49.87	189.00	176.48	197.09	124.36	59.41	177.50	164.96	182.74	54.34	25.96
	20.0	49.15	189.00	175.20	196.83	141.40	67.56	177.33	164.53	183.27	63.98	30.57
2-PYR	0.10	39.57	187.33	170.25	196.53	120.94	57.78	176.67	162.54	181.60	53.66	25.64
	0.38	39.50	187.67	169.51	194.87	115.36	55.12	177.00	163.25	182.88	50.40	24.08
	0.50	42.60	187.67	168.79	196.60	115.41	55.14	163.34	176.83	182.02	51.13	24.43
	1.05	41.20	187.50	169.85	194.68	115.58	55.22	176.83	163.25	182.02	51.24	24.48

	1.97	40.33	186.67	166.91	193.12	114.54	54.72	176.17	160.55	181.88	50.99	24.36
	2.33	40.83	186.00	166.95	194.28	109.81	52.46	175.67	159.55	181.86	49.50	23.65
	4.07	38.20	183.67	161.58	191.13	110.22	52.66	173.67	157.70	182.22	49.07	23.44
	8.72	38.54	178.00	149.63	184.86	125.56	59.99	169.00	149.31	173.92	65.69	31.38
FA (2-PYR + Water)	0.38	40.17	187.00	171.04	194.77	121.57	58.09	176.33	160.95	181.88	54.05	25.82
	1.97	41.67	183.17	161.24	190.27	118.14	56.44	173.83	156.27	179.26	42.30	20.21
	4.07	38.83	182.50	161.42	189.79	118.33	56.53	172.83	155.74	178.66	52.40	25.04
	8.72	38.17	181.50	156.99	189.37	129.35	61.80	172.00	154.43	178.01	56.08	26.79
DA (2-PYR + Water)	0.10	39.83	188.33	172.57	197.04	112.04	53.53	177.33	162.82	183.45	49.34	23.57
	0.50	46.33	186.83	169.92	194.53	123.02	58.77	176.17	162.43	182.20	54.52	26.05
	1.05	49.83	187.50	172.78	194.26	119.96	57.31	176.83	164.10	182.74	52.94	25.29
	2.33	49.33	187.17	169.51	195.11	115.11	55.00	176.67	162.05	182.74	50.36	24.06

Table 7.2.2 – Crystallisation properties of aged PA-12 blends on cool 1. Where T_P - Peak Crystallisation Temperature, T_E - End Crystallisation Temperature, T_O – Onset of Crystallisation, X_c – Degree of Crystallinity and ΔH is the heat of crystallisation.

Additive	wt.%	**Cool 1**				
		T_C (°C)	T_O (°C)	T_E (°C)	ΔH (Jg^{-1})	Xc (%)
PA-12 (7 day aged)		153.25	153.25	135.52	59.53	28.44
FA	1.00	155.43	155.43	136.93	62.20	29.72
	5.00	152.69	152.69	137.79	62.11	29.67
	10.00	150.45	150.45	134.80	64.26	30.70
	20.00	145.90	145.90	129.68	67.56	32.28
DA	1.00	144.67	153.72	133.68	61.40	29.34
	5.00	144.00	153.29	135.94	59.41	28.38
	10.00	143.33	151.59	134.96	61.70	29.48
	20.00	141.00	149.45	130.92	60.38	28.85
CB	1.00	154.45	154.45	134.80	62.87	30.04
	5.00	155.57	155.57	138.07	62.34	29.78
	10.00	154.72	154.72	136.82	67.90	32.44
	20.00	155.09	155.09	137.65	73.26	35.00
Water	1.00	144.47	153.42	136.08	62.05	29.65
	5.00	145.00	154.15	134.23	62.81	30.01

	10.00	144.67	153.39	136.23	63.87	30.51
	20.00	145.00	154.50	136.62	75.29	35.97
2-PYR	0.10	144.33	153.94	135.64	62.75	29.98
	0.38	144.00	152.72	133.67	59.13	28.25
	0.50	144.00	153.49	134.62	59.66	28.50
	1.05	144.00	153.39	134.23	59.97	28.65
	1.97	143.33	151.73	132.95	60.22	28.77
	2.33	142.83	152.30	132.98	58.14	27.78
	4.07	140.83	149.71	129.68	58.14	27.78
	8.72	137.33	146.47	137.33	75.41	36.03
FA (2-PYR + Water)	0.38	143.67	152.87	133.81	63.49	30.34
	1.97	141.17	150.68	131.25	61.07	29.18
	4.07	140.33	149.60	129.81	61.69	29.47
	8.72	140.33	150.16	130.54	65.62	31.35
DA (2-PYR + Water)	0.10	144.33	154.25	133.67	58.75	28.07
	0.50	144.00	153.15	133.95	63.78	30.47
	1.05	144.50	153.86	135.94	61.56	29.41
	2.33	143.83	153.01	134.09	59.39	28.38

7.3 – FTIR of aged PA-12 blends

The FTIR spectra of PA-12 powder blends and blend samples that had been extracted from DSC pans were recorded and compared to PA-12. The samples that had been extracted from DSC pans were subjected to a heat-cool-heat-cool cycle using a heating rate and cooling rate of 10 ℃/min during DSC analysis.

The aim of this work was to characterise aged PA-12 blends and to observe the effect of the additives on the spectra of PA-12 by comparing the blends to aged PA-12 and explore the influence of the addition of additives on the the peak wavenumber of the N-H stretch. The PA-12 powder had been subjected to an ageing process at 170 ℃ for 7 days. The agents and additives added to 7 day aged PA-12 were the FA, DA, carbon black, water, 2-PYR and 2-PYR/water.

7.3.1 – FTIR characterisation of aged PA-12 blends

The FTIR spectra of aged PA-12 powder and aged PA-12 powder blends is displayed in Figure 7.3.1 and 7.3.2. Table 7.3.1 shows the peak wavenumber of the characteristic peaks. The spectra show peaks comparable to virgin and aged PA-12 (see chapter 6), blends created using unaged powder and that reported by H.J. O'Connor et al for a PA-12 part manufactured by MJF (61,68).

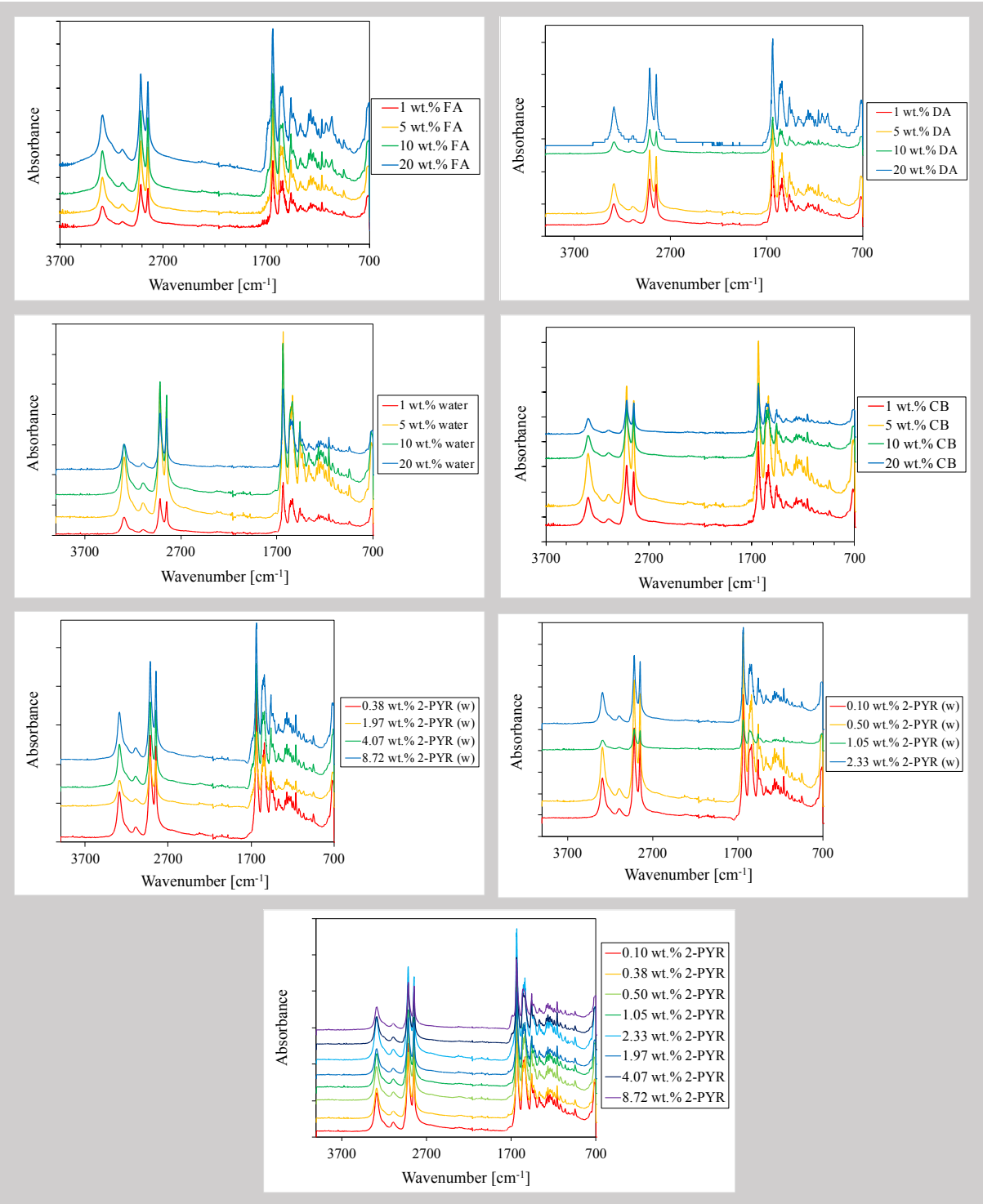

Figure 7.3.1 – FTIR spectra of aged PA-12 powder blends, where “FA” is the Fusing Agent, “DA” is the Detailing Agent, “CB” is carbon black, 2-PYR is 2-pyrollidone and 2-PYR(w) is 2-pyrollidone/water.

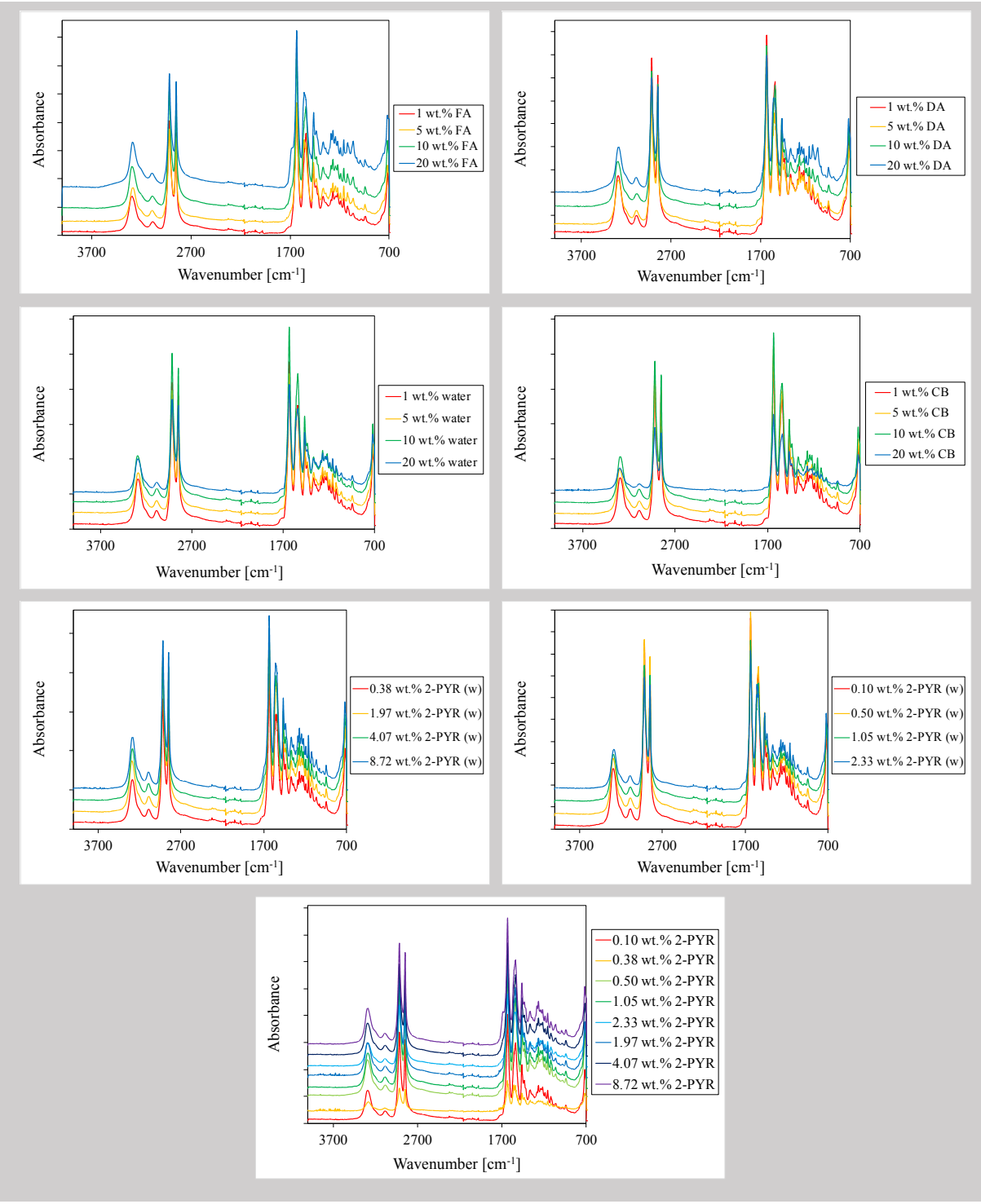

Figure 7.3.2 – FTIR spectra of aged PA-12 blends after being subjected to DSC analysis, where “FA” is the Fusing Agent, “DA” is the Detailing Agent, “CB” is carbon black, 2-PYR is 2-pyrollidone and 2-PYR(w) is 2-pyrollidone/water.

Figure 7.3.1 shows the FTIR spectra of aged PA-12 powder blends. The addition of the FA, DA, carbon black, 2-PYR and water did not have a significant influence on the spectra in that strong new peaks were not observed. For example, a peak at 1634 cm^{-1} was observed in all spectra, this was assigned to the C=O stretch.

Analogous to the virgin PA-12 powder blends, a strong peak within the region of 1660 – 1710 cm^{-1} (peak at *ca.*1681 cm^{-1}) was present in the aged PA-12/FA powder blend and increased with the composition of FA. This peak was also present in the PA-12/DA powder blends. Additionally, this peak was also present in spectra of the aged PA-12/2-PYR and PA-12/2-PYR/water powder blends and was assigned to the C=O stretch of 2-PYR (148). This suggests that 2-PYR was retained in the aged polymer powder. This is a result of hydrogen bond interactions between PA-12 and 2-PYR. Hydrogen bonding can occur since the N-H and C=O moieties are present in both systems. Therefore, this demonstrates that the ageing process did not affect the interaction between PA-12 and 2-PYR.

Figure 7.3.3 shows the region of 3100 – 3500 cm^{-1} for aged PA-12 blends that had been extracted from DSC pans.

In the aged PA-12/FA blend, a shoulder peak at 3203 cm^{-1} grew as the composition of FA increased, as demonstrated in Figure 7.3.3. This trend was also observed in the aged PA-12/2-PYR blend and the PA-12/2-PYR/water blend. Though the shoulder peak was also present in the PA-12/2-PYR/water blend it did not display any trend with increasing composition of 2-PYR. Since the shoulder peak was at 3203 cm^{-1}, it is possible that this can be due to the presence of 2-PYR. This is because deconvolution of the virgin PA-12 blends showed a shoulder peak at 3221.9 cm^{-1} which assigned to N-H stretch of monomeric 2-PYR, as described in Chapter 6.3.

Further investigation into the region 3100 – 3500 cm^{-1} (see Figure 7.3.3) showed that the peak returned to a steady baseline towards higher wavenumbers. This is in contrast to unaged powder PA-12 blends where a clear shoulder peak was observed between 3550 – 3600 cm^{-1}. The shoulder peak in unaged PA-

12 powder blends was assigned to free N-H, as reported by Schroeder and D. Skrovanek. In their work, the free N-H band was assigned at 3440 cm^{-1} and 3444 cm^{-1}, respectively (95,105). The absence of the shoulder peak in the aged PA-12 blends suggests that free N-H was not present or was negligible and therefore undetected. Additionally, the aged samples had been subjected to heat-cool thermal cycles in the DSC which can influence the bonding of PA-12 due to the restructuring of polymer chains during recrystallisation. The absence of this peak was also observed in the virgin PA-12 blends that had been subjected to heat-cool thermal cycles in the DSC. This demonstrates that in virgin and aged PA-12 powder blends free N-H was present and in the DSC counterparts this peak was absent.

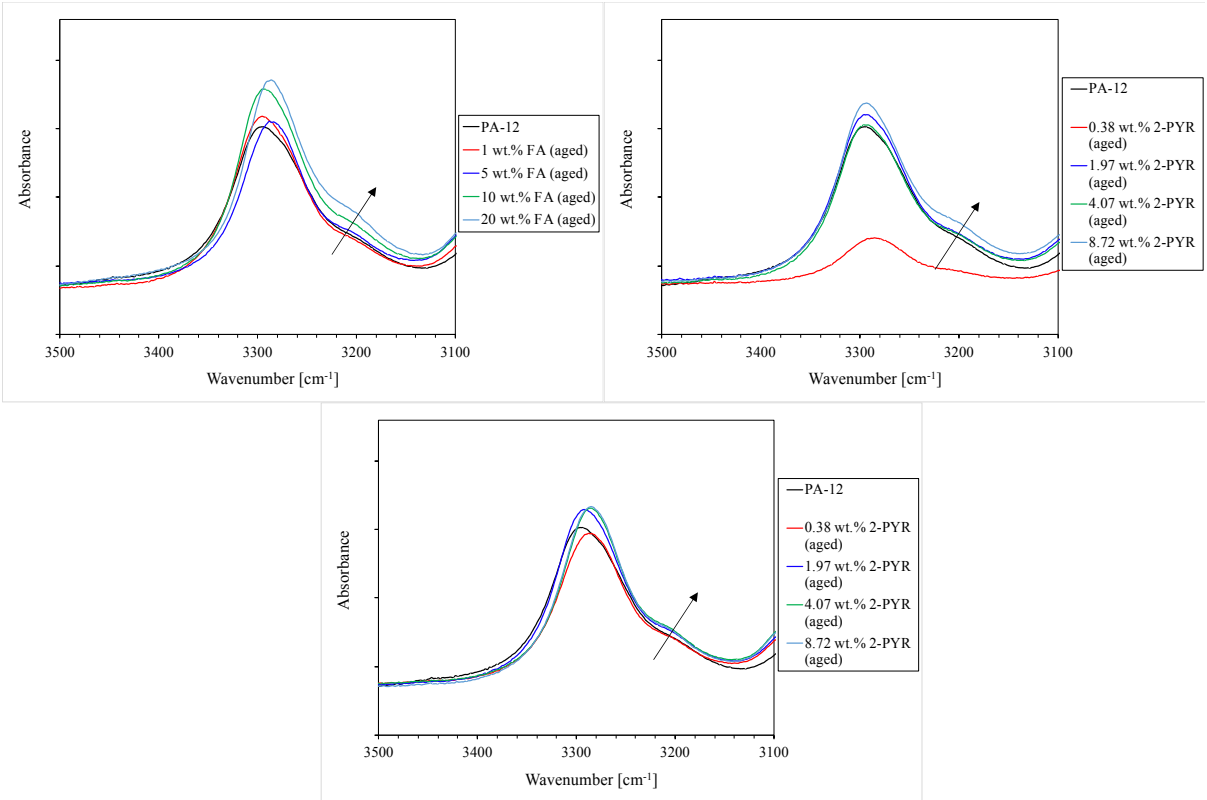

Figure 7.3.3 – FTIR spectra of the N-H stretch of aged PA-12/FA blend (top left), aged PA-12/2-PYR blend (top right) and aged PA-12/2-PYR/water blend (bottom), where samples had been extracted from DSC aluminium pans. The arrow denotes a shoulder peak at ca.3222 cm^{-1}.

In Figure 7.3.4, the region between 1590 – 1770 cm^{-1} is displayed of the FTIR spectra for selected aged blends that were subjected to DSC analysis. These blends were selected since they had the largest proportion of 2-PYR present. The peak at 1690 cm^{-1} is representative of C=O, assigned to 2-PYR and shows that 2-PYR was retained in the aged DSC blends, illustrated by the solid black arrow (148). The dashed black arrow shows the carbonyl species present at *ca*.1720 cm^{-1}. The presence of carbonyl species was a result of products formed from thermo-oxidative degradation. The peak at *ca*.1720 cm^{-1} was established in the FTIR spectra of aged PA-12 powder (see Chapter 7.1). While the strong peak at *ca*.1634 cm^{-1} was assigned to C=O stretch of PA-12. This data shows the different carbonyl species present within the blend.

In the 8.72 wt.% 2-PYR (w) blend, the peak height of the C=O 2-PYR peak is noticeably lower than the 20 wt.% FA and 8.72 wt.% 2-PYR blend, despite all blends containing the same amount of 2-PYR. A reason could be due to the interaction between 2-PYR and water hydrogen, such that in the 8.72 wt.% 2-PYR (w) blend a quantity of 2-PYR could have evaporated with water during the drying phase. Additionally, it is possible that this could have happened during DSC analysis, which was performed up to a temperature of 220 ℃ and water evaporates at 100 ℃. However, this feature would have also been present in the 20 wt.% FA blend, since 20 wt.% FA blend also contained water and 2-PYR. Therfore, this requires further investigation or can be treated as an anomaly.

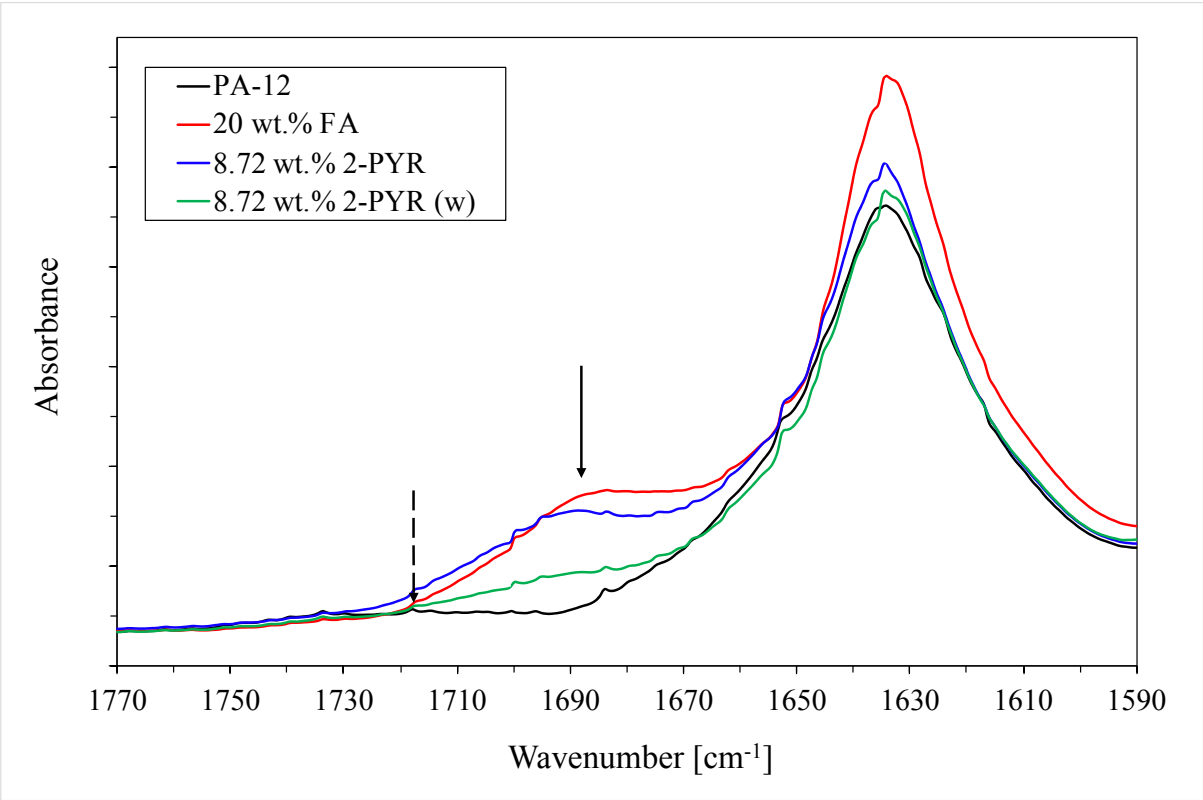

Figure 7.3.4 – FTIR spectra of selected aged PA-12 blends, extracted from a DSC aluminium pan. The solid line arrow shows the C=O region assigned from 2-PYR and the dashed arrow shows the peak at ca.1720 cm^{-1} assigned to degradative carbonyl species.

In Chapter 6.3 the FTIR spectra of virgin PA-12 blends were analysed. It was shown that the absorbance was modified by the addition of the FA to PA-12. In the virgin PA-12/FA blend, the absorbance of the spectra shifted to higher values as the composition of the FA increased. However, this trend was not observed in the virgin PA-12/CB blends. This was due to the interaction of PA-12 and carbon black. In the PA-12/FA blends the carbon black was dispersed as an ink and caused the colour of the powder to change from white to black. Whereas, in the PA-12/CB blends the carbon black was in the form of solid black particles that were dispersed within the white PA-12 powder.

Figure 7.3.5 shows the uncorrected spectra of aged PA-12/FA and PA-12/CB powder blends. In the PA-12/FA blends, the absorbance was modified by the addition of the FA to PA-12. As the composition of

the FA increased, the absorbance of the spectra systematically increased. Whereas, in the aged PA-12/CB the carbon black did not have a significant effect on the absorbance of PA-12. This shows that the behaviour did not change from virgin to aged PA-12/FA and PA-12/CB powder blends, with respect to the influence of carbon black on the absorbance of PA-12. M. Galati et al recorded the spectra of the liquid FA and DA and reported that the FA spectrum had shifted to a lower transmittance when compared to the spectrum of the DA (58). This was due to the role of the FA which was to convert incident IR radiation into heat energy. The FA contained carbon black which is used in MJF and HSS to increase the absorption of IR radiation. This behaviour is consistent with the action of a RAM (146). However, the PA-12/CB blends also contained carbon black that was compositionally identical to the FA and an increase in absorbance with composition was not observed. Therefore, this can be due to the interaction of carbon black. The dispersion and interaction of PA-12 and carbon black in the aged powder blends was comparable to the unaged powder blends. Where in the aged PA-12/FA powder blends the carbon black (in the form of an ink) caused the colour of the powder to change from white to black. Whereas, in the aged PA-12/CB powder blends the carbon black was in the form of solid black particles that were dispersed within the white PA-12 powder.

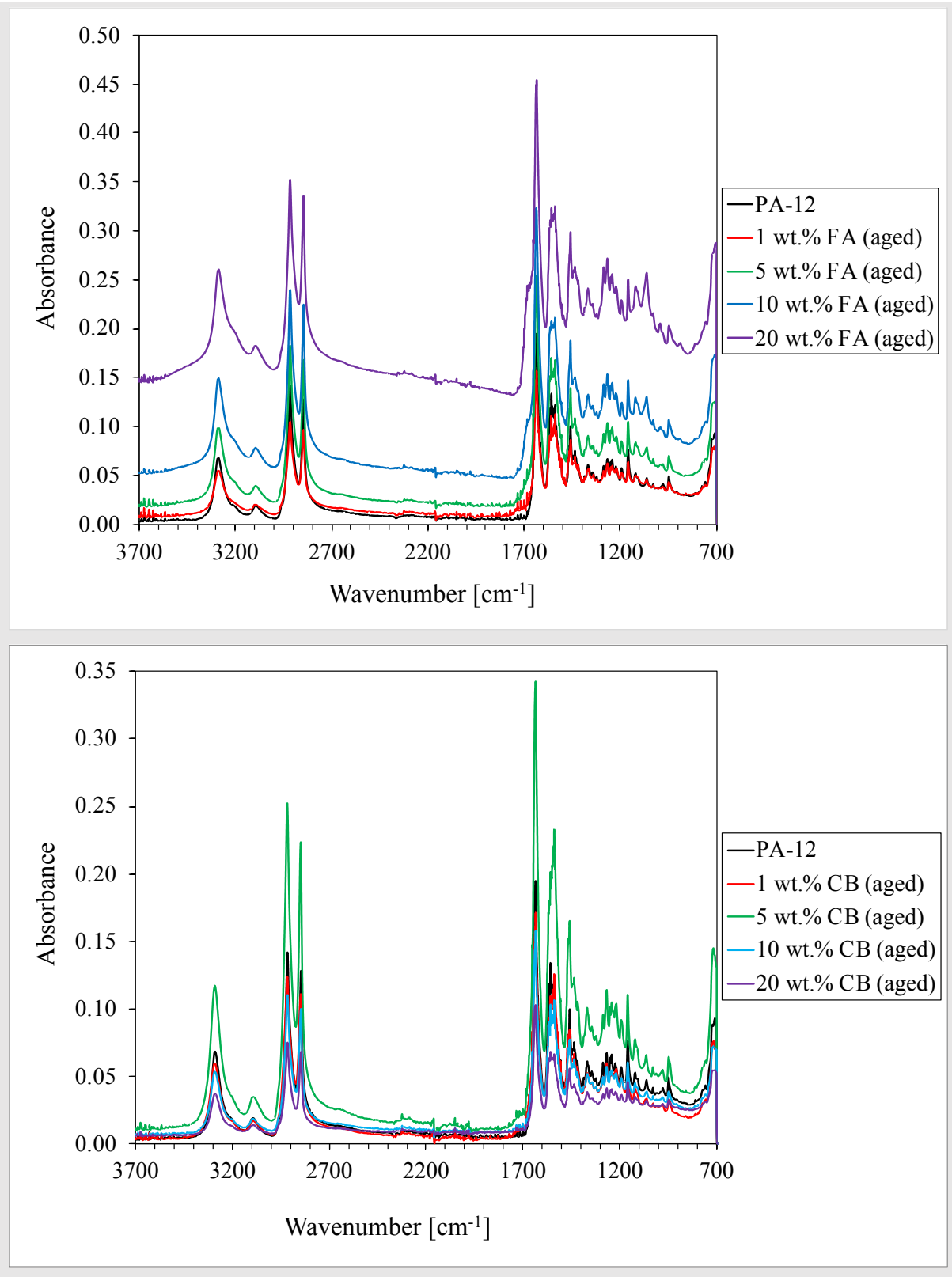

7.3.5 – FTIR spectra of the aged PA-12/FA and aged PA-12/CB powder blends, where the data has not been corrected, where FA is the Fusing Agent and CB is carbon black.

7.3.2 – Peak shift of the N-H stretch

The peak wavenumber of the N-H moity was recorded in order to determine the effect of hydrogen bond interactions between aged PA-12 powder and the FA, DA, CB, water, 2-PYR and 2-PYR/water (151).

Figure 7.3.6 displays the peak wavenumber of the N-H stretch for the powder blends. In general, a unsystematic peak shift of the N-H stretch (*ca*.3290 cm^{-1}) to higher or lower wavenumbers was observed. The shift in peak wavenumber of the N-H stretch suggests hydrogen bond interactions were formed between aged PA-12 and the FA, DA, CB, 2-PYR and 2-PYR/water (151). Common to the FA and DA is the 2-PYR, therefore the shift in peak wavenumber was due to the presence of 2-PYR. This suggests that 2-PYR was retained in the aged polymer powder, this was also demonstrated by the presence of the peak at ~1690 cm^{-1} that was assigned to the C=O stretch of 2-PYR (148). The greatest peak shift was -3.97 cm^{-1}, exhibited by 1.97 wt.% 2-PYR in the PA-12/2-PYR/water blends. The extent of the peak shift may be due to residual water in the blend as a result of 2-PYR and water hydrogen bond interactions. Interestingly, the PA-12/CB blends also exhibited a shift in peak wavenumber. This can be due to residual solvents from incomplete drying.

The N-H stretch (*ca*.3290 cm^{-1}) in the DSC blends shifted unsystematically to higher and lower wavenumbers for blends of different compositions, as displayed in Figure 7.3.6. This suggests hydrogen bond interactions were present between PA-12 and FA, DA, CB, 2-PYR and 2-PYR/water (151). In comparison to the aged PA-12 powder, the shift in peak wavenumber for the aged DSC blends was much larger. This can be attributed to the crystal reconfiguration acquired on recrystallisation. The largest shift in peak wavenumber was -10.50 cm^{-1}, exhibited by 8.72 wt.5 2-PYR (w). In general, the blends that exhibited the largest shift in peak wavenumber were the 2-PYR/water containing blends. This can be due to residual water in the blend as a result of 2-PYR and water hydrogen bond interactions.

The blends that also exhibited a large peak shift were the 20 wt.% FA, 0.38 wt.% 2-PYR, 2.33 wt.% 2-PYR (w) 4.07 wt.% 2-PYR (w), 8.72 wt.% 2-PYR (w) which had a peak shift of -9.6, -10.5, -10.5, -10.3 and -10.5 cm^{-1}, respectively.

The interaction with 2-PYR and water has been studied previously in literature (147,165). It was shown that the largest shifts in peak wavenumber were towards the lower frequency region. This was also reported in blends of thermoplastic polyurethanes and PA-12 (151). The addition of PA-12 to TPU caused the frequency of the N-H band to shift to lower frequencies than the frequency of virgin PA-12. The authors claim that the shift to lower frequency region is due to more high-energy hydrogen bonds formed.

It was clear that the N-H band exhibited a peak shift with the addition of the FA, DA, CB, water, 2-PYR and 2-PYR/water. This demonstrates that hydrogen bonding was present between PA-12 and the additives. The extent of the peak shift was greater in the DSC blends, when compared to the powder blends.

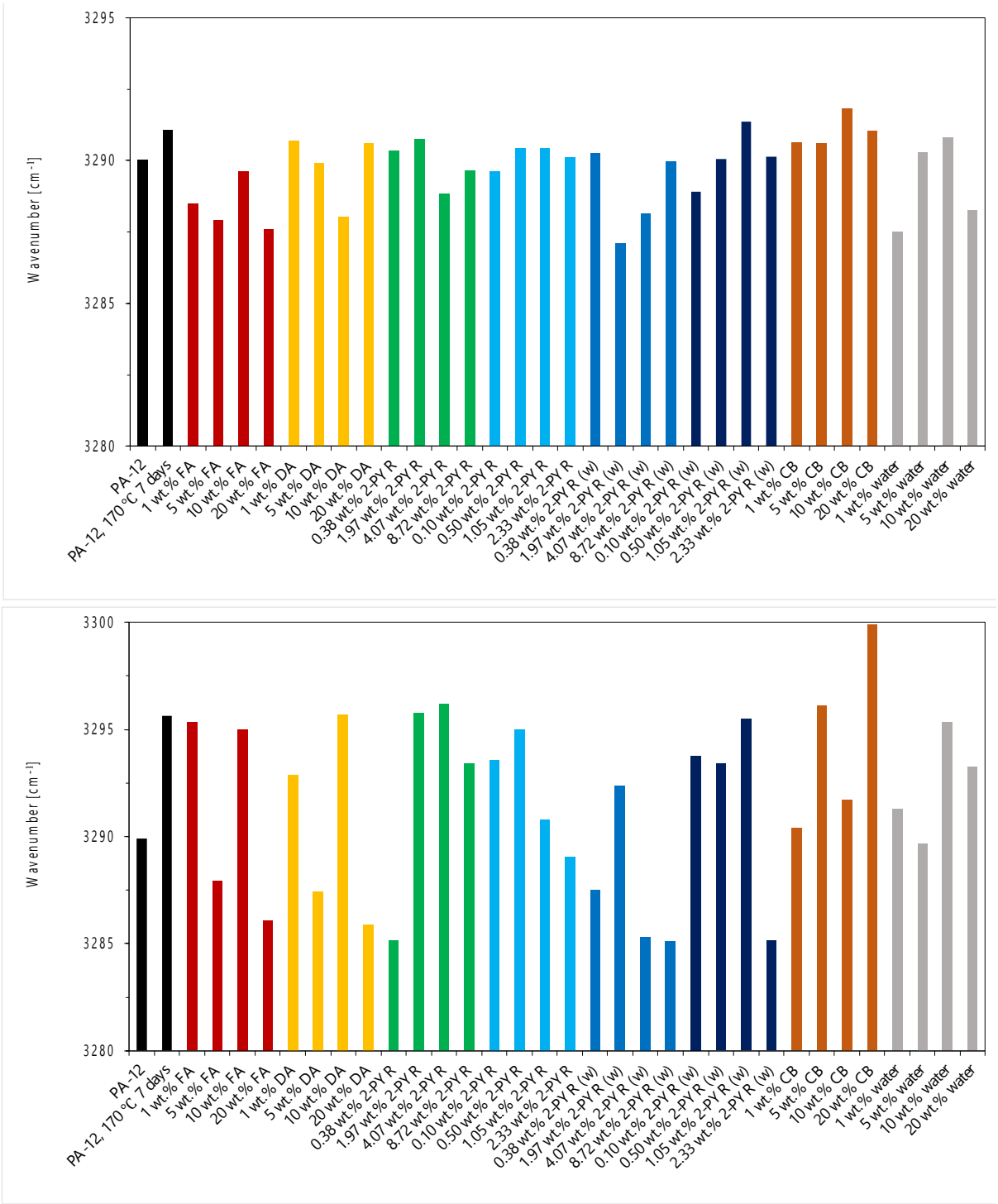

Figure 7.3.6 – Bar chart displaying the shift in peak wavenumber for the νN-H stretch for aged PA-12 powder blends (top) and aged PA-12 blends that had been subjected to DSC (bottom), where “PA-12” represents virgin powder.

7.3.3 – Deconvolution of the N-H stretch in aged PA-12 blends

A shift in peak wavenumber of the N-H stretch was exhibited by some blends. This suggests that hydrogen bonding was present between PA-12 and the FA, DA, CB, water, 2-PYR and 2-PYR/water. The N-H region was examined according to the method demonstrated by M. Davila et al, also following the same procedure to chapter 6.3. In which, the Guassian-Lorentzian method was used to deconvolute the spectra within the region of 3000 – 3500 cm^{-1} (147). The peaks resolved within the region of 3000 – 3500 cm^{-1} were related to 2-PYR. The output shows 2-PYR in the form of a cyclic dimer (3221.9 cm^{-1}) or monomer (3482.8 cm^{-1}). Moreover, overtones of the C=O stretch (3100 cm^{-1}) and the hydrogen bonded C=O of 2-PYR (3311.9 cm^{-1}) were also identified. In the virgin PA-12 blends containing 2-PYR, a peak at 3221 cm^{-1} was observed suggesting that 2-PYR was present as a cyclic dimer (see section 6.3).

Figure 7.3.7 shows the relationship between the peak area and peak height of the ~3222 cm^{-1} peak with composition of 2-PYR. The peak area and peak height of the ~3222 cm^{-1} peak did not show a clear trend with increasing composition of 2-PYR. However, a composition of 8.72 wt.% 2-PYR had the greatest peak area and peak height. This is in contrast to the unaged PA-12 powder blends where an increase in peak area and peak height was observed with increasing composition of 2-PYR.

Since 8.72 wt.% 2-PYR had the greatest peak area and height, this shows that cyclic dimer and the content of the cyclic dimer was the greatest for this blend. Though, it is unclear what fraction of 2-PYR within the blend adopted this configuration. This suggests 2-PYR may also be present as a monomer. According to M. Davila et al, 2-PYR is in the form of a monomer is represented by a a peak at 3482 cm^{-1} (147). However, in Figure 7.3.3 peak a 3482 cm^{-1} was not observed. This can be due to monomeric 2-PYR being undetected since it was present in a small quantity. The presence of monomeric 2-PYR can cause a peak within the region of 3550 – 3600 cm^{-1}, as observed in some unaged PA-12 powder blends. This peak is associated with the free N-H band (see chapter 6.3.1 and chapter 6.3.3). However,

a peak within the region of 3550 – 3600 cm^{-1} was not observed in the aged PA-12 powder blends. This suggests that free N-H was not present.

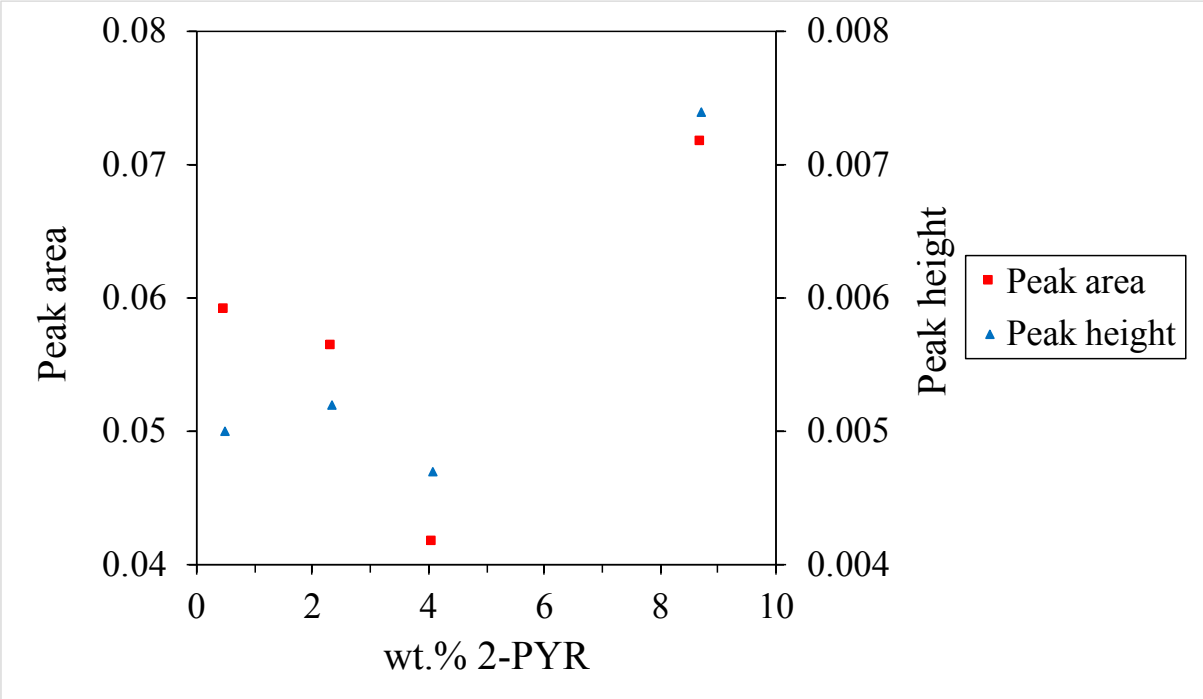

Figure 7.3.7 – Graph of 2-PYR composition vs peak area and peak height of the 3222 cm^{-1} obtained by deconvolution using the Guassian-Lorentzian method for selected powder blends.

7.4 – Optical microscopy of aged PA-12 blends

In chapter 6.4, optical micrographs of virgin powder blends were captured to observe the effect of the FA, DA and additives on the microstructure of PA-12. A slow cooling rate of 0.5 ℃/min was used since it produced distinguished spherulites whilst enabling the nucleation effect provided by the agents to be observed, if any. Therefore, the same cooling rate was used for the aged powder blends.

In AM techniques, PA-12 powder is refreshed with each processing cycle. A small fraction of virgin powder is added to the remaining powder that has already been exposed to a number of processing

cycles. The refresh ratio of new and recycled powder in SLS and MJF are typically 50:50 and 20:80 (51, 55). This suggests that recycled PA-12 will behave differently to virgin PA-12 powder since it has been exposed to high temperatures for prolonged periods of time. For this reason, optical micrographs of aged PA-12 blends were captured in order to observe the effect of the agents and additives on the microstructure and morphology of aged PA-12.

Dadbakhsh et al studied the effect of ageing on the microstructure of PA-12 single layer parts fabricated by SLS (51). In this work, SEM images of the surface were studied. In virgin parts, the spherulites grew from a limited number of nucleation sites and consisted of highly packed lamellae and small interlamellar regions. The appearance of the spherulites was described as “fine”. Although the spherulites in the parts produced from new powder were described as “fine”, the interlamellar regions were difficult to distinguish on the images captured using SEM.

On the other hand, SLS parts fabricated from aged powder contained a number of aggregates that melted at a higher temperature than the surrounding matrix. These served at nucleation points (heterogenous nucleation). This is most likely due to incomplete melting during sintering. As a result, a large number of spherulites were produced. In these spherulites, the crystalline material was limited. The authors note that heterogenous nucleation leads to a “coarser appearance of spherulites”. This suggests that the large amount of amorphous content leads to less defined crystalline regions. In parts fabricated from refreshed powder, the appearance of the spherulites was in-between those observed in the parts made from virgin and aged powder. The authors speculate that the longer molecular length of the aged material contributes to coarser appearance of spherulites due to an increased lamellar thickness.

A similar trend has been reported in literature when assessing the microstructure of SLS parts made from virgin, aged or refreshed powder (13). In parts fabricated using new powder, fine fibrillar/lamellae spherulitic regions were observed due to the aggregation of chain folded crystals. Whereas, in parts made from aged powder “coarser” spherulites were observed.

In parts made from virgin powder, the number of spherulites was limited since the number of nuclei within the melt was also limited. However, the lamellae formed were highly packed and the interlamellar amorphous regions were small. In parts made from aged powder, spherulites nucleate heterogeneously. This is because aged powder contained a number of higher melting point aggregates which acted as effective nucleation sites.

The appearance of the spherulites is difficult to observe in great detail in methods such as optical microscopy. Whereas, SEM produced more detailed images where the “fine” and “coarse” appearance of spherulites was distinguished. This was apparent when the images were compared to each other. In general, the fine details of the lamellae and interlamellar regions were difficult to observe using these methods. From the images captured using optical microscopy and SEM, clusters of lamellae are observed and not the interlamellar regions.

It was demonstrated in literature that the final part microstructure was clearly influenced by the condition of the powder. However, the presence of agents, stabilisers or additives may also influence the microstructure.

In PA-6, the process of ageing at a temperature between T_g and T_m produced larger spherulites in comparison to virgin powder. When stabilisers were added to virgin PA-6, the spherulite size of stabilised PA-6 decreased, when compared to virgin PA-6. This was due to the stabilisers acting as a nucleating agent to induce heterogenous nucleation. In aged, stabilised PA-6 the number of spherulites was sparse. This was due to either the generally low degree of crystallinity of PA-6 itself, the sample preparation method or the crystalline morphology of small molecules becoming damaged during ageing (159). After ageing (between T_g and T_m), the number of spherulites observed in virgin PA-6 was little to none. This study showed that both ageing and additives can influence the microstructure of polyamide.

The effect of the FA, DA, CB and 2-PYR on the microstructure of aged PA-12 was observed using optical microscopy. The samples were heated to 220 ℃ where they were stored at an upper isotherm for 5 minutes to ensure complete melting and cooled at a controlled rate of 0.5 ℃/min to 25 ℃.

The microstructure of the 1 and 20 wt.% FA blends are displayed in Figure 7.4.1. The dark regions in Figure 7.4.1b and Figure 7.4.1c represent carbon black in the FA and the surrounding area is the polymer matrix. The optical micrographs show that carbon black was rejected to the inter-spherulitic regions (155). As the composition of the FA increased, a greater content of carbon black was observed. The FA had a significant effect on the microstructure of PA-12 in that the spherulite size was significantly reduced by the addition of the FA when compared to the microstructure aged PA-12, even at a composition as low as 1 wt.% FA. This suggests that the carbon black in the FA acted as a nucleating agent or impeded the radial growth of spherulites by acting as a physical barrier.

In the PA-12/DA blends (Figure 7.4.1d and Figure 7.4.1e), the spherulite size of PA-12 was not significantly influenced by the addition of the DA. In the 1 wt.% DA blend, the spherulite size was comparable to PA-12. In the 20 wt.% DA blend the spherulite size was slightly reduced by the addition of DA. This shows that only at high compositions of DA the spherulite size was impacted.

In the PA-12/CB blends (Figure 7.4.1f and Figure 7.4.1g), the spherulite size was affected by the addition of the carbon black. In the 1 wt.% CB blend, the spherulite size was comparable to PA-12. Whereas, in the 20 wt.% CB blend, the spherulite size reduced slightly. This is due to the carbon black acting as an impurity to induce nucleation or act as a physical barrier to impede radial growth of spherulites.

In the PA-12/water blends (Figure 7.4.1h and Figure 7.4.1i), the spherulite size was unaffected by the content of water and the spherulite size of the blends was comparable to PA-12. This suggested water evaporated during the drying process.

In the PA-12/2-PYR, 2-PYR was compositionally identical to that in the FA and DA blends. Figure 7.4.1j and Figure 7.4.1k show that the 2-PYR affected the spherulite size of PA-12.

In the 0.1 wt.% 2-PYR blend, the spherulite size was comparable to PA-12. Whereas, in the 8.72 wt.% 2-PYR blend, the spherulite size reduced slightly. The decrease in spherulite size by the addition of 2-PYR is consistent of the action of a plasticizer since polymer chains have increased mobility.

Interestingly, according to DSC data (see chapter 7.2) the degree of supercooling decreased with the addition of 2-PYR suggesting that 2-PYR facilitated crystallisation, while optical microscopy showed that the microstructure was not significantly affected. This was also reflected in the degree of crystallinity, where the degree of crystallinity of PA-12/2-PYR was also not significantly affected by the degree of crystallinity. This difference can be due to the differences in experimental set up on the DSC and optical microscope, in that the DSC offers a more controlled heating and cooling process.

In the PA-12/2-PYR/water blends, where both 2-PYR and water was compositionally identical to that in the FA and DA blends, the spherulite size was impacted by the addition of the 2-PYR and water. This is shown in Figure 7.4.1l, Figure 7.4.1m, Figure 7.4.1n and Figure 7.4.1o.

In the PA-12/2-PYR/water blends that were compositionally identical to the FA, the spherulite size reduced slightly as the composition increased. This is shown in Figure 7.4.1l and Figure 7.4.1m. In the PA-12/2-PYR/water blends that were compositionally identical to the DA, the spherulite size was not greatly impacted. This is shown in Figure 7.4.1n and Figure 7.4.1o. Since in the PA-12/water blends the spherulite size was not impacted by the addition of water, it can be assumed that that 2-PYR influenced

the spherulite size. This agrees with DSC data (see chapter 7.4.2), where the crystallisation properties of PA-12 were modified by the addition of the 2-PYR.

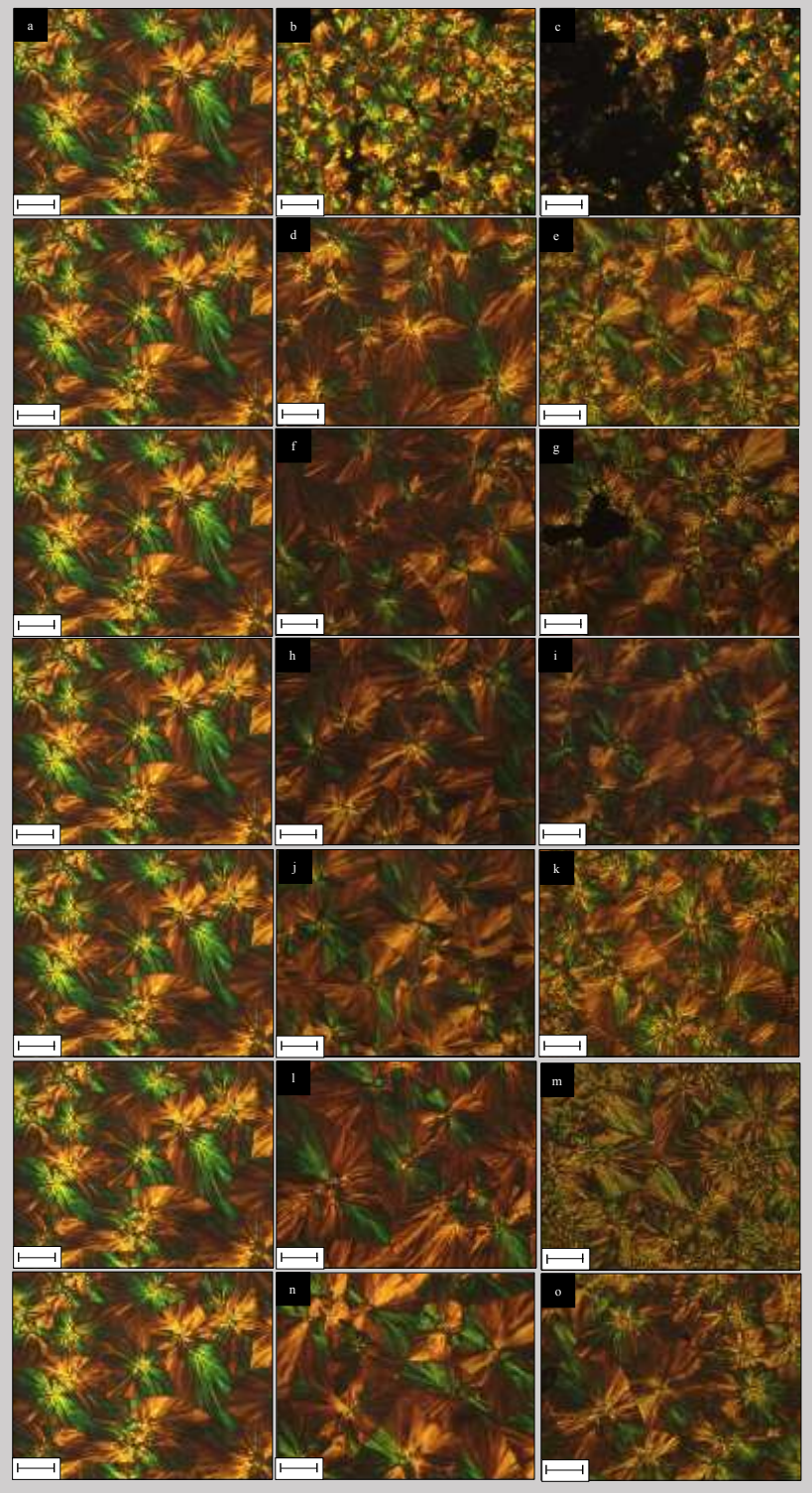

Figure 7.4.1 – Optical micrographs captured at 500x magnification of aged blends (a) PA-12 (b) 1 wt.% FA (c) 20 wt.% FA (d) 1 wt.% DA (e) 20 wt.% DA (f) 1 wt.% CB (g) 20 wt.% CB (h) 1 wt.% water (i) 20 wt.% water (j) 0.1 wt.% 2-PYR (k) 8.72 wt.% 2-PYR (l) 0.38 wt.% 2-PYR/water (m) 8.72 wt.% 2-PYR/water (n) 0.10 wt.% 2-PYR/water (o) 2.33 wt.% 2-PYR/water.

CHAPTER 8 – CONCLUSION

The isothermal and non-isothermal crystallisation kinetics of PA-12 were investigated at a variety of different crystallisation temperatures and cooling rates. The isothermal and non-isothermal crystallisation kinetics are important to consider since this can be used to explore how the build temperature and cooling rate affect the morphology and rate constant of PA-12.

Isothermal crystallisation showed that as the crystallisation temperature increased, the time taken for crystallisation increased. The isothermal crystallisation kinetics of PA-12 powder was studied using the Avrami and Tobin. These models were implemented using the conventional method and NLR. The conventional method showed that both the Avrami and Tobin model were successful in describing the crystallisation kinetics of PA-12, where the Avrami model produced a greater R^2 ranging between 0.9913 – 0.9998, whereas, the Tobin model produced a lower R^2 between 0.9793 – 0.9988. NLR also showed that the Avrami and Tobin model were successful in describing the crystallisation kinetics of PA-12, where the Tobin model produced a greater R^2 ranging between 0.982 – 1, whereas, the Avrami model produced a lower R^2 between 0.962 – 0.997. The quality of fit of NLR data was compared to experimental data by producing a graph of relative crystallinity vs time. The data showed that the Tobin model had the best quality of fit, followed by the Avrami model.

The equilibrium melting temperature of PA-12 was 188℃ and 205℃, this was determined using the Hoffman-Weeks construction from the peak melting temperature and the last trace of crystallinity, respectively.

The non-isothermal crystallisation kinetics of PA-12 powder was studied using the Avrami modified by Jeziorny and the Caze model.

The Avrami model modified by Jeziorny was successful in describing the non-isothermal crystallisation kinetics of PA-12. There is value in implementing different models in that each model is an adaptation or a novel method. However, with various models available and some models being created due to existing ones failing to describe polymer crystallisation, this demonstrates that crystallisation models can be generated specifically for a polymer system. This work has shown amongst the various models implemented, few were only able to describe the isothermal and non-isothermal crystallisation kinetics of PA-12. Of which, these are the conventional methods to investigate the crystallisation kinetics of a polymer system. In MJF, it is thought that a combination of isothermal and non-isothermal crystallisation occurs. This is because crystallisation is influenced both by the temperature within the core of the powder bed and the cooling rate experienced at the surface of the powder bed.

PA-12 blends (unaged and aged) were created in order to study the effect of the FA, DA and their chemical constituents on the thermal properties, chemical properties and morphology of PA-12.

In the unaged PA-12 blends, the FA and DA had a significant effect on the thermal properties of PA-12 by shifting the peak melting temperature to lower temperatures and shifting the crystallisation temperature to higher and lower temperatures, compared to PA-12. Of the chemical constituents making up the FA and DA, 2-PYR and carbon black had the greatest influence on the thermal properties of PA-12.

The FTIR spectra of the powder blends and DSC samples were evaluated, these showed peaks comparable to PA-12. The main findings included; the absorbance signal of the FA blend increased with composition of FA, this was due to carbon black being more readily absorbed by the IR beam. In the PA-12/2-PYR and PA-12/2-PYR/water blend containing 8.72 wt.% 2-PYR a shoulder peak between 3550 – 3600 cm^{-1} was assigned to the free N-H stretching vibration (147). In some blends containing 2-PYR, a peak at ~1690 cm^{-1} was assigned to the amide-I band (C=O stretching). This showed that 2-PYR was retained in the polymer, even after the DSC thermal analysis. The peak shift of the N-H band at 3100 – 3500 cm^{-1} was assessed. The majority of the blends experienced a shift in peak wavenumber

of the N-H band, relative to the peak wavenumber of PA-12; especially after being subjected to DSC analysis. This showed that hydrogen bonds were present between PA-12 and the FA, DA and 2-PYR, in particular.

Optical microscopy showed that the spherulite size was affected by the addition of the FA and carbon black. In the PA-12/FA and PA-12/carbon black blends, the spherulite size decreased significantly with the addition of the FA and carbon black. This was due to the carbon black (also present in the FA) being rejected to the interspherulitic regions and impeding the radial growth of spherulites by acting as a physical barrier.

PA-12 powder was aged in an air ventilating oven at 170 ℃ for 0, 5, 7 and 9 days. As the ageing time increased, PA-12 powder (and DSC counterparts) changed from a white colour to a dark orange colour suggesting that PA-12 had degraded. The thermal behaviour of aged PA-12 was evaluated, it was shown that the peak melting temperature shifted to a higher and then lower temperature with increased ageing time, suggesting that mechanisms such as post-polymerisation and chain scission took place. Meanwhile the crystallisation temperature moved to lower temperatures, suggesting post-crosslinking or post-polymerisation occurred. FTIR spectra were recorded, these were comparable to virgin PA-12. However, in the 9 day aged sample a small peak at 1716.4 cm^{-1} was observed. This was assigned to carbonyl containing compounds that had formed due to degradation products from thermooxidative degradation.

Aged PA-12 blends exhibited similar trends in thermal behaviour to unaged PA-12 blends, in that the FA and DA had a significant effect on the thermal properties of PA-12 by shifting the peak melting temperature to lower temperatures and shifting the crystallisation temperature to higher and lower temperatures, when compared to aged PA-12. Of the chemical constituents making up the FA and DA, 2-PYR and carbon black had the greatest influence on the thermal properties of PA-12.

The FTIR spectra of the aged blends of powder and DSC samples were evaluated, these showed peaks comparable to PA-12. In the blends, a peak at 1690 cm^{-1} (assigned to the amide-I band, C=O stretch)

indicated that 2-PYR was retained within PA-12. The peak shift of the N-H band at 3100 – 3500 cm^{-1} was assessed. The majority of the blends experienced a shift in peak wavenumber of the N-H band, relative to the peak wavenumber of aged PA-12; especially after being subjected to DSC analysis. This showed that hydrogen bonds were present between PA-12 and the FA, DA and 2-PYR, in particular.

Optical microscopy showed that the spherulite size significantly decreased by the addition of the FA and carbon black. This was due to the carbon black (also present in the FA) being rejected to the interspherulitic regions and impeding the radial growth of spherulites by acting as a physical barrier.

The literature has pointed out that carbon black is a fundamental component within the MJF. This research has shown that carbon black significantly impacted the thermal properties and microstructure of PA-12 by acting as a nucleation agent. However, this investigation has also shown that in addition to carbon black, 2-PYR had a significant impact on the thermal properties of PA-12. Meanwhile, 2-PYR did not have a significant impact on the microstructure of PA-12. Where other studies quantify the components of the FA and DA, this study has shown that 2-PYR was retained in the polymer and formed hydrogen bonds with PA-12. In turn, this moderated the thermal properties by 2-PYR acting as a plasticizer. This demonstrates that 2-PYR is also a fundamental component in MJF. It is clear that the FA and DA have been formulated specifically to optimise the build process of MJF, given that they contain identical constituents in different quantities (except for carbon black).

In this work, the thermal properties and chemical properties have been extensively studied. Techniques such as DSC, FTIR and optical microscopy provided an understanding into what makes MJF unique in comparison to other AM techniques. This work adds value to the MJF community as it shows that PA-12 powder can be subjected to multiple cycles before being discarded. The interaction between PA-12 and the agents was not hindered after ageing. This is because the same trends were observed in the virgin and aged powder blends. For example, the use of FA resulted in decreased T_g and peak melting temperature of PA-12 in the virgin and aged blends. In industrial application, PA-12 powder could be

extracted from the build and the thermal properties evaluated. This would show whether PA-12 within the build chamber should be entirely discarded or refreshed, providing that the thermal properties show no signs of major degradation. This can be used as a quality control since parts created from majorly degraded PA-12 are likely to have a negative impact on the final properties of the component.

The isothermal and non-isothermal crystallisation kinetics can be used to determine the crystallisation mechanisms experienced within the powder bed. Both isothermal and non-isothermal crystallisation is experienced in MJF. This is because MJF is not performed in controlled conditions. The melted powder would initially cool down quickly over a temperature range so that another layer can be deposited. This is a non-isothermal process, therefore the cooling rate would affect the peak crystallisation temperature and consequently the microstructure of PA-12. At a high cooling rate, crystallisation occurs at lower temperatures therefore the spherulites are expected to be small as nucleation is favoured. At a lower cooling rate, crystallisation occurs at higher temperatures and spherulitic growth is favoured. However, isothermal crystallisation could occur after or at different regions in the powder bed. At lower crystallisation temperatures, the rate of crystallisation is high favouring nucleation. At higher crystallisation temperatures, the rate of crystallisation is low favouring spherulitic growth. Therefore, the isothermal and non-isothermal crystallisation process will influence the final properties of the component by affecting the microstructure. Additionally, isothermal crystallisation can lead to ageing since PA-12 is being subjected to a high temperature for a prolonged period of time. The extent of the ageing would depend on the location of the part within the powder bed chamber as the temperature distribution is non-uniform. The crystallisation kinetics can help to determine the accuracy of the final geometry of parts with respect to their build position within the powder bed chamber. The cooling mechanisms across the build chamber are expected to vary. This is because the powder closest to the sides of the chamber will have a different heating profile when compared to powder within the core of the chamber. Therefore, a framework of knowledge on the crystallisation kinetics can help identify why components are geometrically inaccurate. An understanding of the heating profile and the crystallisation behaviour can be used to improve the printing process. For example, the size and the geometry of the part can dictate where in the powder bed chamber the part is built. Larger and more complex parts can

be built in the core of the powder bed chamber because this is where the temperature distribution is likely to be more uniform. Furthermore, since the core is the hottest part of the chamber and less likely to lose heat, this will lead to isothermal crystallisation and produce parts with large spherulites, if the temperature remains high and the conditions are stable. Alternatively, a low cooling rate would favour spherulitic growth. Smaller parts can be built closer to the sides of the chamber as they are less likely to be affected by the temperature profile due to their small size. This will result in a part with a uniform microstructure.

The isothermal and non-isothermal crystallisation kinetics can be used to determine the crystallisation mechanisms experienced within the powder bed. Both isothermal and non-isothermal crystallisation is experienced in MJF. This is because MJF is not performed in controlled conditions. The melted powder would initially cool down quickly over a temperature range so that another layer can be deposited. This is a non-isothermal process, therefore the cooling rate would affect the peak crystallisation temperature and consequently the microstructure of PA-12. At a high cooling rate, crystallisation occurs at lower temperature therefore the spherulites are expected to be small as nucleation is favoured. At a lower cooling rate, crystallisation occurs at higher temperatures and spherulitic growth is favoured. However, isothermal crystallisation could occur after or at different regions in the powder bed. At lower crystallisation temperatures, crystallisation is quicker and nucleation is favoured. At higher crystallisation temperatures, crystallisation is longer and spherulitic growth is favoured. Therefore, the isothermal and non-isothermal crystallisation process will influence the final properties of the component by affecting the microstructure. Additionally, isothermal crystallisation can lead to ageing since PA-12 is being subjected to a high temperature for an extensive period of time. The extent of the ageing would depend on the location of the part within the powder bed chamber as the temperature distribution is non-uniform. The crystallisation kinetics can help to determine the accuracy of the final geometry of parts with respect to their build position within the powder bed chamber. The cooling mechanisms across the build chamber are expected to vary. This is because the powder closest to the sides of the chamber will have a different heating profile when compared to powder within the core of

the chamber. Therefore, a framework of knowledge on the crystallisation kinetics can help identify why components are geometrically inaccurate. An understanding of the heating profile and the crystallisation behaviour can be used to improve the printing process. For example, the size and the geometry of the part can dictate where in the powder bed chamber the part is built. Larger and more complex parts can be built in the core of the powder bed chamber because this is where the temperature distribution is likely to be more uniform. Furthermore, since the core is the hottest part of the chamber and less likely to lose heat, this will lead to isothermal crystallisation and produce parts with large spherulites, if the temperature remains high and the conditions are stable. Alternatively, a low cooling rate would favour spherulitic growth. Smaller parts can be built closer to the sides of the chamber as they are less likely to be affected by the temperature profile due to their small size. This will result in a part with a uniform microstructure.

In order to expand the research into the thermal behaviour of PA-12 blends, the PA-12 blends can be created from refreshed powder that was part of the powder feedstock of MJF machines. This will enable the melting and crystallisation properties of refreshed PA-12/FA and PA-12/DA to be evaluated. This is representative of MJF and will provide an insight into the thermal behaviour of PA-12 in application. Additionally, other analysis techniques such as gel permeation chromatography can be used to assess changes in molecular weight between virgin powder, refreshed powder and recycled powder. This information can be coupled with DSC data and linked to the agents used in MJF to determine the mechanisms that occur on ageing or recycling.

AM offers the ability to create complex components, specific components, in addition to many different types of components in one build without the need for tooling. Additionally, such components are manufactured relatively quickly and the properties are comparable, if not, exceed other PBF techniques such as SLS. AM techniques, such as MJF, have a promising future though more research is required to unlock the true potential.

REFERENCES

1. Cowie JMG, Arrighi V. Polymers: Chemistry and Physics of modern materials. 2nd ed. Cowie JMG, Arrighi V, editors. USA: Taylor & Francis Group; 2007.
2. Sawyer LC, Grubb DT. Polymer microscopy. 1996;399.
3. Cowie JMG, McKenzie Grant J. Polymers: chemistry and physics of modern materials. 2nd ed. Keith Stead, editor. Cornell University: Intertext Books; 1973. 298 p.
4. Cowie JMG, Arrighi V, Arrighi V. Polymers. 3rd Edition. CRC Press; 2007. 520 pages.
5. Cheng SZD, Lotz B. Enthalpic and entropic origins of nucleation barriers during polymer crystallization: the Hoffman-Lauritzen theory and beyond. Polymer (Guildf). 2005;46:8662–8681.
6. Zhang M, Guo BH, Xu J. A Review on Polymer Crystallization Theories. Vol. 7, Crystals. 2016. 4 p.
7. Misra GS (Gauri S. Introductory polymer chemistry. J. Wiley & Sons; 1993.
8. Holland BJ, Hay JN. Thermal degradation of nylon polymers. Polym Int. 2000;49:943–8.
9. Zhang J, Adams A. Understanding thermal aging of non-stabilized and stabilized polyamide 12 using 1H solid-state NMR. Polym Degrad Stab. 2016 Dec 1;134:169–78.
10. Dong W, Gijsman P. Influence of temperature on the thermo-oxidative degradation of polyamide 6 films. Polym Degrad Stab. 2010;95(6):1054–62.
11. Wudy K, Drummer D, Kühnlein F, Drexler M. Influence of degradation behavior of polyamide 12 powders in laser sintering process on produced parts. 2014 [cited 2019 Jan 29];1593:160004. Available from: https://doi.org/10.1063/1.4873873
12. Chen P, Tang M, Zhu W, Yang L, Wen S, Yan C, et al. Systematical mechanism of Polyamide-12 aging and its micro-structural evolution during laser sintering. Polym Test. 2018 May 1;67:370–9.
13. Yang F, Jiang T, Lalier G, Bartolone J, Chen X. Process control of surface quality and part microstructure in selective laser sintering involving highly degraded polyamide 12 materials. Polym Test. 2021 Jan 1;93:106920.
14. Valko EI, Chiklis CK. Effects of thermal exposure on the physicochemical properties of polyamides. J Appl Polym Sci [Internet]. 1965 Aug 1 [cited 2023 Feb 12];9(8):2855–77. Available from: https://onlinelibrary.wiley.com/doi/full/10.1002/app.1965.070090820
15. Cowie JMG, Arrighi V. Polymers: Chemistry and Physics of Modern Materials. 3rd ed. CRC Press; 2007.
16. Jena AK, Chaturvedi MC. Phase transformations in materials. Prentice Hall; 1992. 243 p.
17. Frank FC. NUCLEATION-CONTROLLED GROWTH ON A ONE-DIMENSIONAL GROWTH OF FINITE LENGTH. J Cryst Growth. 1974;22:233.
18. Point JJ. A New Theoretical Approach of the Secondary Nucleation at High Supercooling. Macromolecules. 1979;11(2):359.

19. Phillips PJ, Phillips PJ. Polymer crystals. Rep Prog Phys. 1990;53:549–604.

20. Zhao M, Wudy K, Drummer D. Crystallization kinetics of polyamide 12 during Selective laser sintering. Polymers (Basel). 2018;10(2).

21. Neugebauer F, Ploshikhin V, Ambrosy J, Witt • Gerd. Isothermal and non-isothermal crystallization kinetics of polyamide 12 used in laser sintering. J Therm Anal Calorim. 2016;124:925–933.

22. Mousa AA, Bashir MO. Additive Manufacturing: A New Industrial Revolution-A Review. JOURNAL OF SCIENTIFIC ACHIEVEMENTS . 2017;2(3):19–31.

23. Chatham CA, Long TE, Williams CB. A review of the process physics and material screening methods for polymer powder bed fusion additive manufacturing. Prog Polym Sci [Internet]. 2019 Jun [cited 2019 May 28];93:68–95. Available from: https://linkinghub.elsevier.com/retrieve/pii/S0079670018303071

24. Deckard CR. Method and Apparatus for Producing Parts by Selective Laser Sintering. Board of Regents; 4,863,538, 1989. p. 12.

25. Hewlett-Packard. HP 3D Jet Fusion 500/300 Color 3D Printer | HP® United Kingdom [Internet]. 3D Printing Solutions. 2017 [cited 2019 Sep 13]. Available from: https://www8.hp.com/uk/en/printers/3d-printers/products/multi-jet-fusion-500-300.html

26. Edirisinghe MJ, Evans JRG. Review: Fabrication of engineering ceramics by injection moulding. II. Techniques. International Journal of High Technology Ceramics. 1986 Jan;2(4):249–78.

27. O'Connor HJ, Dickson AN, Dowling DP. Evaluation of the mechanical performance of polymer parts fabricated using a production scale multi jet fusion printing process. Addit Manuf. 2018 Aug;22:381–7.

28. Changyu S, Lixia W, Qian L. Optimization of injection molding process parameters using combination of artificial neural network and genetic algorithm method. J Mater Process Technol. 2007;183:412–8.

29. Gibson I, Rosen DW, Stucker B. Additive Manufacturing Technologies. Vol. 1. 2010. 1–446 p.

30. Athreya SR, Kalaitzidou K, Das S. Processing and characterization of a carbon black-filled electrically conductive Nylon-12 nanocomposite produced by selective laser sintering. Materials Science and Engineering: A. 2010 Apr 25;527(10–11):2637–42.

31. Sillani F, Kleijnen RG, Vetterli M, Schmid M, Wegener K. Selective laser sintering and multi jet fusion: Process-induced modification of the raw materials and analyses of parts performance. Addit Manuf. 2019;27:32–41.

32. Chen P, Tang M, Zhu W, Yang L, Wen S, Yan C, et al. Systematical mechanism of Polyamide-12 aging and its micro-structural evolution during laser sintering. Polym Test. 2018 May 1;67:370–9.

33. Gu H, Bashir Z, Yang L. The re-usability of heat-exposed poly (ethylene terephthalate) powder for laser sintering. Addit Manuf. 2019 Aug;28:194–204.

34. Zhu W, Yan C, Shi Y, Wen S, Liu J, Shi Y. Investigation into mechanical and microstructural properties of polypropylene manufactured by selective laser sintering in comparison with injection molding counterparts. Mater Des. 2015 Oct 5;82:37–45.

35. Yuan S, Shen F, Bai J, Chua CK, Wei J, Zhou K. 3D soft auxetic lattice structures fabricated by selective laser sintering: TPU powder evaluation and process optimization. Mater Des. 2017 Apr 15;120:317–27.

36. Bourell D, Kruth JP, Leu M, Levy G, Rosen D, Beese AM, et al. Materials for additive manufacturing. CIRP Annals. 2017;66(2):659–81.

37. Cano AJ, Salazar A, Rodríguez J. Effect of temperature on the fracture behavior of polyamide 12 and glass-filled polyamide 12 processed by selective laser sintering. Eng Fract Mech. 2018 Nov;203:66–80.

38. Yan C, Hao L, Xu L, Shi Y. Preparation, characterisation and processing of carbon fibre/polyamide-12 composites for selective laser sintering. Compos Sci Technol. 2011 Nov 14;71(16):1834–41.

39. Yang J, Shi Y, Yan C. Selective laser sintering of polyamide 12/potassium titanium whisker composites. J Appl Polym Sci. 2010 Aug 15;117(4):2196–204.

40. Athreya SR, Kalaitzidou K, Das S. Mechanical and microstructural properties of Nylon-12/carbon black composites: Selective laser sintering versus melt compounding and injection molding. Compos Sci Technol. 2011 Feb 28;71(4):506–10.

41. Espera AH, Valino AD, Palaganas JO, Souza L, Chen Q, Advincula RC. 3D Printing of a Robust Polyamide-12-Carbon Black Composite via Selective Laser Sintering: Thermal and Electrical Conductivity. Macromol Mater Eng. 2019;304(4):1800718.

42. Verbelen L, Dadbakhsh S, Van den Eynde M, Kruth JP, Goderis B, Van Puyvelde P. Characterization of polyamide powders for determination of laser sintering processability. Eur Polym J. 2016 Feb 1;75:163–74.

43. Caulfield B, McHugh PE, Lohfeld S. Dependence of mechanical properties of polyamide components on build parameters in the SLS process. J Mater Process Technol. 2007 Feb 2;182(1–3):477–88.

44. Dupin S, Lame O, Barrès C, Charmeau JY. Microstructural origin of physical and mechanical properties of polyamide 12 processed by laser sintering. Eur Polym J. 2012 Sep 1;48(9):1611–21.

45. Jain PK, Pandey PM, Rao PVM. Experimental investigations for improving part strength in selective laser sintering. Virtual Phys Prototyp. 2008;3(3):177–88.

46. Lexow MM, Drexler M, Drummer D. Fundamental investigation of part properties at accelerated beam speeds in the selective laser sintering process.

47. Majewski CE, Zarringhalam H, Hopkinson N. Effects of Degree of Particle Melt and crystallinity in SLS Nylon-12 parts. 2008.

48. Craft G, Nussbaum J, Crane N, Harmon JP. Impact of extended sintering times on mechanical properties in PA-12 parts produced by powderbed fusion processes. Addit Manuf. 2018;22(June):800–6.

49. Goodridge RD, Hague RJM, Tuck CJ. Effect of long-term ageing on the tensile properties of a polyamide 12 laser sintering material. Polym Test. 2010 Jun;29(4):483–93.

50. Kruth JP, Levy G, Klocke F, Childs THC, Leuven KU. Consolidation phenomena in laser and powder-bed based layered manufacturing. Annals of the CIRP. 56(2).

51. Dadbakhsh S, Leuven KU, Verbelen L, Verkinderen O, Strobbe D, Van Puyvelde P, et al. Effect of PA12 powder reuse on coalescence behaviour and microstructure of SLS parts. Eur Polym J. 2017;92:250–62.

52. Vasquez M, Haworth B, Hopkinson N. Optimum sintering region for laser sintered Nylon-12. In: Proceedings of the Institution of Mechanical Engineers, Part B: Journal of Engineering Manufacture. 2011. p. 2240–8.

53. Partanen J, Khajavi S, Flores Ituarte I, Khajavi SH. Challenges to implementing additive manufacturing in globalised production environments. Int J Collaborative Enterprise. 2016;5:232–47.

54. Hewlett-Packard. HP Multi Jet 3D Printing Technology - The Latest 3D Printing Technology from HP | HP® United Kingdom [Internet]. 2020. Available from: https://www8.hp.com/uk/en/printers/3d-printers/products/multi-jet-technology.html

55. Riedelbauch J, Rietzel D, Witt G. Analysis of material aging and the influence on the mechanical properties of polyamide 12 in the Multi Jet Fusion process. Addit Manuf. 2019;27:259–66.

56. Emamjomeh A, Prasad K, Novick M, Fung EM. DETAILING AGENT FOR THREE - DIMENSIONAL (3D) PRINTING . Hewlett - Packard Development Company , L . P .; 2019.

57. Hopkinson N, Erasenthiran P. High Speed Sintering – Early Research into a New Rapid Manufacturing Process. Solid Freeform Fabrication Symposium. 2004;312–20.

58. Galati M, Calignano F, Defanti S, Denti L. Disclosing the build-up mechanisms of multi jet fusion: Experimental insight into the characteristics of starting materials and finished parts. J Manuf Process. 2020;57:244–53.

59. HP Development Company L.P. HP Jet Fusion 4200 .

60. Xu Z, Wang Y, Wu D, Ananth KP, Bai J. The process and performance comparison of polyamide 12 manufactured by multi jet fusion and selective laser sintering. J Manuf Process. 2019;47:419–26.

61. O' Connor HJ, Dowling DP. Comparison between the properties of polyamide 12 and glass bead filled polyamide 12 using the multi jet fusion printing process. Addit Manuf. 2019;31:100961.

62. Morales-Planas S, Minguella-Canela J, Lluma-Fuentes J, Travieso-Rodriguez JA, García-Granada AA. Multi Jet Fusion PA12 manufacturing parameters for watertightness, strength and tolerances. Materials. 2018;11(8):1–11.

63. Tasch D, Schagerl M, Wazel B, Wallner G. Impact behavior and fractography of additively manufactured polymers: Laser sintering, multijet fusion, and hot lithography. Addit Manuf. 2019;29:2214–8604.

64. Ulbrich J, Swader R, Petry G, Cox BL, Greene RL, Eliceiri KW, et al. A syringe adapter for reduced muscular strain and fatigue. Appl Ergon. 2020 May 1;85:103061.

65. Columns V density L, Using F, Manufacturing A. Buckling and Post-Buckling Behavior of Uniform and Variable-Density Lattice Columns Fabricated Using Additive Manufacturing. Materials. 2019;12:1–15.

66. Alomarah A, Ruan D, Masood S, Gao Z. Compressive properties of a novel additively manufactured 3D auxetic structure. Smart Mater Struct. 2019;2018:17.

67. Alomarah A, Masood SH, Sbarski I, Faisal B, Gao Z, Ruan D. Compressive properties of 3D printed auxetic structures: experimental and numerical studies. Virtual Phys Prototyp. 2019;15(1):1–21.

68. O'Connor HJ, Dickson AN, Dowling DP. Evaluation of the mechanical performance of polymer parts fabricated using a production scale multi jet fusion printing process. Addit Manuf. 2018;22:381–7.

69. Sagbas B, Gümüş BE, Kahraman Y, Dowling DP. Impact of print bed build location on the dimensional accuracy and surface quality of parts printed by multi jet fusion. J Manuf Process. 2021 Oct 1;70:290–9.

70. Stansbury JW, Idacavage MJ. 3D printing with polymers: Challenges among expanding options and opportunities. Dental Materials. 2016;32:54–64.

71. Schmid M, Amado A, Wegener K. Materials perspective of polymers for additive manufacturing with selective laser sintering. J Mater Res. 2014;29(17).

72. Pandelidi C, Lee KPM, Kajtaz M. Effects of polyamide-11 powder refresh ratios in multi-jet fusion: A comparison of new and used powder. Addit Manuf. 2021 Apr 1;40:101933.

73. Tey WS, Cai C, Zhou K. A Comprehensive Investigation on 3D Printing of Polyamide 11 and Thermoplastic Polyurethane via Multi Jet Fusion. Polymers 2021, Vol 13, Page 2139. 2021 Jun 29;13(13):2139.

74. Safka J, Ackermann M, Filip V, Machacek J, Henyš P. Mechanical Properties of Polypropylene : Additive Manufacturing by Multi Jet Fusion Technology. Materials. 2021;14:2165.

75. Scherer B, Kottenstedde IL, Matysik FM. Material characterization of polyamide 12 and related agents used in the multi-jet fusion process: complementary application of high-resolution mass spectrometry and other advanced instrumental techniques. Mater Des. 2020;151:1203–15.

76. Weast RC. CRC Handbook of Chemistry and Physics, 57th Edition. John Wiley & Sons, Ltd; 1977.

77. Frizziero L, Donnici G, Dhaimini K, Liverani A, Caligiana G. Advanced design applied to an original multi-purpose ventilator achievable by additive manufacturing. Applied Sciences (Switzerland). 2018;8(12).

78. Palma T, Munther M, Damasus P, Salari S, Beheshti A, Davami K. Multiscale mechanical and tribological characterizations of additively manufactured polyamide 12 parts with different print orientations. J Manuf Process. 2019;40:76–83.

79. Habib FN, Iovenitti P, Masood SH, Nikzad M. Fabrication of polymeric lattice structures for optimum energy absorption using Multi Jet Fusion technology. Mater Des. 2018;155:86–98.

80. Zolfagharian A, Khosravani MR, Kaynak A. Fracture resistance analysis of 3D-printed polymers. Polymers (Basel). 2020;12(2):1–18.

81. Vega V, Clements J, Lam T, Abad A, Fritz B, Ula N, et al. The Effect of Layer Orientation on the Mechanical Properties and Microstructure of a Polymer. J Mater Eng Perform. 2011;20(6):978–88.

82. Guo B, Xu Z, Luo X, Bai J. A detailed evaluation of surface, thermal, and flammable properties of polyamide 12/glass beads composites fabricated by multi jet fusion. Virtual Phys Prototyp. 2021;1–15.

83. Liu X, Tey WS, Choo JYC, Chen J, Tan P, Cai C, et al. Enhancing the mechanical strength of Multi Jet Fusion–printed polyamide 12 and its glass fiber-reinforced composite via high-temperature annealing. Addit Manuf. 2021 Oct 1;46:102205.

84. Cai C, Tey WS, Chen J, Zhu W, Liu X, Liu T, et al. Comparative study on 3D printing of polyamide 12 by selective laser sintering and multi jet fusion. J Mater Process Technol. 2021;288(116882).

85. Mele M, Campana G, Pisaneschi G, Monti GL. Investigation into effects of cooling rate on properties of polyamide 12 parts in the multi jet fusion process. Rapid Prototyp J. 2020;26(10):1789–95.

86. Wudy K, Drummer D. Aging effects of polyamide 12 in selective laser sintering: Molecular weight distribution and thermal properties. Addit Manuf. 2019 Jan;25:1–9.

87. Pham DT, Dotchev KD, Yusoff WAY. Deterioration of polyamide powder properties in the laser sintering process. Proc IMechE. 2008;22(C):2163–76.

88. Drummer D, Wudy K, Drexler M. Influence of energy input on degradation behavior of plastic components manufactured by selective laser melting. Phys Procedia. 2014;56(C):176–83.

89. Josupeit S, Schmid HJ. Experimental analysis and modeling of local ageing effects during laser sintering of polyamide 12 in regard to individual thermal histories. J Appl Polym Sci. 2017 Nov 5;134(42):45435.

90. Amado F, Wegener K, Schmid M, Levy G. Characterization and modeling of non-isothermal crystallization of Polyamide 12 and co-Polypropylene during the SLS process. 5th International Polymers and Moulds Innovations Conference. 2012.

91. Rosso S, Meneghello R, Biasetto L, Grigolato L, Concheri G, Savio G. In-depth comparison of polyamide 12 parts manufactured by Multi Jet Fusion and Selective Laser Sintering. Addit Manuf. 2020 Dec 1;36:101713.

92. Yang J, Shi Y, Yan C. Selective Laser Sintering of Polyamide 12/Potassium Titanium Whisker Composites. J Appl Polym Sci. 2010;117:2196–204.

93. Mcferran NLA, Armstrong CG, Mcnally T. Nonisothermal and Isothermal Crystallization Kinetics of Nylon-12. J Appl Polym Sci. 2008;110:1043–58.

94. Vasquez M, Haworth B, Hopkinson N. Methods for Quantifying the STable Sintering Region in Laser Sintered Polyamide-12. Polym Eng Sci. 2013;53(6):1230–40.

95. Skrovanek DJ, Howe SE, Painter PC, Coleman MM. Hydrogen Bonding in Polymers: Infrared Temperature Studies of an Amorphous Polyamide. Vol. 18, National Technical Information Service. Oxford University Press; 1985.

96. Iwamoto R, Murase H. Infrared spectroscopic study of the interactions of nylon-6 with water. J Polym Sci B Polym Phys. 2003;41(14):1722–9.

97. Yan C, Hao L, Xu L, Shi Y. Preparation, characterisation and processing of carbon fibre/polyamide-12 composites for selective laser sintering. Compos Sci Technol. 2011;71(16):1834–41.

98. Zarringhalam H, Hopkinson N, Kamperman NF, de Vlieger JJ. Effects of processing on microstructure and properties of SLS Nylon 12. Materials Science and Engineering A. 2006;435–436:172–80.

99. Bassett D, Olley RH, al Raheil AM. On crystallization phenomena in PEEK. Polymer (Guildf). 1988;29:1745–54.

100. Teo HWB, Chen K, Tran VT, Du H, Zeng J, Zhou K. Non-isothermal crystallization behaviour of polyamide 12 analogous to multi-jet fusion additive manufacturing process. Polymer (Guildf). 2021;235.

101. Bourell DL, Watt TJ, Leigh DK, Fulcher B. Performance limitations in polymer laser sintering. Phys Procedia. 2014;56:147–56.

102. Pliquet M, Rapeaux M, Delange F, Bussiere PO, Therias S, Gardette JL. Multiscale analysis of the thermal degradation of polyamide 6,6: Correlating chemical structure to mechanical properties. Polym Degrad Stab. 2021;185:109496.

103. Shen J, Steinberger J, Göpfert J, Gerner R, Daiber F, Manetsberger K, et al. Inhomogeneous Shrinkage of Polymer Materials in Selective Laser Sintering. Ulm, Germany; 2000.

104. Kinoshita Y. An investigation of the structures of polyamide series. Die Makromolekulare Chemie. 1959 Jan 1;33(1):1–20.

105. Schroeder LR, Cooper SL. Hydrogen bonding in polyamides. J Chem Phys [Internet]. 1976 Oct [cited 2020 Oct 27];47(10):4310–7. Available from: https://doi.org/10.1063/1.1743095

106. Goodridge RD, Dalgarno KW, Wood DJ. Indirect selective laser sintering of an apatite-mullite glass-ceramic for potential use in bone replacement applications. Proc Inst Mech Eng H. 2006 Jan 17;220(1):57–68.

107. Mele M, Campana G, Monti GL. Modelling of the capillarity effect for cylindrical shapes in Multi Jet Fusion technology. Progress in Additive Manufacturing. 2021;11.

108. Hoffman JD, Weeks JJ. Melting process and the equilibrium melting temperature of polychlorotrifluoroethylene. J Res Natl Bur Stand A Phys Chem. 1962;66A(1):13.

109. Marand H, Xu J, Srinivas S. Determination of the Equilibrium Melting Temperature of Polymer Crystals: Linear and Nonlinear Hoffman-Weeks Extrapolations. Macromolecules. 1998;31:8219–29.

110. Jenkins MJ, Cao Y, Kukureka SN. The effect of molecular weight on the crystallization kinetics and equilibrium melting temperature of poly(tetramethylene ether glycol). Polym Adv Technol. 2006 Jan;17(1):1–5.

111. Huang JW, Chang CC, Kang CC, Yeh MY. Crystallization kinetics and nucleation parameters of Nylon 6 and poly(ethylene-co-glycidyl methacrylate) blend. Thermochim Acta. 2008;468:66–74.

112. Lu XF, Hay JN. Isothermal crystallization kinetics and melting behaviour of poly(ethylene terephthalate). Polymer (Guildf). 2001;42:9423±9431.

113. Schmid M, Kleijnen R, Vetterli M, Wegener K. Influence of the Origin of Polyamide 12 Powder on the Laser Sintering Process and Laser Sintered Parts. Applied Sciences. 2017;7(5):462.

114. Kruth JP, Levy G, Klocke F, Childs THC, Leuven KU. Consolidation phenomena in laser and powder-bed based layered manufacturing. Annals of the CIRP. 2007;56(2):730–59.

115. Mark J, Ngai K, Graessley W, Mandelkern L, Samulski E, Koenig J, et al. Physical properties of polymers. In: Physical Properties of Polymers. Cambridge University Press; 2004. p. 209–315.

116. Marand H, Huang Z. Isothermal Lamellar Thickening in Linear Polyethylene: Correlation between the Evolution of the Degree of Crystallinity and the Melting Temperature. 2004;

117. Kelly CA, Hay JN, Turner RP, Jenkins MJ. The effect of a secondary process on the analysis of isothermal crystallisation kinetics by differential scanning calorimetry. Polymers (Basel). 2020;12(1).

118. Layachi A, Frihi D, Satha H, Seguela R, Gherib S. Non-isothermal crystallization kinetics of polyamide 66/glass fibers/carbon black composites. J Therm Anal Calorim. 2016;124:1319–1329.

119. Supaphol P. Application of the Avrami, Tobin, Malkin, and Urbanovici-Segal macrokinetic models to isothermal crystallization of syndiotactic polypropylene. Thermochim Acta. 2001;370:37–48.

120. Zhao M, Wudy K, Drummer D. Crystallization kinetics of polyamide-12 during selective laser sintering. Polymers (Basel). 2018;10(168):14.

121. Paolucci F, Baeten D, Roozemond PC, Goderis B, Peters GWM. Quantification of isothermal crystallization of polyamide 12: Modelling of crystallization kinetics and phase composition. Polymer (Guildf). 2018 Oct;155:187–98.

122. Kalkar AK, Deshpande VD, Kulkarni MJ. Isothermal Crystallization Kinetics of Poly(phenylene sulfide)/TLCP Composites. Polym Eng Sci. 2009;49(2):397–417.

123. Supaphol & P, Spruiell JE. Application of the Avrami, Tobin, Malkin, and Simultaneous Avrami Macrokinetic Models to Isothermal Crystallization of Syndiotactic Polypropylenes. Journal of Macromolecular Science, Part B. 2000;39(2):257–77.

124. Huang JW, Kang CC, Chen TH. Isothermal Crystallization of Poly(ethylene-co-glycidyl methacrylate)/Clay Nanocomposites. J Appl Polym Sci. 2005;97:1051–64.

125. Banks W, Gordon M, roe RJ, Sharples A. The crystallization of polyethylene I. Polymer (Guildf). 1963;4(C):61–74.

126. Vefwoyen O, Dupret F, Legras' R. Isothermal and Non-Isothermal Crystallization Kinetics of Polyethylene Terephthalate: Mathematical Modeling and Experimental Measurement. Polym Eng Sci. 1998;38(9):1594–610.

127. Malkin AY, Beghishev VP, Keapin IA. Macrokinetics of polymer crystallization. Polymer (Guildf). 1983;24:81–4.

128. Verhoyen O, Dupret F, Legras R. Isothermal and non-isothermal crystallization kinetics of polyethylene terephthalate: Mathematical modelling and experimental measurement. Polym Eng Sci. 1998;39(9):1594–610.

129. Liu M, Zhao Q, Wang Y, Zhang C, Mo Z, Cao S. Melting behaviors, isothermal and non-isothermal crystallization kinetics of nylon 1212. Polymer (Guildf). 2003 Apr 1;44(8):2537–45.

130. Papageorgiou GZ, Achilias DS, Bikiaris DN. Crystallization Kinetics of Biodegradable Poly(butylene succinate) under Isothermal and Non-Isothermal Conditions. Macromol Chem Phys. 2007 Jun 19;208(12):1250–64.

131. Ozawa T. Kinetics of non-isothermal crystallization. Polymer (Guildf). 1971 Mar 1;12(3):150–8.

132. Liu T, Mo Z, Wang S, Zhang H. Nonisothermal Melt and Cold Crystallization Kinetics of Poly(Aryl Ether Ether Ketone Ketone). J Appl Polym Sci. 1997;107:599–609.

133. Sajkiewicz P, Carpaneto L, Wasiak A. Application of the Ozawa model to non-isothermal crystallization of poly(ethylene terephthalate). Polymer (Guildf). 2001;42(12):5365–70.

134. Jeziorny A. Parameters characterizing the kinetics of the non-isothermal crystallization of poly(ethylene terephthalate) determined by d.s.c. Vol. 19, Polymer. 1978. p. 1142–4.

135. Li J, Fang Z, Tong L, Gu A, Liu F. Effect of multi-walled carbon nanotubes on non-isothermal crystallization kinetics of polyamide 6. Eur Polym J. 2006 Dec 1;42(12):3230–5.

136. Bianchi O, Oliveira RVB, Fiorio R, Martins JDN, Zattera AJ, Canto LB. Assessment of Avrami, Ozawa and Avrami–Ozawa equations for determination of EVA crosslinking kinetics from DSC measurements. Polym Test. 2008 Sep 1;27(6):722–9.

137. Cazé C, Devaux E, Crespy A, Cavrot JP. A new method to determine the Avrami exponent by d.s.c. studies of non-isothermal crystallization from the molten state. Polymer (Guildf). 1997 Feb 1;38(3):497–502.

138. Seltzer R, de la Escalera FM, Segurado J. Effect of water conditioning on the fracture behavior of PA12 composites processed by selective laser sintering. Materials Science and Engineering A. 2011 Aug 25;528(22–23):6927–33.

139. Athreya SR, Kalaitzidou K, Das S. Processing and characterization of a carbon black-filled electrically conductive Nylon-12 nanocomposite produced by selective laser sintering. Materials Science and Engineering A. 2010 Apr 25;527(10–11):2637–42.

140. Gordon M, Taylor JS. Ideal copolymers and the second-order transitions of synthetic rubbers. i. non-crystalline copolymers. Journal of Applied Chemistry. 1952 May 4;2(9):493–500.

141. Fox TG. Influence of Diluent and of Copolymer Composition on the Glass Temperature of a Polymer System. Bulletin of the American Physical Society. 1956;1:123.

142. Kelley FN, Bueche F. Viscosity and glass temperature relations for polymer-diluent systems. Journal of Polymer Science. 1961 Apr 1;50(154):549–56.

143. Li S, Yang Y, Zha X, Zhou Y, Yang W, Yang M. Nanoscale morphology, interfacial hydrogen bonding, confined crystallization and greatly improved toughness of polyamide 12/polyketone blends. Nanomaterials. 2018;8(11).

144. Vasquez M, Haworth B, Hopkinson N. Methods for Quantifying the STable Sintering Region in Laser Sintered Polyamide-12. Polym Eng Sci. 2017;91:399–404.

145. Jiang Z, Jin J, Xiao C, Li X. Effect of surface modification of carbon black (CB) on the morphology and crystallization of poly(ethylene terephthalate)/CB masterbatch. Colloids Surf A Physicochem Eng Asp. 2012 Feb 5;395:105–15.

146. Thomas HR, Hopkinson N, Erasenthiran P. High Speed Sintering-Continuing research into a new Rapid Manufacturing process [Internet]. 2006 [cited 2019 Jun 20]. Available from: https://sffsymposium.engr.utexas.edu/Manuscripts/2006/2006-59-Thomas.pdf

147. Dávila MJ, Alcalde R, Aparicio S. Pyrrolidone Derivatives in Water Solution: An Experimental and Theoretical Perspective. Ind Eng Chem Res. 2009;48(2):1036–1050.

148. Maiti KS, Samsonyuk A, Scheurer C, Steinel T. Hydrogen bonding characteristics of 2-pyrrolidinone: A joint experimental and theoretical study. Physical Chemistry Chemical Physics. 2012;14(47):16294–300.

149. Kadla JF, Kubo S. Miscibility and Hydrogen Bonding in Blends of Poly(ethylene oxide) and Kraft Lignin. Macromolecules. 2003;36(20):7803–11.

150. Saiwari S, Sripornsawat B, Hayeemasae N. Novel thermoplastic vulcanizates based on polyamide 12 blends: Influence of modified devulcanized natural rubber gloves on properties of the blends. Journal of Metals, Materials and Minerals. 2019;29(3):25–31.

151. Pesetskii SS, Fedorov VD, Jurkowski B, Polosmak ND. Blends of Thermoplastic Polyurethanes and Polyamide 12: Structure, Molecular Interactions, Relaxation, and Mechanical Properties. J Appl Polym Sci. 1999;74:1054–70.

152. Santis F de, Pantani R. Nucleation density and Growth rate of Polypropylene measured by Calorimetric experiments. J Therm Anal Calorim [Internet]. 2013 [cited 2022 Jan 25];112(3):1481–8. Available from: http://link.springer.com/http://link.springer.com/

153. Li TC, Ma J, Wang M, Tjiu WC, Liu T, Huang W. Effect of Clay Addition on the Morphology and Thermal Behavior of Polyamide 6. J Appl Polym Sci [Internet]. 2006 [cited 2019 Jan 28];103:1191–9. Available from: www.interscience.wiley.com

154. Konishi Y, Cakmak M. Structural hierarchy developed in injection molding of nylon 6/clay/carbon black nanocomposites. Polymer (Guildf). 2005 Jun 17;46(13):4811–26.

155. Abbott CS, Sperry M, Crane NB. Relationships between porosity and mechanical properties of polyamide 12 parts produced using the laser sintering and multi-jet fusion powder bed fusion processes. J Manuf Process. 2021 Oct 1;70:55–66.

156. Wang Y, Dinapoli CM, Tofig GA, Cunningham RW, Pearson RA. Selective Laser Sintering Processing Behavior of Polyamide Powders.

157. Fox TG, Flory PJ. Second-Order Transition Temperatures and Related Properties of Polystyrene. I. Influence of Molecular Weight. The Journal of Applied Physics. 1950;21:581–91.

158. El-Mazry C, Correc O, Colin X. A new kinetic model for predicting polyamide 6-6 hydrolysis and its mechanical embrittlement. Polym Degrad Stab. 2012 Jun;97(6):1049–59.

159. Shu Y, Ye L, Yang T. Study on the long-term thermal-oxidative aging behavior of polyamide 6. J Appl Polym Sci. 2008 Oct 15;110(2):945–57.

160. Van Hooreweder B, Moens D, Boonen R, Kruth JP, Sas P. On the difference in material structure and fatigue properties of nylon specimens produced by injection molding and selective laser sintering. Polym Test. 2013 Aug 1;32(5):972–81.

161. Craft G, Nussbaum J, Crane N, Harmon JP. Impact of extended sintering times on mechanical properties in PA-12 parts produced by powderbed fusion processes. Addit Manuf. 2018 Aug 1;22:800–6.

162. Maïza S, Lefebvre X, Brusselle-Dupend N, Klopffer MH, Cangémi L, Castagnet S, et al. Physicochemical and mechanical degradation of polyamide 11 induced by hydrolysis and thermal aging. J Appl Polym Sci. 2019;136(23).

163. Arhant M, le Gac PY, le Gall M, Burtin C, Briançon C, Davies P. Modelling the non Fickian water absorption in polyamide 6. Polym Degrad Stab. 2016;133(November):404–12.

164. Su KH, Lin JH, Lin CC. Influence of reprocessing on the mechanical properties and structure of polyamide 6. J Mater Process Technol. 2007 Oct 1;192–193:532–8.

165. Blumenshine RL, Sears PG. Several Properties of the 2-Pyrrolidone- Water System as Functions of Composition and Temperature [Internet]. Lexington, Ky.; 1966 [cited 2020 Nov 5]. Available from: https://pubs.acs.org/sharingguidelines

166. Marsh JJ, Turner RP, Carter J, Jenkins MJ. Thermal diffusivity and secondary crystallisation kinetics in poly (lactic acid). Polymer. 2019 Sep 28;179:121595.

167. Sharma SK, Verma DS, Khan LU, Kumar S, Khan SB, editors. Handbook of materials characterization. New York, NY, USA:: Springer International Publishing; 2018.

168. Sanders B, Cant E, Amel H, Jenkins M. The Effect of Physical Aging and Degradation on the Re-Use of Polyamide 12 in Powder Bed Fusion. Polymers. 2022 Jun 30;14(13):2682.

APPENDIX A

The effect of HP Fusing Agent and HP Detailing Agent on the thermal properties and microstructure of polyamide-12.

Keywords; polyamide-12, multi-jet fusion, fusing agent, detailing agent, recrystallisation.

Abstract:

Multi Jet Fusion (MJF) is a proprietary additive manufacturing (AM) technique that falls into the subcategory of powder bed fusion (PBF). Key to this technique are the fusing agent (FA) and detailing agent (DA). These agents were deconstructed into their main chemical constituents and the impact of these constituents on the thermal and chemical properties, as well as microstructure, of polyamide-12 (PA-12) was investigated using differential scanning calorimetry (DSC), Fourier Transform Infrared Spectroscopy (FTIR) and optical microscopy. Blends of PA-12 and FA, DA, water, carbon black or 2-pyrrolidone (2-PYR) at varying wt. % compositions were produced and it was apparent that the 2-PYR had a significant impact on the thermal properties of PA-12 via its action as plasticiser: DSC revealed a depression in polymer glass transition temperature (T_g), of up to 17 ℃, and a depression in melting temperature, of up to 10 ℃, with increasing composition of 2-PYR. Moreover, the crystallisation behaviour was also affected by the 2-PYR component in that its presence decreased the supercooling required for the onset of crystallisation. FTIR analysis revealed a small peak at 1690 cm^{-1} which was assigned to 2-PYR and this indicated that 2-PYR was retained in the PA-12 and interacted with the polymer via hydrogen bonding. Optical microscopy showed that the 2-PYR constituent did not affect the spherulite sizes, but in the case of the carbon black constituent, it was found to be rejected to the inter-spherulitic regions and this was coupled with a noTable reduction in spherulite size.

1.0 Introduction

Multi Jet Fusion (MJF) is a proprietary additive manufacturing (AM) technique that falls into the sub category of powder bed fusion (PBF) (1,2). In MJF, a thin layer of polymer powder is spread onto a build platform using a blade (3). An inkjet head scans the surface to selectively deposit a fusing agent (FA) and a detailing agent (DA). An infrared lamp is then used to induce localised melting of the polymer particles in areas containing the FA. This process is repeated until the build is complete. The design freedom offered by PBF techniques, such as MJF, allows for the fabrication of a range of components, including high pressure hydraulic valves, fuel tanks and biomedical devices and even complex components such as lattices and auxetic structures (4–9).

Polyamide-12 (PA-12) is the most common polymeric material used in PBF and in particular, MJF (10). PA-12 is a semi-crystalline thermoplastic polymer with good mechanical and physical properties. PA-12 typically exhibits a tensile strength of ~ 49 MPa (11) and melts in the region of 184 – 187 ℃. The combination of a relatively high onset of melting and low onset of crystallisation provide a wide sintering

window, which prevents the crystallisation during the build and offers greater control of the sintering or fusion process (3,12). More recently, the powder feedstock material selection has expanded to glass-filled PA-12, polyamide-11 and polypropylene (13–15).

In addition to PA-12, the FA and DA are also important components in the build process in that they enable localised heating and prevent thermal bleeding on the powder bed surface, respectively (16). The main difference between the two agents is the presence of carbon black within the FA, in which carbon black is used as a radiation absorbing material to facilitate particle melting and lower the powder bed temperature (16).

Previous work in relation to the characterisation of the FA and DA is limited to chemical/compositional analysis. Recent studies have shown the key constituents include water, 2-pyrrolidone (2-PYR), triethylene glycol and carbon black (only present within the FA) (3,17). Though, the quantity of each organic solvent in the FA and DA was found to differ (17). The increased content of water present within the DA enables a localised cooling effect and this inhibits heat transfer on the powder bed surface (3,17). Whereas, water is used in the FA to allow a homogeneous distribution of carbon black to penetrate through the deposited powder layer (17). After water, 2-PYR has been reported as the next abundant solvent, said to be included due to its inert nature and high boiling point (251 °C) (18). Thermogravimetric Analysis (TGA) has also been used to explore the composition of the agents (14,17). A rapid mass loss was observed for both of the agents due to presence of organic solvents, in particular, water and this was reported to be at temperatures as low as 40 °C (14,17).

Previous work on components fabricated by MJF is dominated by studies that focus on the mechanical properties of the resulting parts, such as modulus or tensile behaviour (4,5,22–25,8,9,11,13,16,19–21), and the focus of thermoanalytical studies is to evaluate the thermal history of the items (largely as a means of quality control). Analysis using differential scanning calorimetry (DSC) typically reveals a double or single melting peak, which are interpreted as partial or complete melting of polymer particles during the manufacturing process, respectively (21,24,26,27). Other studies that investigate the thermal properties of PA-12 include characterisation of the melting and recrystallisation behaviour of virgin and recycled powder using DSC (25)(16)(3).

Current literature relating to MJF is limited to the characterisation of the thermal properties of virgin or refreshed PA-12 feedstock material, and in some instances, the study of the composition of the FA and DA systems. However, the effect of the FA and DA, and their constituent components on the thermal properties such as melting and recrystallisation of PA-12 is limited. Therefore, in this study, the FA and DA systems were deconstructed into their primary chemical constituents and blends of PA-12/carbon black, PA-12/water, PA-12/2-PYR and PA-12/2-PYR/water were created. These blends were characterised using DSC, infrared spectroscopy and optical microscopy in order to understand the effect of these FA and DA system constituents on the thermal behaviour and microstructure of PA-12.

2.0 Materials, experimental methods, and techniques.

2.1 Materials

All materials were provided by MTC (Coventry, UK) and used as received. These were proprietary Hewett Packard (HP) materials. Namely, HP 3D High Reusability PA-12 powder, by trade name V1R10Series, the fusing agent (FA), by trade name V1Q63Series, and the detailing agent (DA), by trade name V1Q64Series. Additionally, 2-pyrrolidone (CAS 616-45-5) (2-PYR) was supplied by Merck (Darmstadt, Germany). The PA-12 polymer exhibited a glass transition temperature (T_g), peak melting temperature (T_m) and crystallisation temperature (T_c) of 50.37, 187.20 and 148.3 °C, respectively (determined as per section 2.3). Furthermore, the average enthalpy of fusion and degree of crystallinity were 105.3 J/g and 50.3 %. These measured values were comparable to those reported elsewhere. (16).

2.2. Sample preparation

Blends of PA12/FA and PA12/DA were prepared via dispersion of the liquid FA (and DA) into the PA-12 powder. The following compositions were produced, 1, 5, 10 and 20 wt.% FA (or DA). These liquid dispersions were designated as liquid-solid dispersions. The FA and DA contain a large proportion of water (17), so to dry the blends, they were stored in a desiccator with silica gel and weighed periodically until the weight was constant. The use of heat in the drying process was avoided to limit the extent to which hydrolysis could occur on heating. To verify that any residual water in the PA-12 blend component was not degrading the polymer during thermal analysis, water was added to PA-12 in varying quantities, then dried as above, and the melting region recorded using differential scanning calorimetry.

To isolate the effect of the carbon black constituent, the FA was allowed to evaporate in a fume cupboard for 48 hrs. The carbon black was found to be present at a concentration of 0.586 g/mL. The recovered carbon black was then mixed with the PA-12 powder to produce blends. The carbon black was added in quantities that would yield the same wt.% carbon black compositions as in the FA blends i.e. 1, 5, 10 and 20 wt.% carbon black. These blends were designated solid-solid dispersions and were stored in a desiccator with silica gel until required. This composition range was in accordance with other reported compositions, where in previous studies, AM components were fabricated at varying compositions in the range 1-10 wt.% carbon black in PA-12 (28,29).

Blends of PA-12/2-PYR were also created, in which liquid 2-PYR was added to PA-12 in compositions within the range of 0.10 – 8.72 wt.% 2-PYR, this was in proportion to the quantity of 2-PYR present within the PA-12/FA and PA-12/DA blends. Also, to assess the effect of any interaction between water and 2-PYR, three-component blends were produced that were compositionally identical to that in the FA and DA. These blends were created from a different batch of PA-12 powder (HP 3D High Reusability PA-12 powder). The thermal properties of this batch were evaluated and the melting and recrystallisation behaviour was comparable to PA-12. However, a lower degree of crystallinity on heat 1 and cool 1 observed. The degree of crystallinity on heat 1 and cool 1 were 41.9 and 23.6 %. All compositions are reported in Table 1.

Table 1 Summary of blends and blend compositions.

Blend	Composition

PA-12/carbon black	1, 5, 10, 20 wt.% carbon black
PA-12/FA	1, 5, 10, 20 wt.% FA
PA-12/DA	1, 5, 10, 20 wt.% DA
PA-12/water	5.2, 26.9, 56.9, 127.9 μL
PA-12/2-PYR	0.10, 0.38, 0.50, 1.05, 1.97, 2.33, 4.07, 8.72 wt.% 2-PYR
PA-12/2-PYR/water (FA)	0.38, 1.97, 4.07, 8.72 wt.% 2-PYR
PA-12/2-PYR/water (DA)	0.10, 0.50, 1.05, 2.33 wt.% 2-PYR

2.3 Thermal analysis

A Mettler Toledo DSC 1 (Mettler-Toledo, Greifensee, Switzerland), calibrated with indium and zinc standards, was used to record the thermal response of the PA-12 powder and the blends described in section 2.2 (39). A standard procedure was adopted in which the samples were weighed into 40 µL aluminium DSC pans sealed with aluminium DSC lids (39). Samples masses were in the region of 6 ± 0.5 mg. All experiments were carried out under nitrogen supplied at a flow rate of 50 mL/min (39). Samples were heated from 25 to 220 °C at 10 °C/min and the glass transition temperature, peak melting temperature, last trace of crystallinity and the heat of fusion were determined from the glass transition region and the melting region. Prior to cooling, samples were stored at the upper isotherm for a period of two minutes to ensure complete melting and eliminate residual crystals, they were then cooled to 25 °C at 10 °C/min. The onset crystallisation temperature, peak crystallisation temperature and the heat of crystallisation were determined from the crystallisation region. For this study, the first heating run was used to evaluate the thermal history of the blend preparation process.

The degree of crystallinity was determined using the enthalpy of fusion for 100 % crystalline PA-12, $\Delta H_f^{100\%}$ = 209.3 J/g (3). Where X_c is the degree of crystallinity, ΔH_f is the enthalpy of fusion, $\Delta H_f^{100\%}$ is the enthalpy of fusion for a 100 % crystalline polymer and f if the filler weight percentage (30).

$$X_C = \left(\frac{\Delta H_f}{\Delta H_f^{100\%}(1-f)} \right) \times 100$$

2.4. Optical microscopy

Micrographs of recrystallised PA-12 and PA-12 blends were captured at a magnification of 500x. Samples were prepared by spreading $\sim 1\ mg$ of PA-12 powder and PA-12 powder blends (as described in section 2.2) between 2 circular glass discs (diameter 16mm). These were placed in a Linkam THMS600 hot-stage controlled by a Linkam LK600 controller. The hot-stage was mounted on a Leitz optical microscope. Digital images were captured using a Pixelink digital camera. Samples were heated to 220 °C and stored at an upper isotherm of 220 °C for two minutes prior to cooling back to 25 °C at a rate of 0.5 °C/min.

2.5 Infrared Spectroscopy (FTIR)

A Nicolet 8700 attached with an attenuated total reflection (ATR) accessory was used to record spectra of PA-12 and PA-12 blends in solid form extracted from the DSC aluminium pans. The spectra were recorded within the wavenumber range of 400 – 4000 cm^{-1}. To define peak position and improve the signal quality, each sample was subjected to 250 scans at resolution of 2 cm^{-1}.

3.0 Results

3.1 The effect of the FA, DA and their chemical constituents on the thermal properties of PA-12.

In the PA-12/FA and PA-12/DA blends, the FA and DA had a significant impact on the thermal properties of PA-12 powder in that a depression in glass transition temperature and peak melting temperature were observed with increasing content of FA and DA. This is illustrated in Figs. 1a, 1b, 2a and 2b. Furthermore, the onset of melting and last trace of crystallinity also shifted to lower temperatures with increasing content of FA and DA. The enthalpy of fusion (and degree of crystallinity) increased with increasing FA content. Whereas, in the PA-12/DA blend the enthalpy of fusion and degree of crystallinity remained constant and were unaffected by the addition of DA.

The crystallisation behaviour displayed a more complex pattern. In the PA-12/FA blends (Fig. 1c), reduced quantities of FA (1 and 5 wt.% FA) shifted the peak crystallisation temperature to slightly higher temperatures compared to the peak crystallisation temperature of PA-12. However, for higher compositions of FA (10 and 20 wt.% FA) the peak crystallisation temperature shifted to lower temperatures. The onset of crystallisation also followed the same trend. In the PA-12/DA blends (Fig. 2c), the crystallisation behaviour differed in that increasing the DA content caused the onset and peak crystallisation temperature to shift to lower temperatures compared to the peak crystallisation temperature of PA-12. Also, the enthalpy of crystallisation increased with increasing content of FA. Whereas, in the PA-12/DA blend, the enthalpy of crystallisation and degree of crystallinity remained constant and were unaffected by the addition of DA.

In the PA-12/carbon black blend system, the thermal behaviour was largely unaffected by the carbon black content, as displayed in Fig, 3 and 4, but the enthalpy of fusion (and degree of crystallinity) determined from the first heat in the DSC increased with increasing carbon black. However, on reheating, no such increase was observed. In the PA-12 and water samples, the thermal behaviour such as the glass transition temperature, melting temperature (peak and last trace) and crystallisation temperatures (onset and peak) were unaffected by the addition of water. Also, the enthalpy of fusion and degree of crystallinity were also unaffected by the addition of water. This suggests that any residual water was not degrading the sample.

In PA-12/2-PYR blends, the 2-PYR had a significant impact on the thermal properties of PA-12 powder in that a depression in glass transition temperature and peak melting temperature was observed for increasing content of 2-PYR. Furthermore, the onset of melting and last trace of crystallinity also shifted to lower temperatures with increasing content of 2-PYR, as displayed in Fig. 3. The enthalpy of fusion and degree of crystallinity remained constant and were unaffected by the increasing content of 2-PYR. Regarding

crystallisation, there was a decrease in onset and peak crystallisation temperature with increasing composition of 2-PYR, as displayed in Fig. 4. The enthalpy of crystallisation and degree of crystallinity were unaffected by the addition of 2-PYR. In the PA-12/2-PYR/water blends, the combined effect of 2-PYR and water on the thermal properties of PA-12 was investigated. Despite the ratio of 2-PYR and water present in the FA and DA being different, the trends observed in each blend subcategory were similar, as displayed in Fig, 3 and 4. A depression in glass transition temperature and peak melting temperature was observed. The enthalpy of fusion and degree of crystallinity remained constant and was unaffected by the addition of 2-PYR and water. The crystallisation behaviour displayed a decrease in onset and peak crystallisation temperature. The enthalpy of crystallisation and degree of crystallinity were unaffected.

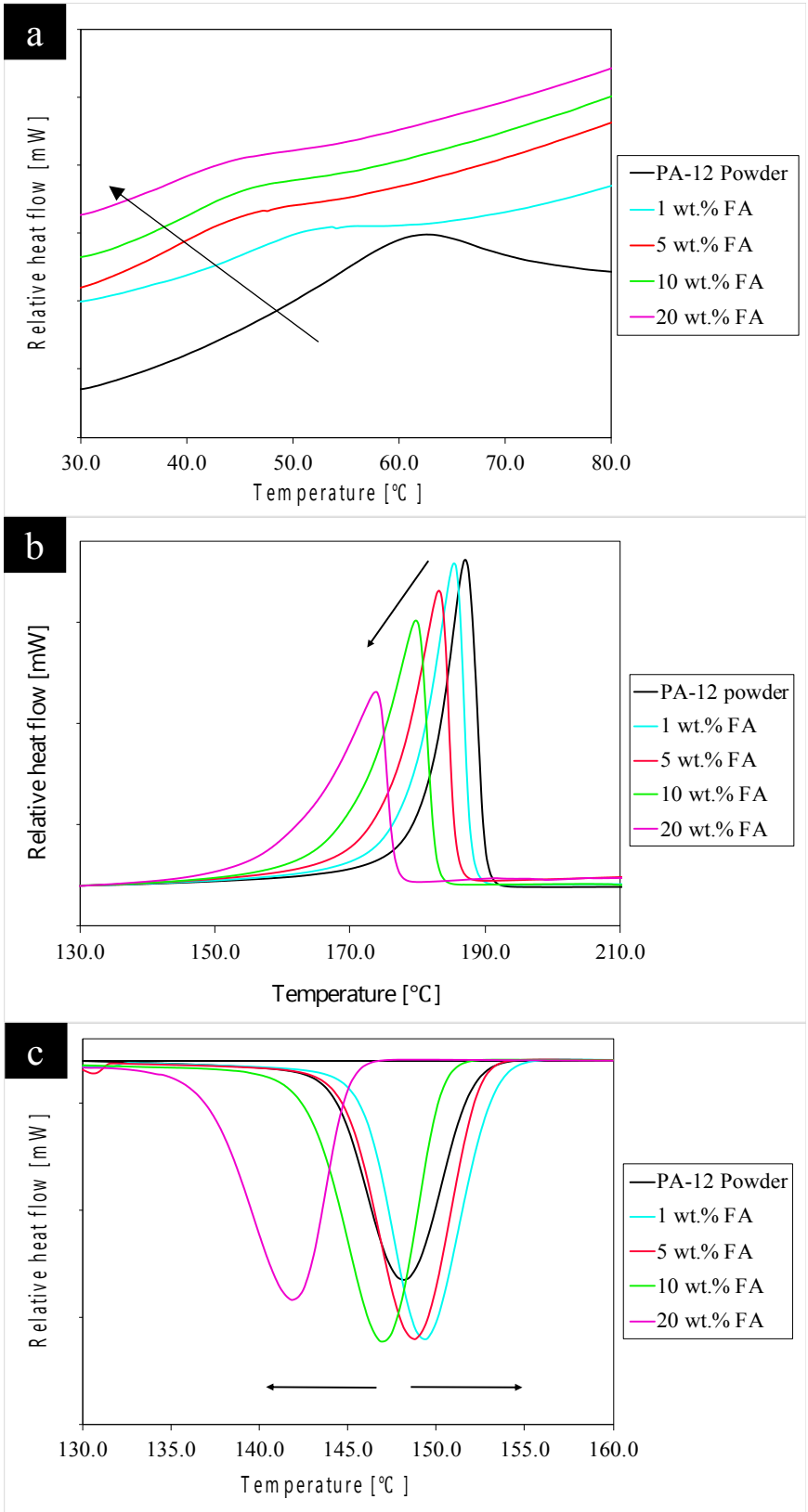

Figure 1 (a) Glass transition region (b) melting region (c) crystallization region of PA-12/FA blends, using a heating and cooling rate of 10 K/min.

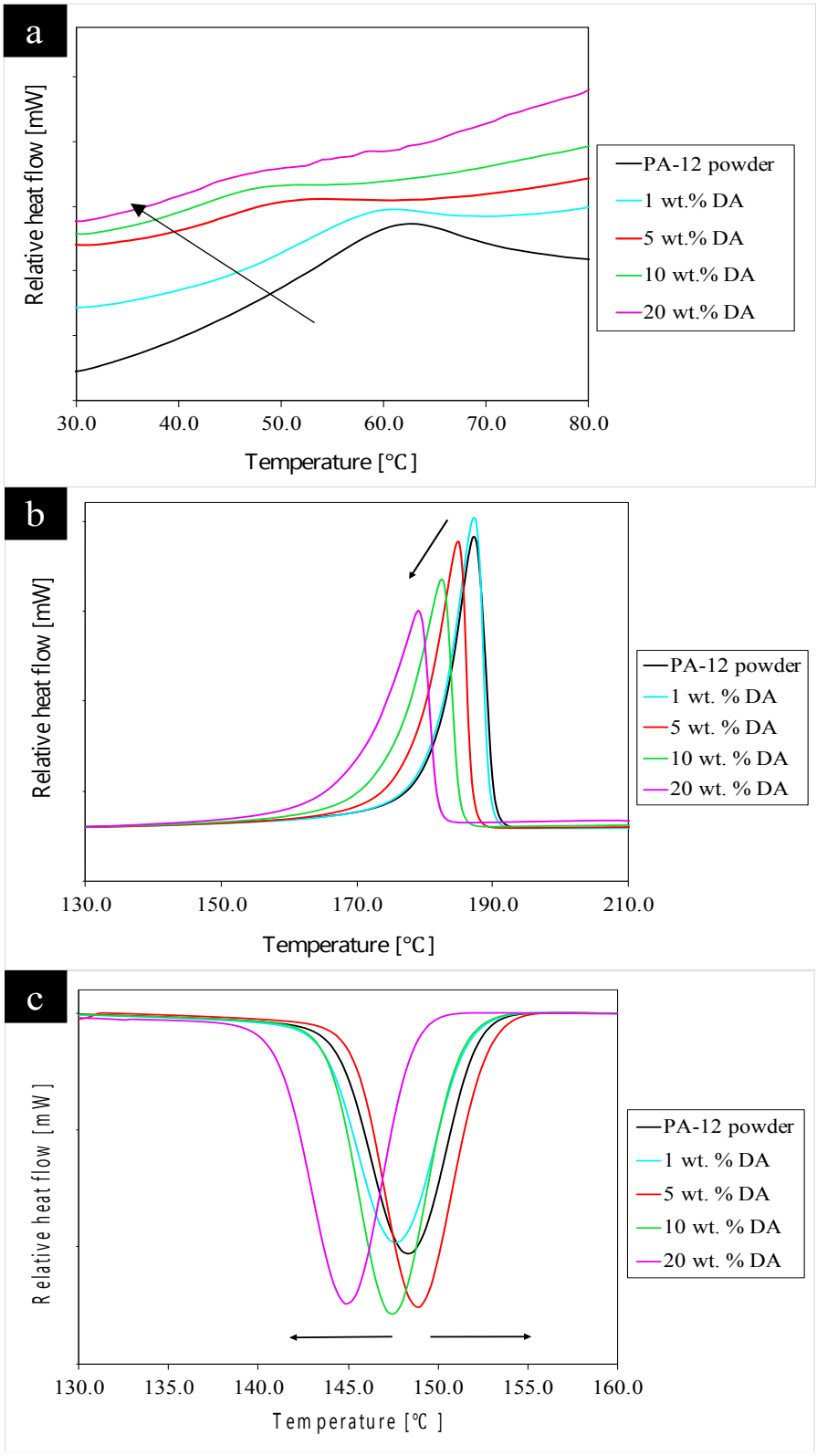

Figure 2 (a) Glass transition region (b) melting region (c) crystallization region of PA-12/DA blends, using a heating and cooling rate of 10 K/min.

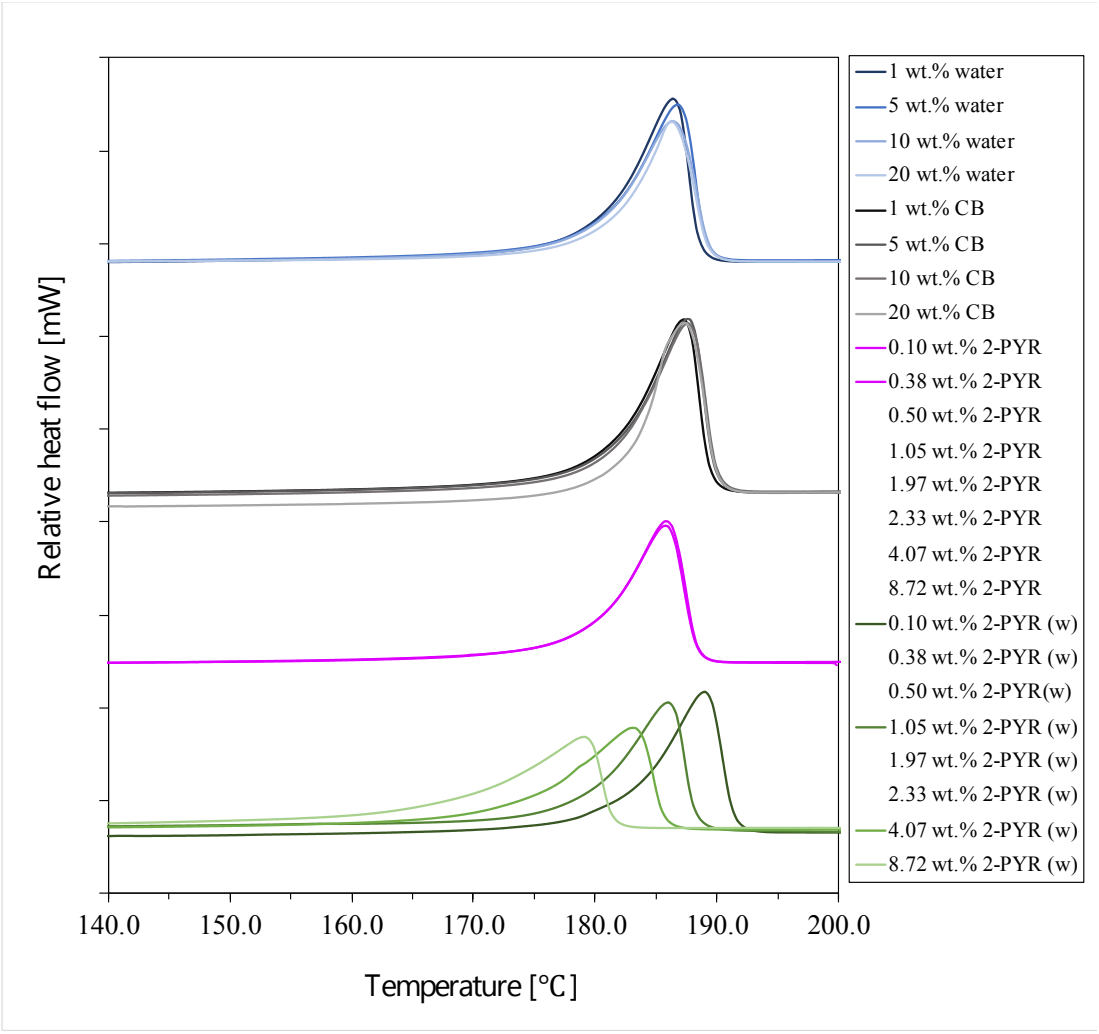

Figure 3 Deconstruction of the FA and DA into key constituents and their influence on the melting temperature on PA-12, using a heating rate of 10 ℃/min. Where CB is carbon black, 2-PYR is 2-pyrrolidone and 2-PYR (w) is 2-pyrrolidone and water blend.

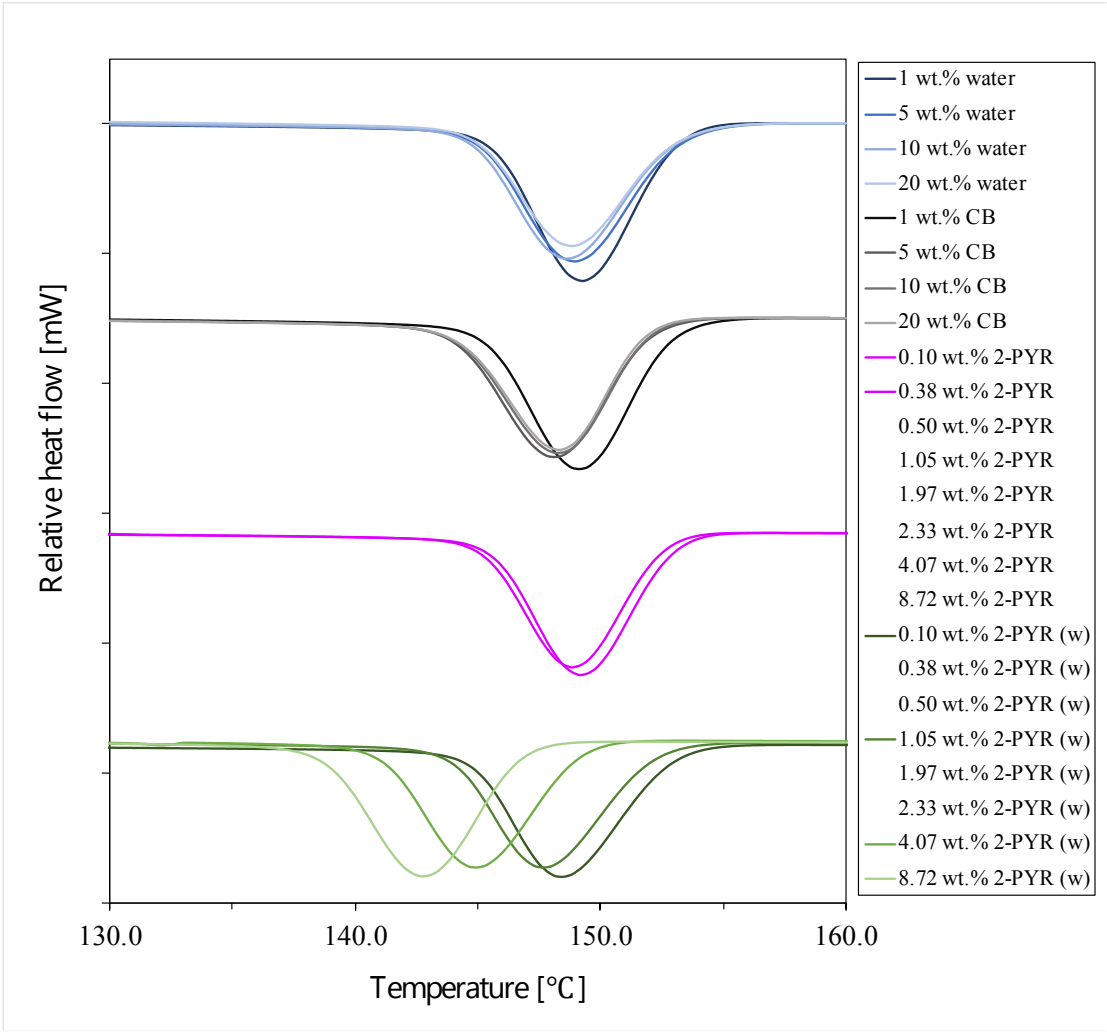

Figure 4 Deconstruction of the FA and DA into key constituents and their influence on the crystallisation temperature on PA-12, using a cooling rate of 10 °C/min. Where CB is carbon black, 2-PYR is 2-pyrrolidone and 2-PYR (w) is 2-pyrrolidone and water blend.

3.2 The effect of the FA, DA and 2-PYR on the microstructure of PA-12.

Optical microscopy was used to observe the effect of the FA, DA and 2-PYR on the microstructure of PA-12 by cooling selected blends from the melt to room temperature using a controlled cooling rate of 0.5 °C/min. The microstructure of PA-12 is shown in Fig. 5a. The microstructure of 1 and 20 wt.% FA blends are displayed in Fig. 5b and 5c, the dark regions represent carbon black and the surrounding area is the semi-crystalline polymer matrix. As the composition of FA increased, there was a greater content of carbon black dispersed within the polymer matrix. This shows that carbon black was retained in the polymer but largely rejected into the inter-spherulitic regions. This has been observed previously by C. Abbott et al (31). Compared to PA-12 (Fig. 5a), the typical spherulite sizes in the 1 and 20 wt.% FA blends were significantly reduced. The microstructure of the 1 and 20 wt.% DA blends are displayed in Fig. 5d and 5e. In the 1 wt.% DA blend, the spherulite size was comparable to PA-12. In the 20 wt.% blend, the spherulite size reduced slightly. The microstructure of the 1 and 20 wt.% CB blends are displayed in Fig. 5f and 5g. In the 1 and 20 wt.% carbon black blend, the spherulite size decreased in comparison to PA-12. The microstructure of 0.38 and 8.72 wt.% 2-PYR blends are displayed in Fig. 5h and 5i. In the 0.38 wt.% 2-PYR blend, the spherulite

size was comparable to PA-12. In the 8.72 wt.% 2-PYR blend, the spherulite size reduced slightly, however this was insignificant in comparison to the reduction in spherulite size caused by the FA, therefore, showing the FA had a greater impact on spherulite size than 2-PYR.

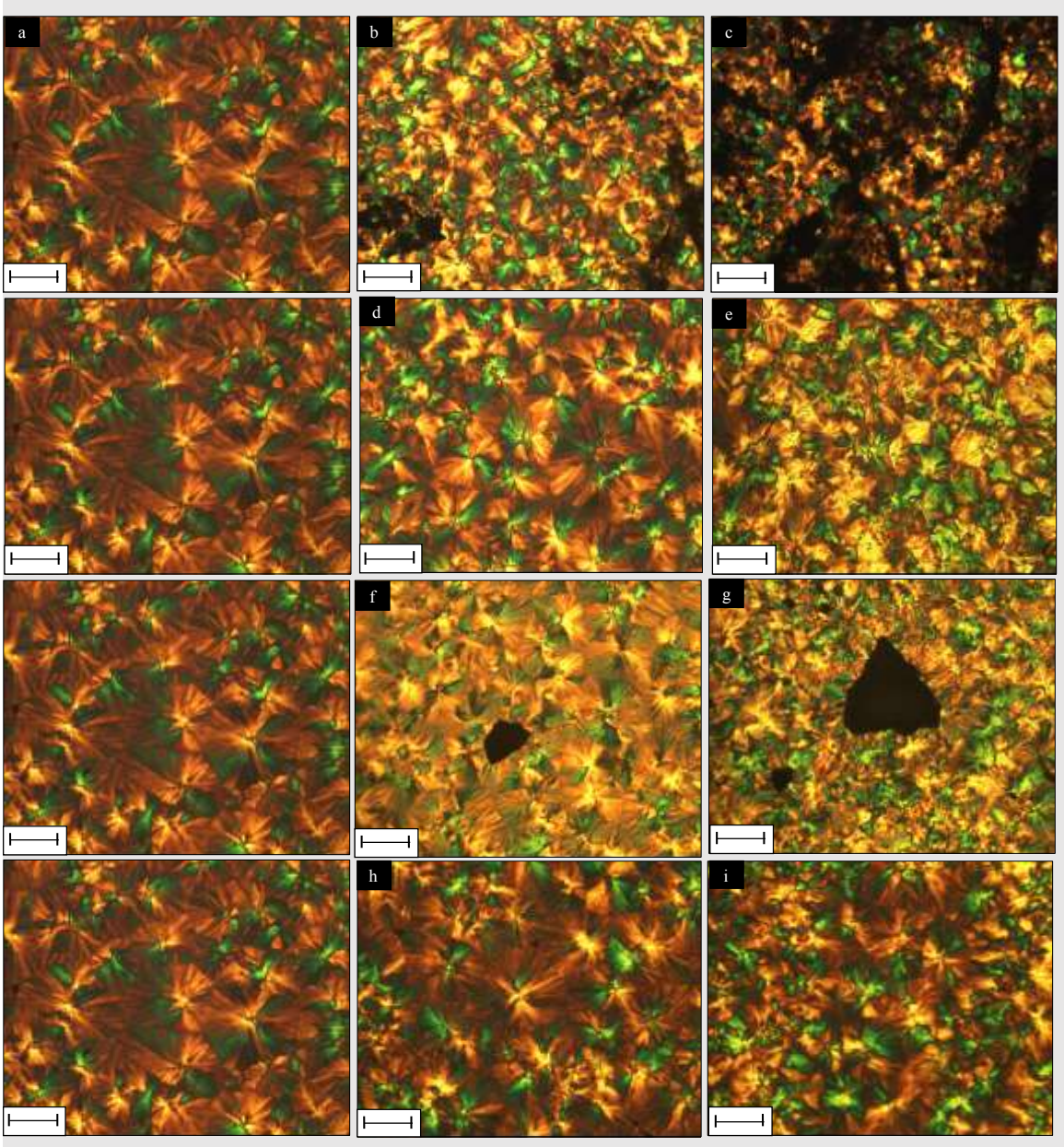

Figure 5 Optical micrographs at a magnification of 500 x of PA-12 and PA-12 blends, a) PA-12, b) 1 wt.% FA, c) 20 wt.% FA, d) 1 wt.% DA, e) 20 wt.% DA, f)1 wt.% carbon black, g) 20 wt.% carbon black, h) 0.38 wt.% 2-PYR i) 8.72 wt.% 2-PYR. Scale bar to 50 μm.

3.3 The effect of blend composition on the N-H stretch and C=O stretch of PA-12.

The FTIR-ATR spectra obtained of PA-12 and PA-12 blends are displayed in Fig. 6. The peak assignments for PA-12 are shown in Table 3 and were comparable to those reported by H.J O'Conner et al for a PA-12

part manufactured by MJF (11,13). In polyamides, the N-H moiety (absorbance band 3100 – 3500 cm^{-1}) can participate in hydrogen bonding with the C=O moiety (absorbance band 1590 – 1670 cm^{-1}) (32,33), but the presence of other molecular species within the polymer can disrupt this interaction and cause the peaks to shift. As displayed in Fig. 7, the peak wavenumber for the N-H band varied between the blends. In the PA-12/FA and PA-12/DA blends, the N-H peak varied unsystematically with the composition of FA and DA. This suggests some form of interaction between the constituents of the FA and DA with the PA-12. This was also true in the PA-12/2-PYR blends, where a shift in peak wavenumber was observed. This suggests the 2-PYR component (common to the FA and DA) caused the shift in peak wavenumber of the N-H band by interacting with PA-12. Similarly, this was also observed in the PA-12/2-PYR/water blends. In the PA-12/carbon black and PA-12/water blends, no significant shift in peak wavenumber was observed.

A strong peak resembling the C=O stretch at ~1634 cm^{-1} was present in all spectra and is displayed for selected blends in Fig. 8. However, in the PA-12/2-PYR blends (in particular, at 8.72 wt.% 2-PYR), a small and wide peak at ~1690 cm^{-1} was observed and increased with 2-PYR composition, illustrated by the upwards arrow in Fig. 8. This was also observed for in the 20 wt.% FA blend, though the appearance of the band was distorted and weak, due to the presence of carbon black within FA. The small and wide peak at ~1690 cm^{-1} was assigned to the amide-I band (C=O stretch) of 2-PYR. In other FTIR studies on 2-PYR in CCl_4 solution, a strong narrow band at 1699 cm^{-1} was assigned to the amide-I band (the C=O stretch) of 2-PYR (34).

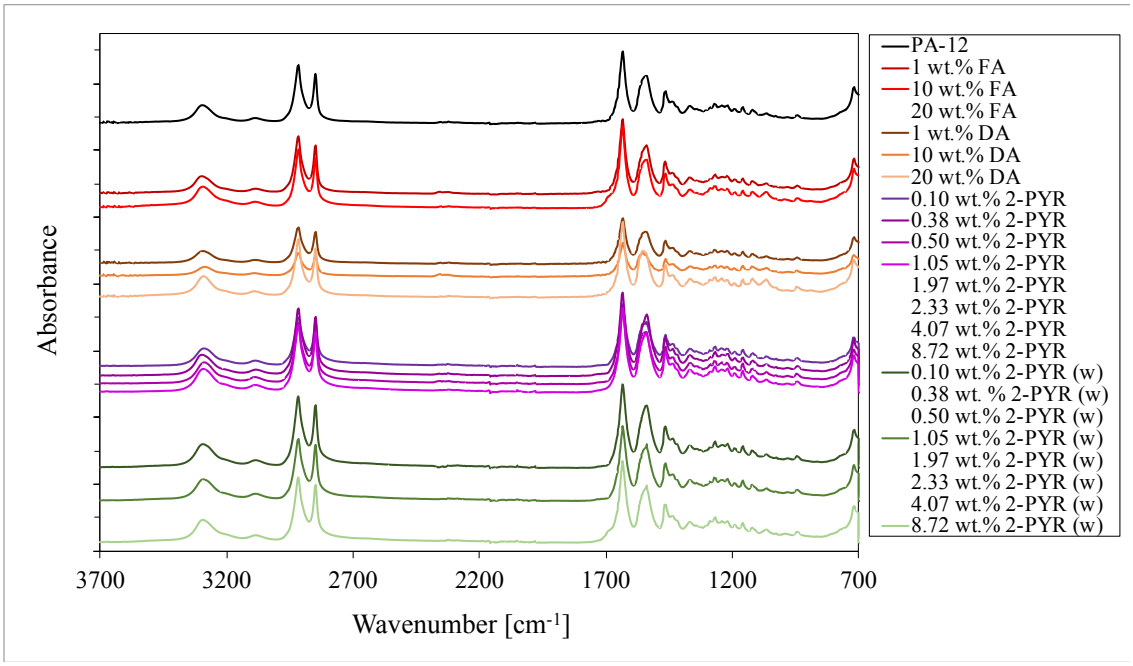

Figure 6 FTIR spectra of PA-12, PA-12/FA, PA-12/DA, PA-12/2-PYR and PA-12/2-PYR/water blends at varying compositions of FA, DA, 2-PYR and water. All recorded spectra were normalised to the same baseline. Where FA is Fusing Agent, DA is Detailing Agents, 2-PYR is 2-pyrrolidone and 2-PYR (w) is 2-pyrrolidone and water.

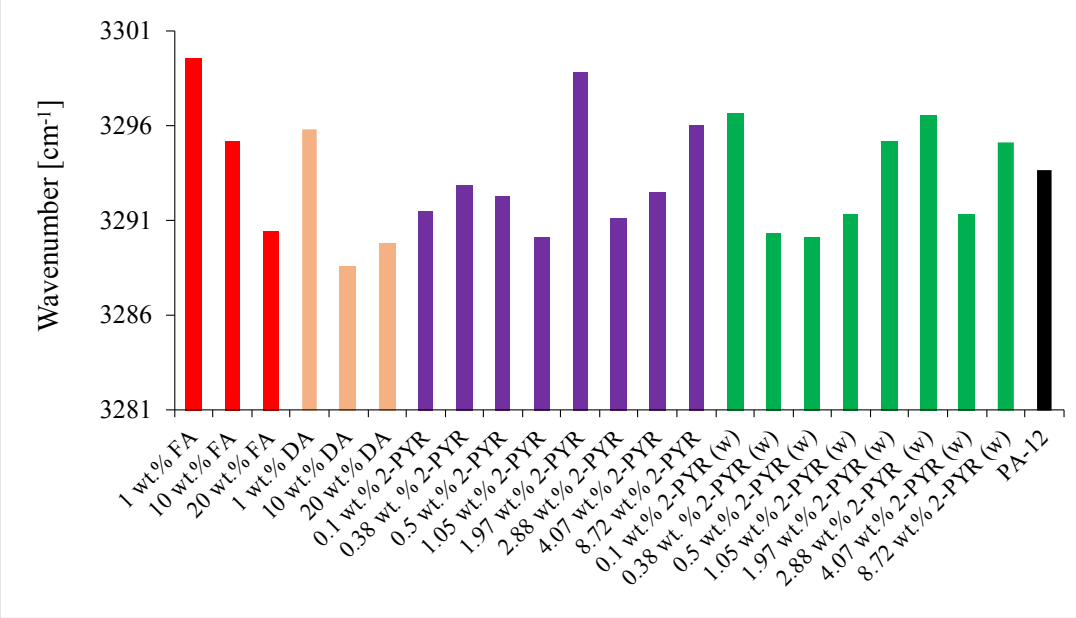

Figure 7 Bar chart showing the peak wavenumber of the N-H stretch for blends exhibiting a shift in peak wavenumber, when compared to the peak wavenumber of PA-12. Where FA is the Fusing Agent, DA is the Detailing Agent, 2-PYR is 2-pyrrolidone and 2-PYR (w) is 2-pyrrolidone and water.

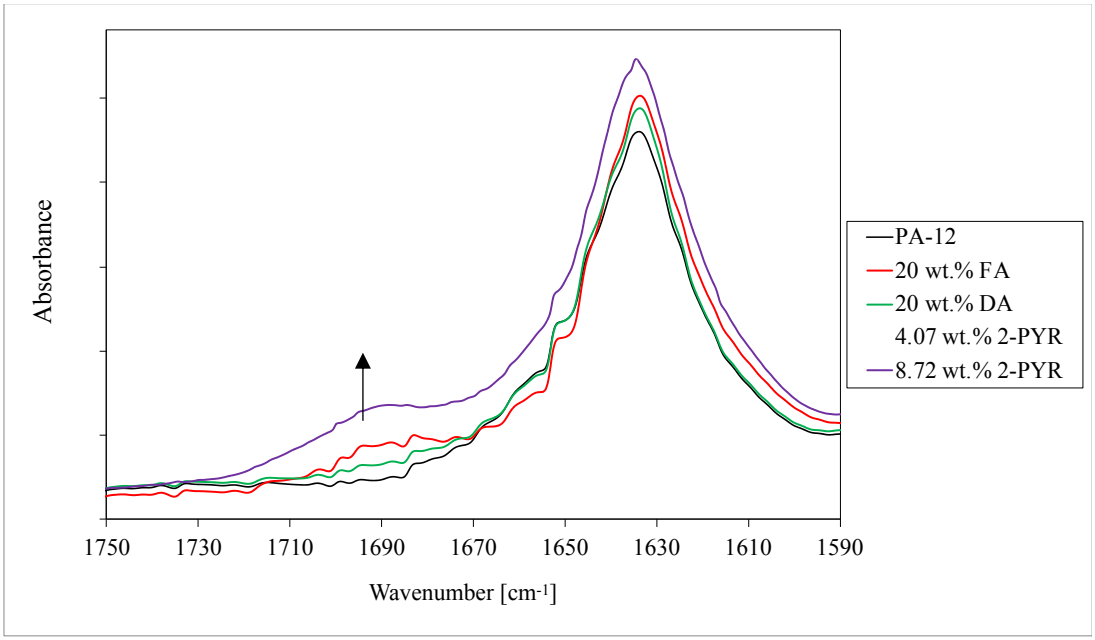

Figure 8 FTIR spectra of PA-12, PA-12/2-PYR, PA-12/FA and PA-12/DA blends showing the carbonyl (C=O) stretch at 1635 cm^{-1}. The upwards arrow indicates a peak at 1690 cm^{-1} that increased with composition of 2-PYR. All recorded spectra were normalised to the same baseline. Where FA is the Fusing Agent, DA is the Detailing Agent and 2-PYR is 2-pyrrolidone.

4.0 Discussion

The FA and DA are composed of water, 2-PYR and carbon black, and in this study, the FA and DA were deconstructed into their chemical constituents and blends of PA-12/carbon black, PA-12/water, PA-12/2-PYR and PA-12/2-PYR/water were created. The blends were characterised using DSC, FTIR and optical microscopy to understand the effect of these constituents on the thermal and microstructural characteristics of PA-12.

In the PA-12/FA and PA-12/DA blends, the FA and DA had a significant effect on the thermal behaviour of PA-12 in that a depression in both the glass transition temperature and melting temperature were observed on first heating. This was also true in the PA-12/2-PYR blends and suggests that the 2-PYR component (common to the FA and DA) was behaving as a plasticizer that mobilised the amorphous phase below T_g and promoted the melting of the crystalline phase.

In the PA-12/FA blend system (containing both 2-PYR and carbon black), the degree of crystallinity (determined from the first heating) was found to increase with increasing FA content. This is consistent with the action of 2-PYR resulting in increased polymer chain mobility and thereby facilitating the crystallisation process. However, this was not observed in the PA-12/DA blend, where the DA does not contain carbon black and also contains less 2-PYR. In relation to MJF, an increase in the degree of crystallinity (determined from the enthalpy of fusion) of the refreshed powder has also been linked to the presence of residual impurities from the DA acting to promote nucleation. (25).

The FA and DA also influenced the recrystallisation behaviour of PA-12 in that the supercooling corresponding to the onset of the recrystallisation process decreased with increasing FA and DA. This suggests that the FA and DA are facilitating the nucleation process in PA-12. The 2-PYR was found to cause a similar effect, but only when the proportion of 2-PYR reached > 4 wt.%. While it is noted that carbon black has previously been found to be acting as a nucleating agent where an increase in peak crystallisation temperature was also reported for injection moulded polyamide/carbon black composites (29), no decrease in the onset supercooling for the PA-12/CB blends was observed, and yet, optical microscopy showed that carbon black was found to limit the spherulite size. This observation would support its possible role as a nucleating agent.

Studies have previously reported that in addition to 2-PYR, water is a major constituent of the FA and DA: water is present in 65% and 83 % and 2-PYR is present in 18.7% and 3.7 % in the FA and DA, respectively (17). Furthermore, water and 2-PYR are known to interact via hydrogen bonding. This interaction arises from the NH and C=O groups that are present in 2-PYR which act as a proton donor and acceptor groups, respectively (35–37). Despite the potential for interaction between water and 2-PYR, the thermal response of the PA-12/2-PYR/water blends was comparable to that of the PA-12/2-PYR blend system indicating that the effect of the 2-PYR was not moderated by the addition of water.

In terms of the microstructure, in the PA-12/FA blends, the carbon black was largely rejected to the interspherulitic regions and the spherulite size was significantly reduced by the FA at compositions of 1 and 20 wt.% FA. Similar behaviour was observed in the PA-12/carbon black blends. This again suggests that

carbon black is capable of acting as a nucleating agent, but alternatively, the segregation of the carbon black may impede the radial growth of the spherulites. Whereas, for the PA-12/2-PYR blends, the spherulite size was comparable to PA-12 in blends of 0.38 and was slightly reduced at a composition of 8.72 wt.% 2-PYR.

In all blends, a shift in peak wavenumber of the N-H stretch was observed, when compared to PA-12. This suggests there was an interaction between the amide band of the polymer and the FA, DA and 2-PYR (33). In these blends, the shift in peak wavenumber was due to 2-PYR. Despite the observation that the C=O (PA-12) in the blends did not display evidence of peak shift, infrared spectroscopy supports the idea that the 2-PYR and PA-12 are capable of interaction in the context of the application of the FA and DA. Furthermore, a shoulder at 1690 cm^{-1} was assigned to 2-PYR, provides evidence that 2-PYR was retained in the polymer. This was also reported for parts fabricated by MJF (17).

5.0 Conclusions

The primary active constituent of the FA and DA is the 2-PYR component, the presence of which is largely responsible for plasticising the PA-12 as evidenced by the depression of the glass transition and melting temperatures. Infrared spectroscopy revealed that a proportion of 2-PYR was retained in the polymer, coupled with a suggestion of an interaction, via hydrogen bonding, between the N-H moiety in PA-12 and the C=O in 2-PYR. The presence of carbon black appeared to reduce the size of the PA-12 spherulites, consistent with heterogeneous nucleation. However, there was no corresponding increase in the temperature at which the onset of recrystallisation occurred, as would be expected if the carbon black was acting as a nucleating agent. Therefore, the action of carbon black on the crystallisation of PA-12 warrants further investigation.

Acknowledgements

To the Manufacturing Technology Centre (MTC) for supplying the HP 3D High Reusability Polyamide-12 powder, Fusing Agent and Detailing Agent to enable this research.

Table 2 Table of melting and recrystallisation parameters of PA-12 blends, where 2-PYR (FA) and 2-PYR (DA) correspond to the PA-12/2-PYR blends that yield the same composition of 2-PYR found in the FA and DA. T_g = Glass transition temperature, T_P = Peak melting and crystallisation temperature, T_O = Onset melting temperature, T_E = Last trace of melting/crystallisation, X_C = Degree of crystallinity.

Additive	wt.%	Heat 1						Cool 1				
		T_g (°C)	T_P (°C)	T_O (°C)	T_E (°C)	ΔH (Jg^{-1})	X_c (%)	T_P (°C)	T_O (°C)	T_E (°C)	ΔH (Jg^{-1})	X_c (%)
PA-12		50.37	187.2	170.6	195.7	105.3	50.3	148.3	155.8	136.4	60.5	28.9
FA	1.00	43.2	185.5	164.7	193.0	101.6	48.6	149.3	157.7	138.9	55.1	27.4
	5.00	38.2	183.2	162.1	191.8	107.0	51.1	148.8	155.4	138.9	59.5	28.4
	10.00	35.6	179.8	151.8	186.2	114.8	54.9	147.0	153.8	136.5	61.2	29.3
	20.00	34.4	173.8	139.9	181.5	116.6	55.7	141.8	147.6	129.3	66.3	31.7
DA	1.00	48.4	187.3	172.1	193.8	104.4	49.9	147.7	155.2	139.1	46.3	22.1
	5.00	43.2	185.0	167.4	192.3	104.4	49.9	149.0	157.2	136.6	56.9	27.2
	10.00	41.1	182.5	161.0	190.2	107.3	51.3	147.5	156.5	136.8	58.9	28.2
	20.00	38.5	179.0	147.8	189.0	106.3	50.8	144.8	152.0	134.1	58.4	27.9
CB	1.00	48.2	187.3	169.4	197.1	105.0	50.2	149.2	158.9	135.8	52.7	26.3
	5.00	48.9	187.7	169.7	196.0	111.2	53.1	148.2	157.4	138.8	52.2	25.0
	10.00	46.7	187.7	168.1	198.2	115.3	55.1	148.2	157.6	136.6	53.5	25.6
	20.00	47.5	187.3	169.1	195.8	117.9	56.3	148.3	157.2	137.7	57.0	27.2
Water	1.00	47.9	187.0	170.2	192.0	108.2	51.7	148.0	156.3	139.9	45.7	21.8

	5.00	47.7	186.8	170.4	192.9	111.5	53.3	149.0	156.4	139.5	55.9	26.7
	10.00	45.6	186.3	168.8	191.9	109.4	52.3	148.7	156.1	141.5	56.5	27.0
	20.00	46.4	186.3	172.4	192.8	95.1	45.4	148.8	157.4	139.0	49.7	23.7
2-PYR	0.10	48.9	185.8	168.0	191.2	103.7	49.5	149.2	155.4	140.5	57.0	27.2
	0.38	51.3	185.8	164.0	192.9	109.0	52.1	148.8	156.5	141.7	56.1	26.8
	0.50	46.1	185.3	167.1	190.8	101.5	48.5	148.7	155.8	140.4	55.6	26.5
	1.05	39.8	184.5	166.6	189.8	102.6	49.0	148.0	154.8	139.6	57.1	27.3
	1.97	46.7	185.7	167.8	191.0	107.1	51.2	149.0	155.5	141.5	58.1	27.7
	2.33	45.6	185.3	168.0	191.1	105.0	50.1	148.7	155.0	140.7	58.3	27.9
	4.07	34.8	181.8	155.4	187.2	109.3	52.2	146.0	152.1	138.8	59.5	28.4
	8.72	33.0	176.3	152.8	181.5	108.1	51.6	141.7	147.8	131.5	61.1	29.2
FA (2-PYR + Water)	0.38	48.9	187.8	167.2	193.9	93.9	44.9	148.0	155.9	139.4	48.7	23.3
	1.97	47.9	186.0	165.7	192.1	91.4	43.7	146.8	155.9	138.5	49.3	23.6
	4.07	38.9	183.2	157.8	190.3	97.5	46.6	145.0	152.9	135.5	51.6	24.6
	8.72	35.0	179.2	150.4	185.7	98.3	46.9	142.7	150.4	133.8	53.7	25.6
DA (2-PYR + Water)	0.10	49.2	189.0	169.2	194.8	95.5	45.6	148.5	156.2	139.6	49.5	23.7
	0.50	48.6	187.5	170.7	193.5	88.6	42.3	147.8	155.1	140.8	48.5	23.2
	1.05	47.5	186.0	168.9	192.0	84.7	40.5	147.7	155.3	140.6	47.4	22.6
	2.33	47.2	186.0	168.3	192.9	88.2	42.2	147.7	154.8	139.4	49.3	23.6

Table 3 FTIR peak assignments for PA-12.

Sample	FTIR Peaks [cm^{-1}]	Peak assignment
PA-12	3292.9	Hydrogen bonded N-H stretch
	2917.4	CH_2 asymmetric stretch
	2849.1	CH_2 symmetric stretch
	1633.5	C=O stretch
	1540.4	C-N stretch, C=O in plane bending
	1367.4	CH bend, CH2 twist
	1269.0	C-N stretch, C=O in plane bending
	1124.3	C-C stretch
	944.8	CONH in plane
	719.4	CH_2 rocking

References

1. Partanen J, Khajavi S, Flores Ituarte I, Khajavi SH. Challenges to implementing additive manufacturing in globalised production environments. Int J Collab Enterp. 2016;5:232–47.

2. Hewlett-Packard. HP Multi Jet 3D Printing Technology - The Latest 3D Printing Technology from HP | HP® United Kingdom [Internet]. 2020. Available from: https://www8.hp.com/uk/en/printers/3d-printers/products/multi-jet-technology.html

3. Galati M, Calignano F, Defanti S, Denti L. Disclosing the build-up mechanisms of multi jet fusion: Experimental insight into the characteristics of starting materials and finished parts. J Manuf Process. 2020;57:244–53.

4. Morales-Planas S, Minguella-Canela J, Lluma-Fuentes J, Travieso-Rodriguez JA, García-Granada AA. Multi Jet Fusion PA12 manufacturing parameters for watertightness, strength and tolerances. Materials (Basel). 2018;11(8):1–11.

5. Tasch D, Schagerl M, Wazel B, Wallner G. Impact behavior and fractography of additively manufactured polymers: Laser sintering, multijet fusion, and hot lithography. Addit Manuf. 2019;29:2214–8604.

6. Ulbrich J, Swader R, Petry G, Cox BL, Greene RL, Eliceiri KW, et al. A syringe adapter for reduced muscular strain and fatigue. Appl Ergon. 2020 May 1;85:103061.

7. Columns VL, Using F, Manufacturing A. Buckling and Post-Buckling Behavior of Uniform and Variable-Density Lattice Columns Fabricated Using Additive Manufacturing. Materials (Basel). 2019;12:1–15.

8. Alomarah A, Ruan D, Masood S, Gao Z. Compressive properties of a novel additively manufactured 3D auxetic structure. Smart Mater Struct. 2019;2018:17.

9. Alomarah A, Masood SH, Sbarski I, Faisal B, Gao Z, Ruan D. Compressive properties of 3D printed auxetic structures: experimental and numerical studies. Virtual Phys Prototyp. 2019;15(1):1–21.

10. Stansbury JW, Idacavage MJ. 3D printing with polymers: Challenges among expanding options and opportunities. Dent Mater. 2016;32:54–64.

11. O'Connor HJ, Dickson AN, Dowling DP. Evaluation of the mechanical performance of polymer parts fabricated using a production scale multi jet fusion printing process. Addit Manuf. 2018;22:381–7.

12. Schmid M, Amado A, Wegener K. Materials perspective of polymers for additive manufacturing with selective laser sintering. J Mater Res. 2014;29(17).

13. O' Connor HJ, Dowling DP. Comparison between the properties of polyamide 12 and glass bead filled polyamide 12 using the multi jet fusion printing process. Addit Manuf. 2019;31:100961.

14. Pandelidi C, Lee KPM, Kajtaz M. Effects of polyamide-11 powder refresh ratios in multi-jet fusion: A comparison of new and used powder. Addit Manuf. 2021 Apr 1;40:101933.

15. Safka J, Ackermann M, Filip V, Machacek J, Henyš P. Mechanical Properties of Polypropylene : Additive Manufacturing by Multi Jet Fusion Technology. Materials (Basel). 2021;14:2165.

16. Sillani F, Kleijnen RG, Vetterli M, Schmid M, Wegener K. Selective laser sintering and multi jet fusion: Process-induced modification of the raw materials and analyses of parts performance. Addit Manuf. 2019;27:32–41.

17. Scherer B, Kottenstedde IL, Matysik F-M. Material characterization of polyamide 12 and related agents used in the multi-jet fusion process: complementary application of high-resolution mass spectrometry and other advanced instrumental techniques. Mater Des. 2020;151:1203–15.

18. Weast RC. CRC Handbook of Chemistry and Physics, 57th Edition. John Wiley & Sons, Ltd; 1977.

19. Frizziero L, Donnici G, Dhaimini K, Liverani A, Caligiana G. Advanced design applied to an original multi-purpose ventilator achievable by additive manufacturing. Appl Sci. 2018;8(12).

20. Palma T, Munther M, Damasus P, Salari S, Beheshti A, Davami K. Multiscale mechanical and tribological characterizations of additively manufactured polyamide 12 parts with different print orientations. J Manuf Process. 2019;40:76–83.

21. Xu Z, Wang Y, Wu D, Ananth KP, Bai J. The process and performance comparison of polyamide 12 manufactured by multi jet fusion and selective laser sintering. J Manuf Process. 2019;47:419–26.

22. Habib FN, Iovenitti P, Masood SH, Nikzad M. Fabrication of polymeric lattice structures for optimum energy absorption using Multi Jet Fusion technology. Mater Des. 2018;155:86–98.

23. Zolfagharian A, Khosravani MR, Kaynak A. Fracture resistance analysis of 3D-printed polymers. Polymers (Basel). 2020;12(2):1–18.

24. Craft G, Nussbaum J, Crane N, Harmon JP. Impact of extended sintering times on mechanical properties in PA-12 parts produced by powderbed fusion processes. Addit Manuf. 2018;22(June):800–6.

25. Riedelbauch J, Rietzel D, Witt G. Analysis of material aging and the influence on the mechanical properties of polyamide 12 in the Multi Jet Fusion process. Addit Manuf. 2019;27:259–66.

26. Cai C, Tey WS, Chen J, Zhu W, Liu X, Liu T, et al. Comparative study on 3D printing of polyamide 12 by selective laser sintering and multi jet fusion. J Mater Process Technol. 2021;288(116882).

27. Mele M, Campana G, Pisaneschi G, Monti GL. Investigation into effects of cooling rate on properties of polyamide 12 parts in the multi jet fusion process. Rapid Prototyp J. 2020;26(10):1789–95.

28. Espera AH, Valino AD, Palaganas JO, Souza L, Chen Q, Advincula RC. 3D Printing of a Robust Polyamide-12-Carbon Black Composite via Selective Laser Sintering: Thermal and Electrical Conductivity. Macromol Mater Eng. 2019;304(4):1800718.

29. Athreya SR, Kalaitzidou K, Das S. Mechanical and microstructural properties of Nylon-12/carbon black composites: Selective laser sintering versus melt compounding and injection molding. Compos Sci Technol. 2011 Feb 28;71(4):506–10.

30. Yang J, Shi Y, Yan C. Selective Laser Sintering of Polyamide 12/Potassium Titanium Whisker Composites. J Appl Polym Sci [Internet]. 2010 [cited 2019 Jan 29];117:2196–204. Available from: www.interscience.wiley.com

31. Abbott CS, Sperry M, Crane NB. Relationships between porosity and mechanical properties of polyamide 12 parts produced using the laser sintering and multi-jet fusion powder bed fusion processes. J Manuf Process. 2021 Oct 1;70:55–66.

32. Skrovanek DJ, Howe SE, Painter PC, Coleman MM. Hydrogen Bonding in Polymers: Infrared Temperature Studies of an Amorphous Polyamide. Vol. 18, National Technical Information Service. Oxford University Press; 1985.

33. Iwamoto R, Murase H. Infrared spectroscopic study of the interactions of nylon-6 with water. J Polym Sci Part B Polym Phys. 2003;41(14):1722–9.

34. Maiti KS, Samsonyuk A, Scheurer C, Steinel T. Hydrogen bonding characteristics of 2-pyrrolidinone: A joint experimental and theoretical study. Phys Chem Chem Phys. 2012;14(47):16294–300.

35. Makarov DM, Egorov GI, Kolker AM. Density of water - 2-pyrrolidone mixture a new vibrating tube densimeter from (278.15–323.15) K and up to 70 MPa. J Mol Liq. 2021;335(116113).

36. Alcalde R, Aparicio S, Garcia B, Davila MJ, Leal JM. Solute–solvent interactions in lactams–water ternary solvents. New J Chem. 2005;29:817–25.

37. Dávila MJ, Alcalde R, Aparicio S. Pyrrolidone Derivatives in Water Solution: An Experimental and Theoretical Perspective. Ind Eng Chem Res. 2009;48(2):1036–1050.

38. Athreya SR, Kalaitzidou K, Das S. Processing and characterization of a carbon black-filled electrically conductive Nylon-12 nanocomposite produced by selective laser sintering. Mater Sci Eng A. 2010 Apr 25;527(10–11):2637–42.

39. Marsh JJ, Turner RP, Carter J, Jenkins MJ. Thermal diffusivity and secondary crystallisation kinetics in poly (lactic acid). Polymer. 2019 Sep 28;179:121595.

APPENDIX B

Scanning electron microscopy of PA-12

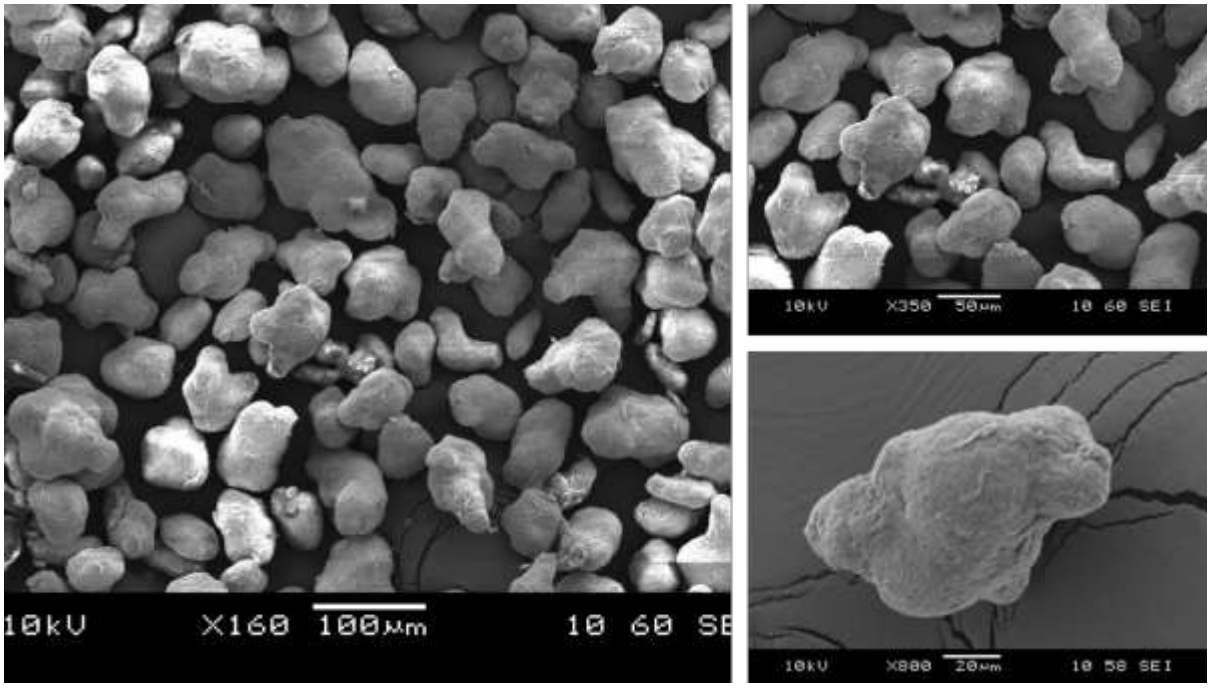

Figure B1: SEM images captured at x160, x350, x800 magnification of PA-12 powder, displaying particle shape, size and texture.

Scanning electron microscopy (SEM) was used to capture images of PA-12 powder at different magnifications to observe the size and shape of PA-12 powder particles, as displayed in Figure B1.

The size of the particles was determined using the scale bar, the particles ranged from $50 - 100\ \mu m$. A more accurate determination of the particle size is shown in section 3.1.4, by PSA. The size of powder particles determined using SEM was comparable to PSA. The shape of the powder particles appeared non-uniform, elongated and irregular in shape, though some powder particles appeared more spherical. This was also reported by M. Galati et al when examining the morphology of new MJF powder (58).

Additionally, it was reported that recycled MJF powder had a similar morphology to virgin powder (58).

The surface texture of the powder particles was also observed. The particles appeared rough and did not display evidence of cracking. In work by Rosso et al, the morphology of refreshed PA-12 used in SLS and MJF was compared (91). Unlike PA-12 used in this study, they reported evidence of cracking in both SLS and MJF grade refreshed powder, though the extent of particle cracking was more evident in SLS powder particles (91). It was noted that refreshed SLS powder was prone to more cracking due to the powder synthesis method, which involved the evaporation of ethanol (91). However, less is known about the synthesis of MJF powder therefore the cracked particle surfaces on refreshed powder could not be accounted for. Additionally, the presence of the cracked powder particles can be appointed to the recycled powder. The rough surface texture may be a result powder post-treatment to obtain a desirable particle size. Some processes that affect the surface texture of powder particles include milling and grinding which is typically used to obtain a finer particle size.

Optical microscopy of PA-12

Hot stage optical microscopy was used to capture images to illustrate coalescence of powder particles using a controlled heating rate, as displayed in Figure B2. At room temperature the shape of the powder particles was comparable to that observed by SEM, where powder particles appeared non-uniform and irregular. On visual examination, the powder particles appeared white. However, the particles appear black when looking through the eyepiece. This was because of the transmission of light from the light source to the user being blocked by the powder particles.

On heating, the powder particles appeared solid until 190 ℃, after which the coalescence rate dramatically increased and the powder particles began to melt. The melting temperature was noted as the temperature at which the particles became transparent, this occurred at a temperature of ~ 195 ℃.

At this point, the interacting particles (circled) fused together with the energy supplied on heating. Progressively, this interaction occurred over all of the powder particles within the image frame as the temperature continued to increase to 220 ℃. An upper isotherm of 220 ℃ was maintained for 5 minutes. Once in the melt, a droplet shape was formed resembling a thin film caused by the amalgamation of particles between 2 circular glass lenses. The melting temperature range was between 190 – 215 ℃. This was greater than the melting temperature range of 180 – 190 ℃ reported by S. Dadbakhsh et al, who studied the coalescence behaviour of virgin PA-12 particles used in SLS (51). The heating rate used in this study was 10 ℃/min. The authors also refer to a pre-melting stage called "softening" that occurred between 160 – 180 ℃. This may have been more visible if the optical microscope used in the experimental work had a higher resolution. The melting temperature of SLS grade PA-12 powder was reported at 186 ℃ by M. Vasquez et al using optical microscopy. The heating rate used in this study was 10 ℃/min (94). This shows that the melting temperature range of PA-12 powder varied when using optical microscopy. This is due to the melting temperature being subjective to the user as this is reported at the point at which the particles become transparent in the field of view.

The melting temperature observed by optical microscopy was comparable to the last trace of crystallinity of powder recorded by DSC on heat 1, where the last trace of crystallinity is when all the crystallinity has been erased and the entire sample has been melted.

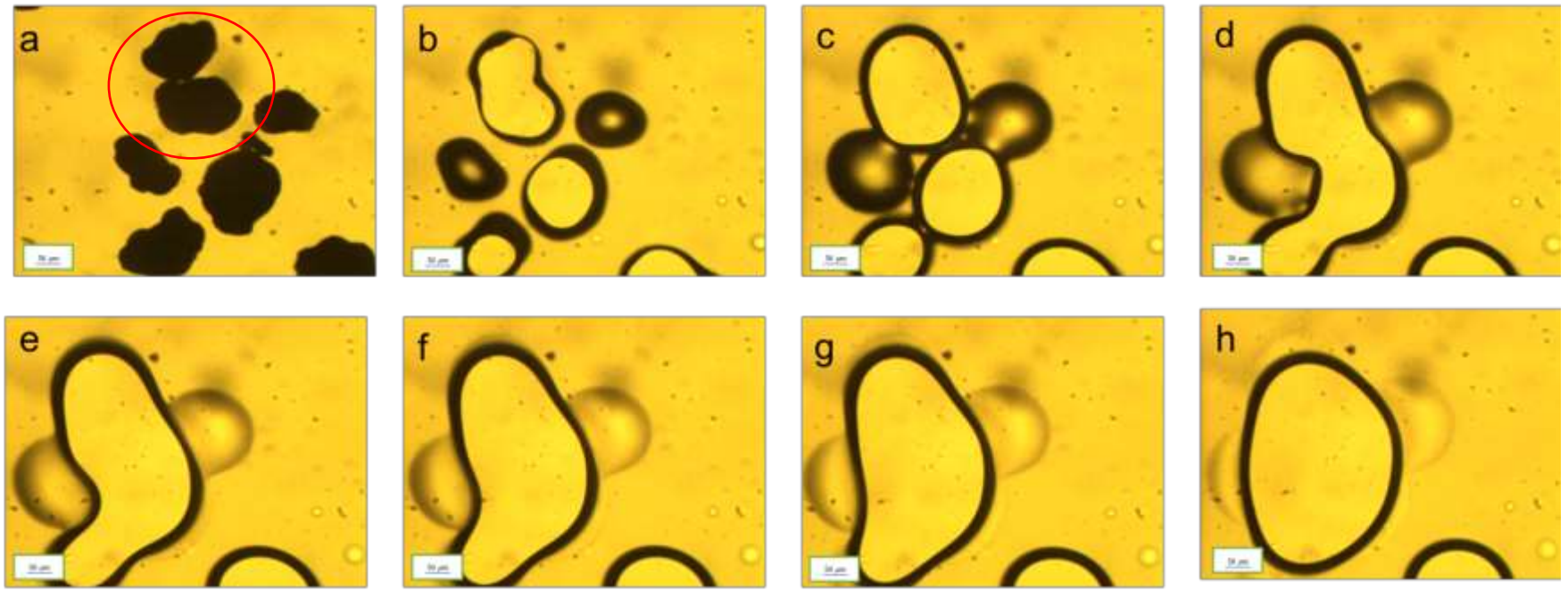

Figure B2: Optical microscopy images (at a 32x magnification without polarising filters of PA12 powder (a) room temperature (b) at 195 ℃ (c) 200 ℃ (d) 205 ℃ (e) 210 ℃ (f) 215 ℃ (g) 220 ℃ (h) 10 mins into the melt phase at 220 ℃. Scale bar to 50 µm.

SEM and optical microscopy of PA-12 blends

The interaction of carbon black and PA-12

In Chapter 6.1, it was shown that the colour of PA-12 powder in the PA-12/FA blends changed from white to black with the addition of the FA. The pigmentation of the powder increased with composition of the FA. This demonstrates that carbon black was retained in the polymer blend. Traces of the carbon black from the FA was also detected in MJF components, this is demonstrated by C. Cai et al using XRD (84). In order to closely examine the PA-12/FA powder blends, SEM images of the 1, 5, 10 and 20 wt.% FA blends were captured, these are displayed in Figure B3. The SEM images show that carbon black was deposited as a residue on the powder surface. As the composition of the FA increased, the amount of carbon black deposited onto the surface of PA-12 particles increased. In the FA, the carbon black was present as an ink suspended in a liquid medium. This allowed for a direct interaction between carbon black within the FA and PA-12 particles when the FA was added to PA-12. However, the dispersion on the powder surface was non-uniform. This suggests that as the powder transforms into a melt on heating, the distribution of carbon black within the melt will also be non-uniform.

In order to investigate the distribution of carbon black within the melt, the 5 wt.% FA blend was heated to a temperature of 220 ℃ at a heating rate of 10 ℃/min using a hot stage. Once the sample was in the melt for 5 minutes, an image was captured. This procedure was repeated with the 5 wt.% CB blend. Figure B4 shows the carbon black distributed within a melt-pool of PA-12 in the PA-12/FA and PA-12/CB blend. In the 5 wt.% FA blend, carbon black was present as an ink which was non-uniformly distributed within the polymer matrix. In the 5 wt.% CB blend, the carbon black was observed as solid black particles that were irregular in shape, these were also non-uniformly distributed within the polymer matrix. Although the distribution of carbon black in the PA-12/FA and PA-12/CB blend was non-

uniform, this shows that the PA-12/FA blend had a greater distribution of CB, as shown in Figure 6.5.2. Though, this could also be due to sample variation.

In literature, the properties of PA-12/CB composites was investigated. Athreya et al characterised PA-12/carbon black powders and parts manufactured by SLS. SEM images showed that carbon black was coated onto the surface of PA-12 powder, where the carbon black was in the form of solid particles (139). This was also observed in (41,156). Figure B5 shows an image of the 20 wt.% CB blend captured using optical microscopy. The image displays carbon black particles as darker particles than PA-12. However, they were not coated on to the surface of PA-12 powder, as in literature (41,139,156). A reason for this is that the size of carbon black in literature (41,139,156) was < 15 μm and was therefore in the nanoscale region and much smaller than PA-12 particles. Whereas, Figure 6.5.3 shows that the particle size of carbon black much larger than in literature (41,139,156). An extension of this work would involve capturing SEM images of PA-12/CB powder blends in order to closely examine the surface of PA-12 and carbon black particles at different compositions of carbon black.

It was noted in (41) that as the composition of carbon black nanoparticles increased within the blend, surface crowding of carbon black particles on PA-12 powder also increased. In turn, this caused the surface roughness of the powder particles to also increase, leading to the inhibition of physical contact between PA-12 powder particles. The SEM images shown in Figure B3 suggests that this was not observed in the PA-12/FA blend. This can be considered a beneficial feature of the FA, where the carbon black is deposited on the PA-12 in the form on an ink, leading to a reduced surface roughness of PA-12 powder particles in comparison to (41). Moreover, the rough powder surface of PA-12/CB blends in (41) was linked to poorer mechanical properties.

This data shows that carbon black, when deposited onto PA-12 in the form of the FA, had a direct interaction with PA-12 by coating the surface in the form of an ink rather than as solid particles.

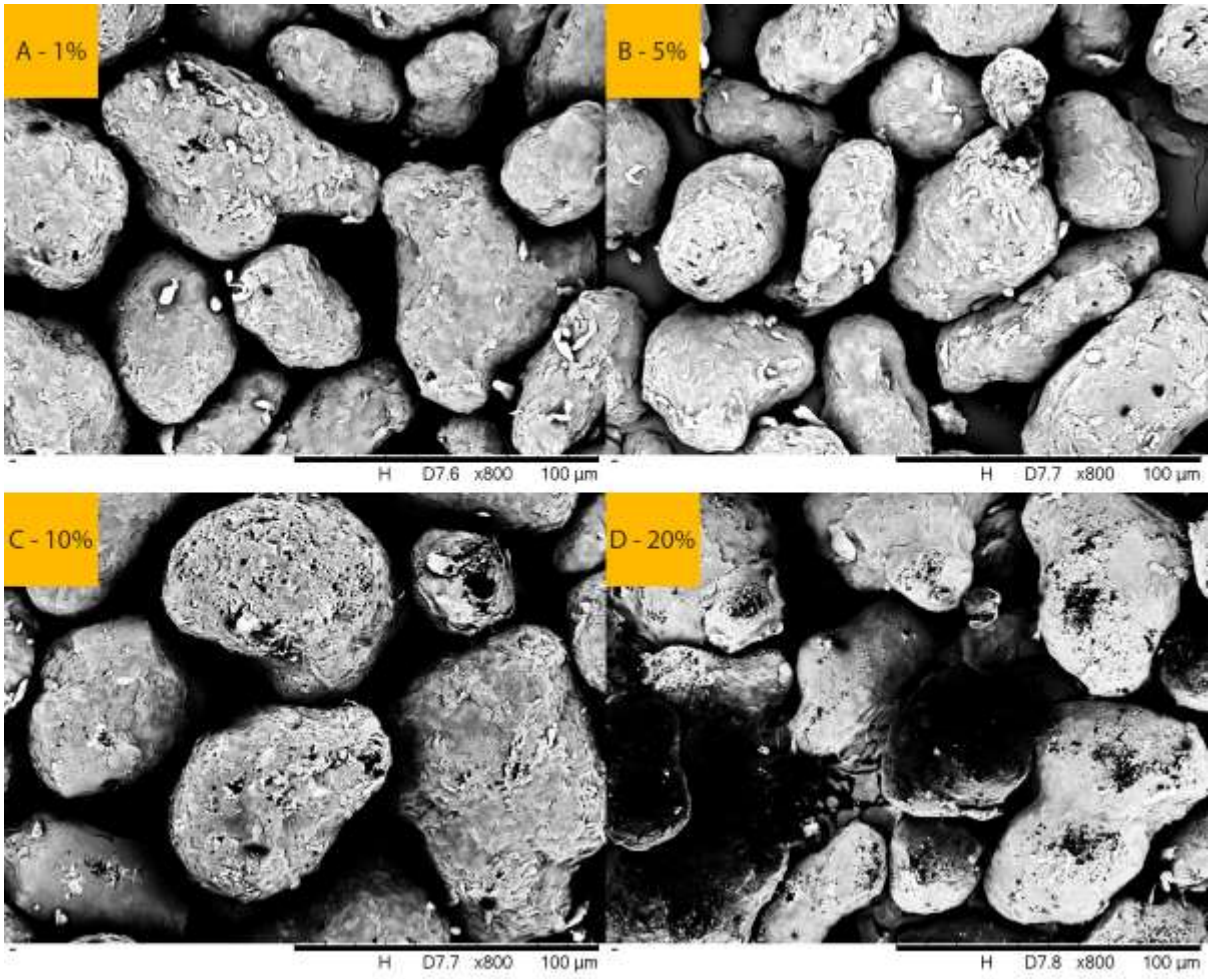

Figure B3 – SEM images at 800 x magnification of solid-liquid PA-12/FA samples at 1, 5, 10 and 20 wt.% FA. The white surface represents PA-12 and the black coating represent carbon black in the FA.

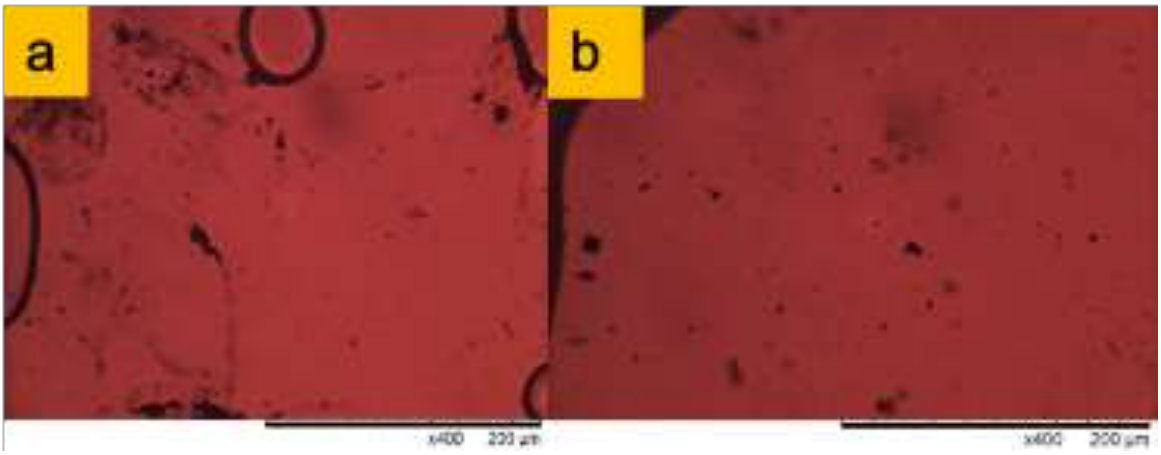

Figure B4 – Optical image of (a 5 wt.% PA-12/FA and (b 5 wt.% PA-12/CB at 220 ℃.

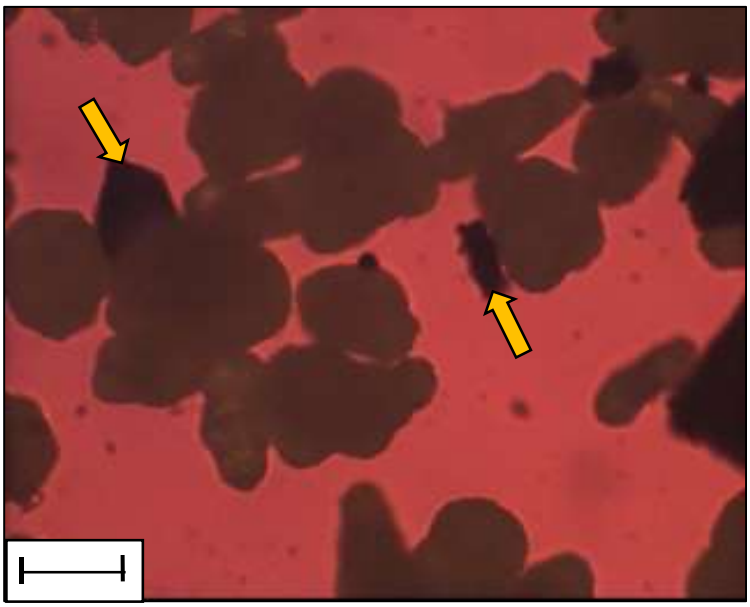

Figure B5 – Optical image of a 20 wt.% CB blend. The arrows demonstrate examples of carbon black particles within the powder blend, that appear darker than PA-12 powder. Scale bar to 50 μm.

Crystallisation of PA-12/FA blends using hot stage optical microscopy

This section will discuss the recrystallisation behaviour of the PA-12/FA blends. The blends were heated from room temperature to 220 ℃ at a heating rate of 10 ℃/min using a hot stage. They were maintained at a temperature of 220 ℃ for 5 minutes. After, the blend was cooled from 220 to 25 ℃ at a cooling rate of 5 ℃/min.

Figure B6 displays images of the 5 wt.% FA blends were captured throughout crystallisation. One image was captured 5 minutes into crystallisation from 220 ℃ and one image was captured at complete crystallisation. This composition was chosen since the FA content was not so large such that the entire image frame of the melt pool was covered by the carbon black within the FA. This enabled the spherulitic development during crystallisation to be observed. In Chapter 6.2 and 6.4, the recrystallisation behaviour of PA-12 was explored. It was speculated that carbon black influenced the recrystallisation behaviour of PA-12 in that carbon black increased in the degree of crystallinity of PA-12 by acting as an impurity to induce heterogenous nucleation or that carbon black impeded radial growth of spherulites.

In Figure B6 an earlier onset of crystallisation was observed for areas of the polymer matrix surrounding the carbon black (where t = 5 minutes). In this region, a large number of nuclei were observed and impingement was quickly achieved. Consequently, the growth of spherulites within this region was limited. On the contrary, in areas further from the carbon black, nuclei emerged later into crystallisation. The size of these spherulites was larger showing that growth was favoured in these regions. This demonstrated that the distribution of carbon black influenced crystallisation and microstructure of the polymer in localised areas.

Though MJF aims to create an even distribution of the FA across the powder bed by the use of an inkjet binder, the deposition of carbon black within the FA cannot be entirely controlled both on the surface of PA-12 powder and on formation of the melt. This suggests that the microstructure cannot be precisely controlled and will vary in localised regions of the polymer matrix.

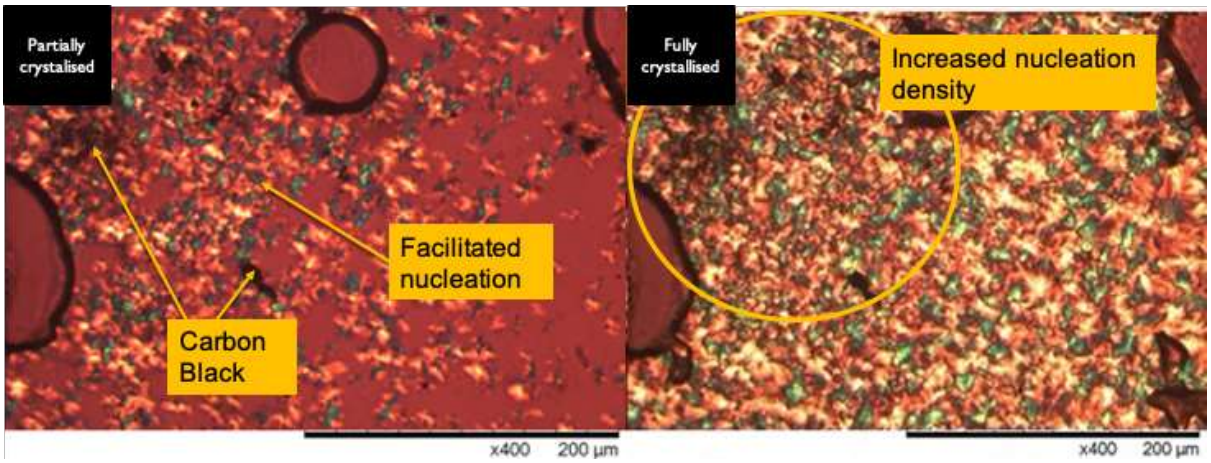

Figure B6 – The microstructural differences caused by nucleating agents. The arrow shows rapid crystallisation and nucleation in areas containing carbon black. This sample was solid-liquid PA-12/FA dispersion of 5 % wt. % FA and ran using the hot stage optical microscope at a cooling rate of 10 K / min.

APPENDIX C

Ozawa model to describe the non-isothermal crystallisation kinetics of PA-12

As described by Papageorgiou et al, the Ozawa model treats crystallisation as “an infinite number of small isothermal crystallization steps” (130).

A plot of ln[-ln(1-C(T))] vs ln ϕ was created, from which the Ozawa exponent, *m*, and the Ozawa rate, k_{ozawa} were obtained by the gradient and intercept, respectively. In this case, k_{ozawa} is a function of temperature (131). In a plot of ln[-ln(1-C(T))] vs ln ϕ, C(T) is the relative crystallinity and ϕ is the cooling rate.

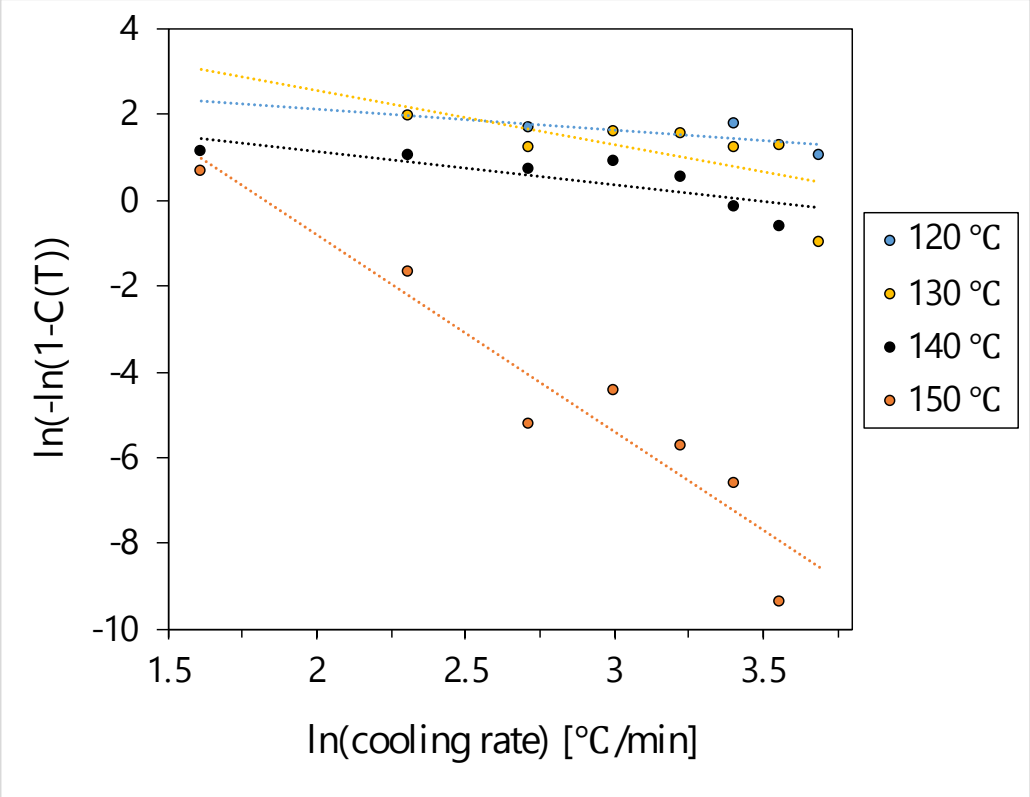

Figure C1: Ozawa plot of ln[-ln(1-C(T))] vs ln(time) vs ln(cooling rate) for PA-12.

In Ozawa's original work, showing the crystallisation behaviour of PET, it was reported that a series of linear parallel lines were obtained within the temperature range of crystallisation (131). The Ozawa plot is shown in C1 and was constructed from data points within the temperature range 120 – 150 ℃, since this covers the entire crystallisation range for all cooling rates explored. It was clear that at higher temperatures, the data deviated from a linear line by curving downwards. Additionally, the slope was steeper at higher temperatures. This shows that the experimental data did not follow the same trend as the Ozawa's original work. In Ozawa's original work on poly(ethylene terephthalate), it was stated that "the slopes of the lines suggest nuclei of crystallisation of poly(ethylene terephthalate) are randomly formed during crystallization…". Additionally, the magnitude of the slopes appeared to be constant, where values of 3.4, 3.6 and 3.6 was obtained at 493, 295 and 500 K, respectively (131). T. Liu et al also implement the Ozawa model on Poly(Aryl Ether Ether Ketone Ketone). In their work, the data did not show a linear trend and instead "obvious zig-zag lines" were observed. This made it difficult to determine an accurate value for the slope and suggested that m was not constant with temperature. It was concluded that the Ozawa equation did not accurately describe the crystallisation kinetics of PEEKK due to the significant presence of secondary crystallisation (132). In Figure 5.2.1, it can be argued that the series of data points also do not show a straight line and instead show a zig-zag pattern. This would lead to the conclusion that the Ozawa model does describe the crystallisation kinetics of PA-12.

In other work, on poly(ethylene terephthalate), the data points also deviated from a straight line (133). Optical microscopy was used to obtain information on the morphology of the crystallites and any other reasons for non-linearity. Optical micrographs showed that in addition to bulk nucleated spherulites, there was a narrow region of transcrystallinity. This was due to very dense nucleation on the polymer surface which led to unidirectional growth perpendicular to the polymer surface. This was linked to spatial constraints in spherulitic growth caused by impingement and transcrystallisation, where the spherulite growth is impeded by dense instantaneous nucleation on the polymer surface.

McFerran et al, also use the Ozawa model on PA-12 (found in automotive multilayer tubing) (93). The same trend was found where the data points curved downwards, deviating from the linear line. The deviation was ascribed to a two-stage process of crystallisation, primary and secondary crystallisation. Following this, values for *m* ascribed to primary and secondary crystallisation were determined. Overall, the magnitude of *m* decreased for secondary crystallisation due to spherulite impingement slowing down crystal growth during secondary crystallisation. Additionally, the data in Figure 5.2.1 did exhibit 'zig-zag' behaviour. Therefore, it is possible that the deviation was due to impingement and secondary crystallisation.

The Ozawa parameters are listed in Table C1. The Ozawa exponent did not show a trend with temperature. Interestingly, some values of *m* were extremely small. At T_c = 120 and 140 ℃, *m* = 0.49 and 0.78, which were small in comparison to literature (93). This is likely due to secondary crystallisation (132). However, at T_c = 150 ℃ the Ozawa exponent *m* = 4.58 which was considerable larger than the other values. The rate constant did not display a trend, the rate for T_c = 130 and 150 ℃ was 166 and 4214 min^{-1}. This data is differs to literature (93). The R^2 values were poor, ranging from 0.3933 – 0.9148. This is unsurprising since the data deviated from the straight line. The unjustified values of parameters *m* and *K* to literature are justified by the low R^2 values. The varying value of *m*, large rate constants and low R^2 values shows that the Ozawa model cannot be used to describe the non-isothermal crystallisation kinetics of PA-12.

Table C1 – Ozawa parameters showing the ozawa exponent, m, the Ozawa rate, *K* and R^2.

Temperature [°C]	*m*	ln*K*	*K* [min^{-1}]	R^2
120	0.49	3.10	22.24	0.3933
130	1.28	5.11	166.04	0.4219
140	0.78	2.71	14.99	0.6650
150	4.58	8.35	4214.98	0.9148

Combined Avrami and Ozawa model to describe the non-isothermal crystallisation kinetics of PA-12

Liu et al combined both the Avrami and Ozawa equation to describe the non-isothermal crystallisation kinetics of Poly(Ary1 Ether Ether Ketone Ketone) (PEEKK) (132). This was used This was used since the Avrami equation modified by Jeziorny was used to describe only the primary non-isothermal crystallisation process. The Ozawa equation also failed to describe the non-isothermal crystallisation kinetics of this PEEKK.

In the combined Avrami and Ozawa model, a graph of log cooling rate vs log time is plotted as a function of relative crystallinity (X_t). The line of best fit passes through each cooling rate as a function of X_t. The parameter *b,* which is the ratio of the Avrami and Ozawa exponent ($b = n/m$), and *F(T)*, which is the kinetic parameter, were obtained from the gradient and intercept, respectively.

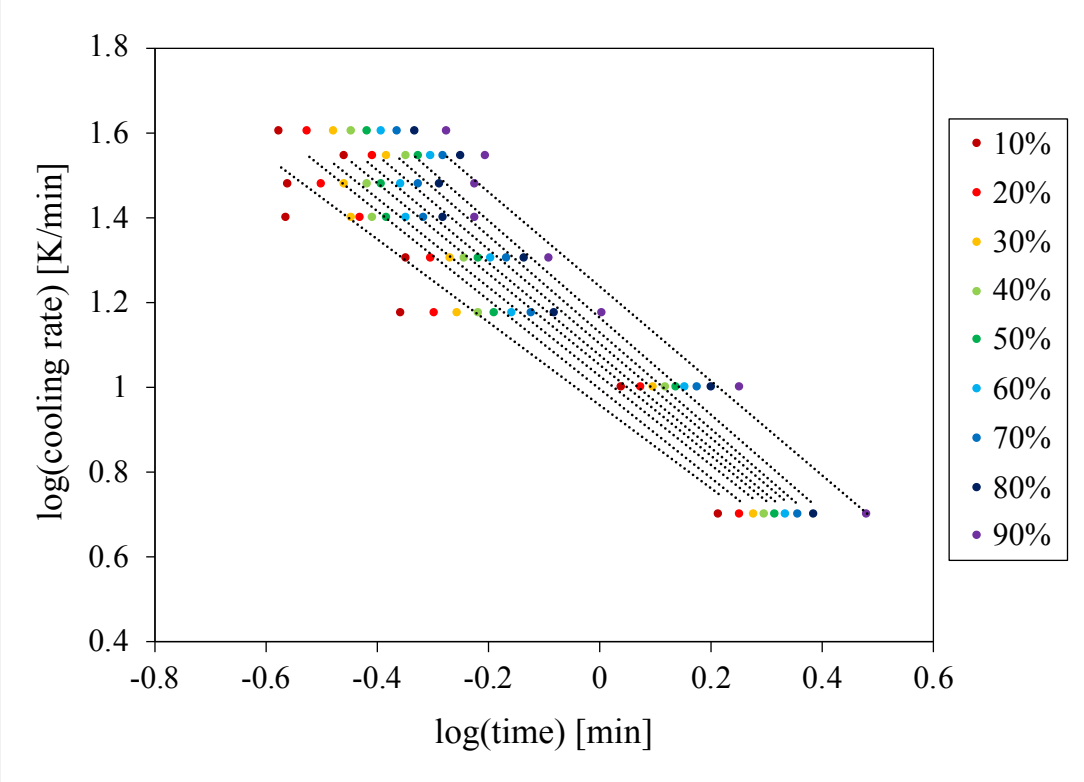

Figure C2 – Avrami-Ozawa plot for PA-12.

Figure C2 shows the Avrami-Ozawa plot that was plotted for X_t = 0.1, 0.2, 0.3, 0.4, 0.5, 0.6, 0.7, 0.8 and 0.9. The data shows a negative corelation for each X_t, in agreement with N. McFerran who studied the crystallisation kinetics of PA-12 used in automotive layer tubing (93). This trend was also observed by J. Li et al who study the non-isothermal crystallisation kinetics of polyamide-6 filled with multi-walled carbon nanotubes (135).

The parameters, *b*, *F(T)* and R^2 are displayed in Table C2. The value of *b* increased slightly as a function of X_t and ranged from 0.98 – 1.15. This suggests the the Avrami and Ozawa exponent were similar since they were within the region of 1 and the difference was 0.13. In the work of Lui et al, *b* was said to have remained constant and varied by ~0.1 (132). In other studies, *b* was reported to have remained constant and varied by ~0.04 (136). Whereas, in the work of N.McFerran et al, it was claimed that *b* decreased

as X_t increased. At $X_t = 0.2$, $b = 0.659$ and at $X_t = 0.9$, $b = 0.425$. The difference between the upper and lower limit of b was 0.234. The trend in b with X_t was explained by the time taken to reach complete crystallisation. Whereby, a higher cooling rate increased the time taken for crystallisation and a lower cooling rate increased the time taken for crystallisation. Therefore, the value of b is considered to the dependant on cooling rate.

The parameter *F(T)* is the kinetic parameter. Table 5.4.1 shows that *F(T)* increased systematically with X_t, in agreement with Liu et al (132). At a cooling rate of $X_t = 10$ %, *F(T)* was 9.08, whereas at a cooling rate of $X_t = 90$ %, *F(T)* was 17.30. The increase of *F(T)* with X_t suggests that at a unit crystallisation time, a higher cooling rate should be used to increase the degree of crystallinity (93,129).

Table C2 – Table of Avrami-Ozawa parameters showing the relative crystallinity, X_t, b, F(T) and R^2.

X_t [%]	*b* *a=n/m*	F(T)	R^2
10	0.9773	9.08	0.901
20	1.0451	9.94	0.929
30	1.0466	10.62	0.923
40	1.0754	11.28	0.929
50	1.0904	11.92	0.931
60	1.1142	12.62	0.938
70	1.1302	13.47	0.945
80	1.1461	14.61	0.950
90	1.1098	17.30	0.964

Overall, the non-isothermal crystallisation data as described by the combined Avrami-Ozawa equation was consistent with Liu et al (132). For example, a negative correlation in a graph of log(cooling rate) vs log(time); an increase in F(T) with relative crystallinity; and *a* remained constant with relative crystallinity. Therefore, the combined Avrami and Ozawa equation was successful in describing the non-isothermal crystallisation kinetics of PA-12.

Comparison of non-isothermal crystallisation models

A range of models were used to assess the non-isothermal crystallisation kinetics of PA-12, these were the Jeziorny-modified Avrami model and the Caze model.

To determine the quality of fit of data, R^2 was evaluated for the Ozawa model, Jeziorny-modified Avrami model and combined Avrami-Ozwa model. Of which, the Jeziorny-modified Avrami model had the greatest R^2 in excess of > 0.99. The combined Avrami-Ozawa model also produced reasonable values of R^2. The Ozawa model produced the lowest R^2, the model did not yield a series of straight lines and instead a curve was produced.

The R^2 data is consistent with the success of the model. The Jeziorny-modified Avrami model and the combined Avrami-Ozawa model had the greatest R^2 values. The Jeziorny-modified Avrami model enabled the transition between primary and secondary crystallisation to be identified, in which the parameters associated with primary and secondary crystallisation were evaluated. The Jeziorny rate, Z_c, showed a dependency with cooling rate in that the Jeziorny rate increased with cooling rate. Additionally, the values of *n* were large for primary crystallisation suggesting complex modes of crystal nucleation and growth. This is unsurprising since non-isothermal crystallisation is a dynamic process. The combined Avrami-Ozawa model showed that the ratio between the Avrami and Ozawa exponent was consistent and the kinetic parameter, *F(T)*, increased with relative crystallinity. Therefore, the

Jeziorny-modified Avrami model and the combined Avrami-Ozawa model were adequate in describing the crystallisation kinetics of PA-12.

The Caze model was also successful in describing the average Avrami exponent. However, in this work, a large range of cooling rates were explored which may result in varying mechanisms of nucleation and growth. This method is somewhat advantageous since an average parameter for a range of non-isothermal conditions is produced. Therefore, it is more applicable to industrial processes where a range of non-isothermal conditions are experienced. To strengthen the meaning of the average Avrami exponent produced by this model, a smaller range of cooling rates can be used to determine the average Avrami exponent. This method is a quick method to determine the average Avrami exponent.

Meanwhile, some models were unable to describe the non-isothermal crystallisation kinetics of PA-12, such as the Ozawa model. In Ozawa's original work, secondary crystallisation was neglected. In turn, since PA-12 exhibits secondary crystallisation, the Ozawa model was unsuccessful. As such, the Ozawa model had the lowest R^2 values.

APPENDIX D

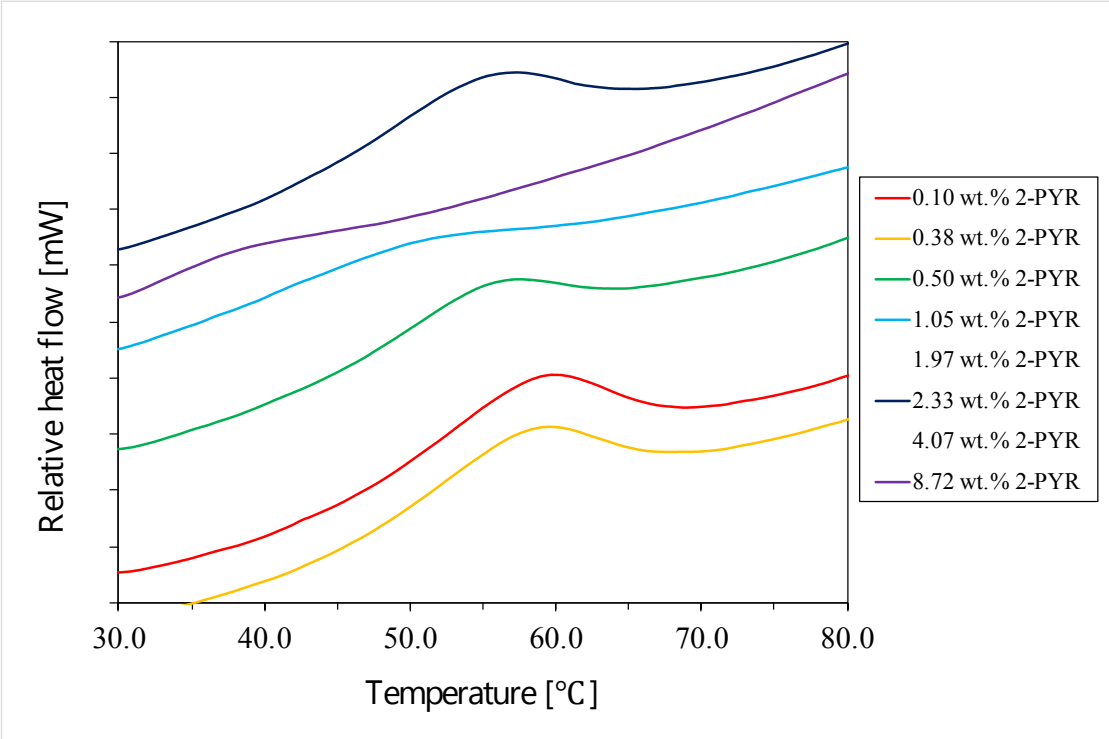

Figure D1 – The T_g of virgin PA-12/2-PYR blends.